



City Research Online

City, University of London Institutional Repository

Citation: De Fazio, C. (2021). From Entanglement to Hydrodynamics: Exploring the Role of Quasiparticles in Integrable Quantum Field Theory. (Unpublished Doctoral thesis, City, University of London)

This is the accepted version of the paper.

This version of the publication may differ from the final published version.

Permanent repository link: <https://openaccess.city.ac.uk/id/eprint/28087/>

Link to published version:

Copyright: City Research Online aims to make research outputs of City, University of London available to a wider audience. Copyright and Moral Rights remain with the author(s) and/or copyright holders. URLs from City Research Online may be freely distributed and linked to.

Reuse: Copies of full items can be used for personal research or study, educational, or not-for-profit purposes without prior permission or charge. Provided that the authors, title and full bibliographic details are credited, a hyperlink and/or URL is given for the original metadata page and the content is not changed in any way.

City Research Online:

<http://openaccess.city.ac.uk/>

publications@city.ac.uk

**From Entanglement to Hydrodynamics:
Exploring the Role of Quasiparticles in
Integrable Quantum Field Theory.**



Cecilia De Fazio

City, University of London
Department of Mathematics

Thesis submitted for the degree of

Doctor of Philosophy

22nd November 2021

Contents

	Page
List of Figures	x
List of Tables	xiii
Acknowledgement	xv
Declaration of Authenticity	xvii
Abstract	xix
Introduction	1
1 Scattering picture in integrable quantum field theory	7
1.1 Integrability	7
1.2 Diagonal S-matrix	10
1.2.1 Bootstrap equations for two-particle S-matrix	11
1.2.2 Pole structure of the two-particle S-matrix	12
1.2.2.1 Stable bound states	12
1.2.2.2 Unstable bound states	13
PART I : Entanglement content of localised excitations.	17
2 Generalities on entanglement	17
2.1 Entanglement in quantum systems	17
2.2 Bipartite systems in pure states: a simple criterion	18
2.2.1 The Schmidt decomposition	20
2.2.2 What is a good measure of entanglement?	21
2.3 Bipartite entanglement measures of pure states	23
2.3.1 Entanglement measured by entropies	24
2.3.2 Entanglement measured by negativities	26

3	Techniques in integrable quantum field theories	29
3.1	Replica model	29
3.2	Branch-point twist fields	32
3.2.1	Entanglement measures as correlators	34
3.2.2	Review of previous results in the ground state	38
3.2.3	Challenges posed by the treatment of excited states	42
3.3	Form factors	46
3.3.1	Infinite-volume form factors bootstrap	47
3.3.2	Finite-volume form factors	50
4	Excited state entropies of a connected region	55
4.1	Entanglement entropies in excited states	55
4.1.1	The scaling limit	56
4.2	Doubling trick	57
4.3	Doubled replica free boson model in infinite volume	59
4.3.1	Diagonalisation of the cyclic permutation action	61
4.3.2	Example: twist-field correlator in a single-particle excitation	63
4.3.3	Form factors of $U(1)$ -fields	64
4.4	Doubled replica free boson model in finite volume	66
4.4.1	Quantisation conditions	67
4.4.2	Finite-volume matrix elements of $U(1)$ -fields	68
4.5	Rényi entropy of a single-particle excited state	69
4.5.1	Computation by contour integration	72
4.5.1.1	Step 1: converting sums to contour integrals	73
4.5.1.2	Step 2: manipulating contour integrals	73
4.5.1.3	Step 3: establishing the large-volume leading contribution	77
4.5.1.4	Step 4: identifying the vacuum-correlator and obtaining results	78
4.6	Rényi entropy of a multi-particle excited state	79
4.6.1	Distinct rapidities	79
4.6.2	Coinciding rapidities	80
4.7	Results	82
4.7.1	Example 1: second Rényi entropy of a single-particle excitation	82
4.7.2	Example 2: second Rényi entropy of a two-particle excitation	83
4.7.3	A simple polynomial structure	85

4.8	Qubit picture	86
4.8.1	Increment of entanglement entropy	89
4.8.2	Increment of single-copy entropy	91
5	Excited state entanglement of two regions	95
5.1	The case of two disconnected regions	95
5.2	Computation by branch-point twist fields	97
5.2.1	Four-point correlation functions in single-particle excited states	99
5.2.2	Multi-particle states	101
5.3	Computation by qubit picture	102
5.3.1	Results for Rényi entropies	104
5.3.2	Results for replica logarithmic negativity	105
5.4	The analytic continuation in n	107
5.4.1	Example of a single-particle excitation	107
5.5	Replica negativity of two adjacent regions	109
5.5.1	$U(1)$ -field decomposition of the $\tilde{\mathcal{T}}^2$ -field	110
5.5.2	The three-point correlation function	111
5.6	Qubit picture for multiple regions	112
5.6.1	Rényi entropies of multiple disconnected regions	112
5.6.2	Replica logarithmic negativities of disconnected regions	115
6	Entanglement increments of localised excitations	117
6.1	Summary of the main results in the free boson	117
6.2	Generalisations and extensions	121
PART II : Generalised hydrodynamics of unstable excitations		127
7	Generalised hydrodynamics of unstable excitations	129
7.1	The model	129
7.2	The thermodynamic Bethe ansatz equations	131
7.2.1	The TBA scaling function	134
7.3	Generalised Hydrodynamics	135
7.3.1	Quasiparticle description via TBA	138
7.3.2	Effects of parity violation on scattering dynamics	140
8	Set-up 1: partitioning protocol	145

8.1	The bipartite quench	145
8.1.1	Numerical analysis	147
8.2	Hydrodynamic scaling functions	148
8.2.1	Equilibrium energy currents and energy densities	149
8.2.2	Out-of-equilibrium energy currents and energy densities	151
8.3	Equilibrium physics with unstable particles	153
8.3.1	Effective velocities	154
8.3.2	Spectral densities	157
8.3.3	Emergence of bound states in the scattering dynamics	158
8.4	Out-of-equilibrium dynamics with unstable particles	161
8.4.1	Effective Velocities	161
8.4.2	Spectral densities	163
8.5	Conclusions	166
9	Set-up 2: inhomogeneous quench	169
9.1	The inhomogeneous quench	169
9.1.1	The initial state	170
9.2	Full dynamics	171
9.2.1	Tail and decay	172
9.2.2	Magnetic-fluid effect	173
9.2.3	Bath vs. no bath	174
9.3	A closer look to the subsidiary peak	175
9.3.1	Effective vs. propagation velocities	176
9.3.2	On the shape of the subsidiary peak	178
9.4	Comparison with free-particle evolution	180
9.5	Conclusions	181
	Conclusion	183
	A Contour-integral approach for two disconnected regions	187
	B Graph partition function	199
B.1	Example: graph partition function for a single-particle state	201
	C Numerics with Mathematica	205

D Numerics with iFluid	209
D.1 Generalities	209
D.2 Precision and consistency checks	210
D.3 Space and rapidity discretisations	211
References	231

List of Figures

1.1	Yang-Baxter equation for a three-particle scattering	9
2.1	Separable state vs. entangled state	19
2.2	Complementary and non-complementary regions	23
3.1	Three bipartite systems	30
3.2	Replica model with a single entanglement region	31
3.3	Action of the branch-point twist field	33
3.4	Replica model with two entanglement regions	35
3.5	Deformation of a branch-cut	44
3.6	Form factor of a local operator	47
3.7	Recursive form factor equation for matrix elements	48
4.1	Typical bipartition of a one-dimensional finite system	56
4.2	Periodic boundary conditions of bosonic fields on a finite-volume replica model	68
4.3	Contour integral manipulation	74
4.4	Increment of the n th Rényi entropy for one-, two- and three-particle excitation	85
4.5	Entanglement entropy of various five-particle states	90
4.6	Four examples of excited state contributions to entanglement entropies	92
5.1	Two disconnected regions in a closed one-dimensional system.	96
5.2	Logarithmic negativities for various n	108
5.3	Procedure of connecting two regions in a ring.	110
6.1	Cross-sectional view of increments of logarithmic negativities	119
6.2	Numerical results in two regions	125
6.3	Numerical results in a connected region	125
7.1	TBA scaling function of the $SU(3)_2$ -HSG model	134
7.2	Kernels of the $SU(3)_2$ -HSG model	141

8.1	Partitioning protocol in integrable models: emergence of steady state currents	146
8.2	The scaled energy current as a c -like function	149
8.3	Energy currents and energy densities at equilibrium	150
8.4	Out-of-equilibrium energy currents and energy densities in set-up 1	151
8.5	Effective velocities at equilibrium	155
8.6	Spectral densities at equilibrium	157
8.7	Effective velocities versus normalized spectral densities	159
8.8	Out-of-equilibrium effective velocity in set-up 1	161
8.9	Discontinuity of the occupation numbers in set-up 1	162
8.10	Out-of-equilibrium spectral densities in set-up 1	164
8.11	Non-equilibrium spectral densities vs. equilibrium spectral densities in set-up 1	165
9.1	Initial state	171
9.2	Out-of-equilibrium spectral density and effective velocity of particle + in set-up 2 (no bath): full decay of the subsidiary peak.	173
9.3	Out-of equilibrium spectral densities and effective velocities in set-up 2 (bath): magnetic-fluid effect.	174
9.4	Evolution of particle density of particle + in set-up 2	175
9.5	Phase-space analysis of the subsidiary peak of particle + at $t = 0$ in set-up 2 (no bath)	178
9.6	Phase-space analysis of the subsidiary peak of particle + at $t = 0$ in set-up 2 (bath)	179
9.7	Out-of-equilibrium particle density of particle + compared to the free-fermion evolution in set-up 2	180
B.1	Structure of the graphs	200
B.2	Graph partition function for $k = 1, n = 4$.	202
D.1	Gauss-Legendre discretisation for rapidity space	212
D.2	Numerical calibration of the discretisation parameters	213

List of Tables

8.1	Excess areas associated to the interacting and subsidiary peaks of the spectral densities	165
9.1	Numerical results for the subsidiary peak of the spectral density of particle + in the absence ($T_a = 0$) and presence ($2T_a = e^3$) of a bath.	176
D.1	Numerical values of the total integrated particle density Q_0 at several times . . .	211
D.2	Discretisation parameters and quadratures chosen for the two numerical simulations in set-up 2	212
D.3	Numerical values of the rapidity discretisation intervals	213

ACKNOWLEDGEMENT

First and foremost, I am extremely grateful to my supervisor Olalla Castro-Alvaredo for her invaluable advice and continuous support during my PhD. Her personality and expertise have been a huge source of inspiration in all my doctoral studies and also much beyond. I want also to say a huge thank you to my collaborators Benjamin Doyon, Francesco Ravanini, István Szécsényi, and Aleksandra Ziólkowska for the delightful discussions and their important contributions. Collaborating with all them has enriched me both as a physicist and a person. I am grateful to the colleagues at the maths department for being so welcoming, I have enjoyed to be part of such a warm community. In particular I wish to thank my office-mates Abeer, Abraa, Alan, Alberto, Ed, Hamish, Johann, Julia, Rebecca, Sam C., Sam W., Suvajit, Patrick, and Taka for the friendly atmosphere in our PhD-office. In the last few years I have met so many good friends that I find hard to include all them in few lines! Thank you all! A warm thank goes to my parents Rosalba and Giuseppe, and to my brother Gianluca for their immeasurable support. I also thank Alessandra and Remo for being very supportive, and for their warm welcome in their family. A special thank goes to Alessandro for being part of my life and such an inspiring person for me. Finally, I want to say a big thank you to Alessandro F., Ann, Isabella, and Luca for their incredible help in a difficult moment of my life.

DECLARATION OF AUTHENTICITY

This report contains genuine work conducted originally by the author. The work presented herein has not been submitted and/or accepted for the award of any other degree or diploma in any university. To the best of my knowledge and belief, this thesis contains no materials previously published or written by other person, except where due references has been made.

Place: London, United Kingdom

Date: 22.11.2021

Name: Cecilia De Fazio

ABSTRACT

In this thesis, we explore the role of quasiparticles in two problems that have integrability at their core: the entanglement content of excited states and the out-of-equilibrium dynamics in the presence of unstable excitations. In the first part, we consider the one-dimensional massive free boson and different partitions of a ring. We compute entanglement entropies and logarithmic negativities in states composed of multiple particle excitations, in the limit of large volume and regions' lengths. We find that the quasiparticle excitations give additive contributions to the vacuum entanglement that depend on very few properties of the state, namely the number of excitations and their (in)distinguishability, and that are independent of the connectivity of the regions. The results have a natural probabilistic interpretation as the entanglement of multi-qubit states where qubits represent the presence or absence of excitations in the regions of the partition. Such a simple structure suggests that the results obtained are universal, a suggestion that is further supported by both analytical and numerical evidence. At the heart of this universality there is the only basic assumption that particle excitations can be localised within the entanglement regions. In the second part of this thesis we apply the generalised hydrodynamic approach to study an integrable model possessing an unstable excitation in its spectrum. Because of the finite lifetime the dynamics of the unstable particle can be studied only indirectly, in terms of the constituent (stable) particles. We find that the out-of-equilibrium dynamics of the stable particles exhibits clear signatures of instability such as decay, creation of tails, and large-time stable populations of mutually interacting particles. We use these signatures to develop a more clear physical picture of the formation of the unstable excitation.

INTRODUCTION

Quantum field theory (QFT) was originally developed to connect the principles of special relativity with those of quantum mechanics, providing the most complete (experimentally verified) description of elementary particles [1]. Remarkably QFT methods have also provided a powerful way to access many-body quantum systems, giving rise to an effective description in terms of *quasiparticles* [2]. Roughly speaking, quasiparticles are a simpler way to approach a very complicated physical problem, that means that under certain conditions, some multi-body systems can be treated as if composed of fictitious bodies for which a better understanding of the problem can be achieved. An example is the emergent Bogoliubov quasiparticles in a weakly-interacting Bose gas [3].

The concept of quasiparticles plays a similar role in *integrable quantum field theories*, i.e. a special subset of 1 + 1-dimensional QFTs characterised by infinitely-many local conserved charges. However, for these theories the simplification of the physical problem comes from the combination of the low dimensionality of the system and the presence of multiple conserved charges. As a consequence the dynamics of integrable systems is severely constrained and this gives rise to a simple scattering picture: quasiparticles are here interpreted as particle excitations above the ground state, defining the incoming and outgoing states, and their two-particle scattering fully characterises any scattering processes in the system. This is a consequence of the factorisation of the scattering-matrix, and of the absence of particle production.

In this thesis we will explore the role of quasiparticles in two problems in the context of integrable quantum field theory. In part I we investigate the entanglement content of multi-particle states by looking at two famous groups of measures: *entanglement entropies* [4, 5] and *logarithmic negativities* [6, 7]. A motivation is that, as functions of the state, these measures provide a macroscopic way to capture *universal properties* of the state i.e.

properties that to a large extent are independent of the details of the theories. In previous pioneering studies, the entanglement of the ground state was found to provide an efficient measure of universal properties such as the central charge of the corresponding Conformal Field Theory (CFT) for systems at criticality [8–14], and of the mass spectrum of the QFT, for systems near criticality [15–18]. We thus aim to address the following questions: what kind of universalities does the excited state entanglement display? Can we use these features to learn more about the fundamental properties of the quasiparticles?

In part II of this thesis we will study a QFT possessing both integrability and unstable excitations. These two properties rarely feature simultaneously. However the family of the homogeneous-sine Gordon models, provides a rare example where both unstable and stable bound states are present in the spectrum [19–22]. Among these, we will consider the $SU(3)_2$ -Homogeneous sine-Gordon model, a theory whose spectrum has two stable particles of the same mass. These form an unstable bound state, associated to a particular pole structure of the scattering matrix. Because of the finite-life time the unstable particle is not part of the asymptotic spectrum and its dynamics can only be studied indirectly. Our goal for part II of this thesis is to develop a more clear dynamical picture of the formation of this unstable particle that goes beyond the pole structure of the scattering matrix.

This thesis is organised as follows:

- In Chapter 1, we review a few key concepts of integrability with a particular focus on the scattering picture.
- In Chapter 2, we start part I of this thesis. In particular, we motivate our interest in the entanglement of bipartite quantum systems, and introduce two groups of measures, namely entanglement entropies and logarithmic negativities.
- In Chapter 3, we focus on integrable QFTs, and review the main integrable-model techniques to compute the entanglement measures introduced in Chapter 2. We pay special attention on the *branch-point twist fields approach* [15], i.e. the idea of expressing the entanglement measures of interest as correlators of symmetry fields, and on how this connects to replica theories. In order to understand the structure of the correlators of branch-point twist fields, we review the main results obtained for the ground state, and the resulting universal properties that the vacuum-state entanglement

displays. We also highlight the challenges of generalizing the branch-point twist field approach to finite volume and excited states. We explain how these challenges may be resolved in the case of the massive free boson theory. To conclude, we review the form factor techniques developed to compute correlation functions of local operators, with special attention to the theory considered in the next chapters.

- In Chapter 4 (based on the works [23, 24]) we focus on the massive free boson theory. In particular, we consider a bipartite system and compute the entanglement entropies in zero-density states. We employ the *doubling trick* i.e. a free-theory technique introduced in [25], and discuss its extension to the replica model. By using a contour integral approach, we compute the twist-field correlators and derive explicit formulae for three states: a single-particle excited state, a k -particle excited state involving distinct momenta only, and a k -particle excited state consisting of equal momenta. We provide concrete examples of all three cases for the 2nd Rényi entropy. We then generalise the results to states composed of a mixture of excitations of equal and distinct momenta. To conclude this chapter we present the *qubit picture*, an alternative approach to obtain our results that gives a natural probabilistic interpretation to the entanglement content of quasiparticles. Additionally the qubit picture allows us to obtain explicit formulae for the entanglement entropy and single-copy entropy.
- In Chapter 5 (based on the works [26, 27]), we extend the techniques developed in Chapter 4 to the study of the entanglement entropies and logarithmic negativities of two regions. We start from the case of two disconnected regions, and consider zero-density states of the same kind of the previous chapter. We discuss the main differences from the previous study case, and evaluate the four-point twist field correlators in a single-particle state, and a k -particle state with all equal or distinct momenta. We present an alternative computation obtained from the qubit picture that reproduces the same results. We then discuss the case of two adjacent regions, and conclude the chapter with the generalisation of the qubit picture to an arbitrary number of disconnected regions.
- In Chapter 6 we conclude part I of this thesis. We review the main formulae obtained in the massive free boson. We then devote the remainder of the chapter to discussing possible generalisations and extensions, based on the works [23, 24, 26, 28].
- In Chapter 7 we start part II. Here, we introduce the main ingredients for the next two chapters. In particular, we introduce the $SU(3)_2$ -homogeneous sine-Gordon model,

and review the *Thermodynamic Bethe Ansatz* (TBA) [29, 30] of this model [31]. We finally introduce the GHD approach [32, 33], and generalise the TBA equations to the *Generalised Gibbs ensemble* [34], with a special attention to the model considered.

- In Chapter 8 we present the numerical results reported in [35], and obtained by implementing the partitioning protocol. We discuss the numerical results for the energy densities and energy currents. We additionally look at the phase-space dynamics. We first study the spectral densities and effective velocities of the individual particles at equilibrium, and develop a dynamical picture of the unstable excitation. We then discuss the differences observed out of equilibrium.
- In Chapter 9 we present the numerical results reported in [36], and conclude part II of this thesis. We introduce the inhomogeneous quench, and motivate our choice of the simulation parameters. We consider two numerical simulations (differing only by the presence or absence of a bath) and explore the effective velocities and densities to outline the full dynamical picture. We then provide further details on the structure of the subsidiary peak and discuss the stark difference between our results and those for a free theory.
- In the last chapter of this thesis, we draw our conclusions.
- In Appendix A we extend the contour integral approach (introduced in Chapter 4) to two disconnected regions.
- In Appendix B (based on [28]) we introduce a graph representation for the main results collected in Chapter 6.
- In Appendices C and D we review the main features of the numerical algorithms used to obtain the results presented in Chapters 8 and 9, respectively.

SCATTERING PICTURE IN INTEGRABLE QUANTUM FIELD
THEORY

1.1 Integrability

Integrability is the property linking all the results in this thesis. Therefore, we devote the first chapter to introducing a few key concepts. We will consider 1 + 1-dimensional QFTs with translation and Lorentz invariance, and focus on the scattering picture and on how integrability constrains the types of scattering that can take place. All the results reported here are standard and can be found for instance in [37, 38].

In this thesis, we consider multi-particle states that are eigenstates of the Hamiltonian. These states are well-defined in QFT and a convenient choice as they will be also eigenstates of any other conserved charges in the theory. Thanks to the relativistic invariance, we do not need to know the explicit form of the Hamiltonian to characterise such states. Denoting \hat{H} and \hat{P} the Hamiltonian and momentum operators, their eigenvalue equations for single-particle states are:

$$\hat{H} |\theta^\mu\rangle = E |\theta^\mu\rangle, \quad \hat{P} |\theta^\mu\rangle = P |\theta^\mu\rangle, \quad [\hat{H}, \hat{P}] = 0. \quad (1.1)$$

The well-known *mass-shell relation* $E^2 - P^2 = m^2$ is satisfied by the relativistic dispersion relation

$$E(\theta^\mu) = m_\mu \cosh \theta^\mu, \quad P(\theta^\mu) = m_\mu \sinh \theta^\mu, \quad (1.2)$$

where the variable θ^μ is called *rapidity* and is just a convenient way of parametrizing such solutions, and the index μ represents the particle species of the single-particle excitation¹. Now if there is only a single-particle, this cannot interact and will propagate freely, therefore if we want to describe scattering processes, we need to consider multi-particle states:

$$|\theta_1^{\mu_1}, \theta_2^{\mu_2}, \dots\rangle = |\theta_1^{\mu_1}\rangle \otimes |\theta_2^{\mu_2}\rangle \dots \quad (1.3)$$

with energy and momentum accordingly

$$E(\theta_1^{\mu_1}, \theta_2^{\mu_2}, \dots) = \sum_i m_{\mu_i} \cosh \theta_i^{\mu_i}, \quad P(\theta_1^{\mu_1}, \theta_2^{\mu_2}, \dots) = \sum_i m_{\mu_i} \sinh \theta_i^{\mu_i}. \quad (1.4)$$

In the context of integrable models, we are interested in the following situation (typically occurring in scattering experiments): the particles are initially located at very large distance to each other, then, they will be at finite distance for a finite period of time before and after the interaction and finally, waiting enough (ideally infinite time) they might be infinitely separated (free again) or involved in stable bound states. It is thus convenient to describe the process in terms of the asymptotic incoming and outgoing states and the way these are related to each other fully characterises the scattering properties of the system. We can define the *scattering matrix* (also called simply *S-matrix*) as the operator mapping the incoming states into the outgoing states. Its elements describe the scattering processes allowed by the theory, for instance the one transforming n incoming particles into m outgoing particles can be schematically written as:

$$S_{n \rightarrow m} = {}^{\text{out}}\langle \lambda_1^{\nu_1}, \dots, \lambda_m^{\nu_m} | \theta_1^{\mu_1}, \dots, \theta_n^{\mu_n} \rangle^{\text{in}}. \quad (1.5)$$

For interacting QFT these elements are typically hard to compute and require the application of perturbative techniques. However, in integrable QFT, the presence of infinitely many local conserved charges, combined with the low dimensionality of the theory, drastically constrains the particle dynamics. In the scattering context, integrable quantum field theories are fully characterised by the following three properties:

- Absence of particle production
- Purely elastic scattering processes

¹In Chapter 3, this index will include also a copy number, namely another index related to the particular geometry of the replica model.

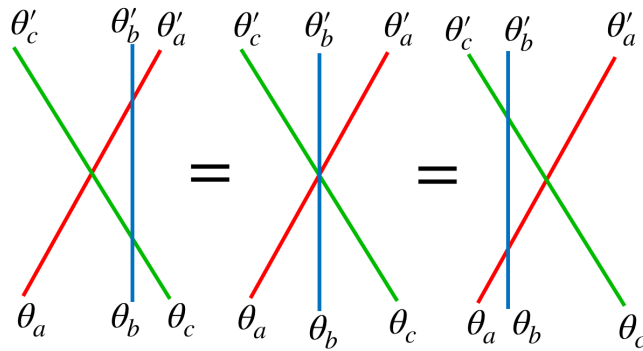


Figure 1.1 Yang-Baxter equation for a three-particle scattering. The three cases differ by a symmetry transformation therefore describe the same physics.

- Factorization of the S-matrix

Note that the statements above are not independent of each others, but they are all direct consequences of the presence of infinitely many conserved charges. The first point obviously implies that phenomena such as particle creation and annihilation cannot occur and that only scattering processes which preserve the number of particles are allowed in integrable systems. Moreover, the elastic scattering implies that as a result of the particle collisions, there might be two possible scenarios (which of course, reflect the properties of the model under consideration): particles have preserved or exchanged their own initial momenta and/or other quantum numbers. In the next subsection we will focus on the former situation, which leads to theories described by a diagonal scattering matrix. This is indeed the case for all the theories analysed in this thesis. The latter scenario (that is, when momenta and/or quantum numbers are exchanged) encodes a more complicated dynamics and leads to theories which are characterised by a non-diagonal scattering matrix (a famous example is the Sine-Gordon model [39]).

Finally, the factorization of the S-matrix can be understood from the following considerations: in the incoming and outgoing basis, one-particle states are characterised by wave functions associated to the solutions of the field equations, and these are well-localised (in momentum or rapidity space) around the center of the wave packet. In non-integrable models the amplitudes of these wave packets keep typically a trace of the details of the scattering process and these are encoded in some parameters characterising the states, i.e. the impact parameters. For instance the impact parameters help us to understand the order of the scattering events (i.e. collisions involving a certain number of particles at a certain finite time and finite length). In contrast, in integral models², for each particle it is possible to shift

²Remarkably, this can be shown to hold in the presence of just two independent conserved quantities [40].

differently the center of the wave packets through the action of a local operator associated to higher charges of the theory [37, 40]. Since this operator commutes with the Hamiltonian, its action must lead to the same physics. As a consequence the S-matrix is independent of the impact parameters. The argument above can be more rigorously expressed in the form of the *Yang-Baxter* equation [41, 42]. A graphical example is displayed in Fig. 1.1 for three particles. The three-particle scattering matrix decomposes into two-particle contributions and is independent of the order of scattering events. The generalisation of the Yang-Baxter equations to n -particle scattering implies the factorization of the corresponding S-matrix into $n(n-1)/2$ two-particle terms. Hence, in integrable models we need only to characterise the two-particle S-matrix in order to fully understand any scattering process involved in the system.

1.2 Diagonal S-matrix

In this thesis we only consider theories with scattering matrices in a diagonal form. In this case we can express the action of two-particle S-matrix on two-particle states as:

$$|\theta_1^{\mu_1}, \theta_2^{\mu_2}\rangle^{in} = S_{1,2}(\theta_1^{\mu_1}, \theta_2^{\mu_2}) |\theta_1^{\mu_1}, \theta_2^{\mu_2}\rangle^{out}. \quad (1.6)$$

Since the asymptotic incoming and outgoing states coincide we can adopt the following convention:

$$\begin{aligned} |\theta_1^{\mu_1}, \theta_2^{\mu_2} \dots, \theta_k^{\mu_k}\rangle^{in} &:= |\theta_1^{\mu_1}, \theta_2^{\mu_2} \dots, \theta_k^{\mu_k}\rangle \propto Z_{\mu_1}(\theta_1^{\mu_1}) Z_{\mu_2}(\theta_2^{\mu_2}) \dots Z_{\mu_k}(\theta_k^{\mu_k}) |0\rangle, \\ |\theta_1^{\mu_1}, \theta_2^{\mu_2} \dots, \theta_k^{\mu_k}\rangle^{out} &:= |\theta_k^{\mu_k}, \theta_{k-1}^{\mu_{k-1}} \dots, \theta_1^{\mu_1}\rangle \propto Z_{\mu_k}(\theta_k^{\mu_k}) Z_{\mu_{k-1}}(\theta_{k-1}^{\mu_{k-1}}) \dots Z_{\mu_1}(\theta_1^{\mu_1}) |0\rangle, \end{aligned} \quad (1.7)$$

where the ordering of the rapidities indicates which state is considered. In particular, the operators $Z_{\mu_1}, Z_{\mu_2}, \dots, Z_{\mu_k}$ satisfy the Zamolodchikov-Faddeev algebra [39], defining the scattering properties of the theory and in particular the S-matrix:

$$Z_{\mu_1}(\theta_1^{\mu_1}) Z_{\mu_2}(\theta_2^{\mu_2}) = S_{\mu_1, \mu_2}(\theta_1^{\mu_1}, \theta_2^{\mu_2}) Z_{\mu_2}(\theta_2^{\mu_2}) Z_{\mu_1}(\theta_1^{\mu_1}), \quad \theta_1^{\mu_1} > \theta_2^{\mu_2}. \quad (1.8)$$

Such operators may be interpreted as excitations over the ground state and the indices μ_i s indicate the corresponding particle species. In free theories these operators are simply the creation operators generating the Fock space of the free theory. In a similar way, the operators

above span the analogue of a Fock space for the integrable theory.

1.2.1 Bootstrap equations for two-particle S-matrix

In this and the next subsections, we provide a brief review of the fundamental properties of the two-particle diagonal S-matrix. One can easily note that the Yang-Baxter equations are trivially satisfied for diagonal scattering, however other constraints can almost totally fix the form of the two-particle scattering matrix. Among these, the symmetries of the theory considered play an important role. In particular, Lorentz invariance implies that scattering matrix elements depend only on rapidity differences

$$S_{\mu_1, \mu_2}(\theta_1^{\mu_1}, \theta_2^{\mu_2}) = S_{\mu_1, \mu_2}(\theta_1^{\mu_1} - \theta_2^{\mu_2}) \quad (\text{Lorentz invariance}). \quad (1.9)$$

Moreover, for parity invariant theories the S-matrix is symmetric

$$S_{\mu_1, \mu_2}(\theta) = S_{\mu_2, \mu_1}(\theta) \quad (\text{parity symmetry}), \quad (1.10)$$

where we have introduced the rapidity difference $\theta := \theta_1^{\mu_1} - \theta_2^{\mu_2}$. In part II of this thesis we analyse a theory that does not satisfy the property above as it breaks the parity invariance. Other properties come from general field theory considerations and are:

$$S_{\mu_1, \mu_2}(\theta) = (S_{\mu_1, \mu_2}(-\theta^*))^* \quad (\text{real analyticity}), \quad (1.11)$$

$$S_{\mu_1, \mu_2}(\theta) S_{\mu_1, \mu_2}(-\theta) = \mathbb{1} \quad (\text{unitarity}), \quad (1.12)$$

$$S_{\mu_1, \mu_2}(\theta) = S_{\mu_1, \bar{\mu}_2}(i\pi - \theta) \quad (\text{crossing symmetry}), \quad (1.13)$$

where $\bar{\mu}$ denotes antiparticles. For many theories [39] the equations above, along with additional requirements for bound states (if there are any) that we will introduce in a while, are sufficient to fix the S-matrix completely, and in general they provide the basis for the *S-matrix bootstrap* namely the procedure whereby a solution for the two-particle S-matrix can be found. In some cases the solutions may be fixed up to some functions that do not involve new poles in the physical sheet. This problem is known as the *CDD ambiguity* [43] and usually requires other means to obtain the exact S-matrix solution.

1.2.2 Pole structure of the two-particle S-matrix

By using analyticity arguments [39] it is possible to identify the physical domain on the θ -plane of the two-particle S-matrix. This domain is usually called the *physical sheet* and is precisely given by $\text{Im}(\theta) \in [0, \pi]$. Bound states are identified with a single-pole lying on the imaginary axis in the physical sheet. Some theories present poles in the unphysical sheet which can (sometimes) be identified with unstable particles, i.e. bound states that do not survive in the asymptotic states but do affect the dynamics of the stable particles. Examples of theories with such a feature are the homogeneous sine-Gordon models [19–22] introduced in the introduction. In part II of this thesis we will focus on the simplest of these theories. Although we are not going to treat theories with stable bound states, below, we want to introduce them for clarity, and to justify how they differ from the “resonance” poles that we will see in part II.

1.2.2.1 Stable bound states

We consider the scattering process $\mu_1 + \mu_2 \rightarrow \mu_3$ such that a stable particle of type μ_3 is created by the collision of a type- μ_1 and a type- μ_2 particle at rapidity $\theta = iu_{\mu_1 \mu_2}^{\mu_3}$ with $u_{\mu_1 \mu_2}^{\mu_3} \in [0, \pi]$. Crucially integrability imposes that stable bound states are still part of the asymptotic particle content and thus are on the same footing as the other particles (this is known as *nuclear democracy* principle [44]). The S-matrix near the bound-state pole can be expressed as:

$$S_{\mu_1 \mu_2}(\theta) \sim i \frac{(\Gamma_{\mu_1 \mu_2}^{\mu_3})^2}{\theta - iu_{\mu_1 \mu_2}^{\mu_3}}, \quad (1.14)$$

where $\Gamma_{\mu_1 \mu_2}^{\mu_3}$ is the on-shell three-particle vertex functions. The conservation of energy and momentum in the scattering process implies a relation between the masses of the particles and the pole position

$$m_{\mu_3}^2 = m_{\mu_1}^2 + m_{\mu_2}^2 + 2m_{\mu_1} m_{\mu_2} \cos u_{\mu_1 \mu_2}^{\mu_3}. \quad (1.15)$$

The existence of the bound state implies that also single-poles in the other channels, namely $S_{\mu_1 \mu_3}(iu_{\mu_1 \mu_3}^{\mu_2})$ and $S_{\mu_2 \mu_3}(iu_{\mu_2 \mu_3}^{\mu_1})$, are singular. Note that (1.15) can be seen as the geometrical relation known as *Carnot’s theorem* where the sides of the triangles are given by the masses m_i, m_j and m_n , this implies a geometric relation among the external angles of this triangle:

$$u_{\mu_1 \mu_2}^{\mu_3} + u_{\mu_1 \mu_3}^{\mu_2} + u_{\mu_2 \mu_3}^{\mu_1} = 2\pi, \quad (1.16)$$

and leads to the consistency for the S-matrix amplitudes:

$$S_{\mu_4, \bar{\mu}_3}(\theta) = S_{\mu_4, \mu_1}(\theta + i\bar{u}_{\mu_3 \mu_1}^{\mu_2}) S_{\mu_2, \mu_4}(\theta - i\bar{u}_{\mu_2 \mu_3}^{\mu_1}) \quad (\text{bootstrap equation}), \quad (1.17)$$

where the particle of type μ_4 is only involved indirectly and is called the “spectator” particle. The equation above provides an additional S-matrix constraint in the presence of stable bound states.

1.2.2.2 Unstable bound states

We consider a scattering process $\mu_1 + \mu_2 \rightarrow \tilde{\mu}$ where the resulting particle is now unstable. This corresponds to having a singularity in the S-matrix at rapidity

$$\theta_R = \sigma_{\mu_1 \mu_2}^{\tilde{\mu}} - i\bar{\sigma}_{\mu_1 \mu_2}^{\tilde{\mu}}, \quad (1.18)$$

with a pole lying in the non-physical sheet, i.e. $\bar{\sigma}_{\mu_1 \mu_2}^{\tilde{\mu}} > 0$. The parameter $\sigma_{\mu_1 \mu_2}^{\tilde{\mu}}$ is called *resonance parameter* and is a characteristic of the theory.

Unlike stable particles, the unstable excitations are not part of the asymptotic spectrum and their dynamics is not described by elements of the S-matrix, therefore the bootstrap equation (1.17) cannot be formulated for them³. Of course, the mass conservation is still a valid constraint and imposes that unstable particles can be created if the centre-of-mass energy of the two particles is close enough to the mass of the unstable particle $M_{\tilde{\mu}}$. This last property is quite general and holds for any bound states, but additionally unstable particles are characterised by a finite life-time. The mass $M_{\tilde{\mu}}$ and the decay width $\Gamma_{\tilde{\mu}}$ (inverse of the lifetime) can be computed via the *Breit-Wigner formulae* [46]:

$$2M_{\tilde{\mu}}^2 = \sqrt{A^2 + B^2} + A, \quad \frac{\Gamma_{\tilde{\mu}}^2}{2} = \sqrt{A^2 + B^2} - A, \quad (1.19)$$

for

$$A = m_{\mu_1}^2 + m_{\mu_2}^2 + 2m_{\mu_1}m_{\mu_2} \cosh \sigma_{\mu_1 \mu_2}^{\tilde{\mu}} \cos \bar{\sigma}_{\mu_1 \mu_2}^{\tilde{\mu}}, \quad B = 2m_{\mu_1}m_{\mu_2} \sinh \sigma_{\mu_1 \mu_2}^{\tilde{\mu}} \sin \bar{\sigma}_{\mu_1 \mu_2}^{\tilde{\mu}}. \quad (1.20)$$

Note that if $\sigma_{\mu_1 \mu_2}^{\tilde{\mu}}$ is vanishing, then $B = 0$ and the created particle has infinite life-time. The bound state becomes a “virtual state”, meaning that θ_R becomes purely imaginary as for the case of stable bound states. However the pole is still located outside the physical strip and cannot be interpreted as a stable particle of the theory.

The formulae above will be used for the $SU(3)_2$ -homogenous sine-Gordon model in Section 7.1 in order to provide a first characterization of the unstable excitation of the model.

³Although attempts to achieve this were made for instance in reference [45].

PART I : ENTANGLEMENT CONTENT OF LOCALISED
EXCITATIONS.

GENERALITIES ON ENTANGLEMENT

2.1 Entanglement in quantum systems

Entanglement is a genuine quantum phenomenon occurring between two or more parts of a quantum system. Its most direct consequence is that a local measurement performed on a subsystem may affect the outcome of other measurements potentially performed far away. When this happens we say that the quantum system is in an *entangled state*. In contrast, if the local measurement does not add any information on the other sub-parts, we say that the quantum system is in a *separable state*.

The concept of entanglement has played a crucial role in the early stages of quantum physics, where this new form of correlation was perceived as the qualitative feature that most distinguished the quantum from the classical nature [47]. It is not surprising that the existence of entanglement had been at the centre of the scientific debate for some time (a famous example is the *Einstein-Podolsky-Rosen paradox* [48]). The subsequent development of *Bell's inequalities* [49] finally made these quantum correlations accessible to experimental verification, which was first conducted by Alain Aspect and collaborators [50] using a pair of maximally entangled photons.

In the last few decades, it has become possible to control quantum correlations and entanglement has consequently been viewed as a new resource to achieve tasks that have been considered impossible or inefficient at classical level (a representative example is quantum

teleportation [51]). In this context, both technological and the theoretical progresses have raised the quest to develop efficient theoretical measures of entanglement that could not only distinguish between entangled and unentangled states but also quantify the amount of entanglement that quantum systems possess. Interestingly, a large variety of quantities have been identified as good measures of entanglement in many different contexts of many-body quantum systems [52] as in general there is not a unique way to quantify entanglement.

It is also important to stress that whether or not a state is entangled is strictly related to how the quantum system is partitioned, and in particular, the answer may be different for different partitions. This does not mean that the physics is arbitrary, but instead the partition is part of the phenomenon and is indeed a piece of information encoded in the entanglement. In this part of the thesis, we will focus on bipartite systems as bipartite entanglement measures are best understood. They are indeed the simplest realisations in which one can study the entanglement properties of a quantum state. In the next section we will analyse bipartite systems in detail and establish a simple criterion to understand whether or not a state is entangled.

2.2 Bipartite systems in pure states: a simple criterion

Consider a bipartition of a quantum system into two complementary regions, say A and B . The typical scenario that one expects to observe in experimental realisations of such a system is as follow: there are two observers, traditionally named Alice and Bob, each one accesses a restricted part of the system, (let us say that Alice makes only observations on A and Bob only on B). Formally, this simple setting requires that the total Hilbert space \mathcal{H} factorises into two component Hilbert spaces \mathcal{H}_A and \mathcal{H}_B , each one generated by a set of independent observables associated to a part of the system:

$$\mathcal{H} = \mathcal{H}_A \otimes \mathcal{H}_B . \quad (2.1)$$

A direct consequence is that an observable \mathcal{O} living in \mathcal{H}_A acts trivially on the other Hilbert space $\mathcal{O} = \mathcal{O}_A \otimes \mathbb{1}_B$. Let us now suppose that the bipartite system is in a certain state $|\psi\rangle \in \mathcal{H}$. By performing their local measurements the observers are expected to transform the state into some other state. Of course, both Alice and Bob would like to describe their outcomes in terms of the set of observables that is accessible to them. Hence, it is natural to expand the state $|\psi\rangle$ in the form:

$$|\psi\rangle = \sum_{i,j} C_{i,j} |\phi_i\rangle_A \otimes |\chi_j\rangle_B , \quad \sum_{i,j} |C_{i,j}|^2 = 1 , \quad (2.2)$$

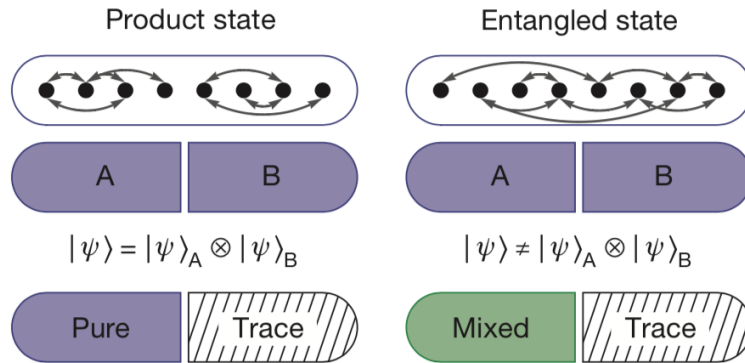


Figure 2.1 : Pictorial representation of a one-dimensional system in a separable/factorizable state (left) and in an entangled state (right). The picture is taken from [53].

where $\{|\phi_i\rangle\}_A$ and $\{|\chi_j\rangle\}_B$ are two orthonormal bases of \mathcal{H}_A and \mathcal{H}_B , respectively, and $C_{i,j}$ s are normalised complex coefficients.

Crucially, it is rather convenient to assume that the system experienced by Alice and Bob is originally in a **pure state**, and thus that the state $|\psi\rangle$ is macroscopically described by a density operator ρ , expressed in the following form:

$$\rho = |\psi\rangle\langle\psi|. \quad (2.3)$$

The main simplification is that in a pure bipartite state an observer like Alice or Bob (who can only measure one subsystem) will be equipped with a clear criterion to establish whether or not the total quantum system is in a entangled state. Indeed *as a result of a certain local measurement* (no matter in which of the two subsystems this is performed), *the observer will obtain an effective mixed quantum state if there is entanglement with the rest of the system, or a pure state if the two parts are not entangled.* A schematic representation of the possible outcomes is shown in Fig. 2.1. Thanks to this criterion, bipartite entanglement measures of pure states are conceptually easier to study, and they have been widely investigated in the literature. Remarkably, a local measurement on a sub-part can give information on the entire system without actually accessing the observables associated to the other part, in this sense entanglement unveils the presence of non-local properties in quantum systems.

An important consequence of this simple criterion is that *unentangled states are entirely factorizable.* However one should admit that it may be hard to check directly the factorizability of a state in extended quantum systems, where the number of degrees of freedom is generally large. Nevertheless it is clear even at this stage that the property of a state of being entangled or not is strictly connected to fundamental concepts of statistical mechanics. Indeed the criterion

above may be more rigorously re-formulated in terms of some macroscopic observable, namely the *reduced density operator*, accessible to the two observers. In particular, the reduced density operator allows the observer Alice to forget about the rest of the system by tracing out the degrees of freedom associated to the subsystem B :

$$\rho_A = \mathbf{Tr}_{\mathcal{H}_B} \{\rho\}. \quad (2.4)$$

Similarly, the observer Bob will experience the state $|\psi\rangle$ through the reduced density operator ρ_B restricted to the subsystem B , and obtained by tracing out the degrees of freedom associated to A .

2.2.1 The Schmidt decomposition

In this subsection we analyse the role of the reduced density operator in the discernment of entangled and separable states. If we use (2.2) to expand the state $|\psi\rangle$, and we then evaluate the reduced density matrix (2.4) associated to subsystem A , we have that:

$$\rho_A = \sum_{i_1, i_2} \left(\sum_j C_{i_1, j} C_{i_2, j}^* \right) |\phi_{i_1}\rangle_A \langle \phi_{i_2}|. \quad (2.5)$$

Note that the states $|\phi_i\rangle_A$ live only in the subspace \mathcal{H}_A as expected. The expression above is true for any choices of orthonormal bases of \mathcal{H}_A and \mathcal{H}_B in expression (2.2). However the two observer Alice and Bob may find it useful to express their outcomes in a “common language” that allows them to compare their results. For such purpose, Alice employs a basis composed of the eigenstates $\{|\tilde{\phi}_i\rangle_A\}$ of ρ_A with non-zero eigenvalues λ_i . The *Schmidt decomposition* provides the expansion of the states in (2.5) in this special basis:

$$|\psi\rangle = \sum_i \sqrt{\lambda_i} |\tilde{\phi}_i\rangle_A \otimes |\tilde{\chi}_i\rangle_B, \quad |\tilde{\chi}_i\rangle_B = \sum_j \frac{C_{i, j}}{\sqrt{\lambda_i}} |\chi_j\rangle_B. \quad (2.6)$$

Similarly Bob employs a basis composed of the eigenstates $\{|\hat{\chi}_i\rangle_B\}$ of ρ_B with non-zero eigenvalues λ_i , and the state (2.5) becomes

$$|\psi\rangle = \sum_j \sqrt{\lambda_j} |\hat{\phi}_j\rangle_A \otimes |\hat{\chi}_j\rangle_B, \quad |\hat{\phi}_j\rangle_A = \sum_i \frac{C_{i, j}}{\sqrt{\lambda_j}} |\phi_i\rangle_A. \quad (2.7)$$

Indeed, the density operators ρ_A and ρ_B are “equally mixed” and have thus a common spectrum. If they have a different number of eigenvalues, the latter will differ only by a

number of zero eigenvalues. Furthermore, the non-zero eigenvalues satisfy the following constraint:

$$\sum_i \lambda_i = 1, \quad 0 < \lambda_i \leq 1 \quad \forall i. \quad (2.8)$$

The two observers are expected to perform their measurements on the state via the reduced density matrices:

$$\rho_A = \sum_{i=1}^N \lambda_i |\tilde{\phi}_i\rangle_A \langle \tilde{\phi}_i|, \quad \rho_B = \sum_{i=1}^N \lambda_i |\hat{\chi}_i\rangle_B \langle \hat{\chi}_i| \quad (2.9)$$

where N is called *Schmidt number* and is the number of non-zero eigenvalues of both ρ_A and ρ_B . If $N = 1$ then the bipartite state $|\psi\rangle$ is **separable** as it factorises into two separate pure states of \mathcal{H}_A and \mathcal{H}_B . In contrast, if $N > 1$ the state $|\psi\rangle$ is **entangled** and the subsystems are described by mixed states.

To sum up, given the spectrum of the reduced density operator, the Schmidt decomposition provides us with a qualitative criterion to establish whether or not there is entanglement between two parts of a quantum bipartite system. However, it should be pointed out that the diagonalization of ρ_A is generally a hard task in extended quantum systems, again due to the great number of degrees of freedom. Nevertheless there are a few cases where this task is effectively possible. For instance a well-known example in the context of quantum information theory is provided by *qubit states*. We will look into this example in Section 4.8 where we will evaluate various entanglement measures in states formed of qubits. The computation basis in which multi-qubit states are expressed is also meaningful in integrable QFT as it provides the key-ingredient of the semi-classical interpretation of the entanglement contribution given by a certain type of excited states, presented in Chapters 4 and 5.

Once a criterion to identify the presence of entanglement is established, the following question is how to quantify the amount of entanglement. In particular which specific features do we need in order to have a good measure of entanglement? We wish to address this question in the next subsection.

2.2.2 What is a good measure of entanglement?

An entanglement measure may be generally defined as a mathematical quantity that captures the fundamental and characteristic properties of entanglement and at the same time

helps us to quantify it. In particular, a good bipartite entanglement measure E^1 , formally called *entanglement monotone*, is expected to satisfy the following postulates [54]:

- **P1:** E maps density matrices into non-negative real numbers: $\rho \longrightarrow E(\rho) \in \mathbb{R}_0^+$.
- **P2:** E gives value zero if the state is separable: $E(\rho) = 0$.
- **P3:** E does not increase under *Local Operations and Classical Communication* (LOCC).

The three statements above are natural requirements if one thinks again about the Alice-and-Bob experiment. For instance, consider an entanglement measure that is a function of only the reduced density operators (we will see in the next section that this is actually the case of the entanglement entropies). Since ρ_A and ρ_B possess a common spectrum, one may expect this entanglement measure to be a function of only their eigenvalues. An important consequence of **P1** is that *good bipartite entanglement measures must be independent of the subsystem chosen to perform the measurements* i.e. both Alice's and Bob's outcomes must lead to the same conclusion. One likewise expects that entanglement measures quantify zero-entanglement in the absence of entangled states (in a similar way as seen in the Schmidt decomposition).

Theoretically speaking **P3** is less intuitive as this is related to the technological demand of exchanging information between distantly separated laboratories, which in quantum information is also known as *distance lab scenario*. Again the case of Alice and Bob can help us to understand the problem: they initially share a pure state, and by performing local measurements on their part of the system they actually transform this pure state into some other states. The *Local Operations* are literally the set of operations that they use to perform their measurements, but they are only able to communicate over long distance by using *Classical Communication* devices. Classical correlations are generated by LOCCs and in this sense an operational definition of separable states can be given as those states that can be generated exclusively by the action of LOCCs, that is why entanglement measures must not increase under these transformations. The LOCCs may be mathematically implemented by some unitary local operators U that keep the entanglement measure E invariant:

$$E(U^\dagger \rho U) = E(\rho). \tag{2.10}$$

¹There are additional properties such as *convexity* that hold for more general entanglement measures involving also mixed states. We do not consider these properties in this thesis as we focus only on bipartite measures of pure states.

In contrast, entangled states are characterised by the presence of quantum correlations that are exactly what entanglement measures need to quantify. These requires the implementation of non-local operations that can not be simulated classically i.e. a measurement of Alice may affect Bob’s outcomes without employing any classical communication devices.

2.3 Bipartite entanglement measures of pure states

We are now ready to introduce two groups of measures, respectively *entanglement entropies* and the *logarithmic negativities* which will be the focus of the next chapters and in particular of the excited state entanglement contributions discussed in Chapter 4 and 5.

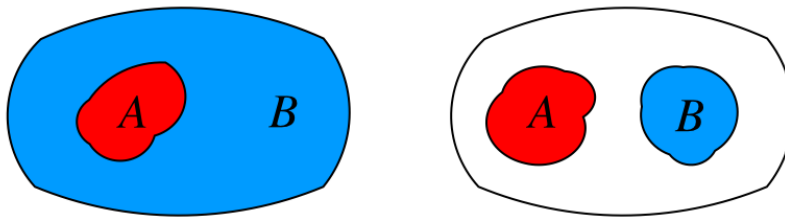


Figure 2.2 Complementary (left) and non-complementary (right) regions in a bipartite system. The entanglement entropies measure the entanglement between the red and blue regions in the right picture, whereas the logarithmic negativity measures the entanglement between the red and blue regions in the presence of a environment i.e. the remaining white region.

The entanglement entropies and the logarithmic negativity are entanglement monotones that are defined for two different bipartitions of a system, as displayed in Fig. 2.2. The entanglement entropies measures the amount of entanglement between two **complementary parts** such as A and B in Fig. 2.2 (left), this setting is indeed the simplest way to bipartition a system. A more general partition arises from the presence of two **non-complementary** entanglement regions, e.g. the A and B regions displayed in Fig. 2.2 (right), and in this context the logarithmic negativity is known to be a good measure of entanglement. Strictly speaking the other negativities (formally called *replica logarithmic negativities*) are not entanglement measures in the sense discussed in Subsection 2.2.2, as they may have negative values. However they are more accessible to techniques and may be used to compute the logarithmic negativity, as we will see in a while. To some extent, the logarithmic negativities are more general than entanglement entropies as they account for the presence of an “environment” in the system (typically occurring in experimental set-ups). However they

turns out to be more complicated functions of the reduced density matrices, so they are harder to treat. We will discuss the two groups of entanglement measures in more detail in these last two subsections of the chapter.

2.3.1 Entanglement measured by entropies

Consider a system composed of two complementary connected regions (like the red and blue regions in the left picture of Fig. 2.2), say A and B . The *von Neumann entropy* [4], also called *entanglement entropy*, can be expressed as a function of the reduced density matrix:

$$S(\rho_A) = -\text{Tr}\{\rho_A \log \rho_A\}. \quad (2.11)$$

If the state is expressed in the Schmidt decomposition (discussed in Section 2.2.1), equation (2.11) becomes:

$$S(\rho_A) = -\sum_i \lambda_i \log \lambda_i, \quad (2.12)$$

where λ_i s are the non-zero eigenvalues of ρ_A , satisfying the constraint (2.8). Note that if $\lambda_i = 1$ exists this is the only non-zero eigenvalue and thus $S(\rho_A) = 0$ as expected from **P2** in Section 2.2.2. The entanglement entropy verifies also the other conditions [54, 55], in particular it is invariant under local unitary operations i.e. it is a function of λ_i s only.

The entanglement entropy is probably the most studied bipartite entanglement measures. It has indeed attracted attention in many different areas of many-body quantum physics [56], ranging from quantum information [51] to condensed matter and out-of-equilibrium dynamics [57–59] as well as having applications in QFT (notably in conformal field theories [9, 10], and in integrable quantum field theories [15] which are the focus of this thesis) and in quantum gravity [60].

The reasons for such extensive interest are numerous. Its simple definition makes its study in extended quantum systems at very different energy-scales possible. The way the entanglement entropy scales with the size of the sub-part of the system characterises the quantum state and can be used as a macroscopic way to learn more about its fundamental properties. For instance, near criticality, the entanglement entropy encodes universal information about the quantum critical points, such as the central charge of the corresponding CFT.

Furthermore, the entanglement entropy measures quantum correlations more generally. Since it is a simple function of the state, there is no need a priori for the precise characterization of any other observables. Although some computational techniques may require the introduction

of other operators, if we can access the eigenvalue spectrum of the reduced density matrix, we can in principle characterise the entire entanglement content of the state.

Another important advantage is the existence of a very successful technique, called *replica trick* that makes the evaluation of the entanglement entropy amenable to extended quantum systems (we will discuss this method in the context of QFT in the next chapter). A crucial step required by the replica trick is the computation of the *Rényi entropy of order α* [5], a bipartite entanglement measure defined in terms of a positive real parameter α :

$$S_\alpha(\rho_A) = \frac{1}{1-\alpha} \log \mathbf{Tr}\{\rho_A^\alpha\}, \quad \alpha \in \mathbb{R}^+, \quad (2.13)$$

and whose limit to one gives the entanglement entropy:

$$S(\rho_A) = \lim_{\alpha \rightarrow 1} S_\alpha(\rho_A). \quad (2.14)$$

Similar to the entanglement entropy, the Rényi entropy of order α can be expressed in terms of the non-zero eigenvalues of ρ_A , via the Schmidt decomposition:

$$S_\alpha(\rho_A) = \frac{1}{1-\alpha} \log \left(\sum_k \lambda_k^\alpha \right), \quad (2.15)$$

and satisfies the conditions discussed in Section 2.2.2. To some extent, the Rényi entropies provide more complete knowledge about the quantum state as they constitute a “spectrum” of entropies in the parameter $\alpha \in \mathbb{R}^+$ including also the entanglement entropy. Additionally, some of the Rényi entropies can be measured in experiments [53].

In Chapter 4 we will consider another interesting quantity which is the *single-copy entropy* (also known as *single-copy entanglement*) [61–63]. In the replica model this is given by the limit

$$S_\infty(\rho_A) = \lim_{\alpha \rightarrow \infty} S_\alpha(\rho_A). \quad (2.16)$$

In Chapter 5 we will also consider the case where the subsystem A consists of two disconnected regions A_1 and A_2 (both still connected to B). This leads to a more structured bipartite system as the entropies now depend on the reduced density matrix $\rho_{A_1 \cup A_2}$,

evaluated in $\mathcal{H}_{A_1} \otimes \mathcal{H}_{A_2}$. However, they take the same functional form:

$$S(\rho_{A_1 \cup A_2}) = -\mathbf{Tr}\{\rho_{A_1 \cup A_2} \log \rho_{A_1 \cup A_2}\}, \quad S_\alpha(\rho_{A_1 \cup A_2}) = \frac{1}{1-\alpha} \log \mathbf{Tr}\{\rho_{A_1 \cup A_2}^\alpha\}, \quad \alpha \in \mathbb{R}^+ . \quad (2.17)$$

Note that although this situation looks similar to the example on the right of Fig. 2.2, the entanglement entropies are quite distinct from the logarithmic negativities. Indeed the former measure the entanglement between the union of A_1 and A_2 and the rest of the system, while the latter would be related to the entanglement between A_1 and A_2 . Similarly the expressions in (2.17) may be extended to an arbitrary number of sub-regions A_i .

2.3.2 Entanglement measured by negativities

The *logarithmic negativity* measures the amount of entanglement between two non-complementary regions A and B , immersed in an “environment” C . An example with two disconnected regions is represented in the right picture of Fig. 2.2, however in principle the two regions may share a boundary (this is the limit of adjacent regions we will consider in Chapter 5). In both cases, the bipartite Hilbert space may be seen as having the structure

$$\mathcal{H} = \mathcal{H}_{A \cup B} \otimes \mathcal{H}_C . \quad (2.18)$$

Note that the state described by $\rho_{A \cup B}$ is a mixed state for non-zero value of the logarithmic negativity and the subsystem $A \cup B$ is accordingly entangled with the environment C . The logarithmic negativity is an entanglement monotone [6, 7, 64, 65] according to the definition in Section 2.2.2. It can be expressed as

$$\mathcal{E}(\rho_{A \cup B}) = \log \|\rho_{A \cup B}^{T_B}\|_{\mathbf{Tr}} , \quad (2.19)$$

and depends on the reduced density operator $\rho_{A \cup B}$ via the operation T_B , which represents the partial transposition on subsystem B . Crucially, after partially transposing $\rho_{A \cup B}$, the resulting operator $\rho_{A \cup B}^{T_B}$ is no longer guaranteed to be positive-definite and it may have negative eigenvalues. The operation $\cdot \mapsto \|\cdot\|_{\mathbf{Tr}}$ involved in (2.19) represents the *trace norm* of $\rho_{A \cup B}^{T_B}$, namely the sum of all its singular values [66, 67]. Since $\rho_{A \cup B}^{T_B}$ is Hermitian, the trace norm is simply the sum of the absolute values of its eigenvalues. The matrix elements of $\rho_{A \cup B}^{T_B}$ can be obtained from those of the reduced density matrix $\rho_{A \cup B}$. In particular, let $\{|e_i^A\rangle\}$ and $\{|e_j^B\rangle\}$ be the orthonormal bases of \mathcal{H}_A and \mathcal{H}_B respectively such that the state $|e_i^A, e_j^B\rangle = |e_i^A\rangle \otimes |e_j^B\rangle$

lives in $\mathcal{H}_{A \cup B}$, we have that:

$$\langle e_i^A, e_j^B | \rho_{A \cup B}^{T_B} | e_k^A, e_\ell^B \rangle = \langle e_i^A, e_\ell^B | \rho_{A \cup B} | e_k^A, e_j^B \rangle. \quad (2.20)$$

Similarly to the case of the entanglement entropy, powerful methods were developed in [13, 14] to study the logarithmic negativity in CFT using the replica approach and related techniques, where the logarithmic negativity of the ground state in the limit of adjacent regions exhibits universal scaling, again related to the central charge. In 1+1-dimensional QFTs, the universal scaling properties of logarithmic negativity of the ground state have been investigated in [18] by using the replica approach. In this context, it is convenient to define the replica logarithmic negativity for a positive integer parameter n :

$$\mathcal{E}_n(\rho_{A \cup B}) := \log \mathbf{Tr} \{ (\rho_{A \cup B}^{T_B})^n \}, \quad n \in \mathbb{N}. \quad (2.21)$$

The idea is to calculate (2.21) and then to analytically continue the resulting function of n to $n = 1$. An important conclusion from the work [13] is that the replica negativity (2.21) has two different natural analytic continuations $\mathcal{E}_e(n)$ and $\mathcal{E}_o(n)$ for different parities of n (even and odd, respectively) and the logarithmic negativity is obtained by taking the limit $n \rightarrow 1$ from the function $\mathcal{E}_e(n)$ in the even sector:

$$\mathcal{E}(\rho_{A \cup B}) = \lim_{n \rightarrow 1} \mathcal{E}_e(n). \quad (2.22)$$

Finally, the logarithmic negativities can be expressed in terms of the non-zero eigenvalues of the operator $\rho_{A \cup B}^{T_B}$ via the Schmidt decomposition, in a similar way as seen for the entanglement entropies. Indeed, we have that:

$$\mathcal{E}(\rho_{A \cup B}) = \log \sum_i |\lambda_i^{(t)}| \quad \mathcal{E}_n(\rho_{A \cup B}) = \log \sum_i |\lambda_i^{(t)}|^n, \quad (2.23)$$

where $\lambda_i^{(t)}$ are the non-vanishing eigenvalues of the partially transposed reduced density matrix. This formulation is useful to combine the replica model approach with the qubit picture i.e. a technique that we will introduce in Chapter 4, and that will allow us to obtain the excited state contributions to the logarithmic negativity in Chapter 5.

TECHNIQUES IN INTEGRABLE QUANTUM FIELD THEORIES

3.1 Replica model

Let us consider a one-dimensional bipartite system in a (1+1)-dimensional QFT with local Lagrangian density $\mathcal{L}[\varphi](x, y)$, and expressed in Euclidean coordinates. We suppose that the entire system is in a pure state, and by identifying two regions A and B in the system, we aim to evaluate the corresponding entanglement entropies and/or logarithmic negativities.

We first focus on systems of infinite length for simplicity, and extend the techniques to finite volume in the course of this chapter. Of course, there is not a unique way to partition such a system. The simplest partition is provided by the case 1 in Fig. 3.1 where we find a segment A of coordinates $(x, 0)$ for $x \in [x_0, x_1]$ connected to a complementary region B formed of two semi-infinite intervals. We have seen in Section 2.3 that the entanglement entropies provide good measures of entanglement for this particular setting. We may be interested in more intricate partitions such as case 2 and case 3 in Fig. 3.1 where both regions A and B are of finite length and immersed in an environment C . In particular, in case 2 the two regions are chosen to be disconnected, while in case 3 these are joint at the point $x_1 = x_2$. All partitions are suitable to evaluate the amount of entanglement of subsystem A with respect to B and we know from Section 2.3 that the logarithmic negativity provides a good measure of entanglement based on the last two partitions. Additionally, in case 2, we can evaluate the entanglement entropy that the two regions together $A \cup B$ share with the environment C . Note that if the regions A

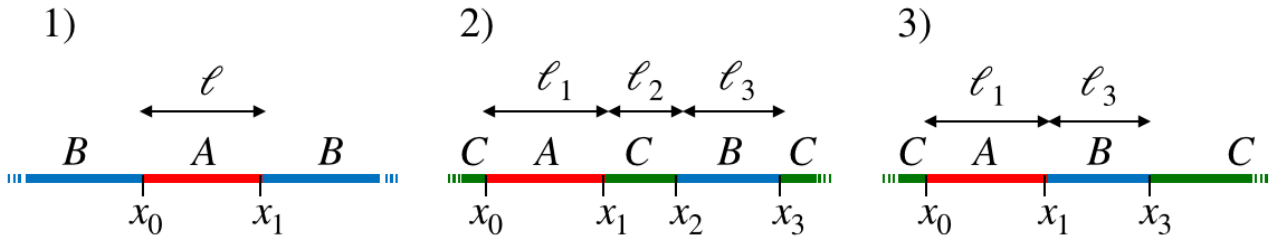


Figure 3.1 The three partitions of a one-dimensional system that are considered in this chapter. In particular the system is composed of: a single entanglement region A (case 1), two disconnected entanglement regions A and B with separation of length ℓ_2 (case 2), and two adjacent entanglement regions joint at $x_1 = x_2$ (case 3).

and B are connected as in case 3, this is equivalent to case 1 for the entanglement entropies.

As pointed out in the previous chapter, there exists a method to evaluate such entanglement measures, which may be more generally referred to as *replica model*. It is of course convenient to start from the simplest partition, i.e. case 1 and then to extend the discussion to the other two. In order to use this method we need to consider the Rényi entropy of order $\alpha = n$ for a fixed non-negative integer $n \neq 1$, this is simply the function:

$$S_n(\rho_A) = \frac{1}{1-n} \log \mathbf{Tr}\{\rho_A^n\}, \quad 1 < n \in \mathbb{N}. \quad (3.1)$$

Assuming that the Rényi entropies with integer index n can be computed, the appropriate limit to the entanglement entropy $S_1 := \lim_{n \rightarrow 1} S_n$ must be carefully taken as it requires finding the correct analytic continuation in the parameter n (this last step is usually called *replica trick*). Looking at formula (3.1) it is clear that the n th Rényi entropy is a function of the n th power of the reduced density operator ρ_A . In particular, given a complete orthonormal basis $\{|\varphi_i\rangle\}$ of \mathcal{H}_A , we can expand the quantity

$$\mathbf{Tr}\{\rho_A^n\} = \prod_{j=1}^n \sum_{k_j} {}_A\langle\varphi_{k_1}|\rho_A|\varphi_{k_2}\rangle_A {}_A\langle\varphi_{k_2}|\rho_A|\varphi_{k_3}\rangle_A \cdots {}_A\langle\varphi_{k_n}|\rho_A|\varphi_{k_1}\rangle_A. \quad (3.2)$$

The formula above inspired the idea of replicating the theory, indeed the expansion on the right hand side can be interpreted as the partition function of a new theory in a n -sheeted Riemann surface \mathcal{M}_n , also called *replica model* and composed of n copies of the original theory [8–10]:

$$\exp\{(1-n)S_n(\rho_A)\} = \mathbf{Tr}\{\rho_A^n\} = \frac{\mathcal{Z}^{(n)}}{Z_1^n}, \quad (3.3)$$

where Z_1 is a normalization factor required to recover $\mathbf{Tr}\{\rho_A^n\} = 1$ for $n = 1$. In the new manifold \mathcal{M}_n , the n copies are sequentially connected by means of a branch cut that is now

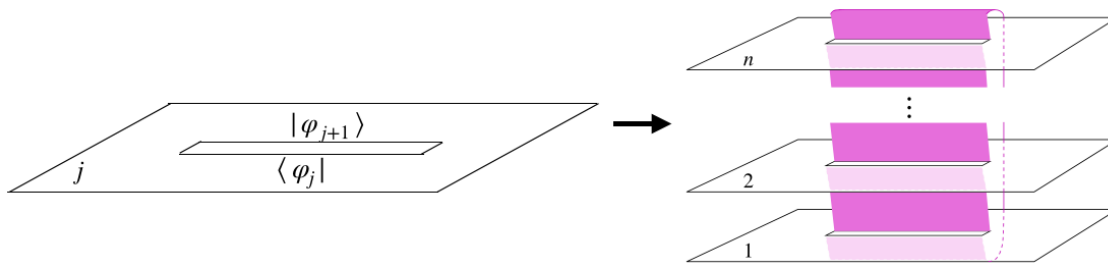


Figure 3.2 A single copy of the original QFT (left) and the n -copy model (right). Figure taken from [16] and re-adapted.

interpreted as the entanglement region. A pictorial representation is shown in Fig. 3.2. The Riemann surface \mathcal{M}_n has non-zero curvature at the branch points, precisely occurring at coordinates $(x_0, 0)$ and $(x_1, 0)$, which are identified with the boundary points of the entanglement region in the original theory.

In the path integral formulation, the partition function $\mathcal{Z}^{(n)}$ can be expressed as

$$\mathcal{Z}^{(n)} = \int [\mathcal{D}^n \Phi]_{\mathcal{M}_n} \exp \left[- \int_{\mathcal{M}_n} dx dy \mathcal{L}^{(n)}[\Phi](x, y) \right], \quad (3.4)$$

where $[\mathcal{D}^n \Phi]_{\mathcal{M}_n}$ is an infinite measure on the set of configurations of the field Φ of the new theory, identified with the n -tuple $\Phi = (\varphi_1, \dots, \varphi_n)$ and living in \mathcal{M}_n . Each copy $j = 1, \dots, n$ is described by a copy of the original field φ_j and the Lagrangian density of the new theory is

$$\mathcal{L}^{(n)}[\Phi](x, y) := \mathcal{L}[\varphi_1](x, y) + \dots \mathcal{L}[\varphi_n](x, y), \quad (3.5)$$

so that the energy density in the new model is the sum of the energy densities of the n individual copies.

Crucially, a new global symmetry σ is induced in the replica model. Indeed the new theory is invariant under cyclic permutations over the copies as it follows naturally from equation (3.2) and the properties of the trace. As a consequence, a local field φ_i living in the i th copy satisfies $\varphi_{i+n} = \varphi_i$ and, in particular $\varphi_{n+1} = \varphi_1$ for $i = 1$.

Furthermore, since the Lagrangian density $\mathcal{L}^{(n)}$ is local its integral does not depend explicitly on the manifold \mathcal{M}_n and the partition function (3.4) can be evaluated as an object computed from a model in \mathbb{R}^2 where the structure of the Riemann surface is implemented through appropriate boundary conditions on the fields $\varphi_1, \dots, \varphi_n$. Indeed, although the symmetry σ leaves the action invariant it does change the manifold on which the path integral (3.4) is defined. This is

reminiscent of the case of N indistinguishable particles in classical statistical mechanics. In this case the partition function is evaluated in a restricted manifold of the phase-space in such a way to avoid over-counting of states differing by permutations of particles. Similar constrains can be implemented in the presence of a cyclic permutation symmetry by imposing the following boundary condition on the n -tuple Φ :

$$\mathcal{C}(x_0, x_1) \quad : \quad \varphi_i(x, 0^+) = \varphi_{i+1}(x, 0^-), \quad \forall x \in [a, b], \quad i = 1, \dots, n. \quad (3.6)$$

Under the condition above, equation (3.4) becomes:

$$\mathcal{Z}^{(n)}(x_0, x_1) := \mathcal{Z}^{(n)} = \int_{\mathcal{C}(x_0, x_1)} [\mathcal{D}^n \Phi]_{\mathbb{R}^2} \exp \left[- \int_{\mathbb{R}^2} dx dy \mathcal{L}^{(n)}[\Phi](x, y) \right]. \quad (3.7)$$

3.2 Branch-point twist fields

The innovative idea of expressing the partition function (3.7) as a correlator of quantum fields associated to the branch points of a Riemann surface emerged from the study of the entanglement entropy in the context of CFT [10]. In [15] such idea was re-elaborated in the context of QFT with a more general interpretation of these fields as twist fields implementing the cyclic permutation symmetry of the n -copy model.

Twist fields exist in general whenever a theory is equipped with a global symmetry. In [15] the concept of twist field was employed for the first time in the context of entanglement measures, but the idea of implementing a symmetry by means of appropriate fields is actually much older. Probably the earliest evidence of twist fields in the literature can be found in [68], where the twist fields are associated to the \mathbb{Z}_n symmetry induced in an orbifolded CFT. In QFT a very simple example of twist fields is provided by the Ising order and disorder fields which implement the \mathbb{Z}_2 symmetry in the free massive Majorana fermion theory [69, 70].

In the replica model, the twist fields resulting from the cyclic permutation symmetry are called *branch-point twist fields* as they sit at the branch points $(x_0, 0)$ and $(x_1, 0)$ and their action on the fundamental fields $\varphi_1, \dots, \varphi_n$ is akin to imposing condition (3.6) on the path integral. Remarkably, the partition function in (3.7) can be re-written as a correlator of branch-point twist fields:

$$\mathcal{Z}^{(n)}(x_0, x_1) \sim \langle \mathcal{T}(x_0, 0) \tilde{\mathcal{T}}(x_1, 0) \rangle_{\mathcal{L}^{(n)}, \mathbb{R}^2}. \quad (3.8)$$

In the expression above we have introduced the Hermitian conjugate of the twist field $\tilde{\mathcal{T}} := \mathcal{T}^\dagger$,

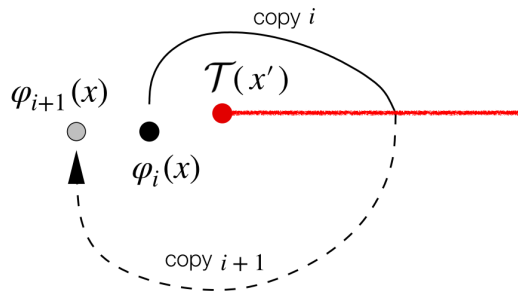


Figure 3.3 The action of the branch-point twist field in copy i . The twist field \mathcal{T} acts as a sort of “elevator” sending φ_i to the next copy whenever the copy-field crosses the branch cut. Picture taken from [15].

also called *anti-twist field*, implementing the inverse symmetry, i.e. σ^{-1} . The two twist-fields formally generate two semi-infinite branch cuts originated respectively at $(x_0, 0)$ and $(x_1, 0)$ that extend indefinitely. In (3.8) these are combined to form a branch cut of finite length $\ell = |x_0 - x_1|$. The fact that σ is a symmetry ensures that \mathcal{T} and $\tilde{\mathcal{T}}$ commute with the Lagrangian density $\mathcal{L}^{(n)}$ and thus are local. Furthermore, it ensures that the partition function (3.8) is invariant under continuous deformation of the branch cut which is implemented by some appropriate symmetry transformation.

Crucially, the branch-point twist fields act non-trivially on the fundamental fields of the theory. Indeed, following from condition (3.6), a local field φ_i living in copy i and \mathcal{T} satisfy the following exchange relations:¹

$$\begin{aligned} \varphi_i(z) \mathcal{T}(z') &= \mathcal{T}(z') \varphi_{i+1}(z) & x' \geq x, \\ \varphi_i(z) \mathcal{T}(z') &= \mathcal{T}(z') \varphi_i(z) & x' \leq x, \end{aligned} \quad (3.9)$$

for $z = (x, y)$, $z' = (x', y')$. In particular, the resulting action of the twist field \mathcal{T} is to send the local field φ_i to the next copy when it crosses the branch cut. Similarly, the field $\tilde{\mathcal{T}}$ sends the local field φ_i to the previous copy and its exchange relations are:

$$\begin{aligned} \varphi_i(z) \tilde{\mathcal{T}}(z') &= \tilde{\mathcal{T}}(z') \varphi_{i-1}(z) & x' \geq x, \\ \varphi_i(z) \tilde{\mathcal{T}}(z') &= \tilde{\mathcal{T}}(z') \varphi_i(z) & x' \leq x. \end{aligned} \quad (3.10)$$

In both equations (3.9) and (3.10) $i = 1, \dots, n$. Properties (3.9) and (3.10) imply that the

¹For simpler twist fields such as the field σ in the Ising model, the exchange relations with the fundamental fields of the theories are implemented via a factor of local commutativity [70–72], this will be introduced in Section 3.3. Relations (3.9) and (3.10) generalise these exchange relations to branch-point twist fields, characterised by more complicated locality properties.

branch-point twist fields \mathcal{T} and $\tilde{\mathcal{T}}$ are *semi-local* with respect to the fundamental fields of the theory.

It is important to stress that the definition of twist field as a symmetry field does not imply that the twist field \mathcal{T} is unique. Indeed there might be several realizations of a field satisfying property (3.9). However the fields \mathcal{T} and $\tilde{\mathcal{T}}$ will be uniquely defined if we additionally impose that they are *primary fields* in the CFT limit and thus that they have the lowest scaling dimension. Under this assumption, the scaling dimensions of the branch-point twist fields are [15]:

$$d_n := 2 \Delta_{\mathcal{T}} = 2 \Delta_{\tilde{\mathcal{T}}} = \frac{c}{12} \left(n - \frac{1}{n} \right), \quad (3.11)$$

where c is the central charge associated to the CFT and $\Delta_{\mathcal{T}}$ and $\Delta_{\tilde{\mathcal{T}}}$ are the conformal weights of the primary fields². The requirement of primary fields is also necessary to recover the CFT results presented in [10] under an appropriate normalisation (also known as CFT normalisation):

$$\langle \mathcal{T}(x_0, 0) \tilde{\mathcal{T}}(x_1, 0) \rangle = |x_0 - x_1|^{-2d_n}, \quad \text{as } m |x_0 - x_1| \rightarrow 0. \quad (3.12)$$

3.2.1 Entanglement measures as correlators

Let us now consider a pure state $|\psi\rangle$ of the original QFT that can be either the ground state or an excited state of a finite number of excitations, namely a *zero-density state*. The general ideas of computing the partition function $\mathcal{Z}^{(n)}(x_0, x_1)$ as a correlator of branch-point twist fields holds in both cases. In particular, as a consequence of (3.8), the n th Rényi entropy evaluated in $|\psi\rangle$ can be expressed as a correlator of branch-point twist fields in the replica model:

$$S_n(x_0, x_1) = \frac{\log \left(z_n \varepsilon^{2d_n} \langle \Psi | \mathcal{T}(x_0, 0) \tilde{\mathcal{T}}(x_1, 0) | \Psi \rangle \right)}{1 - n}, \quad (3.13)$$

where $|\Psi\rangle = |\psi\rangle_1 \otimes |\psi\rangle_2 \otimes \dots \otimes |\psi\rangle_n$ lives in the replica model and $\ell = |x_1 - x_0|$ is the size of the entanglement region. The parameter ε is a short-distance cut-off and is independent of n . The n -dependence is all absorbed in the non-universal factor z_n including the norm of the state. For $n = 1$, $z_1 = 1$ as the branch-point twist fields simply become the identity in this case, and thus $\partial z_n / \partial n = 0$. If $|\Psi\rangle$ is an excited state, the factor z_n normalises away the infinite-volume divergence occurring for colliding rapidities of asymptotic states. In this case the correlator in (3.13) is usually treated in finite volume (we will discuss this point more in

²If the QFT is not a CFT, these are the conformal dimensions of the underlying CFT which describes the UV fixed point of the QFT.

detail in Section 3.2.3).

We have already mentioned that the link connecting the replica model with the computation of entanglement entropy comes through the replica trick. Mathematically speaking, the replica trick is simply the limit of $S_n(\ell)$ as n approaches 1. We can use the identity $\rho_A \log \rho_A = \lim_{n \rightarrow 1^+} \frac{\partial}{\partial n} \rho_A^n$ and the properties of the trace to write the entanglement entropy as:

$$S_1(x_0, x_1) = - \lim_{n \rightarrow 1^+} \frac{\partial}{\partial n} \left(\varepsilon^{2dn} \langle \Psi | \mathcal{T}(x_0, 0) \tilde{\mathcal{T}}(x_1, 0) | \Psi \rangle \right). \quad (3.14)$$

However, we need to extend the notion of replica as in the replica model the parameter n is by construction a positive integer strictly greater than 1, more precisely, we need to take carefully its analytic continuation to $n \in]1, +\infty[$. This analytic continuation problem is not generally solved in QFTs. In the integrable cases, this problem was addressed in [15, 73] for the entanglement entropy of the ground state, while for a zero-density state, which is the focus of the next two chapters, the entanglement entropy is an analytic function of n and so the analytic continuation is trivial.

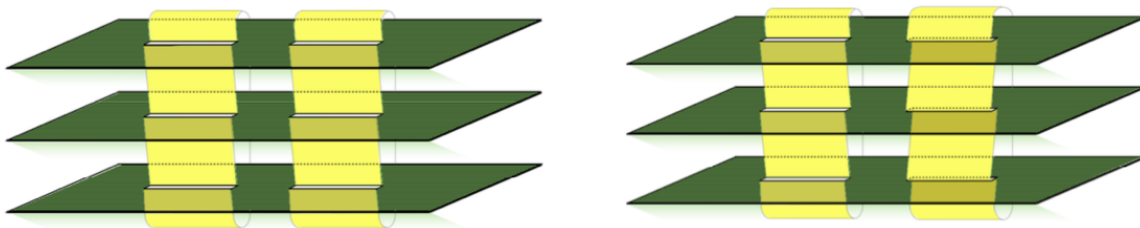


Figure 3.4 The Riemann surface constructed to compute $\text{Tr}\{(\rho_{A \cup B})^n\}$ (left) and $\text{Tr}\{(\rho_{A \cup B}^{T_B})^n\}$ (right). They differ by the the second branch cut implementing different connectivities of the Riemann sheets. Both pictures are taken from [14].

We can now consider more complicated partitions such as case 2 in Fig. 3.1. In this case we have two disconnected regions and, as pointed out at the beginning of the chapter, the entanglement entropies measure the quantum correlations that the union of the two regions $A \cup B$ shares with the rest of the system. The idea of replicating the model seen for a single region can be easily extended to the case of two regions. The main difference is that the boundary condition (3.6) is now implemented at the boundary points x_0, x_1, x_2, x_3 . As shown in the left picture of Fig. 3.4, this corresponds to having two branch cuts in the resulting replica model, each associated to a particular entanglement region. As a consequence the n th Rényi

entropy is now given by a four-point correlation function:

$$S_n(x_0, x_1, x_2, x_3) = \frac{\log \left(z_n \varepsilon^{4d_n} \langle \Psi | \mathcal{T}(x_0, 0) \tilde{\mathcal{T}}(x_1, 0) \mathcal{T}(x_2, 0) \tilde{\mathcal{T}}(x_3, 0) | \Psi \rangle \right)}{1 - n}. \quad (3.15)$$

More generally, if we want to extend the calculation of entanglement entropies to any number of disconnected regions, we will obtain correlators involving as many branch-point twist fields as boundary points in the system. The entanglement entropy of two disconnected regions is obtained in a similar way to (3.14), now involving a four-point correlation function:

$$S_1(x_0, x_1, x_2, x_3) = - \lim_{n \rightarrow 1^+} \frac{\partial}{\partial n} \left(\varepsilon^{4d_n} \langle \Psi | \mathcal{T}(x_0, 0) \tilde{\mathcal{T}}(x_1, 0) \mathcal{T}(x_2, 0) \tilde{\mathcal{T}}(x_3, 0) | \Psi \rangle \right). \quad (3.16)$$

Interestingly, also the operator $\mathbf{Tr} \{ (\rho_{A \cup B}^{T_B})^n \}$ can be obtained as a correlator of twist fields. In particular, the replica logarithmic negativity (2.21) can be expressed as:

$$\mathcal{E}_n(x_0, x_1, x_2, x_3) = \log \left(z_n \varepsilon^{4d_n} \langle \Psi | \mathcal{T}(x_0, 0) \tilde{\mathcal{T}}(x_1, 0) \tilde{\mathcal{T}}(x_2, 0) \mathcal{T}(x_3, 0) | \Psi \rangle \right), \quad (3.17)$$

where the effect of the partial transposition is to exchange the two fields associated to the boundary points of the interval B . As shown in Fig. 3.4, the partial transposition changes also the branch cut associated to the region B . Therefore, the correlators (3.15) and (3.17) are defined in different Riemann surfaces.

Crucially, as pointed out in Subsection 2.3.2, the replica trick needs to be performed in the even sector of the replica model. This corresponds to posing $n = 2m$ for a fixed integer number m and then to taking the analytic continuation in m towards $m \rightarrow 1/2$:

$$\mathcal{E}_1(x_0, x_1, x_2, x_3) = \lim_{m \rightarrow \frac{1}{2}} \mathcal{E}_{2m}(x_0, x_1, x_2, x_3). \quad (3.18)$$

Note that we have not yet used any special properties of integrability, and the idea of expressing entanglement measures as correlators can be more generally extended to any 1+1-dimensional QFT. However, as we will see in the course of the chapter, this idea is particularly useful in integrable models where the existence of exact methods to compute correlations functions makes the expressions (3.13), (3.15), and (3.17) effectively computable. This is also the case for 1+1 dimensional CFT where the structure of correlators is severely constrained. However, for four-point functions such as those in (3.16) and (3.17) CFT

computations are also extremely challenging as can be seen from the extensive study of the compactified massless free boson carried out in [11–14]. One should also stress that even in 1+1 dimensions the application of these methods may be intricate if we consider a correlator of many quantum fields as the complexity of the computation drastically increases with the number of fields considered. For this reason it may be convenient to consider some special limit of expression (3.17) that “reduces” the number of boundary points and thus also the number of fields in the correlator.

For instance, one can simplify the structure of (3.17) by taking $x_1 \rightarrow x_2$ to obtain two adjacent entanglement regions (like case 3 in Fig. 3.1). This limit was studied in the context of CFT in [11–14]. If we take such a limit in QFT we will deal with a three-point correlation function:

$$\mathcal{E}_n(x_0, x_2, x_3) = \lim_{x_1 \rightarrow x_2} \mathcal{E}_n(x_0, x_1, x_2, x_3) = \log \left(z_n \varepsilon^{2d_n + \tilde{d}_n} \langle \Psi | \mathcal{T}(x_0, 0) \tilde{\mathcal{T}}^2(x_2, 0) \mathcal{T}(x_3, 0) | \Psi \rangle \right), \quad (3.19)$$

where $\tilde{\mathcal{T}}^2(x_2, 0) = \lim_{x_1 \rightarrow x_2} \tilde{\mathcal{T}}(x_1, 0) \tilde{\mathcal{T}}(x_2, 0)$ is a *composite twist field*³ obtained by colliding the two anti-twist fields in (3.17). In particular, the field $\tilde{\mathcal{T}}^2$ implements a non-sequential cyclic permutation symmetry over the copies. For n even, the action of this symmetry factorises into two components, each acting only on even-numbered or odd-numbered sheets, therefore the twist field $\tilde{\mathcal{T}}^2$ is accordingly:

$$\tilde{\mathcal{T}}^2 = \tilde{\mathcal{T}}_e \otimes \tilde{\mathcal{T}}_o, \quad (3.20)$$

where $\tilde{\mathcal{T}}_e$ and $\tilde{\mathcal{T}}_o$ act respectively on sheets of only even- and odd- copy numbers. The field $\tilde{\mathcal{T}}^2$ is fully defined in CFT through the operator product expansion of two anti-twist fields. Its conformal weights follows naturally from (3.20):

$$\Delta_{\mathcal{T}^2}(n) = 2 \Delta_{\mathcal{T}}(n/2), \quad (3.21)$$

and defines its scaling dimension is $\tilde{d}_n = 2 \Delta_{\mathcal{T}^2}(n)$.

There are other limits of expression (3.17) that one can potentially consider, for instance the case of two disjoint semi-infinite intervals discussed in [18]. However these cases do not have a finite volume counterpart. We will see that an important requirement for treating correlators of twist fields in excited states is to work in finite volume, thus semi-infinite intervals are not of interest in the treatment of excited states.

³In the context of entanglement, the composite twist fields appeared first in the work [74] and was then studied in more details in the Ising model [75].

The general idea of expressing entanglement measures in terms of correlators of branch-point twist fields has been applied to the study of many different models, especially in the context of massive QFT. While the original paper [15] considered the Ising and sinh-Gordon theories, free theories were further studied in [76, 77], whereas the generalization of these results to non-unitary QFT, including the Lee-Yang model was studied in [78, 79]. The connection between entanglement entropy and scaling functions was explored in [74, 80] and, more recently, branch-point twist fields have been employed to study the out-of-equilibrium dynamics of entanglement [81, 82].

3.2.2 Review of previous results in the ground state

In order to understand the structure of the correlators of branch-point twist fields in excited states, it is instructive to look first into the entanglement entropies evaluated in the ground state. In this subsection we choose the state $|\psi\rangle$ to be the ground state $|0\rangle$ of the field theory considered.

An important result obtained in CFT is the logarithmic growth of the n th Rényi entropy of the ground state with the subsystem size ℓ [9, 10]:

$$S_n(\ell) = \frac{c(n+1)}{6n} \log \frac{\ell}{\epsilon}, \quad (3.22)$$

where c is the central charge of the CFT and ϵ a short-distance cut-off. In terms of the branch-point twist fields this result follows naturally from the power-law scaling of the two-point correlation function (3.13) [15, 16]. The entanglement entropy can be obtained by simply taking the limit $n \rightarrow 1$ of (3.22)

$$S_1(\ell) = \frac{c}{3} \log \frac{\ell}{\epsilon}. \quad (3.23)$$

More generally, both the n th Rényi entropy and the entanglement entropy grow linearly with the number of boundary points, as a consequence of the power-law scaling of the correlators of twist fields in CFT. Thus entanglement entropies in the ground state of CFT satisfy a sort of area-law [83]. They also violate the area law in the sense that they grow logarithmically with the system's size. The results above capture the universal features⁴ of entanglement entropies, showing these depends on very few details of the theory, in this case just the central charge. We thus expect that systems that are physically very diverse but described by the same CFT,

⁴Here, as well as in the rest of the section the term “universality” means the presence of common features among a certain number of theories. It is true that the results (3.23) and (3.22) are not universal in a strict sense as they depend on the cut-off ϵ , but the proportionality to c is independent of the regulator.

display the same entanglement properties.

To fully exploit the power of this universality, one should consider its connection to the study of critical systems. Indeed a field theory may be interpreted as a particular scaling limit of a quantum spin chain with a correlation length $\xi = 1/m$ given by the inverse of the mass of the field theory considered. For such a system the cut-off ϵ could be taken to be proportional to the lattice spacing and would be in general a small number compared to the other length scales ℓ and ξ . In this context, the entanglement entropies may be used to study the behaviour of quantum chains near or far from a criticality. For instance we can consider a system at *short-distance* (in the so called *ultraviolet regime*), i.e. when the size of the subsystem is much smaller of the correlation length $\xi \gg \ell \gg \epsilon$. In this case, even if ξ is finite the subsystem will be perceived as critical, and the entanglement entropies will be given by (3.22) and (3.23) at the lowest order.

In contrast, if we are interested in the *large-distance limit* (also called *Infrared regime*) i.e. $\ell \gg \xi \gg \epsilon$, the universal features of chain (if there are any) are described by a QFT, and the entanglement entropies will be given by the dominant contributions to (3.13) and (3.14) in such a limit. These contributions can be evaluated by combining several techniques as we will see below. The starting point is again the correlator of branch-point twist fields in (3.13) that in QFTs can be naturally expanded in terms of a complete sets of states:

$$\begin{aligned} \langle 0 | \mathcal{T}(\mathbf{x}_0) \tilde{\mathcal{T}}(\mathbf{x}_1) | 0 \rangle &= \langle 0 | \mathcal{T}(\mathbf{x}_0) \times \mathbb{1} \times \tilde{\mathcal{T}}(\mathbf{x}_1) | 0 \rangle = \\ &= \sum_{k=1}^{\infty} \sum_{\mu_1, \dots, \mu_k} \int_{\theta_1^{\mu_1} > \dots > \theta_k^{\mu_k}} \frac{d\theta_1^{\mu_1} \dots d\theta_k^{\mu_k}}{(2\pi)^k} \exp \left[-\ell \sum_{j=1}^k m_{\alpha_j} \cos \theta_j^{\mu_j} \right] | \langle 0 | \mathcal{T}(0) | \theta_1^{\mu_1}, \dots, \theta_k^{\mu_k} \rangle |^2, \end{aligned} \quad (3.24)$$

where ℓ now expresses the space-like relativistic distance in Minkowsky space-time between the two points $\mathbf{x}_0 = (x_0, 0)$ and $\mathbf{x}_1 = (x_1, 0)$. The expansion (3.24) is obtained by inserting a complete set of states:

$$\mathbb{1} = \sum_{k=1}^{\infty} \sum_{\mu_1, \dots, \mu_k} \int_{\theta_1^{\mu_1} > \dots > \theta_k^{\mu_k}} \frac{d\theta_1^{\mu_1} \dots d\theta_k^{\mu_k}}{(2\pi)^k} | \theta_1^{\mu_1}, \dots, \theta_k^{\mu_k} \rangle \langle \theta_k^{\mu_k}, \dots, \theta_1^{\mu_1} |. \quad (3.25)$$

The structure of the n -copy model is incorporated in the indices $\mu_j = (i_j, \alpha_j)$, including the copy number i_j and the particle species associated to a single excitation of rapidity $\theta_j^{\mu_j}$ for any $j = 1, \dots, k$.

The advantage of using expression (3.24) is that in integrable QFTs there are effective

methods to exactly compute the matrix elements $\langle 0 | \mathcal{T}(0) | \theta_1^{\mu_1}, \dots, \theta_k^{\mu_k} \rangle$, also called *form factors*. Such methods are usually referred to as the *form factor program* [84, 85] and they provide the most powerful and successful approach to the computation of correlation functions, both analytically and numerically. Form factors are in fact the building blocks of the expansion in (3.24), and will be discussed in more detail in Section 3.3. Furthermore the right hand side of (3.24) presents an exponential factor inside the sums, coming from covariance transformations⁵. This factor defines a precise ordering of the dominant contributions at large distance ℓ . Indeed in such limit, the form factor contributions involving large number of particles tend to be negligible and the leading terms are obtained from the lowest particle contributions.

From the form factor expansion it follows that the leading contribution will come from the zero-particle form factor, also called vacuum expectation value. Since the latter is independent of ℓ , the leading contribution is independent of the region's size. This leads to the famous result that the entanglement entropy of gapped systems saturates for large system size to a constant that depends on the gap (correlation length). More precisely the n th Rényi entropy saturates at large distance $\ell \gg m^{-1} \gg \epsilon$ with saturation constant governed by the central charge:

$$S_n(\ell) = -\frac{c(n+1)}{6n} \log m_1 \epsilon + 2U_n + O(e^{-2\ell m_1}) \quad (3.26)$$

where m_1 is the mass of the lightest particle of the theory and U_n is a model-dependent constant. This result follows from the clustering property, i.e. the factorization of correlation functions at large distance, and from the scaling properties of vacuum expectation values in (1+1)-dimensional QFT. The exponential corrections to saturation come from the higher particle contributions. For instance the first correction is obtained from either the one- or two-particle form factor (if the one-particle form factor is zero). However, when $n \rightarrow 1$ the leading correction to the entanglement entropy comes from the two-particle form factor term in all cases. For an integrable QFT with N particle species, the formula of the entanglement entropy up to the first correction is [15, 16]:

$$S_1(\ell) = -\frac{c}{3} \log(m_1 \epsilon) + 2U_1 - \frac{1}{8} \sum_{\alpha=1}^N K_0(2\ell m_\alpha) + O(e^{-3\ell m_1}) \quad (3.27)$$

Similarly to (3.23), the result above encodes universal information not only about the

⁵In the standard derivation of (3.24) that can be found in many sources, including [15, 16], the exponential factor is obtained by using the Euclidean rotation invariance in order to bring the points in the pure imaginary time direction (with a distance ℓ), and to use imaginary-time translation covariance to extract the real-exponential factor depending on ℓ .

underlying CFT. Remarkably the first exponential correction captures the mass spectrum of the QFT irrespective of its scattering matrix. This means that this term looks the same for both a free theory containing N fermions of masses m_α as above and an interacting theory with the same mass spectrum. The first correction take also a universal form given by the *modified Bessel function* K_0 . This turns out to be a very general property and has been shown to hold beyond integrability [17].

Consider instead two connected regions A and B as shown in Fig. 3.1, we may wonder if the logarithmic negativity displays universal properties in a similar fashion. Like in the single-region case, the correlator (3.19) (now involving three points) can be computed in CFT by using the scaling properties of the twist field \mathcal{T} and the composite twist-field $\tilde{\mathcal{T}}^2$ [13, 14]. After taking the limit $n \rightarrow 1$ the logarithmic negativity is:

$$\mathcal{E}(\ell_1, \ell_3) = \frac{c}{4} \log \frac{\ell_1 \ell_3}{\epsilon(\ell_1 + \ell_3)}. \quad (3.28)$$

In QFT we need to insert the completeness relation (3.25) twice in the correlator (3.19) in order to obtain a form factor expansion. Again the saturation constant comes from the zero-particle term and follows from the clustering properties i.e. $\langle 0 | \mathcal{T} \tilde{\mathcal{T}}^2 \mathcal{T} | 0 \rangle \sim \langle 0 | \mathcal{T} | 0 \rangle \langle 0 | \tilde{\mathcal{T}}^2 | 0 \rangle \langle 0 | \mathcal{T} | 0 \rangle$ for large distances $\ell_1, \ell_3 \gg m^{-1} \gg \epsilon$. As a consequence, the large-distance vacuum expectation values of the fields involved in the correlator (3.19) fully define the large-volume leading term:

$$\mathcal{E}_n(\ell_1, \ell_3) = (\tilde{d}_n + 2d_n) \log(m_1 \epsilon) + 2E_n + O(e^{-2(\ell_1 + \ell_3)m_1}), \quad (3.29)$$

where d_n and \tilde{d}_n are the conformal dimension of \mathcal{T}^2 and $\tilde{\mathcal{T}}$ respectively, and E_n is a characteristic constant of the theory⁶. The next-to-leading correction comes from two-particle terms of the form factor expansion such as $\langle 0 | \mathcal{T} | 0 \rangle \langle 0 | \tilde{\mathcal{T}}^2 | \theta_1^{\mu_1}, \theta_2^{\mu_2} \rangle \langle \theta_2^{\mu_2}, \theta_1^{\mu_1} | \mathcal{T} | 0 \rangle$. If we take $\ell_3 \rightarrow \infty$, the exponential corrections to the logarithmic negativity (once the replica trick is performed) takes a universal functional form given again by the modified Bessel function K_0 [18]:

$$\mathcal{E}_n(\ell_1) = -\frac{c}{4} \log(m_1 \epsilon) + 2E_1 - \frac{2}{3\sqrt{3}\pi} \sum_{\alpha=1}^N K_0(\sqrt{3}m_1 \ell_1) + O(e^{-a m_1 \ell_1}), \quad (3.30)$$

where the point x_2 is taken at the origin, N is the number of particle species in the theory,

⁶Note that E_n and U_n in (3.26) are not independent to each other as both quantities are consequences of the scaling properties of the vacuum expectation value of \mathcal{T} .

and $a > \sqrt{3}$.

In the presence of two disconnected regions $x_1 \neq x_2$ (as displayed in the right-picture of Fig. 3.1) the entanglement entropies as well as logarithmic negativities involve the computation of a full four-point correlation function, which as mentioned before, it is generally a hard task, even in integrable QFT. This partition has been extensively studied in CFT [11, 12, 14], where the logarithmic negativities were proven to be scale-invariant functions, depending only on the ratio:

$$\mathbf{r} = \frac{(x_2 - x_0)(x_3 - x_1)}{(x_1 - x_0)(x_3 - x_2)} = \frac{(\ell_1 + \ell_2)(\ell_2 + \ell_3)}{\ell_1 \ell_3}, \quad \mathcal{E}_n(\ell_1, \ell_2, \ell_3) = \mathcal{E}_n(\mathbf{r}). \quad (3.31)$$

An explicit functional expression for any n of the n th replica negativity has been obtained for the compactified free boson. However, even in this case the continuation in the parameter n is non-trivial and not fully understood analytically.

3.2.3 Challenges posed by the treatment of excited states

The results reviewed in Section 3.2.2 bring to light the connection between universal properties and entanglement measures as well as the fact that the entanglement encodes fundamental information on the theory. Since entanglement measures are functions of the state (through the reduced density operator) only, it appears clear that bipartite entanglement measures may be used to investigate further the properties of a given state. Much has been done for the ground state and it would be now interesting to study entanglement measures in excited states as these are expected to display additional universal features associated to the presence of excitations.

Excited state entanglement measures will be extensively studied in Chapters 4 and 5, where we will consider a free massive free boson theory and assume the bipartite system to be in a pure state formed of a finite number of excitations, also called *zero-density state*. One may reasonably wonder how different is the computation of correlators of twist fields in such a case, and more generally what are the challenges posed by the treatment of excited states. To address these questions it is again useful to start from the case of a single entanglement region, and to extend the discussion to other partitions. Hence, considering a bipartite system in a pure state $|\psi\rangle$ (now including a finite number of excitations), the n th Rényi entropy can be computed as a two-point correlation function of twist fields in $|\Psi\rangle = |\psi\rangle_1 \otimes \cdots \otimes |\psi\rangle_n$ in the n -copy model. Following a similar construction to the one seen in Subsection 3.2.2, the correlator (3.13) can be expanded by introducing a complete set of states between the two

fields, schematically:

$$\langle \Psi | \mathcal{T}(0) \tilde{\mathcal{T}}(\ell) | \Psi \rangle \propto \sum_{|\Phi\rangle} \langle \Psi | \mathcal{T}(0) | \Phi \rangle \langle \Phi | \tilde{\mathcal{T}}(\ell) | \Psi \rangle, \quad (3.32)$$

where we set \mathbf{x}_0 to the origin and \mathbf{x}_1 to the length of the entanglement region ℓ for simplicity, and omitted the time-dependence for a shorter notation. The state $|\Phi\rangle$ and $|\Psi\rangle$ live in the replica model and are characterized by a discrete set of rapidities (or momenta). If the rapidities in one state coincide with some in the other state, the matrix elements $\langle \Psi | \mathcal{T}(0) | \Phi \rangle$ and $\langle \Phi | \mathcal{T}(\ell) | \Psi \rangle$ ⁷ will develop, in the usual infinite-volume normalization of the states, δ -function singularities. A common way to regularise these singularities is to move the computation to finite-volume and use the volume (in one-dimension this is a length L) as a natural regulator. This procedure leads to consider finite-volume form factors [86, 87]. Indeed, in finite volume a systematic prescription exists to compute the “physical part” of matrix elements of local operators. This consists of subtracting the contributions of any occurring singularities in a way which is controlled by the particular pole structure of the infinite volume form factors. This choice permits to obtain information on both the finite and the infinite volume behaviours of the system. Indeed the correlator will be given as an infinite sum of contributions in powers of $1/L$, whose ordering is related to the pole-structure of the form factors involved and can be used to select the dominant contribution at infinite volume.

The first challenge is given by the fact that the branch-point twist fields are not local in the sense required to apply the techniques presented in [86, 87]. Although they are local with respect to the Lagrangian density of the replica model (as they implement a symmetry) they are non-local with respect to the fundamental fields of the theory due to the properties (3.9) and (3.10). Indeed, due to the complex geometry of the replica model, form factors of twist fields present additional poles that need to be taken into account in the finite-volume regularization. It is however very plausible that the standard general ideas for the computation of finite-volume non-diagonal form factors (i.e. the elements whose pole structure is more similar to those of standard local operators) will be still applicable to branch-point twist fields. The analysis of the free boson theory that will be conducted in Chapters 4 and 5, aims to confirm that this is exactly the case.

Second we need to address the problem of extending the replica model to a finite volume as

⁷This matrix element can be evaluated at the origin by using space-time translation. This of course introduces some factor in the expansion (3.32).

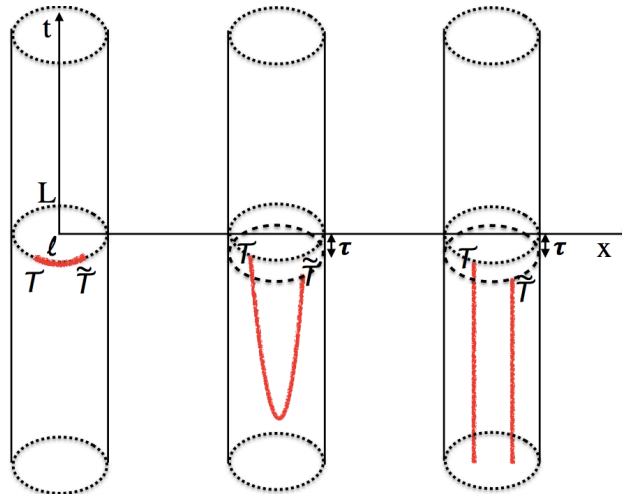


Figure 3.5 Continuous deformation of a branch-cut along the space direction to obtain two semi-infinite branch-cuts along the time direction of the cylinder. This transformation does not change the value of the twist-field correlator, and allows us to make sense of twist field form factors in finite volume.

the original QFT is now mapped into a cylinder with the time-coordinate along its axis and the space-coordinate along its circumference. As argued in 3.2, in finite volume the branch-point twist field and its Hermitian conjugate are associated to two semi-infinite branch cuts and the two fields combine to create a branch cut of finite length in the correlator (3.8). However, once we write down the expansion (3.32) in finite volume we need to evaluate the matrix elements ${}_L\langle\Psi|\mathcal{O}(0)|\Phi\rangle_L$ and ${}_L\langle\Phi|\mathcal{O}(0)|\Psi\rangle_L$. The main problem is that for these matrix elements, an infinitely long branch cut extending in space is incompatible with working in finite volume L . This conflict can be resolved by adopting an approach which is reminiscent of that taken in [88] for the Ising field theory and the matrix elements of its \mathbb{Z}_2 twist field σ . We may use the fact that the branch cut can be continuously deformed without changing the value of the correlation function. Therefore, we may continuously “stretch” the branch cut along the time direction as indicated in Fig. 3.5. The result is a product of fields with branch cuts extending in the time direction. Indeed in the situation where the branch cut was along the space-direction, the exchange relation (3.9) imposes continuity between the field φ_i above and the field φ_{i+1} below the branch extending toward the right. After the deformation as in Fig. 3.5, this becomes the continuity between φ_i on the left and φ_{i+1} on the right of the branch extending towards negative times. In this configuration, the fields are well defined in the quantization on the circle. The operator ordering of the two-point function in the quantization scheme on the circle, is implemented in the path integral by a time ordering: an infinitesimal shift τ along the cylinder, as in Fig. 3.5.

Crucially, the presence of the branch cuts and more generally of the symmetry σ ⁸ affects the boundary conditions of the fundamental fields of the theory. In particular, in parallel to the situation seen in [88], the Hilbert space of quantization on the circle is divided into sectors characterised by periodicity conditions associated to the symmetry. For the Ising model, the \mathbb{Z}_2 symmetry leads to two sectors, Ramond-Ramond and Neveu-Schwarz with periodic and anti-periodic boundary conditions for the fields of the theory. In the case of the Replica model, we have in particular n sectors labelled by cyclic elements of the permutation group. In the cylinder picture of Fig. 3.5, the state $|\Phi\rangle_L$ lies between the twist fields, in the time slice of extent τ introduced by the operator ordering. This means that in finite volume, the state on the left and the right of the element ${}_L\langle\Psi|\mathcal{T}(0)|\Phi\rangle_L$ in (3.32) lie in different sections and thus satisfy different boundary conditions.

Finally, the question arises as to how the matrix elements of branch-point twist fields with states in different sectors can be computed. For a general integrable interacting theory the computation of the matrix elements of branch-point twist fields is still an open problem due to the regularization problem discussed above. However, for free theories there are additional resources at our disposal. More precisely, for free theories, it is possible to express the branch-point twist fields in terms of simpler $U(1)$ twist fields, where the permutation symmetry has been diagonalized. This is achieved by employing the so-called *doubling trick* introduced in [25] and employed successfully in the branch-point twist field context in [15, 89], where it allowed for the computation of the vacuum expectation value of the branch-point twist field. A similar idea was also used in [90] in the study of the entanglement entropy of free theories. In sections 4.2, 4.3 and 4.4 we will extend this idea to the study of the excited state entanglement in finite volume.

The doubling trick is the simple idea that a real free fermion (Majorana) and a real free boson theory can be doubled to construct a complex free fermion (Dirac) and a complex free boson theory. This doubling induces a $U(1)$ symmetry in the new theory to which a $U(1)$ twist field is associated. The doubled free theory will be replicated in the replica model, and the $U(1)$ symmetry on each individual copy is extended to a $U(n)$ symmetry, which includes cyclic permutation of the copies. Diagonalising the cyclic permutation, in the new basis the branch-point twist field is then expressed as a product of n individual $U(1)$ twist fields \mathcal{T}_p for $p = 1, \dots, n$. The diagonalisation of the branch-point twist fields in terms of the much simpler $U(1)$ fields leads to the factorisation of the expansion (3.32) into n independent sums that can

⁸Note that here we use σ meaning the cyclic permutation symmetry while above we were referring to the spin field σ in the Ising model. They are two totally different objects.

be computed separately in each copy. As we will see in Chapter 4, this is a key-point in the computation of the entanglement contributions generated by the excited states.

All considerations made so far are independent of the number of twist fields considered in the correlators therefore they can be extended to two entanglement regions. We will deal with this case in more detail in Chapter 5.

3.3 Form factors

To conclude this chapter, we review the fundamental properties of the building blocks composing the expansion (3.24) and (3.32), namely *form factors*. By definition, *elementary form factors* are tensor valued functions, representing matrix elements of some local operator \mathcal{O} located at the origin and evaluated between a multi-particle incoming state and the vacuum:

$$F_k^{\mathcal{O}}(\theta_1^{\mu_1}, \theta_2^{\mu_2}, \dots, \theta_k^{\mu_k}) := \langle 0 | \mathcal{O}(0) | \theta_1^{\mu_1}, \theta_2^{\mu_2}, \dots, \theta_k^{\mu_k} \rangle. \quad (3.33)$$

We may also refer to the quantity above as a k -particle form factor. To express the incoming state we have used the convention (1.7).

Form factors may be potentially used to expand correlators of local fields in any theory possessing translation invariance. However, they are particularly relevant in integrable models, where the presence of infinitely many local conserved charges as well as standard physical requirements like Lorenz covariance imposes enough constraints to such matrix elements so that exact solutions for many theories have been obtained once known the S -matrix. Many examples can be found in the literature, see e.g. [71, 91] for the Ising model, [92, 93] for sinh-Gordon model, [94] for sine-Gordon model, [95] for Lee-Yang model. These constraints are partially inherited from the scattering properties of the excitations, and provide the bootstrap equations for the elementary form factors.

Elementary form factors are the building blocks of ground-state correlators (an example is given by equation (3.24)). In a more general setting we would need the definition of *form factor* as a local operator \mathcal{O} evaluated at the origin and between asymptotic states (a graphical representation is shown in Fig. 3.6) :

$$F_{m+k}^{\mathcal{O}}(\lambda_1^{\nu_1}, \dots, \lambda_m^{\nu_m}; \theta_1^{\mu_1}, \dots, \theta_k^{\mu_k}) = \langle \lambda_m^{\nu_m} \dots \lambda_1^{\nu_1} | \mathcal{O}(0, 0) | \theta_1^{\mu_1} \dots \theta_k^{\mu_k} \rangle. \quad (3.34)$$

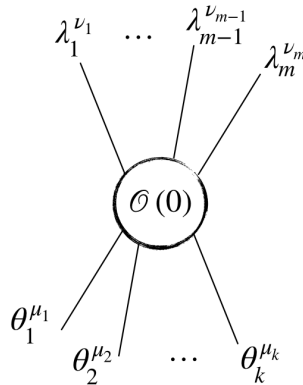


Figure 3.6 General definition of a $m + k$ -particle form factor of local operator. The incoming state is represented at the bottom while the outgoing state is at the top of the figure.

Elements such as (3.34) are suitable for the treatment of correlators in excited states such as expansion (3.32). Of course these elements are related to the elementary form factors through the recursive equation:

$$\begin{aligned}
 F_{m,k}^{\mathcal{O}}(\lambda_1^{\nu_1}, \dots, \lambda_m^{\nu_m}; \theta_1^{\mu_1}, \dots, \theta_k^{\mu_k}) = & \quad (3.35) \\
 & F_{m-1,k+1}(\lambda_1^{\nu_1}, \dots, \lambda_{m-1}^{\nu_{m-1}}; \lambda_m^{\bar{\nu}_m} + i\pi, \theta_1^{\mu_1}, \dots, \theta_k^{\mu_k}) + \\
 & + \sum_{j=1}^k \left[2\pi \delta_{\mu_j \nu_m} \delta(\lambda_m^{\nu_m} - \theta_j^{\mu_j}) \prod_{p=1}^{j-1} S_{\nu_m \mu_p}(\lambda_m^{\nu_m} - \theta_p^{\mu_p}) \times \right. \\
 & \left. \times F_{m-1,k-1}^{\mathcal{O}}(\lambda_1^{\nu_1}, \dots, \lambda_{m-1}^{\nu_{m-1}}; \theta_1^{\mu_1}, \dots, \theta_{j-1}^{\mu_{j-1}}, \theta_{j+1}^{\mu_{j+1}}, \dots, \theta_k^{\mu_k}) \right]
 \end{aligned}$$

where $\bar{\mu}_m$ denotes the anti-particle of μ_m . The terms including the S-matrix are called *disconnected* and are zero if the two asymptotic states do not have any rapidities in common. In this case the decomposition in elementary form factors is straightforward as (3.35) only involves the crossing property of the excitations in the outgoing state. More generally a $k + m$ form factor can be reduced to elementary form factors by using an appropriate number of iterations of equation (3.35), a graphical example is displayed in Fig. 3.7 for $k = 3$ and $m = 1$.

3.3.1 Infinite-volume form factors bootstrap

We now concentrate on an integrable QFT in infinite volume. A first fundamental constraint comes from relativistic invariance and implies that k -particles form factors of scalar operators are functions of the rapidity differences $\theta_{ij} := \theta_i^{\mu_i} - \theta_j^{\mu_j}$ for any $i, j = 1, \dots, k$:

$$F_k^{\mathcal{O}}(\theta_1^{\mu_1}, \theta_2^{\mu_2}, \dots, \theta_k^{\mu_k}) = F_k^{\mathcal{O}}(\theta_{12}, \theta_{13}, \dots, \theta_{ij}, \dots), \quad \text{for } i < j. \quad (3.36)$$

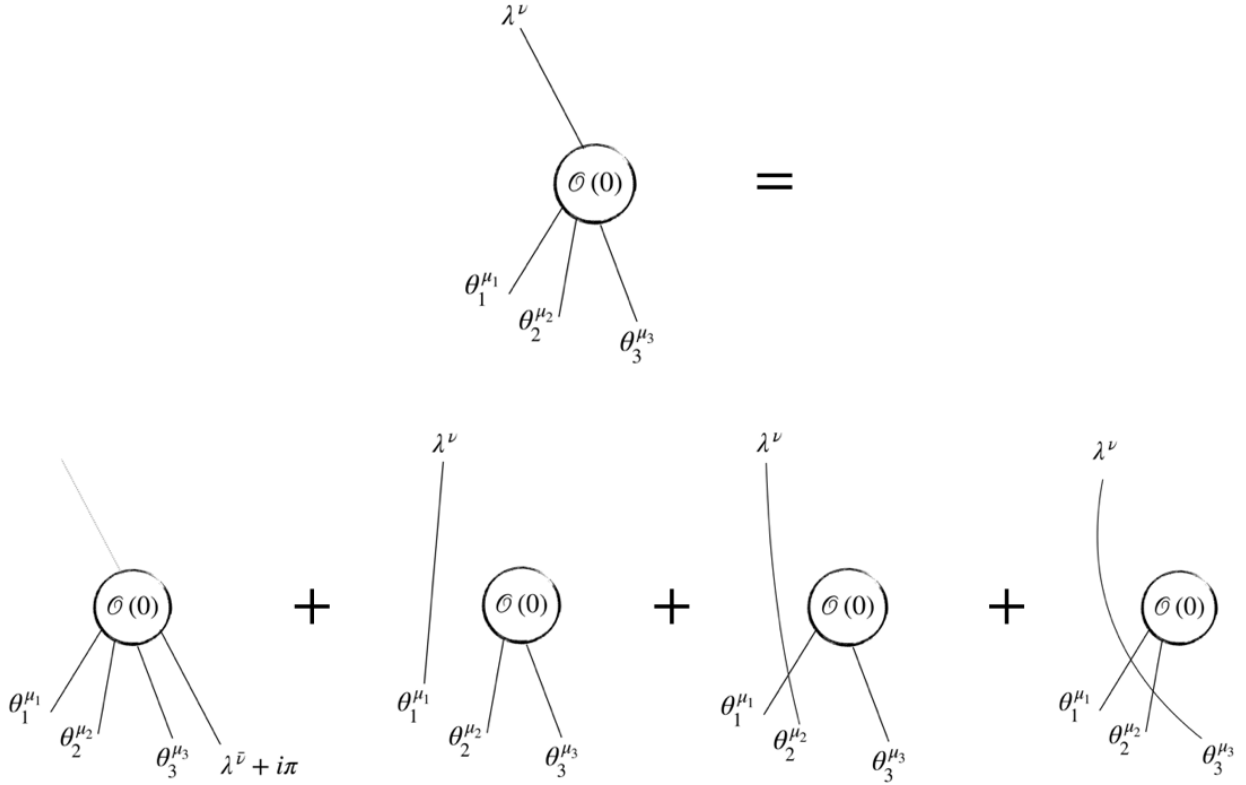


Figure 3.7 Equation (3.35) for $k = 3$ and $m = 1$. The disconnected terms vanish for $\{\theta_i^{\mu_i}\} \neq \lambda^\nu$.

Other equations are closely related to the properties of the S -matrix and can be expressed as:

I. Exchange :

$$F_k^\mathcal{O}(\theta_1^{\mu_1}, \dots, \theta_j^{\mu_j}, \theta_{j+1}^{\mu_{j+1}}, \dots, \theta_k^{\mu_k}) = S_{\mu_j, \mu_{j+1}}(\theta_{j, j+1}) F_k^\mathcal{O}(\theta_1^{\mu_1}, \dots, \theta_{j+1}^{\mu_{j+1}}, \theta_j^{\mu_j}, \dots, \theta_k^{\mu_k}), \quad (3.37)$$

II. Crossing :

$$F_k^\mathcal{O}(\theta_1^{\mu_1} + 2i\pi, \theta_2^{\mu_2}, \dots, \theta_k^{\mu_k}) = \prod_{j=2}^k S_{\mu_1, \mu_j}(\theta_{1j}) F_k^\mathcal{O}(\theta_2^{\mu_2}, \dots, \theta_k^{\mu_k}, \theta_1^{\mu_1}), \quad (3.38)$$

III. Kinematic residue :

$$-i \operatorname{Res}_{\theta^\mu = \theta_0^\mu} F_{k+2}^\mathcal{O}(\theta^\mu + i\pi, \theta_0^\mu, \theta_1^{\mu_1}, \dots, \theta_k^{\mu_k}) = \left(1 - \prod_{j=1}^k S_{\mu, \mu_j}(\theta_{0j}) \right) F_k^\mathcal{O}(\theta_1^{\mu_1}, \dots, \theta_k^{\mu_k}) \quad (3.39)$$

IV. Bound-state residue :

$$-i \operatorname{Res}_{\theta^\alpha = \theta_0^\beta} F_{k+2}^\mathcal{O}(\theta^\alpha + iu_{\alpha\gamma}^\beta/2, \theta_0^\beta - iu_{\beta\gamma}^\alpha/2, \theta_1^{\mu_1}, \dots, \theta_k^{\mu_k}) = \Gamma_{\alpha\beta}^\gamma F_{k+1}^\mathcal{O}(\theta_0^\gamma, \theta_1^{\mu_1}, \dots, \theta_k^{\mu_k}), \quad (3.40)$$

where $\Gamma_{\alpha\beta}^\gamma$ is the on-shell three-particle vertex functions associated to the (bound-state) poles of the S -matrix. As seen for the S -matrix in Subsection 1.2.2.1, this equation is indeed related to the presence of bound states in the asymptotic spectrum of the theory.

The form factor bootstrap program consists of finding solutions to the equations above. However, considered a certain theory, it is generally a non-trivial task to match the solutions of the form factor bootstrap to a specific operator. In the case of twist fields, the equations (3.37)-(3.39) require some modifications due to their non trivial actions on the fields of the theory. In particular, the form factor bootstrap program has been extended in [15] to the branch-point twist fields, with modifications accounting for the special exchange relations (3.9) and (3.10). For form factors of simpler twist fields, such as the $U(1)$ fields introduced in Subsection 3.2.3, these modifications may be formally implemented via the *factor of local commutativity* ω . The latter defines the exchange relations of a twist field \mathcal{O} with the fundamental fields φ of the theory [71]. In rapidity-space, these exchange relations are implemented on the particle-creation operators:

$$Z_\mu(\theta) \mathcal{O}(0) = \omega \mathcal{O}(0) Z_\mu(\theta), \quad (3.41)$$

where the operators $Z_\mu(\theta)$ satisfy the commutation relations (1.8) and define the asymptotic states (1.7). The locality can be restored by choosing $\omega = 1$. This relation changes equations I and III above and they become:

$$\begin{aligned} F_k^\mathcal{O}(\theta_1^{\mu_1} + 2i\pi, \theta_2^{\mu_2}, \dots, \theta_k^{\mu_k}) &= \omega F_k^\mathcal{O}(\theta_2^{\mu_2}, \dots, \theta_k, \theta_1) \\ &= \omega \prod_{i=2,k} S_{\mu_i, \mu_1}(\theta_{i1}) F_k^\mathcal{O}(\theta_1^{\mu_1}, \dots, \theta_k^{\mu_k}), \end{aligned} \quad (3.42)$$

and

$$-i \operatorname{Res}_{\theta^\mu = \theta_0^\mu} F_{k+2}^\mathcal{O}(\theta^\mu + i\pi, \theta_0^\mu, \theta_1^{\mu_1}, \dots, \theta_k^{\mu_k}) = \left(1 - \omega \prod_{j=1}^k S_{\mu, \mu_j}(\theta_{0j}) \right) F_k^\mathcal{O}(\theta_1^{\mu_1}, \dots, \theta_k^{\mu_k}). \quad (3.43)$$

These modifications are essential in order to implement the right equations for form factors of fields satisfying (3.42). Examples of applications can be found in [96] for various operators in the Federbush model. In free theories, the bootstrap program for form factors of $U(1)$ fields⁹ was implemented in [89, 97], and consists of the two modified equations (3.42) and (3.43) along with the exchange equation (3.37). The bound-state residue equation (3.40) is indeed discarded due to the absence of bound states. In Subsection 4.3.3, we will present the solutions of these equations for the free boson theory.

⁹An earlier treatment of form factor of $U(1)$ -field can be found in [72] in the Ising model.

3.3.2 Finite-volume form factors

We are now interested in extending the concept of form factors to finite volume. A natural way to implement a finite volume QFT is to map the theory into a cylinder with the space direction along the circumference and time extending to infinity. The fundamental fields will be thus subjected to periodic boundary conditions over the circumference. As a consequence the momenta of multi-particle states $|\theta_1^{\mu_1}, \dots, \theta_k^{\mu_k}\rangle$ for any $k \in \mathbb{N}$ are quantised. For a quasiparticle of particle species μ_i and rapidity $\theta_i^{\mu_i}$ in a finite volume L , the quantisation condition is given by the *Bethe-Yang equations*:¹⁰

$$e^{im_{\mu_i}L \sinh \theta_i^{\mu_i}} \prod_{j \neq i}^k S_{\mu_i \mu_j}(\theta_{ij}) = 1, \quad (3.44)$$

where m_{μ_i} is the mass of the particle and $m_{\mu_i} \sinh \theta_i^{\mu_i}$ is its momentum. The equation above can be seen as the analogy of the box quantisation in quantum mechanics for integrable systems¹¹. It is obtained by demanding that the wave function remains unchanged after a particle has taken a trip around the circle and returned to its original location. Along the way the i th particle will interact with the other particles of the theory, and this introduces the product of S-matrix elements $S_{\mu_i \mu_j}$ in (3.44).

In large volume, the energy of a k -particle state differs from its value in infinite-volume by the *Casimir Energy* $E_o(L)$ which represents the vacuum energy in finite volume. In particular, we have :

$$E_L(\theta^{\mu_1}, \dots, \theta^{\mu_k}) = E_o(L) + \sum_{j=1}^k m_{a_j} \cosh \theta^{\mu_j} + O(e^{-\tilde{\mu}L}). \quad (3.45)$$

Corrections to the formula above come from virtual scattering processes due to the compactness of the cylinder, depend on a characteristic mass scale $\tilde{\mu}$, and are expected to be exponentially suppressed for large volume. The value of $E_o(L)$ depends on the normalisation. From the infinite volume viewpoint it is natural to choose the vacuum energy to be zero as this choice reproduces exactly the same energy for both infinite and large volume up to the exponential corrections.

Taking the logarithm of the Bethe-Yang equations [98, 99] we obtain the quantization

¹⁰Here, we follow the convention introduced in Chapter 1, and thus we assume that the state $|\theta_1^{\mu_1}, \dots, \theta_k^{\mu_k}\rangle$ is part of the eigenbasis of the Hamiltonian.

¹¹The underlying assumptions for the validity of equation (3.44) are the factorization of the S -matrix and the absence of particle production.

condition for the i th quasiparticle:

$$Q_{\mu_i}(\theta_1^{\mu_1}, \dots, \theta_k^{\mu_k}) := m_{\mu_i} L \sinh \theta_i^{\mu_i} + \sum_{i \neq j} -i \log S_{\mu_i \mu_j}(\theta_{ij}) = 2\pi I_i^{\mu_i}, \quad I_i^{\mu_i} \in \mathbb{Z}. \quad (3.46)$$

The finite volume states $|\{I_1^{\mu_1}, \dots, I_k^{\mu_k}\}\rangle_L$ are related to the infinite volume states $|\theta_1^{\mu_1}, \dots, \theta_k^{\mu_k}\rangle$ via [86, 87]:

$$|\{I_1^{\mu_1}, \dots, I_k^{\mu_k}\}\rangle_L = \frac{1}{\sqrt{\rho(\theta_1^{\mu_1}, \dots, \theta_k^{\mu_k})}} |\theta_1^{\mu_1}, \dots, \theta_k^{\mu_k}\rangle + O(e^{-\tilde{\mu}L}). \quad (3.47)$$

The quantity $\rho(\theta_1^{\mu_1}, \dots, \theta_k^{\mu_k})$ is the density of states in rapidity-space and can be seen as the Jacobian of the mapping between rapidity and quantum number spaces:

$$\rho(\theta_1^{\mu_1}, \dots, \theta_k^{\mu_k}) = \det \mathcal{J}, \quad \mathcal{J}_{i,j} = \frac{\partial Q_{\mu_i}(\theta_1^{\mu_1}, \dots, \theta_k^{\mu_k})}{\partial \theta_j^{\mu_j}}. \quad (3.48)$$

Under this transformation, a vacuum correlation function in finite volume is expected to differ from one in infinite volume only by terms that are suppressed in large volume [100]:

$$\langle 0 | \mathcal{O}(\tau, 0) \tilde{\mathcal{O}}(0, 0) | 0 \rangle - {}_L \langle 0 | \mathcal{O}(\tau, 0) \tilde{\mathcal{O}}(0, 0) | 0 \rangle_L \sim O(e^{-\tilde{\mu}L}). \quad (3.49)$$

This implies that the k -particle elementary form factors of a local operator in finite volume are:

$${}_L \langle 0 | \mathcal{O}(0) |\{I_1^{\mu_1}, \dots, I_k^{\mu_k}\}\rangle_L = \frac{1}{\sqrt{\rho(\theta_1^{\mu_1}, \dots, \theta_k^{\mu_k})}} F_k^{\mathcal{O}}(\theta_1^{\mu_1}, \theta_2^{\mu_2}, \dots, \theta_k^{\mu_k}) + O(e^{-\tilde{\mu}L}). \quad (3.50)$$

In free theories, we have many simplifications. For instance, equation (3.46) simply becomes:

$$Q_{\mu_i}(\theta_1^{\mu_1}, \dots, \theta_k^{\mu_k}) = m_{\mu_i} L \sinh \theta_i^{\mu_i} = 2\pi I_i^{\mu_i}, \quad I_i^{\mu_i} \in \mathbb{Z}. \quad (3.51)$$

Hence, in finite volume and in the absence of interaction, the state $|\theta_1^{\mu_1}, \dots, \theta_k^{\mu_k}\rangle$ composed of solutions of the Bethe-Yang equations is fully characterised by the set of quantum numbers $\{I_1^{\mu_1}, \dots, I_k^{\mu_k}\}$. Furthermore the density of states $\rho(\theta_1^{\mu_1}, \dots, \theta_k^{\mu_k})$ becomes diagonal and takes the following form:

$$\rho(\theta_1^{\mu_1}, \dots, \theta_k^{\mu_k}) = \prod_{j=1}^k m_{\mu_j} L \cosh \theta_j^{\mu_j}. \quad (3.52)$$

If we now go back to the correlator of branch-point twist fields in excited states (3.32), the expansion on the right hand side presents a special structure in free theories. In particular, as

we will see explicitly in Subsection 4.4.1, the presence of branch cuts modifies the quantization conditions of the Bethe-Yang solutions associated to the intermediate states $|\Phi\rangle_L$. It is then possible to argue that the intermediate states possess distinct quantum numbers from the external state $|\Psi\rangle_L$. In free theories this corresponds to having two disjoint sets of rapidities on the two sides of the matrix elements $\langle\Psi|\mathcal{T}(0)|\Phi\rangle$ and $\langle\Psi|\mathcal{T}(0)|\Phi\rangle$, and an expansion (3.32) that is accordingly formed of only *non-diagonal form factors* [86]. Note that in interacting theories, the fact that the two states $|\Psi\rangle_L$ and $|\Phi\rangle_L$ are characterised by different quantum numbers is not a sufficient condition to have distinct Bethe-Yang solutions in the two states, due to the S-matrix dependence of the quantization condition (3.46). In this case one needs to account for the presence of identical rapidities and thus consider *diagonal form factors* [87].

For the purpose of this thesis, it is thus enough to consider only non-diagonal form factors as in Chapters 4 and 5 we will treat the massive free boson. In particular, given two disjoint sets of quantum numbers $\{J_1^{\nu_1}, \dots, J_m^{\nu_m}\} \neq \{I_1^{\mu_1}, \dots, I_k^{\mu_k}\}$, a non-diagonal form factor of a local operator \mathcal{O} is the finite volume part of the matrix element (3.34):

$${}_L\langle\{J_1^{\nu_1}, \dots, J_m^{\nu_m}\}|\mathcal{O}(0)|\{I_1^{\mu_1}, \dots, I_k^{\mu_k}\}\rangle_L = \frac{F_{m+k}^{\mathcal{O}}(\lambda_m^{\nu_m} + i\pi, \dots, \lambda_1^{\nu_1} + i\pi, \theta_1^{\mu_1}, \dots, \theta_k^{\mu_k})}{\sqrt{\rho(\lambda_1^{\nu_1}, \dots, \lambda_m^{\nu_m}) \rho(\theta_1^{\mu_1}, \dots, \theta_k^{\mu_k})}} + O(e^{-\tilde{\mu}L}) \quad (3.53)$$

where the rapidities $\lambda_1^{\nu_1}, \dots, \lambda_m^{\nu_m}$ and $\theta_1^{\mu_1}, \dots, \theta_k^{\mu_k}$ are Bethe-Yang solutions with quantum numbers $\{J_1^{\nu_1}, \dots, J_m^{\nu_m}\}$ and $\{I_1^{\mu_1}, \dots, I_k^{\mu_k}\}$ respectively. Note we have used equation (3.35) to express the finite-volume element in terms of elementary infinite-volume form factors.

EXCITED STATE ENTROPIES OF A CONNECTED REGION

4.1 Entanglement entropies in excited states

In this chapter we investigate the entanglement properties of excited states in a free boson theory, based on the results obtained in [23, 24], where the methodology discussed in Chapter 3 was extended to the treatment of excited states and finite-volume systems. Before these two works, a quite limited number of studies focused on the entanglement content of excited states. In conformal field theory, universal results for certain types of excited states were studied. In [101, 102], the increment of Rényi entropy in an excited state $|\Upsilon\rangle$ with as compared to the ground state of a CFT for the configuration of Fig. 4.1 was found to be

$$S_n^\Upsilon(r) - S_n^0(r) = \frac{(1+n)(h+\bar{h})}{3n}(\pi r)^2 + O(r^{2\Delta_\psi}), \quad (4.1)$$

for small values of $r = \frac{\ell}{L}$, where the excitation is given by the CFT field Υ with scaling dimension $h + \bar{h}$, and $\Delta_\psi = h_\psi + \bar{h}_\psi$ is the smallest scaling dimension of any field in the theory. In particular, the excited state was defined as

$$|\Upsilon\rangle = \lim_{\xi, \bar{\xi} \rightarrow -i\infty} \Upsilon(\xi, \bar{\xi}) |0\rangle, \quad (4.2)$$

where $\xi, \bar{\xi}$ are coordinates on the cylinder. Interestingly, a measurement of the entanglement entropy of a low-lying excited state in CFT at finite volume can provide information about the primary field content of the theory. The most extensive numerical study of other kinds of excited

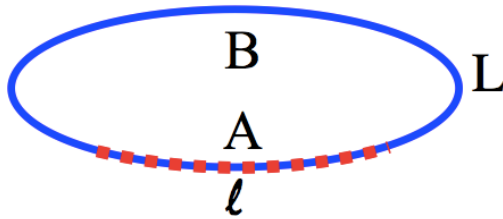


Figure 4.1 Typical bipartition of a one-dimensional finite system of total length L into region A of length ℓ and region B of length $L - \ell$.

states in critical systems was conducted in [103], considering states that are macroscopically different from the ground state.

In this chapter we are instead interested in zero-density states which are defined as a finite set of excitations above the ground state. They are of zero-density states in the sense that in the scaling limit the number of excitations remains fixed and finite whereas all length scales tend to infinity. In this context, the most extensive numerical study in gapped quantum spin chains was carried out in [104] where the entanglement contribution and its maximal value have been obtained for certain excited states approaching the semi-classical limit for large volumes and appropriate regime. Some of these results were obtained and generalised in [23, 24] with a more general interpretation of the validity regime in terms of localised excitations (this will be discussed in Chapter 6).

4.1.1 The scaling limit

We consider the situation depicted in Fig. 4.1: a zero-temperature finite-size system (say a ring) is partitioned into two complementary connected regions A and B of length ℓ and $L - \ell$, respectively. We suppose that the entire system is in a state $|\phi\rangle_L$ with zero energy density (i.e. formed of finite numbers of asymptotic particles, at various momenta) and described by a free massive bosonic theory. We focus on the scaling limit obtained where both the system's size L and the entanglement region's size ℓ are sent to infinity in a fixed proportion given by their ratio r

$$\ell, L \rightarrow \infty \quad \text{with} \quad r = \frac{\ell}{L} \in [0, 1]. \quad (4.3)$$

We want to compute the entanglement contribution generated by the excitations with respect to the ground state which is nothing but the difference between the Rényi entropy in the excited state and in the ground state. In the limit above this quantity turns out to be a function of the ratio r only

$$\lim_{L \rightarrow \infty} S_n^\phi(rL, L) - S_n^0(rL, L) =: \Delta S_n^\phi(r). \quad (4.4)$$

In the replica model, the entropy increment (4.4) can be formally written as a ratio of branch-point twist field correlators,

$$\Delta S_n^\phi(r) = \lim_{L \rightarrow \infty} \frac{1}{1-n} \log \left[\frac{{}_L \langle \phi | \mathcal{T}(0) \tilde{\mathcal{T}}(rL) | \phi \rangle_L}{{}_L \langle 0 | \mathcal{T}(0) \tilde{\mathcal{T}}(rL) | 0 \rangle_L} \right]. \quad (4.5)$$

where $S_n^0(r)$ and $S_n^\psi(r)$ are respectively the entanglement entropy in the ground state and in the zero-density state.

In Section 3.2.3 we have motivated our interest in excited state entanglement measures as an effective approach to capture universal information on the state. We have also highlighted that there are additional complications that one needs to account for in the treatment of correlators in excited states as these present δ -function singularities. We are going to address this problem in Section 4.4 where a finite volume approach allows us to treat these singularities. In free theories, a fundamental step in the computation of (4.5) is provided by the application of the doubling trick, which allows us to overcome the regularization problem of correlators of branch-point twist fields in finite volume (a problem that is still not generally resolved for interaction theories). The doubling trick in fact permits us to express the branch-point twist fields in terms of simpler fields for which the standard finite-volume techniques [86, 87] are applicable. In order to introduce the general ideas behind the doubling trick in the next two Sections 4.2 and 4.3 we will consider the free boson theory in infinite-volume and then extend the discussion to finite volume in Section 4.4.

4.2 Doubling trick

The doubling trick was first introduced in [25] by Fonseca and Zamolodchikov. It was employed to find differential equations that are satisfied by certain combinations of correlation functions in the Ising model. This technique was later used in order to obtain vacuum expectation values $\langle \mathcal{T} \rangle$ in infinite volume in the works [15] (free fermion) and [89] (free boson). The main idea of the doubling trick is to “double” the free theory in order to have an additional continuous symmetry. Let us consider in particular two independent free massive real bosons ϕ_a and ϕ_b . We can construct a free massive complex boson as:

$$\Phi = \frac{\phi_a + i\phi_b}{\sqrt{2}} \quad \text{and} \quad \Phi^\dagger = \frac{\phi_a - i\phi_b}{\sqrt{2}}. \quad (4.6)$$

The new theory possesses in fact an internal continuous $U(1)$ symmetry. This symmetry can then be exploited in order to obtain information about the original (not doubled) theory.

More precisely the two real fields ϕ_a and ϕ_b satisfy the *Klein-Goldon equation* and can be expressed in terms of the mode expansion:

$$\phi_a(x, t) = \int d\theta \left[a(\theta) e^{iP(\theta)x - iE(\theta)t} + a^\dagger(\theta) e^{-iP(\theta)x + iE(\theta)t} \right], \quad (4.7)$$

and $a(\theta)$ and $a^\dagger(\theta)$ are respectively the annihilation and creation operators associated to the real free boson field ϕ_a . A similar expression can be written for ϕ_b . The operators $a(\theta)$ and $a^\dagger(\theta)$ generate the Hilbert space \mathcal{H}_a :

$$\begin{aligned} a(\theta) |0\rangle_a &= 0, \\ a^\dagger(\theta) |0\rangle_a &= |\theta\rangle_a, \end{aligned} \quad (4.8)$$

where $|0\rangle_a$ is the vacuum and $a^\dagger(\theta)$ creates a single-particle state in the θ -space with energy and momentum given by

$$E(\theta) = m \cosh \theta; \quad P(\theta) = m \sinh \theta. \quad (4.9)$$

Furthermore a and a^\dagger satisfy the algebra:

$$[a(\theta), a(\theta')] = 0 = [a^\dagger(\theta), a^\dagger(\theta')], \quad (4.10)$$

$$[a(\theta), a^\dagger(\theta')] = \delta(\theta - \theta'). \quad (4.11)$$

The complex fields Φ and Φ^\dagger are also solutions of the Klein-Goldon equation and are expressed as:

$$\Phi(x, t) = \int d\theta \left[\alpha^+(\theta) e^{iP(\theta)x - iE(\theta)t} + (\alpha^-)^\dagger(\theta) e^{-iP(\theta)x + iE(\theta)t} \right], \quad (4.12)$$

$$\Phi^\dagger(x, t) = \int d\theta \left[\alpha^-(\theta) e^{iP(\theta)x - iE(\theta)t} + (\alpha^+)^\dagger(\theta) e^{-iP(\theta)x + iE(\theta)t} \right], \quad (4.13)$$

where $(\alpha^\pm)^\dagger(\theta)$ and $\alpha^\pm(\theta)$ are the creation and annihilation operators of the complex free boson $\Phi(x, t)$. These create / annihilate a particle with rapidity θ and $U(1)$ charge \pm respectively, and similarly to the real case they generate the Hilbert space \mathcal{H} .

Crucially, a state in the complex theory can be chosen in such a way to reproduce a state

in the real theory. Indeed the creation and annihilation operators of the real free boson can be related to those of the complex field via the transformation:

$$a(\theta) = \frac{\alpha^+(\theta) + \alpha^-(\theta)}{\sqrt{2}} ; \quad a^\dagger(\theta) = \frac{(\alpha^+)^\dagger(\theta) + (\alpha^-)^\dagger(\theta)}{\sqrt{2}} , \quad (4.14)$$

and

$$b(\theta) = \frac{\alpha^+(\theta) - \alpha^-(\theta)}{i\sqrt{2}} ; \quad b^\dagger(\theta) = -\frac{(\alpha^+)^\dagger(\theta) - (\alpha^-)^\dagger(\theta)}{i\sqrt{2}} . \quad (4.15)$$

These relations are obtained by inserting the expressions (4.12), (4.13) and (4.7) for both ϕ_a and ϕ_b in (4.6). Using the transformations above it is possible to show that the operators $(\alpha^\pm)^\dagger(\theta) \alpha^\pm(\theta)$ satisfy the commutation relations:

$$[\alpha^\pm(\theta), (\alpha^\pm)^\dagger(\theta')] = \delta(\theta - \theta') . \quad (4.16)$$

All the other commutation relations are zero, since ϕ_a and ϕ_b commute with each other. A direct consequence is that a complex state can be factorised into two terms in the two real theories:

$$|\Phi\rangle = |\phi\rangle_a \otimes |\phi\rangle_b , \quad (4.17)$$

where $|\Phi\rangle$ is a state in the complex theory, and $|\phi\rangle_a$ and $|\phi\rangle_b$ are states in the two real theories. Therefore our computation of the correlator in (4.5) proceeds as follow: we employ the doubling trick and thus evaluate the correlator $\langle \mathcal{T}(0) \tilde{\mathcal{T}}(\ell) \rangle$ in a carefully chosen complex state $|\Phi\rangle$ that reproduces the real result. In the complex theory we can take full advantage of the presence of the $U(1)$ symmetry which will be essential to expand the correlator in matrix elements that are regular in finite volume. At the end of the computation we will find results for the real theory by imposing $|\phi\rangle_b = |0\rangle_b$. A more explicit formulation for such correlator will be given in the next section where we address the problem of extending the replica model to the presence of a $U(1)$ symmetry.

4.3 Doubled replica free boson model in infinite volume

We now need to construct the Replica model of the free doubled free boson theory. As we have seen in Section 3.1, the n -copy model arises from the presence of the cyclic permutation symmetry. In addition, in the new complex theory the doubling induces a $U(1)$ symmetry duplicating each copy of the replica model. In the replica theory we have n copies of the

complex free boson, Φ_j with $j = 1, \dots, n$. Since the components $\phi_{a,j}, \phi_{b,j}$ are commuting fields and the permutation symmetry acts in a factorized way, the branch-point twist field also factorises:

$$\mathcal{T} = \mathcal{T}_a \otimes \mathcal{T}_b. \quad (4.18)$$

In rapidity-space, a state $|\Phi\rangle$ can be written as:

$$|\Phi\rangle = |\phi\rangle_a \otimes |0\rangle_b = |\phi\rangle_{a,1} \otimes \dots \otimes |\phi\rangle_{a,n} \otimes |0\rangle_{b,1} \otimes \dots \otimes |0\rangle_{b,n}. \quad (4.19)$$

Note that in each copy, we have conventionally chosen the excitations to live in one of the two real theories. Again, as seen for the original theory, any real multi-particle state $|\phi\rangle_a$ can be expressed by an appropriate combination of creation operators $(\alpha_j^\pm)^\dagger(\theta)$ in the complex replica theory. In particular, the operators $(\alpha_j^\pm)^\dagger(\theta)$ are now associated to the complex free boson Φ_j living in copy j , and they generate the eigenstates of the U(1)-charge and of the Hamiltonian in the j th complex theory. It follows from (4.14) that a single-particle excitation in copy j is given by the operator:

$$(a_j)^\dagger(\theta) = \frac{1}{\sqrt{2}}((\alpha_j^+)^\dagger(\theta) + (\alpha_j^-)^\dagger(\theta)). \quad (4.20)$$

One natural state that we can choose to consider in this construction is a multi-particle state $|k\rangle_a := |\theta_1, \dots, \theta_k\rangle_a$ characterised by k distinct rapidities¹:

$$|\mathbf{k}\rangle = |k\rangle_a \otimes |0\rangle_b = \frac{1}{2^{\frac{kn}{2}}} \prod_{j=1}^n \prod_{i=1}^k \left((\alpha_j^+)^\dagger(\theta_i) + (\alpha_j^-)^\dagger(\theta_i) \right) |\mathbf{0}\rangle. \quad (4.21)$$

The treatment of this state in (4.21) will be indeed an important study case to obtain information on the entanglement content of a generic state. In a factorized state such as (4.21) the correlator of branch-point twist fields factorise into two real components:

$$\langle \mathbf{k} | \mathcal{T}(0) \tilde{\mathcal{T}}(\ell) | \mathbf{k} \rangle = {}_a \langle k | \mathcal{T}_a(0) \tilde{\mathcal{T}}_a(\ell) | k \rangle_a \times {}_b \langle 0 | \mathcal{T}_b(0) \tilde{\mathcal{T}}_b(\ell) | 0 \rangle_b. \quad (4.22)$$

We therefore obtain the real free boson results as

$${}_a \langle k | \mathcal{T}_a(0) \tilde{\mathcal{T}}_a(\ell) | k \rangle_a = \frac{\langle \mathbf{k} | \mathcal{T}(0) \tilde{\mathcal{T}}(\ell) | \mathbf{k} \rangle}{{}_b \langle 0 | \mathcal{T}_b(0) \tilde{\mathcal{T}}_b(\ell) | 0 \rangle_b}. \quad (4.23)$$

¹In the case of some coinciding rapidities, the normalisation of the state needs to be slightly modified. This case will be discussed in more detail in Section 4.6.2.

Note that the ratio of correlators in equation (4.5) gives:

$$\frac{{}_a\langle k|\mathcal{T}_a(0)\tilde{\mathcal{T}}_a(\ell)|k\rangle_a}{{}_a\langle 0|\mathcal{T}_a(0)\tilde{\mathcal{T}}_a(\ell)|0\rangle_a} = \frac{\langle \mathbf{k}|\mathcal{T}_a(0)\tilde{\mathcal{T}}_a(\ell)|\mathbf{k}\rangle}{\langle \mathbf{0}|\mathcal{T}_a(0)\tilde{\mathcal{T}}_a(\ell)|\mathbf{0}\rangle}, \quad (4.24)$$

where we have introduced the ground state of the complex theory² $|\mathbf{0}\rangle = |0\rangle_a \otimes |0\rangle_b$, and divided out the vacuum-correlator ${}_b\langle 0|\mathcal{T}_b(0)\tilde{\mathcal{T}}_b(\ell)|0\rangle_b$. Therefore complex results reproduce exactly real results.

4.3.1 Diagonalisation of the cyclic permutation action

In the doubled replica model, the combination of the $U(1)$ symmetry of the complex field on each replica, and of the permutation symmetry of the replica, implies the existence of a $U(n)$ symmetry of the model. Cyclic permutations form a subgroup of the $U(n)$ symmetry group of rotations amongst the copies, which can be diagonalized. The diagonal basis is a new set of n independent complex free bosons, each of which has its own $U(1)$ symmetry, and the cyclic permutation action is expressed as a product of $U(1)$ actions on each of these bosons. Therefore, the branch-point twist field acts as a product of $U(1)$ twist fields in the diagonal basis. In matrix form, the cyclic permutation symmetry act as

$$T \begin{pmatrix} \Phi_1 \\ \Phi_2 \\ \vdots \\ \Phi_{n-1} \\ \Phi_n \end{pmatrix} = \begin{pmatrix} \Phi_2 \\ \Phi_3 \\ \vdots \\ \Phi_n \\ \Phi_1 \end{pmatrix}, \quad \text{such that, } T = \begin{pmatrix} 0 & 1 & 0 & \cdots & 0 \\ 0 & 0 & 1 & \cdots & 0 \\ \vdots & \vdots & \vdots & \ddots & \vdots \\ 0 & 0 & 0 & \cdots & 1 \\ 1 & 0 & 0 & \cdots & 0 \end{pmatrix}. \quad (4.25)$$

The eigenvalues of the matrix T are exactly the n th roots of unity $\lambda_p = e^{\frac{2\pi i p}{n}}$ for $p = 1, \dots, n$. The cyclic permutation action is diagonalized by the fields

$$\tilde{\Phi}_p = \frac{1}{\sqrt{n}} \sum_{j=1}^n e^{-\frac{2\pi i j p}{n}} \Phi_j, \quad (4.26)$$

which are themselves canonically normalized complex free boson fields. Since the cyclic permutation symmetry acts diagonally on the basis $\tilde{\Phi}_p$, the branch-point twist field and the anti-twist field can be factorised into $U(1)$ -fields \mathcal{T}_p and their Hermitian conjugates \mathcal{T}_{-p}

²Throughout the next sections we will focus on evaluating correlators in complex states such as $|\mathbf{k}\rangle$. We thus introduce the convention that states with bond letters are complex.

respectively:

$$\mathcal{T} = \prod_{p=1}^n \mathcal{T}_{+p}, \quad \tilde{\mathcal{T}} = \prod_{p=1}^n \mathcal{T}_{-p}. \quad (4.27)$$

The new twist fields \mathcal{T}_{+p} and \mathcal{T}_{-p} satisfy the following exchange relations with the new basis:

$$\begin{aligned} \mathcal{T}_{\pm p}(x, t) \tilde{\Phi}_q(y, t) &= \left(e^{\pm \frac{2\pi i p}{n}} \right)^{\delta_{q,p}} \tilde{\Phi}_q(y, t) \mathcal{T}_{\pm p}(x, t) & \text{for } y > x &, \\ &= \tilde{\Phi}_q(y, t) \mathcal{T}_{\pm p}(x, t) & \text{for } x > y &, \end{aligned} \quad (4.28)$$

for $q, p = 1, \dots, n$ with $q \equiv q + n$ and $p \equiv p + n$. It follows that the field \mathcal{T}_n is the identity field. Remarkably the only effect of the $U(1)$ field is to add a phase $\lambda_{\pm p} = e^{\pm \frac{2\pi i p}{n}}$ when the two fields $\mathcal{T}_{\pm p}$ and $\tilde{\Phi}_q$ are in the same copy. For free bosons, such $U(1)$ fields have been studied and it is known that they have scaling dimensions [105]

$$\Delta_p = \frac{p}{2n} \left(1 - \frac{p}{n} \right), \quad (4.29)$$

so that

$$2 \sum_{p=1}^n \Delta_p = \frac{1}{6} \left(n - \frac{1}{n} \right) = d_n, \quad (4.30)$$

which reproduces (3.11) for $c = 2$ (the central charge of the complex free boson).

In the diagonal basis (4.26), the creation operators are

$$(\tilde{\alpha}_p^{\pm})^{\dagger}(\theta) = \frac{1}{\sqrt{n}} \sum_{j=1}^n e^{\pm \frac{2\pi i j p}{n}} (\alpha_j^{\pm})^{\dagger}(\theta), \quad (4.31)$$

and are related to the older operators by the inverse transformations:

$$(\alpha_j^{\pm})^{\dagger}(\theta) = \frac{1}{\sqrt{n}} \sum_{p=1}^n e^{\mp \frac{2\pi i j p}{n}} (\tilde{\alpha}_p^{\pm})^{\dagger}(\theta). \quad (4.32)$$

Recalling the state (4.19) and expressing the operators $\alpha_j^{\pm}(\theta)$ there in terms of the tilde operators through (4.32), we obtain after some manipulations that

$$|\mathbf{k}\rangle = \frac{1}{(2n)^{\frac{nk}{2}}} \prod_{j=1}^n \sum_{\epsilon_1, \dots, \epsilon_k = \pm 1} \sum_{p_1, \dots, p_k = 1}^n e^{-\frac{2\pi i j}{n} \sum_{i=1}^k p_i \epsilon_i} (\tilde{\alpha}_{p_1}^{\epsilon_1})^{\dagger}(\theta_1) \cdots (\tilde{\alpha}_{p_k}^{\epsilon_k})^{\dagger}(\theta_k) |\mathbf{0}\rangle. \quad (4.33)$$

Thus in the new basis correlators of branch-point twist fields evaluated in the state (4.33) factorise into correlators of $U(1)$ -fields on the copies $p = 1, \dots, n$, and the expression above is

useful to express such decomposition. One can understand the structure of the resulting expansions by looking at a specific case. In the next section we will derive the factorization of the branch-point twist field correlator in a single particle excitation, and identify the building blocks of the resulting form factor expansions. Despite the simplicity of the state under consideration, this example may be also instructive to understand the structure of more complicated expansions such as those derived for multiparticle states.

In order to simplify the writing, from now onwards we will use the short-hand notations:

$$\tilde{\alpha}_j^+(\theta) := \mathfrak{a}_j(\theta) \quad \text{and} \quad \tilde{\alpha}_j^-(\theta) := \mathfrak{b}_j(\theta). \quad (4.34)$$

where \mathfrak{a}_j^\dagger and \mathfrak{b}_j^\dagger are both associated to the new basis, and create excitations with respectively positive or negative $U(1)$ -charge in copy j . In particular the excitations created by \mathfrak{a}_j^\dagger will be simply referred to as *particles*, while those created by \mathfrak{b}_j^\dagger will be called *antiparticles*.

4.3.2 Example: twist-field correlator in a single-particle excitation

We consider a single particle excitation $|\mathbf{1}\rangle$ obtained from (4.19) for $k = 1$. In order to write the state $|\mathbf{1}\rangle$ in the new basis, it is convenient to express it in terms of the population of quasiparticles in each copy of the Replica model. We thus introduce the integer set $\{N^\pm\} = \{N_1^+, N_1^-, \dots, N_n^+, N_n^-\}$, where N_j^\pm is the number of particle/antiparticles living in the j th-copy. From (4.33), the single particle state becomes:

$$|\mathbf{1}\rangle = \sum_{\{N^\pm\}} C_n(\{N^\pm\}) \prod_{p=1}^n [\mathfrak{a}_p^\dagger(\theta)]^{N_p^+} [\mathfrak{b}_p^\dagger(\theta)]^{N_p^-} |\mathbf{0}\rangle, \quad (4.35)$$

where $C_n(\{N^\pm\})$ contain the phase factors resulting from the transformation (4.32) and associated to the configuration $\{N^\pm\}$. The sum runs over the integer sets $\{N^\pm\}$ and is constrained by the conservation of the total number of quasiparticles in the replica model, formally:

$$N := \sum_{p=1}^n (N_p^+ + N_p^-) = n. \quad (4.36)$$

Thus, in the state (4.35) the correlator of branch-point twist fields becomes

$$\begin{aligned} \langle \mathbf{1} | \mathcal{T}(0) \tilde{\mathcal{T}}(\ell) | \mathbf{1} \rangle &= \sum_{\{N^\pm\}} \sum_{\{\tilde{N}^\pm\}} C_n^*(\{N^\pm\}) C_n(\{\tilde{N}^\pm\}) \\ &\times \prod_{p=1}^n \langle \mathbf{0} | [\mathfrak{a}_p(\theta)]^{N_p^-} [\mathfrak{b}_p(\theta)]^{N_p^+} \mathcal{T}_{+p}(0) \mathcal{T}_{-p}(\ell) [\mathfrak{a}_p^\dagger(\theta)]^{\tilde{N}_p^+} [\mathfrak{b}_p^\dagger(\theta)]^{\tilde{N}_p^-} | \mathbf{0} \rangle_p. \end{aligned} \quad (4.37)$$

Note that above the factorization follows naturally from the operators \mathfrak{a}_p , \mathfrak{b}_p and their Hermitian conjugates, on which the permutation symmetry acts in a diagonal way by construction. Therefore the factorization of branch-point twist fields into $U(1)$ -fields is a property that holds more generally for any multi-particle states expanded in the basis (4.31).

One direct consequence of the factorization in (4.37) is that each correlator of $U(1)$ -fields can be treated as an independent form factor expansion in each copy of the replica model. Indeed we can obtain the expansions in the usual way of inserting a complete set of states between the two fields in each correlator, namely \mathcal{T}_{+p} and \mathcal{T}_{-p} so that we have in total n independent sums. We will present the explicit form of these expansions in Section 4.5 where we will also deal with the full computation of their leading contributions in the scaling limit (4.3). For the time being it is worthwhile to introduce only their fundamental components which for any copy $p = 1, \dots, n$ are matrix elements of the form:

$${}_p\langle \mathbf{0} | \prod_{i_1=1}^s \mathfrak{a}_p(\theta_{i_1}) \prod_{i_2=1}^q \mathfrak{b}_p(\beta_{i_2}) \mathcal{T}_{\pm p}(0) \prod_{i_4=1}^{q'} \mathfrak{b}_p^\dagger(\beta'_{i_4}) \prod_{i_3=1}^{s'} \mathfrak{a}_p^\dagger(\theta'_{i_3}) | \mathbf{0} \rangle_p, \quad (4.38)$$

where the θ_i s denote the rapidities of particles, and the β_i s denote those of antiparticles. Note that here and later, the order of the creation and annihilation operators is irrelevant as they all commute in the free boson case. The only non-zero elements are those preserving the charge on the left and the right of the twist field. If we assume distinct rapidities $\theta_i \neq \theta'_i$ and $\beta_i \neq \beta'_i$ for all i , we can easily relate the element above to an elementary form factor of $U(1)$ -fields:³

$${}_p\langle \mathbf{0} | \prod_{i_1=1}^s \mathfrak{a}_p(\theta_{i_1}) \prod_{i_2=1}^q \mathfrak{b}_p(\beta_{i_2}) \mathcal{T}_{\pm p}(0) \prod_{i_4=1}^{q'} \mathfrak{b}_p^\dagger(\beta'_{i_4}) \prod_{i_3=1}^{s'} \mathfrak{a}_p^\dagger(\theta'_{i_3}) | \mathbf{0} \rangle_p = \quad (4.39)$$

$$F_{s+s'+q+q'}^{p,n}(\theta'_1, \dots, \theta'_{s'}, \beta_1 + i\pi, \dots, \beta_q + i\pi; \beta'_1, \dots, \beta'_{q'}, \theta_1 + i\pi, \dots, \theta_s + i\pi) \delta_{s-q, s'-q'},$$

where $\delta_{s-q, s'-q'}$ ensures the conservation of the $U(1)$ charge. The expression above is obtained by iterating the property (3.35) as in this case the disconnected terms are simply zero.

4.3.3 Form factors of $U(1)$ -fields

In this subsection we implement the bootstrap equations (3.42), (3.43) and (3.37) for form factors of $U(1)$ -fields. These equations can be easily solved for two-particle matrix elements.

³Here, we have used a slightly different notation from the one employed in Section 3.3. The reason is to emphasise the presence of an equal number of particles and antiparticles in non-zero form factors of $U(1)$ field.

In particular, we define the two-particle form factors of the $U(1)$ field in the p th copy as

$$F^{p|+-}(\theta_1 - \beta_2) := {}_p\langle \mathbf{0} | \mathcal{T}_p(0) \mathfrak{a}_p^\dagger(\theta_1) \mathfrak{b}_p^\dagger(\beta_2) | \mathbf{0} \rangle_p = F^{p|-+}(\beta_2 - \theta_1), \quad (4.40)$$

$$F^{p|++}(\theta_1 - \theta_2) := {}_p\langle \mathbf{0} | \mathcal{T}_p(0) \mathfrak{a}_p^\dagger(\theta_1) \mathfrak{a}_p^\dagger(\theta_2) | \mathbf{0} \rangle_p = 0, \quad (4.41)$$

$$F^{p|--}(\beta_1 - \beta_2) := {}_p\langle \mathbf{0} | \mathcal{T}_p(0) \mathfrak{b}_p^\dagger(\beta_1) \mathfrak{b}_p^\dagger(\beta_2) | \mathbf{0} \rangle_p = 0. \quad (4.42)$$

The twist field preserves the total $U(1)$ charge therefore the two last two form factors are vanishing. The form factor program for such fields implies:

I. Exchange :

$$F^{p|\pm\mp}(\theta) = F^{p|\mp\pm}(-\theta) \quad (4.43)$$

II. Crossing :

$$F^{p|\pm\mp}(\theta + 2\pi i) = \gamma_p^\pm F^{p|\mp\pm}(-\theta) = \gamma_p^\pm F^{p|\pm\mp}(\theta), \quad (4.44)$$

III. Kinematical residue :

$$\text{Res}_{\theta=0} F^{p|\pm\mp}(\theta + i\pi) = i(1 - \gamma_p^\pm) \tau_p, \quad (4.45)$$

where γ_p^\pm are the factors of local commutativity introduced in Subsection 3.3.1, and here associated to the bosons \pm . From the exchange relations (4.28) we expect that $\gamma_p^+ = (\gamma_p^-)^{-1} = e^{\frac{2\pi i p}{n}}$. Furthermore we define the vacuum expectation value as:

$$\tau_p = {}_p\langle \mathbf{0} | \mathcal{T}_p(0) | \mathbf{0} \rangle_p. \quad (4.46)$$

Based on the equations above it is easy to make a general ansatz:

$$F^{p|+-}(\theta) = \frac{Ae^{a\theta}}{\cosh \frac{\theta}{2}}, \quad (4.47)$$

where A and a are constants to be determined. It is then straightforward to show that the bootstrap equations I-III are satisfied for

$$a = \frac{p}{n} - \frac{1}{2} \quad \text{and} \quad A = -\tau_p \sin \frac{\pi p}{n}. \quad (4.48)$$

The final solution is thus

$$F^{p|+-}(\theta) = -\tau_p \sin \frac{\pi p}{n} \frac{e^{\left(\frac{p}{n} - \frac{1}{2}\right)\theta}}{\cosh \frac{\theta}{2}}. \quad (4.49)$$

Another solution can be obtained by shifting $p \mapsto p + n$ but if we assume $p \leq n$ the solution above is singled out. Note that such type of form factor has been known for a long time [72, 89, 97].

One important simplification that comes out in free theories is that higher-particle form factors factorise into two-particle contributions. An explicit expression for them can be easily obtained by employing Wick's theorem and accounting for all possible ways to perform Wick's contractions among the excitations. In particular for the complex free boson theory we have

$$\begin{aligned} F_{2m}^{p,n}(\theta_1, \dots, \theta_m; \beta_1, \dots, \beta_m) &= {}_p\langle \mathbf{0} | \mathcal{T}_p(0) \mathfrak{a}_p^\dagger(\theta_1) \cdots \mathfrak{a}_p^\dagger(\theta_m) \mathfrak{b}_p^\dagger(\beta_1) \cdots \mathfrak{b}_p^\dagger(\beta_m) | \mathbf{0} \rangle_p \\ &= \tau_p \sum_{\sigma \in S_m} f_p^n(\theta_{\sigma(1)} - \beta_1) \cdots f_p^n(\theta_{\sigma(m)} - \beta_m), \end{aligned} \quad (4.50)$$

where we introduced the normalized two-particle form factor

$$f_p^n(\theta) := \frac{F^{p|+-}(\theta)}{\tau_p}, \quad (4.51)$$

and σ are all elements of the permutation group S_m of m indices. Thus once we have the two-particle form factor solution (4.49), we are then able to compute form factor elements for any number of particles.

4.4 Doubled replica free boson model in finite volume

Correlators such as (4.37) needs to be treated in finite volume. The original free boson complex theory is thus mapped into a cylinder of circumference L , and the resulting replica model is composed of n copies of the original cylinder with a branch-cut indentified with the entanglement region. As explained in Subsection 3.2.3 after some manipulation, we obtain two semi-infinite branch cuts located at the boundary points of the entanglement region and extending infinitely along the time direction.

In Subsection 3.3.2 we have seen that finite-volume matrix element of local operators may be expressed in terms of the infinite-volume form factors by mean of the change of variable (3.47), up to exponential corrections controlled by the volume. We expect such corrections to be negligible in the scaling limit (4.3) where the volume is taken infinitely large. Roughly speaking the main difference between the infinite-volume states and the finite-volume states is that in finite volume their rapidities are quantised. In particular, in the replica model the quantisation conditions are affected by the presence of the branch cuts. We will use the following

simple example to explain what these quantization conditions are in general.

Consider a simple matrix element on sector p of the form

$${}_p\langle\mathbf{0}|\prod_{i=1}^k\mathfrak{a}_p(\theta_i)\mathcal{T}_{+p}(0)\mathcal{T}_{-p}(\ell)\prod_{i=1}^k\mathfrak{a}_p^\dagger(\theta_i)|\mathbf{0}\rangle_p = \sum_{|\mathbf{q}\rangle_p}{}_p\langle\mathbf{0}|\prod_{i=1}^k\mathfrak{a}_p(\theta_i)\mathcal{T}_{+p}(0)|\mathbf{q}\rangle_p \times {}_p\langle\mathbf{q}|\mathcal{T}_{-p}(\ell)\prod_{i=1}^k\mathfrak{a}_p^\dagger(\theta_i)|\mathbf{0}\rangle_p. \quad (4.52)$$

We will think of this matrix element as a particular building block of a more complicated two-point function. This means that the external state $\prod_{i=1}^k\mathfrak{a}_p^\dagger(\theta_i)|\mathbf{0}\rangle_p$ depends on rapidities $\{\theta_i\}$ which are the same rapidities of the original excited state $|\mathbf{k}\rangle$ in (4.21). Here $|\mathbf{q}\rangle_p$ are intermediate states composed of q excitations, of which s are particles and $q-s$ are antiparticles. In particular the states $|\mathbf{q}\rangle_p$ are of the form:

$$|\mathbf{q}\rangle_p = \prod_{i=1}^s\mathfrak{a}_p^\dagger(\beta_i)\prod_{i=s+1}^q\mathfrak{b}_p^\dagger(\beta_i)|\mathbf{0}\rangle_p, \quad (4.53)$$

and the sum over intermediate states is a sum over $q = 0, \dots, \infty$ and over β_i s. The sum is constrained by the charge conservation. The latter requires

$$2s - q = k. \quad (4.54)$$

and fixes either s or q in the sum. In the next two subsections we extend the expansion (4.52) to finite volume.

4.4.1 Quantisation conditions

In finite volume L one must first choose a sector in order to determine the quantum numbers of the external state and intermediate states in (4.52). As shown in Fig. 4.2, different sections may lead to different boundary conditions due to the presence of the branch cuts.

Consider a certain copy j , we choose the external state to be in the section where the field Φ_j is periodic $\Phi_j(x+L) = \Phi_j(x)$ and it does not cross the branch cut. This choice leads to the standard quantisation conditions (3.51) discussed in Section 3.3.2. In contrast the intermediate states $|\mathbf{q}\rangle_{p,L}$ will be chosen in a section between the two fields that means that the field Φ_j will cross the branch cut associated to the branch-point twist field \mathcal{T} and it will move to the next copy. As a consequence the quantisation condition becomes $\Phi_i(x+L) = \Phi_{i+1}(x)$. In the diagonal basis (4.31) the field $\tilde{\Phi}_p(x)$ only gains a phase resulting from the exchange with the twist-field \mathcal{T}_{+p} and has quasi-periodic condition $\tilde{\Phi}_p(x+L) = e^{\frac{2\pi ip}{n}}\tilde{\Phi}_p(x)$. As a result the

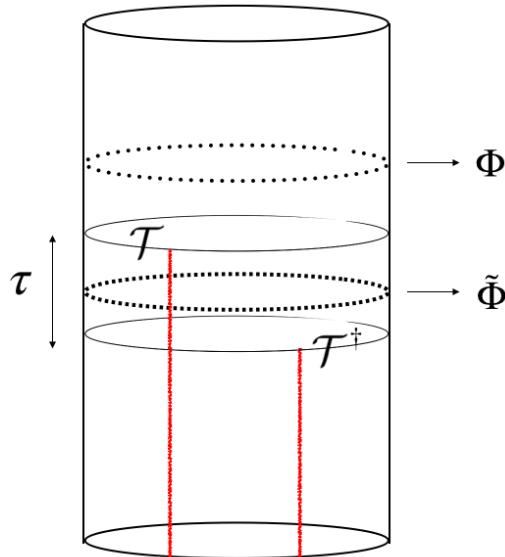


Figure 4.2 A single copy of the finite-volume replica model. The quantization conditions in the presence of the branch cuts can be understood as follow: the field Φ is periodic in a sector of the cylinder that do not involve any branch cut. By performing a trip around the entire circumference the field Φ does not change, and this leads to standard quantization conditions of the external state in the expansion (4.52). In contrast the field $\tilde{\Phi}$ gains a phase after the same trip around the circumference as it lies in a sector that crosses the branch cut associated to the twist field \mathcal{T}_p . The intermediate states in (4.52), formed of excitations associated to the field $\tilde{\Phi}$ are accordingly subjected to quantization conditions of the form (4.56) and (4.57).

quantization of momenta (rapidities) is for the external state:

$$P(\theta_i) = mL \sinh \theta_i = 2\pi I_i \quad \text{with} \quad I_i \in \mathbb{Z} \quad \text{and} \quad i = 1, \dots, k. \quad (4.55)$$

while for the intermediate states

$$P(\beta_i) = mL \sinh \beta_i = 2\pi J_i^+ + \frac{2\pi p}{n} \quad \text{with} \quad J_i^+ \in \mathbb{Z} \quad \text{and} \quad i = 1, \dots, s, \quad (4.56)$$

$$P(\beta_i) = mL \sinh \beta_i = 2\pi J_i^- - \frac{2\pi p}{n} \quad \text{with} \quad J_i^- \in \mathbb{Z} \quad \text{and} \quad i = s + 1, \dots, q. \quad (4.57)$$

These latter quantization conditions provide the generalization of the Bethe-Yang equations (3.51) in the presence of the branch cut induced by the $U(1)$ twist field \mathcal{T}_p , and can be naturally extended to more general external states such as $|\mathbf{k}\rangle$.

4.4.2 Finite-volume matrix elements of $U(1)$ -fields

Let $|\{I_i\}_k\rangle_{p,L}$ be the external state in finite volume with quantum numbers $\{I_i\}_k = \{I_1, \dots, I_k\}$, and $|\{J_i^\pm\}_{s,q-s}\rangle_{p,L}$ be the quantised intermediate states with quantum numbers $\{J_i^\pm\}_{s,q-s} = \{J_1^+, \dots, J_s^+, J_{s+1}^-, \dots, J_q^-\}$. The expansion (4.52) becomes in finite

volume

$$\begin{aligned}
 & {}_{p;L}\langle \{I_i\}_k | \mathcal{T}_{+p}(0) \mathcal{T}_{-p}(\ell) | \{I_i\}_k \rangle_{p,L} \\
 &= \sum_{s=k}^{\infty} \frac{1}{s!(s-k)!} \sum_{\{J_i^\pm\}_{s,q-s}} {}_{p;L}\langle \{I_i\}_k | \mathcal{T}_p(0) | \{J_i^\pm\}_{s,q-s} \rangle_{p,L} \times {}_{p;L}\langle \{J_i^\pm\}_{s,q-s} | \mathcal{T}_p(0) | \{I_i\}_k \rangle_{p,L}.
 \end{aligned} \tag{4.58}$$

Remarkably conditions (4.55), (4.56) and (4.56) ensure that the external state and the intermediate states possess always excitations with distinct rapidities $\{\theta_i\}_k = \{\theta_1, \dots, \theta_k\} \neq \{\beta_i\}_q = \{\beta_1, \dots, \beta_q\}$ and thus the matrix elements in (4.58) are non-diagonal finite volume form factors such as (3.53). For instance we can write the matrix element:

$${}_{p;L}\langle \{I_i\}_k | \mathcal{T}_p(0) | \{J_i^\pm\}_{s,q-s} \rangle_{p,L} = \frac{F_{k+q}^{p,n}(\{\theta_i\}_k; \{\beta_i\}_{q-s}, \{\beta_i + i\pi\}_s)}{\sqrt{\rho(\{\theta_i\}_k)\rho(\{\beta_i\}_q)}}, \tag{4.59}$$

up to exponentially decaying corrections $O(e^{-\mu L})$. The form factor in the numerator is exactly the same function as in infinite volume up to the quantization conditions on the rapidities discussed earlier. The functions in the denominator are the densities of the left- and right-states, respectively. In free theories, these functions are given by (3.52):

$$\rho(\{\theta_i\}_k) = \prod_{i=1}^k LE(\theta_i), \quad \rho(\{\beta_i\}_q) = \prod_{i=1}^q LE(\beta_i). \tag{4.60}$$

with $E(\theta) = m \cosh \theta$.

Although (4.58) only shows the form factor expansion of a particular correlator, the above analysis easily extends to any other cases, and a generalisation of expression (4.59) to a generic matrix element such as (4.39) can be easily obtained.

4.5 Rényi entropy of a single-particle excited state

We now recall the example in Subsection 4.3.2 and proceed to compute the increment of Rényi entropy (4.4) given by a single-particle excited state. The single-particle excitation is the simplest example of zero-density excited states and can be used as starting point to carry out computation for more complicated states.

In the infinite volume replica model, the state considered is given by expression (4.19) for $k = 1$:

$$|\mathbf{1}\rangle = \frac{1}{2^{\frac{n}{2}}} \prod_{j=1}^n \left((\alpha_j^+)^\dagger(\theta) + (\alpha_j^-)^\dagger(\theta) \right) |\mathbf{0}\rangle. \quad (4.61)$$

As explained in Subsection 4.3.2, such a state admits a more intuitive expression after changing to the new basis of creation operators (4.31), as per (4.33). Here we write it as

$$|\mathbf{1}\rangle = \sum_{\{N^\pm\}} C_n(\{N^\pm\}) \prod_{p=1}^n [\mathfrak{a}_p^\dagger(\theta)]^{N_p^+} [\mathfrak{b}_p^\dagger(\theta)]^{N_p^-} |\mathbf{0}\rangle, \quad (4.62)$$

and $C_n(\{N^\pm\})$ are coefficient characterising the state $|\mathbf{1}\rangle$. The set of integers $\{N^\pm\} := \{N_1^+, N_1^-, \dots, N_n^+, N_n^-\} =: \{N^+\} \cup \{N^-\}$ are the boson occupation numbers of particles/antiparticles in each sector. In finite volume the one-particle state above satisfies the Bethe-Yang equation (4.55) with quantum numbers given by a set of n identical integers $\{I\}_n$ characterising the finite volume state $|\mathbf{1}\rangle_L := |\{I\}_n\rangle_L = |\{I\}_{N_1^\pm}\rangle_{1;L} \otimes \dots \otimes |\{I\}_{N_n^\pm}\rangle_{n;L}$.

Therefore the two point correlation function of branch-point twist fields in finite volume is:

$${}_L\langle \mathbf{1} | \mathcal{T}(0) \tilde{\mathcal{T}}(\ell) | \mathbf{1} \rangle_L = \sum_{\{N^\pm\}} \sum_{\{\tilde{N}^\pm\}} [C_n(\{N^\pm\})]^* C_n(\{\tilde{N}^\pm\}) \prod_{p=1}^n \mathcal{F}_p(N_p^\pm, \tilde{N}_p^\pm), \quad (4.63)$$

where $*$ denotes complex conjugation, and

$$\mathcal{F}_p(N_p^\pm, \tilde{N}_p^\pm) = {}_{p;L}\langle \{I\}_{N_p^\pm} | \mathcal{T}_{+p}(0) \mathcal{T}_{-p}(\ell) | \{I\}_{\tilde{N}_p^\pm} \rangle_{p;L}, \quad (4.64)$$

is the finite-volume two-point function in sector p . As standard, an expansion in form factors can be obtained by inserting a complete set of states between the two fields so that (4.64) becomes a sum over products of the form factors (4.50). Explicitly,

$$\mathbb{1} = \sum_{m^\pm=0}^{\infty} \sum_{\{J_i^\pm\}_{m^\pm}} \frac{1}{m^+! m^-!} | \{J_i^\pm\}_{m^\pm} \rangle_{p;L} {}_{p;L}\langle \{J_i^\pm\}_{m^\pm} |, \quad (4.65)$$

where the quantum numbers $\{J_i^+\}_{m^+} = \{J_1^+, \dots, J_n^+\}$ are associated to the Bethe-Yang solutions of equation (4.56) associated to the particles $\{\theta_i\}_{m^+} = \{\theta_1, \dots, \theta_{m^+}\}$ that are solutions to the Yang-Bethe equation (4.56). Similarly, the integers $\{J_i^-\}_{m^-}$ correspond to quantum numbers of antiparticles of rapidities $\{\beta_i\}_{m^-} = \{\beta_1, \dots, \beta_{m^-}\}$ satisfying equation (4.57). The combinatorial factors $m^\pm!$ prevent us from over-counting states with the same set of quantum numbers, but differently ordered. We can now insert the complete set of states (4.65) into the two-point

function (4.64), and arrive to

$$\begin{aligned}
 & \sum_{m^\pm=0}^{\infty} \sum_{\{J_i^\pm\}_{m^\pm}} \frac{1}{m^+!m^-!} \frac{e^{i\ell[\sum_{i=1}^{m^+} P(\theta_i) + \sum_{i=1}^{m^-} P(\beta_i) - (\tilde{N}_p^+ + \tilde{N}_p^-)P(\theta)]}}{\left[\sqrt{LE(\theta)}\right]^{N_p^+ + N_p^- + \tilde{N}_p^+ + \tilde{N}_p^-} \prod_{i=1}^{m^+} LE(\theta_i) \prod_{i=1}^{m^-} LE(\beta_i)} \\
 & \times F_{N_p^- + N_p^+ + m^- + m^+}^{p,n}(\{\theta + i\pi\}_{N_p^-}, \{\theta_i\}_{m^+}; \{\theta + i\pi\}_{N_p^+}, \{\beta_i\}_{m^-}) \\
 & \times F_{\tilde{N}_p^- + \tilde{N}_p^+ + m^- + m^+}^{n-p,n}(\{\theta\}_{\tilde{N}_p^+}, \{\beta_i + i\pi\}_{m^-}; \{\theta\}_{\tilde{N}_p^-}, \{\theta_i + i\pi\}_{m^+}). \quad (4.66)
 \end{aligned}$$

As mentioned in Subsection 4.3.2 there are various constraints to the expansion (4.63). In particular :

1. The total particle number of the excited state $|\mathbf{1}\rangle_L$ must be preserved in the replica model. Thus the integer sets $\{N^\pm\}$ are subject to the condition

$$\sum_{p=1}^n \sum_{\epsilon=\pm} N_p^\epsilon = n. \quad (4.67)$$

2. According to the Wick theorem, only form factors of a even particle number are not vanishing. As a consequence $N_p^- + N_p^+ + m^- + m^+$ must be an even number.
3. In sector n , the $U(1)$ twist-fields coincide with the identity, and the two-point function (4.66) becomes simply ${}_n\langle I \rangle_{N_n^\pm} | \{I\}_{\tilde{N}_n^\pm} \rangle_{n;L}$ which is non zero only if $N_n^\pm = \tilde{N}_n^\pm$, and its value is just the normalization of the finite-volume states:

$$\mathcal{F}_n(N_n^\pm, N_n^\pm) = N_n^+! N_n^-!. \quad (4.68)$$

4. $U(1)$ -charge conservation implies that

$$N_p^- + m^+ = N_p^+ + m^- \quad \text{and} \quad \tilde{N}_p^- + m^+ = \tilde{N}_p^+ + m^-, \quad (4.69)$$

which is equivalent to $N_p^+ - N_p^- = m^+ - m^- = \tilde{N}_p^+ - \tilde{N}_p^-$. As a result, only form factors involving the same amount of particles and antiparticles are not vanishing.

The constraints above are useful to select and compute the leading contribution of the expansion (4.66) in the limit (4.3). This task will be addressed in the next section in detail. In general there are two equivalent ways to compute such contribution, both presented in [24].

The first way is based on the intuition that the large-volume leading contribution comes

from terms of the expansion (4.66) where the rapidities of the external states approach those of the intermediate states. In this case, the leading behaviour is dictated by the structure of the two-particle form factor near the kinematic poles:

$$f_p^n(\theta_i - \theta + i\pi) \underset{\theta \approx \theta_i}{=} \frac{mL \sin \frac{\pi p}{n} \cosh \theta_1 e^{\frac{i\pi p}{n}}}{\pi(J^+ - I + \frac{p}{n})}. \quad (4.70)$$

Hence the two-particle form factors grow linearly with L for large volume, and combine with the L s of the density functions in the denominator to give a leading term with an overall non-negative power of the volume L . In particular, in the scaling limit (4.3) the leading term turns out to be of 0th power in L and thus volume-independent. The computation involves the application of the Wick theorem (4.50) to extract the contributions near the kinematic poles in the expansion (4.66), and the evaluation of a final re-summation of these contributions over the quantum numbers. In [24] this method has been generalised and successfully employed to the study of the free fermion.

Alternatively we can note that the expansion (4.66) may be expressed by replacing the sums $\sum_{\{J_i^\pm\}_{m^\pm}}$ by a set of contour integrals such that the sum over residues enclosed by the contours reproduces the original sum. The latter substitution provides the starting point of the second approach to compute the leading large-volume contribution. This technique turns out to be more amenable to generalization to the case of multiple entanglement regions that will feature in Chapter 5. Furthermore it can be naturally extended to the treatment of multiparticle states with very few modifications as we will see in Section 4.6. For these two reasons, it is convenient for us to focus on this second approach. We will make full use of it in the next subsection.

4.5.1 Computation by contour integration

Although the expansion (4.66) looks rather complicated, there is a systematic way employed in [24] to obtain its leading term in the limit (4.3) by means of manipulation of multidimensional contour integrals. This method was first developed to compute thermal correlators in integrable QFTs [106, 107] and can be easily extended to our study case. The computation presented in [24] requires the implementation of several steps that can be naturally generalised for use in free boson theories with multiple entanglement regions. In this section we discuss each step in detail.

4.5.1.1 Step 1: converting sums to contour integrals

The starting point of the computation is to rewrite each sum $\sum_{J_i^+}$ in the expansions (4.66) in such a way to express its summand as the result of a carefully chosen contour integral around the Bethe-Yang solution θ_i . More precisely this implies to express each sum as:

$$\sum_{J_i^+ \in \mathbb{Z}} \frac{h(\theta_i, \dots)}{LE(\theta_i)} = \sum_{J_i^+} \int_{\mathcal{C}_{J_i^+}} \frac{d\tilde{\theta}_i}{2\pi} \frac{h(\tilde{\theta}_i, \dots)}{e^{i(LP(\tilde{\theta}_i) - \frac{2\pi p}{n})} - 1}, \quad (4.71)$$

where θ_i describes a particle of an intermediate state $|\{J_i^+\}_{m^+}\rangle_{p;L}$, and $\mathcal{C}_{J_i^+}$ is a small contour encircling θ_i with positive orientation. The function $h^+(\theta_i, \dots)$ includes the product of the two form factors on the left hand side of the expansion (4.66) which is exactly the function we wish to regularise. The denominator inside the integral is the exponential form of equation (4.56) so as to ensure that the integrand has a pole exactly when the equation (4.56) is satisfied. Note that the integration variable $\tilde{\theta}_i$ is not a solution of the equation (4.56). Similarly, we can express the sum associated to an antiparticle with rapidity β_i as

$$\sum_{J_i^- \in \mathbb{Z}} \frac{h^-(\beta_i, \dots)}{LE(\beta_i)} = \sum_{J_i^-} \int_{\mathcal{C}_{J_i^-}} \frac{d\tilde{\beta}_i}{2\pi} \frac{h(\tilde{\beta}_i, \dots)}{e^{i(LP(\tilde{\beta}_i) + \frac{2\pi p}{n})} - 1}, \quad (4.72)$$

In order to simplify the notation from now onwards we will omit the tilde on the integration variables.

Transforming every sum in (4.66) into a contour integral we obtain the expression

$$\begin{aligned} \mathcal{F}_p(N_p^\pm, \tilde{N}_p^\pm) &= \sum_{m^\pm=0}^{\infty} \frac{1}{m^+!m^-!} \frac{1}{[\sqrt{LE(\theta)}]^{N_p^+ + N_p^- + \tilde{N}_p^+ + \tilde{N}_p^-}} \left[\prod_{i=1}^{m^+} \sum_{J_i^+ \in \mathbb{Z}} \int_{\mathcal{C}_{J_i^+}} \frac{d\theta_i}{2\pi} \right] \\ &\times \left[\prod_{k=1}^{m^-} \sum_{J_k^- \in \mathbb{Z}} \int_{\mathcal{C}_{J_k^-}} \frac{d\beta_k}{2\pi} \right] \frac{e^{i\ell[\sum_{i=1}^{m^+} P(\theta_i) + \sum_{i=1}^{m^-} P(\beta_i) - (\tilde{N}_p^+ + \tilde{N}_p^-)P(\theta)]}}{\prod_{i=1}^{m^+} [e^{i(LP(\theta_i) - \frac{2\pi p}{n})} - 1] \prod_{i=1}^{m^-} [e^{i(LP(\beta_i) + \frac{2\pi p}{n})} - 1]} \\ &\times F_{N_p^- + N_p^+ + m^- + m^+}^{p,n}(\{\theta + i\pi\}_{N_p^-}, \{\theta_i\}_{m^+}; \{\theta + i\pi\}_{N_p^+}, \{\beta_i\}_{m^-}) \\ &\times F_{\tilde{N}_p^- + \tilde{N}_p^+ + m^- + m^+}^{n-p,n}(\{\theta\}_{\tilde{N}_p^+}, \{\beta_i + i\pi\}_{m^-}; \{\theta\}_{\tilde{N}_p^-}, \{\theta_i + i\pi\}_{m^+}). \end{aligned} \quad (4.73)$$

4.5.1.2 Step 2: manipulating contour integrals

This step provides the core of the computation and consists in combining the small contours around the Bethe-Yang solutions into a contour encircling the real axis for each variable. While doing so, the contour will cross the kinematic poles of the form factors, whenever $\theta_i = \theta$ or

$\beta_i = \theta$ for some i , and we need to subtract the residua of these poles.

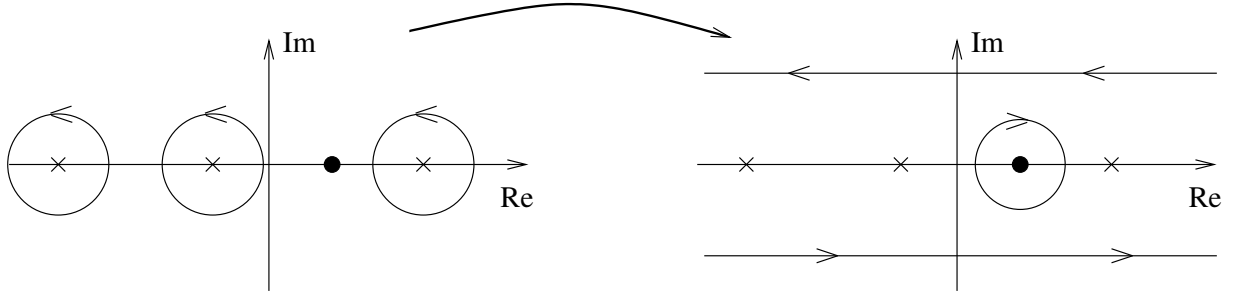


Figure 4.3 Graphical representation of the contour integral manipulation to obtain regular correlators, (picture taken from [107]). The black dot shows a singularity not enclosed inside \mathcal{C}^\Leftarrow , i.e. the contour surrounding the entire real axis.

Each sum $\sum_{J_i^\pm}$ is the sum of small contours around the solutions of equation (4.56) θ_i or (4.57) β_i :

$$\mathcal{C}_i^\pm := \sum_{J_i^\pm \in \mathbb{Z}} \mathcal{C}_{J_i^\pm} = \mathcal{C}^\Leftarrow - \mathcal{C}_\theta, \quad (4.74)$$

where \mathcal{C}^\Leftarrow is the contour encircling the real axis whereas \mathcal{C}_θ the one enclosing the point $\theta_i = \theta$ or $\beta_i = \theta$ at which the functions $h^\pm(\theta_i, \dots)$ have kinematic poles.

We now focus on a specific particle with rapidity $\theta_j \in \{\theta_i\}_{m^+}$, and compute the residue for a single-contour integral $\mathcal{C}_{J_j^+} = -\mathcal{C}_\theta$. We then extend the result to the multi-contour in (4.73) by using some combinatorial arguments. In particular the integral considered is:

$$\begin{aligned} & - \int_{\mathcal{C}_\theta} \frac{d\theta_j}{2\pi} \frac{e^{i\ell(P(\theta_j) - P(\theta))}}{e^{i(LP(\theta_j) - \frac{2\pi p}{n})} - 1} F_{N_p^- + N_p^+ + m^- + m^+}^{p,n}(\{\theta + i\pi\}_{N_p^-}, \{\theta_i\}_{m^+}; \{\theta + i\pi\}_{N_p^+}, \{\beta_i\}_{m^-}) \\ & \times F_{\tilde{N}_p^- + \tilde{N}_p^+ + m^- + m^+}^{n-p,n}(\{\theta\}_{\tilde{N}_p^-}, \{\beta_i + i\pi\}_{m^-}; \{\theta\}_{\tilde{N}_p^+}, \{\theta_i + i\pi\}_{m^+}). \end{aligned} \quad (4.75)$$

The pole structure of the form factors in the integrand gives the right prescription to select the dominant contributions at large volume. Indeed it is easy to see from (4.45) that the contribution from residues at θ coming from a single kinematic singularity is of order L^0 in the volume and therefore they will be strongly suppressed by the power of L in the denominator of (4.73). However, if we consider terms where both form factors have a kinematic pole at the same location $\theta_j = \theta$, then we have to calculate the residue of a second order pole, and this can change the order in the volume. From the kinematic residue equation (4.45) it follows that

near the kinematic poles the integrand may be approximated as

$$\begin{aligned}
 & - \int_{\mathcal{C}_\theta} \frac{d\theta_j}{2\pi} \frac{e^{i\ell(P(\theta_j)-P(\theta))}}{e^{i(LP(\theta_j)-\frac{2\pi p}{n})} - 1} \frac{-iN_p^+ \left(1 - e^{-\frac{2\pi ip}{n}}\right)}{\theta_j - \theta} \frac{-i\tilde{N}_p^+ \left(1 - e^{\frac{2\pi ip}{n}}\right)}{\theta - \theta_j} \\
 & \times F_{N_p^- + N_p^+ + m^- + m^+ - 2}^{p,n}(\{\theta + i\pi\}_{N_p^-}, \{\theta_i\}_{m^+} \setminus \{\theta_j\}; \{\theta + i\pi\}_{N_p^+ - 1}, \{\beta_i\}_{m^-}) \\
 & \times F_{\tilde{N}_p^- + \tilde{N}_p^+ + m^- + m^+ - 2}^{n-p,n}(\{\theta\}_{\tilde{N}_p^+ - 1}, \{\beta_i + i\pi\}_{m^-}; \{\theta\}_{\tilde{N}_p^-}, \{\theta_i + i\pi\}_{m^+} \setminus \{\theta_j + i\pi\}), \quad (4.76)
 \end{aligned}$$

where a pair θ_j and θ have been contracted in both form factors, and the variable θ_j is absent in $\{\theta_i\}_{m^+} \setminus \{\theta_j\} = \{\theta_1, \dots, \theta_{j-1}, \theta_{j+1}, \dots, \theta_{m^+}\}$. The combinatorial factors N_p^+ , \tilde{N}_p^+ are the result of the pairing of θ_i with the θ s.

Evaluating the residue we have that

$$\begin{aligned}
 & -iN_p^+ \tilde{N}_p^+ \left(1 - e^{\frac{2\pi ip}{n}}\right) \left(1 - e^{-\frac{2\pi ip}{n}}\right) \frac{d}{d\theta_i} \left(\frac{e^{i\ell(P(\theta_j)-P(\theta))}}{e^{i(LP(\theta_j)-\frac{2\pi p}{n})} - 1} \right)_{\theta_j=\theta} \\
 & \times F_{N_p^- + N_p^+ + m^- + m^+ - 2}^{p,n}(\{\theta + i\pi\}_{N_p^-}, \{\theta_i\}_{m^+} \setminus \{\theta_j\}; \{\theta + i\pi\}_{N_p^+ - 1}, \{\beta_i\}_{m^-}) \\
 & \times F_{\tilde{N}_p^- + \tilde{N}_p^+ + m^- + m^+ - 2}^{n-p,n}(\{\theta\}_{\tilde{N}_p^+ - 1}, \{\beta_i + i\pi\}_{m^-}; \{\theta\}_{\tilde{N}_p^-}, \{\theta_i + i\pi\}_{m^+} \setminus \{\theta_j + i\pi\}). \quad (4.77)
 \end{aligned}$$

Using the Bethe-Yang equation (4.55) and simplifying, the final result is

$$\begin{aligned}
 & LE(\theta) N_p^+ \tilde{N}_p^+ g_p^n(r) \\
 & F_{N_p^- + N_p^+ + m^- + m^+ - 2}^{p,n}(\{\theta + i\pi\}_{N_p^-}, \{\theta_i\}_{m^+} \setminus \{\theta_j\}; \{\theta + i\pi\}_{N_p^+ - 1}, \{\beta_i\}_{m^-}) \\
 & \times F_{\tilde{N}_p^- + \tilde{N}_p^+ + m^- + m^+ - 2}^{n-p,n}(\{\theta\}_{\tilde{N}_p^+ - 1}, \{\beta_i + i\pi\}_{m^-}; \{\theta\}_{\tilde{N}_p^-}, \{\theta_i + i\pi\}_{m^+} \setminus \{\theta_j + i\pi\}), \quad (4.78)
 \end{aligned}$$

where the function $g_p^n(r)$ provides the fundamental blocks of the final result and is defined as

$$g_{\pm k}^n(r) := 1 - (1 - e^{\pm \frac{2\pi ik}{n}})r, \quad k = 1, \dots, n. \quad (4.79)$$

An entirely similar computation can be done for a rapidity $\beta_j \in \{\beta_i\}_{m^-}$ paired with $\theta \in \{\theta\}_{N_p^-}$. The residue with contour integral $\mathcal{C}_{J_j^-} = -\mathcal{C}_\theta$ is

$$\begin{aligned}
 & - \int_{\mathcal{C}(\theta)} \frac{d\beta_j}{2\pi} \frac{e^{i\ell(P(\beta_j)-P(\beta))}}{e^{i(LP(\beta_j)+\frac{2\pi p}{n})} - 1} F_{N_p^- + N_p^+ + m^- + m^+}^{p,n}(\{\theta + i\pi\}_{N_p^-}, \{\theta_i\}_{m^+}; \{\theta + i\pi\}_{N_p^+}, \{\beta_i\}_{m^-}) \\
 & \times F_{\tilde{N}_p^- + \tilde{N}_p^+ + m^- + m^+}^{n-p,n}(\{\theta\}_{\tilde{N}_p^+}, \{\beta_i + i\pi\}_{m^-}; \{\theta\}_{\tilde{N}_p^-}, \{\theta_i + i\pi\}_{m^+}). \quad (4.80)
 \end{aligned}$$

This residue can be evaluated separately from the residue (4.75) as it involves different sets of

rapidities. It gives the result:

$$\begin{aligned}
 & LE(\theta) N_p^- \tilde{N}_p^- g_{-p}^n(r) \\
 & F_{N_p^- + N_p^+ + m^- + m^+ - 2}^{p,n}(\{\theta + i\pi\}_{N_p^- - 1}, \{\theta_i\}_{m^+}; \{\theta + i\pi\}_{N_p^+}, \{\beta_i\}_{m^-} \setminus \{\beta_k\}) \\
 & \times F_{\tilde{N}_p^- + \tilde{N}_p^+ + m^- + m^+ - 2}^{n-p,n}(\{\theta\}_{\tilde{N}_p^+}, \{\beta_i + i\pi\}_{m^-} \setminus \{\beta_j + i\pi\}; \{\theta\}_{\tilde{N}_p^- - 1}, \{\theta_i + i\pi\}_{m^+}). \quad (4.81)
 \end{aligned}$$

It is important to note, that both results (4.78) and (4.81) are proportional to the volume therefore any residue such as the ones above will produce a factor $LE(\theta) g_{\pm p}^n(r)$ up to combinatorial factors resulting from pairing particles of the intermediate state with the remaining θ s.

We now need to account for all possible contractions between the intermediate and the external states in the expansion (4.73). In particular what we need to do is to extend the computations above to more intricate integrals with multi-dimensional contours of the type:

$$\underbrace{\mathcal{C}_i^\pm \times \dots \times \mathcal{C}_i^\pm}_{m^\pm} = \sum_{k^\pm=1}^{N_*^\pm} \frac{m^\pm!}{k^\pm! (m^\pm - k^\pm)!} (-1)^{k^\pm} (\mathcal{C}^\rightleftharpoons)^{m^\pm - k^\pm} (\mathcal{C}_\theta)^{k^\pm}, \quad (4.82)$$

where each \mathcal{C}_i^\pm is given by expression (4.74) and $N_*^\pm \leq m^\pm$ is the maximal number of second-order poles for residua of the type of (4.78) and (4.81) respectively. Since each second-order pole residue with contour integral \mathcal{C}_θ contributes with a factor L to the form factor expansion (4.73) each term in the right hand side of (4.82) will contribute as L^{k^\pm} and the large-volume leading term is expected to come from the maximal power $k^\pm = N_*^\pm$. Therefore in the scaling limit (4.3) it is reasonable to expect that

$$\underbrace{\mathcal{C}_i^\pm \times \dots \times \mathcal{C}_i^\pm}_{m^\pm} \sim \frac{m^\pm!}{N_*^\pm! (m^\pm - N_*^\pm)!} (-1)^{N_*^\pm} (\mathcal{C}^\rightleftharpoons)^{m^\pm - N_*^\pm} (\mathcal{C}_\theta)^{N_*^\pm}, \quad \text{for } V \rightarrow \infty. \quad (4.83)$$

The other terms of the sum (4.82) will lead to next-to-leading order contributions so that these will not be considered in this computation.

We conclude this part of the computation by redefining the number $m^\pm \mapsto m^\pm - N_*^\pm$ and relabelling appropriately the rapidities of the intermediate states. Note that although, in general, the order in which the integrals over the various contours are performed matters, in both (4.82) and (4.83) we can obviate this by employing the fact that all such orderings are equivalent under relabeling of rapidities and that in this case all such relabelings are equivalent due to

the symmetries of the free boson form factors. This is another strength of the theory under consideration, which will be crucial in the treatment of multiple-point correlation functions, but that of course is no longer valid in interacting theories. We finally obtain the expansion:

$$\begin{aligned}
 \mathcal{F}_p(N_p^\pm, N_p^\pm) = & \sum_{m^\pm=0}^{\infty} \left[\prod_{\epsilon=\pm} \frac{1}{N_*^\epsilon! m^\epsilon!} \binom{N_p^\epsilon}{N_*^\epsilon} \binom{\tilde{N}_p^\epsilon}{N_*^+} (N_*^\epsilon!)^2 [g_{ep}^n(r)]^{N_*^\epsilon} \frac{1}{[\sqrt{LE}(\theta)]^{N_p^\epsilon + \tilde{N}_p^\epsilon - 2N_*^\epsilon}} \right] \\
 & \times \left[\prod_{i=1}^{m^+} \int_{\mathcal{C}_{\leftarrow}} \frac{d\theta_i}{2\pi} \right] \left[\prod_{i=1}^{m^-} \int_{\mathcal{C}_{\leftarrow}} \frac{d\beta_i}{2\pi} \right] \frac{e^{i\ell(\sum_{i=1}^{m^+} P(\theta_i) + \sum_{i=1}^{m^-} P(\beta_i))}}{\prod_{i=1}^{m^+} (e^{i(LP(\theta_i) - \frac{2\pi p}{n})} - 1) \prod_{i=1}^{m^-} (e^{i(LP(\beta_i) + \frac{2\pi p}{n})} - 1)} \quad (4.84) \\
 & \times F_{N_p^- + N_p^+ + m^- + m^+ - N_*^- - N_*^+}^{p,n}(\{\theta + i\pi\}_{N_p^- - N_*^-}, \{\theta_i\}_{m^+}; \{\theta + i\pi\}_{N_p^+ - N_*^+}, \{\beta_i\}_{m^-}) \\
 & \times F_{\tilde{N}_p^- + \tilde{N}_p^+ + m^- + m^+ - N_*^- - N_*^+}^{n-p,n}(\{\theta\}_{\tilde{N}_p^+ - N_*^+}, \{\beta_i + i\pi\}_{m^-}; \{\theta\}_{\tilde{N}_p^- - N_*^-}, \{\theta_i + i\pi\}_{m^+}).
 \end{aligned}$$

The factor $1/(N_*^\epsilon! m^\epsilon!)$ comes from the contour integral (4.83) and the relabelling $m^\pm \mapsto m^\pm - N_*^\pm$ whereas the factorials come from selecting the θ s in the contractions. Indeed by iterating the calculation of the second-pole residues (4.75) and (4.80) for N_*^ϵ times, the resulting combinatorial factors are:

$$N_p^\epsilon (N_p^\epsilon - 1) \dots (N_p^\epsilon - N_*^+ + 1) \tilde{N}_p^\epsilon (\tilde{N}_p^\epsilon - 1) \dots (\tilde{N}_p^\epsilon - N_*^+ + 1) = \binom{N_p^\epsilon}{N_*^\epsilon} \binom{\tilde{N}_p^\epsilon}{N_*^+} (N_*^\epsilon!)^2$$

that means that any time we contract a θ in the external state with one rapidity of the intermediate states there is one less selection option available.

4.5.1.3 Step 3: establishing the large-volume leading contribution

Starting from the expansion (4.84) we can now make some important observations that allow us to extract its leading contributions in the scaling limit (4.3). In particular, it is quite intuitive that residues such as (4.75) and (4.80) can be performed as long as there is at least one rapidity θ available in both form factors. Since the leading contribution comes from the largest number of second order poles we have that:

$$N_*^+ = \min\{N_p^+, \tilde{N}_p^+\}, \quad N_*^- = \min\{N_p^-, \tilde{N}_p^-\}, \quad (4.85)$$

On the other hand, each term of the expansion (4.84) contributes with the R th power of the volume L where

$$R = \min\{N_p^+, \tilde{N}_p^+\} + \min\{N_p^-, \tilde{N}_p^-\} - \frac{N_p^+ + N_p^- + \tilde{N}_p^+ + \tilde{N}_p^-}{2}, \quad (4.86)$$

and we expect the leading contribution to maximise this power. It turns out that R is maximal when the external states have exactly the same amount of particles $N_p^\pm = \tilde{N}_p^\pm$, and the corresponding term of the expansion (4.84) has a power $R = 0$. Indeed if we suppose $N_p^\pm < \tilde{N}_p^\pm$ it is easy to see that R will be negative and the corresponding term will be suppressed for large volume. Similar results may be obtained in all the other cases.

4.5.1.4 Step 4: identifying the vacuum-correlator and obtaining results

Substituting $\tilde{N}_p^\pm = N_*^\pm = N_p^\pm$ in the expansion (4.84) and simplifying the combinatorial factors, we obtain:

$$\begin{aligned} \mathcal{F}_p(N_p^\pm, N_p^\pm) &= \left[\prod_{\epsilon=\pm} N_*^{\epsilon!} [g_{\epsilon p}^n(r)]^{N_*^\epsilon} \right] \\ &\times \sum_{m^\pm=0}^{\infty} \frac{1}{m^+!m^-!} \left[\prod_{i=1}^{m^+} \int_{\mathcal{C}_\Leftarrow} \frac{d\theta_i}{2\pi} \right] \left[\prod_{i=1}^{m^-} \int_{\mathcal{C}_\Leftarrow} \frac{d\beta_i}{2\pi} \right] \frac{e^{i\ell(\sum_{i=1}^{m^+} P(\theta_i) + \sum_{i=1}^{m^-} P(\beta_i))}}{\prod_{i=1}^{m^+} (e^{i(LP(\theta_i) - \frac{2\pi p}{n})} - 1) \prod_{i=1}^{m^-} (e^{i(LP(\beta_i) + \frac{2\pi p}{n})} - 1)} \\ &\times F_{m^+m^-}^{p,n}(\{\theta_i\}_{m^+}; \{\beta_i\}_{m^-}) F_{m^+m^-}^{m-p,n}(\{\beta_i + i\pi\}_{m^-}; \{\theta_i + i\pi\}_{m^+}). \end{aligned} \quad (4.87)$$

the sum in last two lines is the spectral form factor decomposition of the vacuum correlator ${}_{p;L}\langle \mathbf{0} | \mathcal{T}_{+p}(0) \mathcal{T}_{-p}(0) | \mathbf{0} \rangle_{p;L}$ and can be easily factorised out. We can finally express the ratio of correlators as

$$\frac{{}_L\langle \mathbf{1} | \mathcal{T}(0) \tilde{\mathcal{T}}(\ell) | \mathbf{1} \rangle_L}{{}_L\langle \mathbf{0} | \mathcal{T}(0) \tilde{\mathcal{T}}(\ell) | \mathbf{0} \rangle_L} = \sum_{\{N^\pm\}} |C_n(\{N^\pm\})|^2 \prod_{p=1}^n \prod_{\epsilon=\pm} (N_p^{\epsilon!}) (g_{\epsilon p}^n(r))^{N_p^\epsilon} + \mathcal{O}(L^{-1}), \quad (4.88)$$

Note that for $p = n$, the factor reproduces the norm of the finite-volume state as expected, since $g_{\pm n}(r) = 1$ and ${}_{n;L}\langle \mathbf{0} | \mathcal{T}_n(0) \tilde{\mathcal{T}}_n(\ell) | \mathbf{0} \rangle_{n;L} = 1$. Finally the increment of entanglement (4.5) for a single-particle excitation is:

$$\Delta S_n^1(r) = \frac{1}{1-n} \log \left[\sum_{\{N^\pm\}} |C_n(\{N^\pm\})|^2 \prod_{p=1}^n \prod_{\epsilon=\pm} (N_p^{\epsilon!}) (g_{\epsilon p}^n(r))^{N_p^\epsilon} \right]. \quad (4.89)$$

The result above is θ -independent and in particular it does not depend on the energy of the state $|\mathbf{1}\rangle_L$ but only of the ratio $r = \ell/L$ kept fixed in the scaling limit (4.3). It does not explicitly depend on the mass m of the free boson. However we know that such information is encoded in the ground-state contribution and thus it does not feature in this subtracted version.

4.6 Rényi entropy of a multi-particle excited state

In the previous section we have rigorously discussed all the computational steps that lead to evaluate the increment of entanglement in a single-particle excitation. This computation provides the basis for computing entanglement increments for more complicated states. In particular in this section we will look into states whose particles are all distinguishable or all indistinguishable in their rapidities. These two extreme cases are crucial to construct the general formulae for the entanglement increment of a generic state discussed in Subsection 4.7.3.

4.6.1 Distinct rapidities

We now consider a k -particle state (4.21) involving only excitations with distinct rapidities $\theta_1 \neq \dots \neq \theta_k$. In infinite volume this state can be expressed in the form

$$|\underbrace{\mathbf{1}, \mathbf{1}, \dots, \mathbf{1}}_k\rangle = \prod_{q=1}^k \sum_{\{N^{q,\pm}\}} C_n(\{N^{q,\pm}\}) \prod_{p=1}^n [\mathfrak{q}_p^\dagger(\theta_q)]^{N_p^{q,+}} [\mathfrak{q}_p^\dagger(\theta_q)]^{N_p^{q,-}} |\mathbf{0}\rangle, \quad (4.90)$$

where the $C_n(\{N^{q,\pm}\})$ coefficients take the same form for each value of q , more precisely, for fixed q they are exactly the same as for the one-particle state (4.62). Similarly to (4.67), the integers $\{N^{q,\pm}\}$ satisfy the following restrictions

$$\sum_{p=1}^n \sum_{\epsilon=\pm} N_p^{q,\epsilon} = n, \quad q = 1, \dots, k. \quad (4.91)$$

In finite volume, the set of equal rapidities $\{\theta_q\}_{N_p^{q,\pm}} = \{\theta_q, \theta_q, \dots\}$ satisfy the Bethe-Yang equation (4.55) with equal integers $\{I_q\}_{N_p^{q,\pm}} = \{I_q, I_q, \dots\}$ for all $q = 1, \dots, k$. The two-point function takes the form

$${}_L \langle \mathbf{1}, \mathbf{1}, \dots, \mathbf{1} | \mathcal{T}(0) \tilde{\mathcal{T}}(\ell) | \mathbf{1}, \mathbf{1}, \dots, \mathbf{1} \rangle_L \quad (4.92)$$

$$= \left[\prod_{q=1}^k \sum_{\{N^{q,\pm}\}} \sum_{\{\tilde{N}^{q,\pm}\}} [C_n(\{N^{q,\pm}\})]^* C_n(\{\tilde{N}^{q,\pm}\}) \right] \prod_{p=1}^n \mathcal{F}_p(\{N_p^{q,\pm}\}, \{\tilde{N}_p^{q,\pm}\}), \quad (4.93)$$

where

$$\mathcal{F}_p(\{N_p^{q,\pm}\}, \{\tilde{N}_p^{q,\pm}\}) = {}_{p;L} \langle \{I_1\}_{N_p^{1,\pm}}, \dots, \{I_k\}_{N_p^{k,\pm}} | \mathcal{T}_{+p}(0) \mathcal{T}_{-p}(\ell) | \{I_1\}_{N_p^{1,\pm}}, \dots, \{I_k\}_{N_p^{k,\pm}} \rangle_{p;L}. \quad (4.94)$$

To find the leading contribution in the volume to $\mathcal{F}_p\left(\{N_p^{q,\pm}\},\{\tilde{N}_p^{q,\pm}\}\right)$, we follow the same steps as in Section 4.5. As seen in Subsection 4.5.1, we need to focus on the contributions arising when some intermediate rapidity approaches one of the rapidities of the excited state in both of the form factors generating second-order poles. In other words, we need to pair up the intermediate rapidities with the same rapidity of the excited state from the in- and out-states. Since the sets of rapidities $\{\theta_q\}_{N_p^{q,\pm}}$ are all distinct, the computation of the leading contribution can be seen as iterating the procedure described in Section 4.5.1 independently for each set. Carrying out the calculation, the result will be

$$\begin{aligned} & \mathcal{F}_p\left(\{N_p^{q,\pm}\},\{\tilde{N}_p^{q,\pm}\}\right) \\ &= \prod_{q=1}^k N_p^{q,+}! N_p^{q,-}! [g_p^n(r)]^{N_p^{q,+}} [g_{-p}^n(r)]^{N_p^{q,-}} {}_{p;L}\langle \mathbf{0} | \mathcal{T}_p(0) \mathcal{T}_{-p}(\ell) | \mathbf{0} \rangle_{p;L} + O(L^{-1}). \end{aligned} \quad (4.95)$$

As a consequence, in the scaling limit (4.3), the result for a state involving k distinct rapidities factorizes into k single-particle state contributions. That is

$$\begin{aligned} \lim_{L \rightarrow \infty} \frac{{}_L\langle \mathbf{1}, \dots, \mathbf{1} | \mathcal{T}(0) \tilde{\mathcal{T}}(rL) | \mathbf{1}, \dots, \mathbf{1} \rangle_L}{{}_L\langle \mathbf{0} | \mathcal{T}(0) \tilde{\mathcal{T}}(\ell) | \mathbf{0} \rangle_L} &= \prod_{q=1}^k \left[\sum_{\{N^{q,\pm}\}} |C_n(\{N^{q,\pm}\})|^2 \prod_{p=1}^n \prod_{\epsilon=\pm} N_p^{q,\epsilon}! [g_{\epsilon p}^n(r)]^{N_p^{q,\epsilon}} \right] \\ &= \lim_{L \rightarrow \infty} \left[\frac{{}_L\langle \mathbf{1} | \mathcal{T}(0) \tilde{\mathcal{T}}(rL) | \mathbf{1} \rangle_L}{{}_L\langle \mathbf{0} | \mathcal{T}(0) \tilde{\mathcal{T}}(\ell) | \mathbf{0} \rangle_L} \right]^k. \end{aligned} \quad (4.96)$$

The equation above implies that the increment of the n th Rényi entropy given by a k -particle state with only distinct particles is k times as big as the one generated by a single-particle excited state:

$$\Delta S_n^{1,1,\dots}(r) = \sum_{q=1}^k \Delta S_n^1(r) = k \Delta S_n^1(r), \quad (4.97)$$

where $\Delta S_n^1(r)$ is given by (4.89). Like (4.89), the result above does not depend on the explicit values of rapidities $\theta_1, \dots, \theta_k$ but only on the assumption that they are different from each other. Indeed such a simple result (4.97) no longer holds if all or some rapidities of the excited state coincide. We will see this in the next subsection where we consider an excited state with only coinciding rapidities.

4.6.2 Coinciding rapidities

Let us consider a k -particle excited state where all the rapidities coincide, and are denoted by θ . In this case the norm of the k -particle state is $k!$ and needs to be modified in (4.33).

The properly normalized infinite-volume state can then be written as

$$|\mathbf{k}\rangle = \frac{1}{\sqrt{k!^n}} \sum_{\{N^\pm\}} D_n^k(\{N^\pm\}) \prod_{p=1}^n [\mathfrak{a}_p^\dagger(\theta)]^{N_p^+} [\mathfrak{b}_p^\dagger(\theta)]^{N_p^-} |\mathbf{0}\rangle, \quad (4.98)$$

The expression above looks very similar to (4.62). Although both states depend on a single rapidity variable, the state (4.98) obeys a different selection rule which is

$$\sum_{p=1}^n \sum_{\epsilon=\pm} N_p^\epsilon = nk, \quad (4.99)$$

and that depends on the number of excitations k . The same condition holds for \tilde{N}_p^\pm . As a consequence we expect the final results to give numerically different values than (4.89). The coefficients $D_n^k(\{N^\pm\})$ are related to the coefficients $C_n(\{N^\pm\})$ of the previous subsections by

$$D_n^k(\{N^\pm\}) = \prod_{q=1}^k \sum_{\{N^{q,\pm}\}} C_n(\{N^{q,\pm}\}) \prod_{p=1}^n \prod_{\epsilon=\pm} \delta_{N_p^\epsilon, \sum_{q=1}^k N_p^{q,\epsilon}}. \quad (4.100)$$

The two point function is then

$${}_L\langle \mathbf{k} | \mathcal{T}(0) \tilde{\mathcal{T}}(\ell) | \mathbf{k} \rangle_L = \frac{1}{(k!)^n} \sum_{\{N^\pm\}} \sum_{\{\tilde{N}^\pm\}} [D_n^k(\{N^\pm\})]^* D_n^k(\{\tilde{N}^\pm\}) \prod_{p=1}^n \mathcal{F}_p(N_p^\pm, \tilde{N}_p^\pm), \quad (4.101)$$

where \mathcal{F}_p is the same function as for the one-particle case (4.64) with integers N_p^\pm obeying (4.99). It follows from the computation in Section 4.5 that the leading large-volume term of the two-point function is

$$\lim_{L \rightarrow \infty} \frac{{}_L\langle \mathbf{k} | \mathcal{T}(0) \tilde{\mathcal{T}}(rL) | \mathbf{k} \rangle_L}{{}_L\langle \mathbf{0} | \mathcal{T}(0) \tilde{\mathcal{T}}(rL) | \mathbf{0} \rangle_L} = \frac{1}{(k!)^n} \sum_{\{N^\pm\}} |D_n^k(\{N^\pm\})|^2 \prod_{p=1}^n \prod_{\epsilon=\pm} (N_p^\epsilon)! [g_{ep}^n(r)]^{N_p^\epsilon}, \quad (4.102)$$

and finally the increment to the n th Rényi entropy given by a k -particle excited state of equal rapidities in the scaling limit (4.3) is:

$$\Delta S_n^k(r) = \frac{1}{1-n} \log \left[\frac{1}{(k!)^n} \sum_{\{N^\pm\}} |D_n^k(\{N^\pm\})|^2 \prod_{p=1}^n \prod_{\epsilon=\pm} (N_p^\epsilon)! [g_{ep}^n(r)]^{N_p^\epsilon} \right]. \quad (4.103)$$

4.7 Results

Results (4.89), (4.97) and (4.103) depend explicitly on the coefficients $C_n(\{N^\pm\})$ and $D_n^k(\{N^\pm\})$ which are expected to have a universal form for each n . However, we have not found a closed formula for these coefficients for a general n yet. In order to make the result above more concrete it may be instructive to start from two simple examples. In Subsections 4.7.1 and 4.7.2 we will consider the second Rényi entropy, namely the quantity (4.5) for a two-copy model, evaluated in a single- and a two-particle state respectively. For more complicated states, the coefficients $C_n(\{N^\pm\})$ and $D_n^k(\{N^\pm\})$ can be systematically evaluated by using a standard computer software such as Mathematica. Once the coefficients are known we can easily evaluate formula (4.102) for several values of k , and we observe that the results are always polynomials in r that possess the $r \leftrightarrow 1 - r$ symmetry as expected. We will discuss the general formulae and the resulting properties in Subsection 4.7.3.

4.7.1 Example 1: second Rényi entropy of a single-particle excitation

We compute the second Rényi Entropy, i.e. $n = 2$, of a single-particle excited state. From (4.61) we can easily write down the state

$$\begin{aligned}
 |\mathbf{1}\rangle &= \frac{1}{4}\mathfrak{a}_2^\dagger(\theta)\mathfrak{a}_2^\dagger(\theta)|0\rangle_2 + \frac{1}{4}\mathfrak{b}_2^\dagger(\theta)\mathfrak{b}_2^\dagger(\theta)|0\rangle_2 + \frac{1}{2}\mathfrak{a}_2^\dagger(\theta)\mathfrak{b}_2^\dagger(\theta)|0\rangle_2 \\
 &\quad - \frac{1}{4}\mathfrak{a}_1^\dagger(\theta)\mathfrak{a}_1^\dagger(\theta)|0\rangle_1 - \frac{1}{4}\mathfrak{b}_1^\dagger(\theta)\mathfrak{b}_1^\dagger(\theta)|0\rangle_1 - \frac{1}{2}\mathfrak{a}_1^\dagger(\theta)\mathfrak{b}_1^\dagger(\theta)|0\rangle_1 \\
 &= \frac{1}{4}\left[(\mathfrak{a}_2^\dagger(\theta) + \mathfrak{b}_2^\dagger(\theta))^2 - (\mathfrak{a}_1^\dagger(\theta) + \mathfrak{b}_1^\dagger(\theta))^2\right]|\mathbf{0}\rangle, \tag{4.104}
 \end{aligned}$$

and identify the nonzero coefficients $C_2(N_1^+, N_1^-, N_2^+, N_2^-)$ of the expansion (4.62) as

$$\begin{aligned}
 C_2(2, 0, 0, 0) &= -\frac{1}{4}, & C_2(0, 0, 2, 0) &= \frac{1}{4}, \\
 C_2(0, 2, 0, 0) &= -\frac{1}{4}, & C_2(0, 0, 0, 2) &= \frac{1}{4}, \\
 C_2(1, 1, 0, 0) &= -\frac{1}{2}, & C_2(0, 0, 1, 1) &= \frac{1}{2}. \tag{4.105}
 \end{aligned}$$

Note that in this particular case the all terms of the expansions (4.63) are naturally constrained by the the $U(1)$ -charge conservation to have identical external states on the two sides of the correlators of $U(1)$ i.e. $\{N_2\} = \{\tilde{N}_2\}$. This is a consequence of the low number of particles and

antiparticles considered in the two-copy model. The coefficients (4.105) can be directly plugged into (4.88), and, considering the scaling limit (4.3), we obtain

$$\begin{aligned}
 \lim_{L \rightarrow \infty} \frac{{}_L \langle \mathbf{1} | \mathcal{T}(0) \tilde{\mathcal{T}}(rL) | \mathbf{1} \rangle_L}{{}_L \langle \mathbf{0} | \mathcal{T}(0) \tilde{\mathcal{T}}(\ell) | \mathbf{0} \rangle_L} &= \frac{2!}{16} [g_1^2(r)]^2 + \frac{2!}{16} [g_{-1}^2(r)]^2 + \frac{1}{4} g_1^2(r) g_{-1}^2(r) \\
 &+ \frac{2!}{16} [g_2^2(r)]^2 + \frac{2!}{16} [g_{-2}^2(r)]^2 + \frac{1}{4} g_2^2(r) g_{-2}^2(r) \\
 &= \frac{1}{2} + \frac{1}{2} [g_1^2(r)]^2 = r^2 + (1-r)^2,
 \end{aligned} \tag{4.106}$$

where we used the fact that $g_2^2(r) = g_{-2}^2(r) = 1$ and $g_1^2(r) = g_{-1}^2(r) = 1 - 2r$. Therefore the difference of Rényi entropies is

$$\Delta S_2^1(r) = -\log(r^2 + (1-r)^2), \tag{4.107}$$

Note that the argument of the logarithm has a very simple polynomial structure with order given by n .

4.7.2 Example 2: second Rényi entropy of a two-particle excitation

Let us consider a two-particle excited state with distinct rapidities which we represent as $|\mathbf{1}, \mathbf{1}\rangle$. From the general expression (4.33) it is easy to see that

$$\begin{aligned}
 |\mathbf{1}, \mathbf{1}\rangle &= \frac{1}{4} \left[(\mathfrak{a}_2^\dagger(\theta_1) + \mathfrak{b}_2^\dagger(\theta_1))^2 - (\mathfrak{a}_1^\dagger(\theta_1) + \mathfrak{b}_1^\dagger(\theta_1))^2 \right] \\
 &\times \frac{1}{4} \left[(\mathfrak{a}_2^\dagger(\theta_2) + \mathfrak{b}_2^\dagger(\theta_2))^2 - (\mathfrak{a}_1^\dagger(\theta_2) + \mathfrak{b}_1^\dagger(\theta_2))^2 \right] |\mathbf{0}\rangle.
 \end{aligned} \tag{4.108}$$

The state can be fully characterized by the coefficients $C_2(\{N^{q,\pm}\})$ with $q = 1, 2$ and these give two copies of the coefficients (4.105) of the one-particle state (4.104). Substituting these values into the formula we obtain exactly the square of (4.106), that is

$$\lim_{L \rightarrow \infty} \frac{{}_L \langle \mathbf{1}, \mathbf{1} | \mathcal{T}(0) \tilde{\mathcal{T}}(rL) | \mathbf{1}, \mathbf{1} \rangle_L}{{}_L \langle \mathbf{0} | \mathcal{T}(0) \tilde{\mathcal{T}}(\ell) | \mathbf{0} \rangle_L} = \left[\frac{1}{2} + \frac{1}{2} [g_1^2(r)]^2 \right]^2 = [r^2 + (1-r)^2]^2. \tag{4.109}$$

Note that the polynomial above is of forth power, suggesting that a general formula involves a polynomial of kn th order for a k -particle excitation.

Consider instead a two-particle excited state of equal rapidities. In infinite volume, the state may be written as

$$|\mathbf{2}\rangle = \frac{1}{2!} \left[\frac{1}{4} \left[(\mathfrak{a}_2^\dagger(\theta) + \mathfrak{b}_2^\dagger(\theta))^2 - (\mathfrak{a}_1^\dagger(\theta) + \mathfrak{b}_1^\dagger(\theta))^2 \right] \right]^2 |\mathbf{0}\rangle. \tag{4.110}$$

The coefficients $D_2^2(N_1^+, N_1^-, N_2^+, N_2^-)$ entering the formula (4.102) can be read off by either expanding (4.110) and looking at the coefficients of all distinct states in the ensuing linear combination, or by using (4.100)

$$\begin{aligned}
 D_2^2(4, 0, 0, 0) &= \frac{1}{16}, & D_2^2(0, 4, 0, 0) &= \frac{1}{16}, & D_2^2(0, 0, 4, 0) &= \frac{1}{16}, & D_2^2(0, 0, 0, 4) &= \frac{1}{16}, \\
 D_2^2(2, 0, 2, 0) &= -\frac{1}{8}, & D_2^2(2, 0, 0, 2) &= -\frac{1}{8}, & D_2^2(0, 2, 2, 0) &= -\frac{1}{8}, & D_2^2(0, 2, 2, 0) &= -\frac{1}{8}, \\
 D_2^2(3, 1, 0, 0) &= \frac{1}{4}, & D_2^2(1, 3, 0, 0) &= \frac{1}{4}, & D_2^2(0, 0, 3, 1) &= \frac{1}{4}, & D_2^2(0, 0, 1, 3) &= \frac{1}{4}, \\
 D_2^2(1, 1, 2, 0) &= -\frac{1}{4}, & D_2^2(1, 1, 0, 2) &= -\frac{1}{4}, & D_2^2(2, 0, 1, 1) &= -\frac{1}{4}, & D_2^2(0, 2, 1, 1) &= -\frac{1}{4}, \\
 D_2^2(2, 2, 0, 0) &= \frac{3}{8}, & D_2^2(0, 0, 2, 2) &= \frac{3}{8}, & D_2^2(1, 1, 1, 1) &= -\frac{1}{2}.
 \end{aligned} \tag{4.111}$$

Plugging the coefficients into (4.102) leads to

$$\begin{aligned}
 \lim_{L \rightarrow \infty} \frac{L \langle \mathbf{2} | \mathcal{T}(0) \tilde{\mathcal{T}}(rL) | \mathbf{2} \rangle_L}{L \langle \mathbf{0} | \mathcal{T}(0) \tilde{\mathcal{T}}(\ell) | \mathbf{0} \rangle_L} &= \frac{1}{2!^2} \left\{ \left(\frac{1}{16} \right)^2 4! \left([g_1^2(r)]^4 + [g_{-1}^2(r)]^4 + [g_2^2(r)]^4 + [g_{-2}^2(r)]^4 \right) \right. \\
 &+ \left(\frac{3}{8} \right)^2 2!2! \left([g_1^2(r)]^2 [g_{-1}^2(r)]^2 + [g_2^2(r)]^2 [g_{-2}^2(r)]^2 \right) \\
 &+ \left(\frac{1}{8} \right)^2 2!2! \left([g_1^2(r)]^2 + [g_{-1}^2(r)]^2 \right) \left([g_2^2(r)]^2 + [g_{-2}^2(r)]^2 \right) \\
 &+ \left(\frac{1}{4} \right)^2 3! \left([g_1^2(r)]^3 g_{-1}^2(r) + g_1^2(r) [g_{-1}^2(r)]^3 \right) \\
 &+ \left(\frac{1}{4} \right)^2 3! \left([g_2^2(r)]^3 g_{-2}^2(r) + g_2^2(r) [g_{-2}^2(r)]^3 \right) \\
 &+ \left(\frac{1}{4} \right)^2 2! g_1^2(r) g_{-1}^2(r) \left([g_2^2(r)]^2 + [g_{-2}^2(r)]^2 \right) \\
 &+ \left(\frac{1}{4} \right)^2 2! \left([g_1^2(r)]^2 + [g_{-1}^2(r)]^2 \right) g_2^2(r) g_{-2}^2(r) \\
 &+ \left(\frac{1}{2} \right)^2 g_1^2(r) g_{-1}^2(r) g_2^2(r) g_{-2}^2(r) \left. \right\} \\
 &= \frac{3}{8} + \frac{3}{8} [g_1^2(r)]^4 + \frac{1}{4} [g_1^2(r)]^2 \\
 &= r^4 + 4r^2(1-r)^2 + (1-r)^4,
 \end{aligned} \tag{4.112}$$

where the last line follows from noting once more that $g_2^2(r) = g_{-2}^2(r) = 1$ and $g_1^2(r) = g_{-1}^2(r) = 1 - 2r$. This then gives the expression

$$\Delta S_2^2(r) = -\log(r^4 + 4r^2(1-r)^2 + (1-r)^4). \tag{4.113}$$

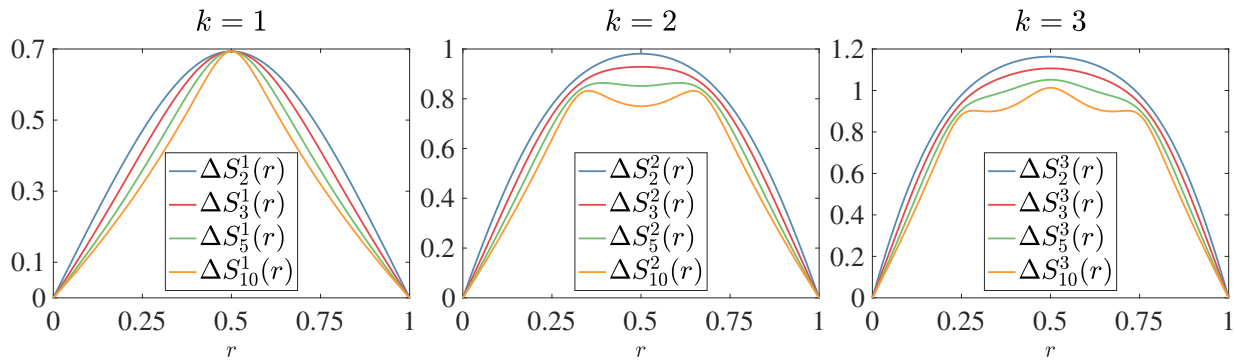


Figure 4.4 Increment of Rényi entropy for one-, two- and three-particle excited states consisting of identical particles in several n -copy models with $n = 2, 3, 5, 10$. For a fixed n , the entropies grow with the number of excitations in the state. Furthermore, they show the $r \mapsto 1 - r$ symmetry, which is expected for partitions involving two complementary parts. Other observations can be found at the end of this page.

4.7.3 A simple polynomial structure

In [23, 24] the calculation of (4.101) was performed for various values of k and n by using Mathematica. Already looking at the two examples above, it is actually not hard to work out the general pattern. Let us start from the n th Rényi entropy of a single-particle excitation. We find the following results:

$$\Delta S_n^1(r) = \frac{\log(r^n + (1-r)^n)}{1-n}. \quad (4.114)$$

For a k -particle state with particles of all different rapidities/momenta the result follows from (4.97) and, is simply as above, multiplied by k . If we consider instead k particles which have all equal rapidities/momenta the increment of the n th Rényi entropy has the following structure

$$\Delta S_n^k(r) = \frac{\log \sum_{q=0}^k [f_q^k(r)]^n}{1-n}, \quad f_q^k(r) = \binom{k}{q} r^q (1-r)^{k-q}, \quad (4.115)$$

where the argument of the logarithm is a polynomial of order kn , as predicted in Subsection 4.7.2. Note that for $k = 1$, the expression above give exactly (4.114). In Fig. 4.4 we present several examples of the function (4.115) for $k = 1, 2, 3$. Looking at these examples we can make the following observations:

1. The functions ΔS_n^k do not depend on the rapidities/momenta of the excited states but are single-valued functions of the parameter $r = \ell/L$ for fixed n and k .
2. The functions ΔS_n^k are symmetric under the exchange $r \mapsto 1 - r$ and thus more generally independent of the subsystem ℓ or $L - \ell$ chosen as entanglement region. As discussed in

Chapter 2, this is a fundamental property that any quantity measuring the entanglement shared by two complementary parts must satisfy.

3. As a consequence of the previous point, the functions ΔS_n^k show a zero r -derivative at $r = 1/2$, which corresponds to a maximum in the case of the second Rényi entropy. In Fig. 4.4 we can observe that for large n the functions ΔS_n^k shows a local maximum/minimum at $r = 1/2$ if n is odd/even.
4. For fixed k and r , the function $\Delta S_n^k(r)$ does not increase with n . According to (2.14) and (2.16) the function $\Delta S_n^k(r)$ is bounded from above and below by the increments of entanglement entropy $\Delta S_1^k(r)$ and of single-copy entropy $\Delta S_\infty^k(r)$ respectively:

$$\Delta S_\infty^k(r) \leq \Delta S_n^k(r) \leq \Delta S_1^k(r) \quad (4.116)$$

Finally, we can generalise the results above for generic states containing a mixture of excitations with equal and distinct rapidities. In particular we denote $\Delta S_n^{k_1, k_2, \dots}(r)$ the Rényi entropies of an excited state consisting of k_i particles of momentum p_i for $p_i \neq p_j$ for $i \neq j$ we find

$$\Delta S_n^{k_1, k_2, \dots}(r) = \sum_j \Delta S_n^{k_j}(r), = \sum_j \frac{\log \sum_{q_j=0}^k [f_{q_j}^{k_j}(r)]^n}{1-n} \quad (4.117)$$

where $f_{q_j}^{k_j}(r)$ is the function $f_q^k(r)$ in (4.115) with $k = k_j$ and $q = q_j$.

4.8 Qubit picture

The properties listed in the previous subsection may be better understood if one considers the qubit interpretation of multiparticle excited states, first presented in [23, 24] and then extended to more complicated cases in [26, 28]. Such interpretation starts from the simple observation that in the scaling limit (4.3) the entanglement increments (4.115) equate the Rényi entropies of simple states formed of qubits. These “multi-qubit states” are associated with the presence or the absence of the excitations in the entanglement region ℓ .

In order to explain the qubit interpretation, consider a bipartite Hilbert space $\mathcal{H} = \mathcal{H}_{\text{int}} \otimes \mathcal{H}_{\text{ext}}$. Each factor $\mathcal{H}_{\text{int}} \simeq \mathcal{H}_{\text{ext}}$ is the Hilbert space for N_j distinguishable sets each of j indistinguishable qubits, for $j = 1, 2, 3, \dots$. Making the relation with the entanglement problem described above, we associate \mathcal{H}_{int} with the interior of the entanglement region of

length ℓ and \mathcal{H}_{ext} with its exterior. In particular, we identify a state $|1\rangle$ with the presence of a single-particle excitation and $|0\rangle$ with its absence. With k particles lying on $(0, L)$, we construct the state $|\Psi_{\text{qb}}\rangle \in \mathcal{H}$ by the (naive) picture according to which equal-rapidity particles are indistinguishable, and a particle can lie anywhere in $(0, L)$ with flat probability: any given particle has probability r of lying in the entanglement region, and $1 - r$ of lying outside. We make a linear combination of qubit states following this picture, with coefficients that are square roots of the total probability of a given qubit configuration, taking proper care of (in)distinguishability. Then, the Rényi entropies of the resulting state $|\Psi_{\text{qb}}\rangle$ are given exactly by

$$S_n^{\Psi_{\text{qb}}}(r) = \frac{\log(\text{Tr} \rho_{\mathcal{H}_{\text{int}}}^n)}{1 - n}, \quad \rho_{\mathcal{H}_{\text{int}}} = \text{Tr}_{\mathcal{H}_{\text{ext}}} |\Psi_{\text{qb}}\rangle\langle\Psi_{\text{qb}}|, \quad (4.118)$$

and the statement is that $S_n^{\Psi_{\text{qb}}}(r) = \Delta S_n^{\Psi}(r)$ for some excited state $|\Psi\rangle_L$. In order to understand how these qubit states look like, we can look at some simple examples. For instance, according to the qubit picture, the state:

$$|\Psi_{\text{qb}}^{(1)}\rangle = \sqrt{r} |1\rangle \otimes |0\rangle + \sqrt{1-r} |0\rangle \otimes |1\rangle, \quad (4.119)$$

describes the probability distribution for a particular single-excitation of the free boson QFT, say $|\mathbf{1}\rangle_L$. This leads to two possible configurations: either the particle is located within the entanglement region with a probability r or outside of it, with probability $1 - r$. It is actually very easy to see that the n th Rényi entropy of the state above exactly reproduces formula (4.114). We may have more complicated multi-qubit states if more particles are present, for instance two particles of coinciding rapidities:

$$|\Psi_{\text{qb}}^{(2)}\rangle = \sqrt{r^2} |2\rangle \otimes |0\rangle + \sqrt{2r(1-r)} |1\rangle \otimes |1\rangle + \sqrt{(1-r)^2} |0\rangle \otimes |2\rangle. \quad (4.120)$$

There are now three possible configurations as either the two particles are in the same region, with probability r^2 , or one is in the region and one outside of it (no matter which one), with probability $2r(1-r)$, or both are outside the region, with probability $(1-r)^2$. The particle configuration changes if the two particles are distinguishable i.e. characterised by two different rapidities/momenta:

$$|\Psi_{\text{qb}}^{(1,1)}\rangle = \sqrt{r^2} |1, 1\rangle \otimes |0, 0\rangle + \sqrt{r(1-r)} (|1, 0\rangle \otimes |0, 1\rangle + |0, 1\rangle \otimes |1, 0\rangle) + \sqrt{(1-r)^2} |0, 0\rangle \otimes |1, 1\rangle. \quad (4.121)$$

Indeed, by counting the various ways two distinct particles can be distributed inside or

outside an entanglement region we obtain four configurations in total, as now it matters which particle is inside/outside. The entanglement of the excited state will change accordingly.

We can now extend the qubit picture to a generic state in the entanglement region problem, given that this state is characterised by a certain number of sets N_j containing equal rapidities. We can construct the corresponding multi-qubit state as follow: the Hilbert space of the exterior and interior can be split into sectors $\mathcal{H}_{\text{int}} \simeq \mathcal{H}_{\text{ext}} \simeq \otimes_{j=1}^N \mathbb{C}^{k_j+1}$, where N is the total number of sets N_j , and $K = \sum_{j \geq 1} k_j$ the total number of qubits. In particular, each set N_j containing k_j indistinguishable qubits is equipped by an Hilbert space \mathbb{C}^{k_j+1} with basis elements $|q_j\rangle$ for $q_j = 1, \dots, k_j$ labelling the number of particles in the interior state. Similarly $|\bar{q}_j\rangle$ where $\bar{q}_j = k_j - q_j$ is a basis of the sector of the Hilbert space associated to the exterior. Hence, we can define a basis of \mathcal{H}_{int} that is $\{|Q\rangle = |q_1, \dots, q_N\rangle; q_j \leq k_j, j = 1, \dots, N\}$, and a basis of \mathcal{H}_{ext} that is $\{|\bar{Q}\rangle = |\bar{q}_1, \dots, \bar{q}_N\rangle; \bar{q}_j \leq k_j, j = 1, \dots, N\}$. The multi-qubit state is

$$|\Psi_{\text{qb}}^{(k_1, k_2, \dots, k_N)}\rangle = \sum_{Q, \bar{Q}} \mathbf{C}_{Q, \bar{Q}} |Q\rangle \otimes |\bar{Q}\rangle, \quad \mathbf{C}_{Q, \bar{Q}} = \sqrt{p_Q} \prod_{j=1}^N \delta_{q_j + \bar{q}_j, k_j} \quad (4.122)$$

where p_Q is the probability of finding the particle configuration Q in the entanglement region according to the naive picture above, given by

$$p_Q = \prod_{j=1}^N \binom{k_j}{q_j} r^{q_j} (1-r)^{k_j - q_j}. \quad (4.123)$$

One can easily observe that the state

$$|\Psi_{\text{qb}}^{(k_1, k_2, \dots, k_N)}\rangle = \bigotimes_{j=1}^N |\Psi_{\text{qb}}^{(k_j)}\rangle \quad (4.124)$$

factorises into states $|\Psi_{\text{qb}}^{(k_j)}\rangle$ living in $\mathbb{C}^{k_j+1} \otimes \mathbb{C}^{k_j+1}$ for $j = 1, \dots, N$, which are

$$|\Psi_{\text{qb}}^{(k_j)}\rangle = \sum_{q_j=0}^{k_j} \sqrt{f_{q_j}^{k_j}(r)} |q_j\rangle \otimes |k_j - q_j\rangle, \quad f_{q_j}^{k_j}(r) = \binom{k_j}{q_j} r^{q_j} (1-r)^{k_j - q_j}. \quad (4.125)$$

The coefficients $f_{q_j}^{k_j}(r)$ are of the same form as the one in equation (4.115) and provide the Schimidt decomposition (2.7) for the multi-qubit state. If we trace out the degree of freedom associated to the j th sector of the Hilbert space \mathcal{H}_{ext} , we then obtain the reduced density

matrix in a diagonal form:

$$\rho_{\text{int}}^{(k_j)} = \text{Tr}_{\text{ext}} |\Psi_{\text{qb}}^{(k_j)}\rangle \langle \Psi_{\text{qb}}^{(k_j)}| = \sum_{q_j=0}^{k_j} f_{q_j}^{k_j}(r) |q_j\rangle \langle q_j|. \quad (4.126)$$

Recalling the multi-qubit state (4.122) its reduced density matrix to the total Hilbert space \mathcal{H}_{ext} also factorises as a consequence of (4.124), and the n th Rényi entropy of the state becomes:

$$S_n^{\Psi_{\text{qb}}^{(k_1, k_2, \dots, k_N)}} = \sum_{j=1}^N S_n^{\Psi_{\text{qb}}^{(k_j)}} = \sum_{j=1}^N \frac{\log \sum_{q_j=0}^{k_j} [f_{q_j}^{k_j}(r)]^n}{1-n}, \quad (4.127)$$

which reproduces exactly (4.117).

4.8.1 Increment of entanglement entropy

The qubit picture not only offers an interesting probabilistic interpretation of the Rényi entropies' increments presented in Subsection 4.7.3, but it also provides a simple method to obtain results for the entanglement entropy. Indeed, the eigenvalues of the reduced density matrix are known from the qubit states, and in particular, are given by the functions

$$f_q^k(r) = \binom{k}{q} r^q (1-r)^{k-q}, \quad (4.128)$$

for choices of k and q dictated by the excited states. Let's consider the case of a single particle excitation where $f_0^1(r) = 1-r$ and $f_1^1(r) = r$, using (2.12) we obtain that the increment of entanglement entropy is

$$\Delta S_1^1(r) = -r \log r - (1-r) \log(1-r), \quad (4.129)$$

Note that according to the qubit picture, the increment of Von Neumann entropy of a single particle excitation maximises where the particle has equal probability of being found in ℓ or $L-\ell$ and its maximum is exactly $\log 2$. In this sense the qubit picture provides a semi-classical interpretation of the entanglement entropy as a measure of how uncertain is the localisation of the quasiparticle in the two regions ℓ and $L-\ell$.

The entanglement entropy contribution given by a k -particle state of all distinct rapidities is simply:

$$\Delta S_1^{1,1,\dots,1}(r) = k \Delta S_1^1(r) = k [-r \log r - (1-r) \log(1-r)], \quad (4.130)$$

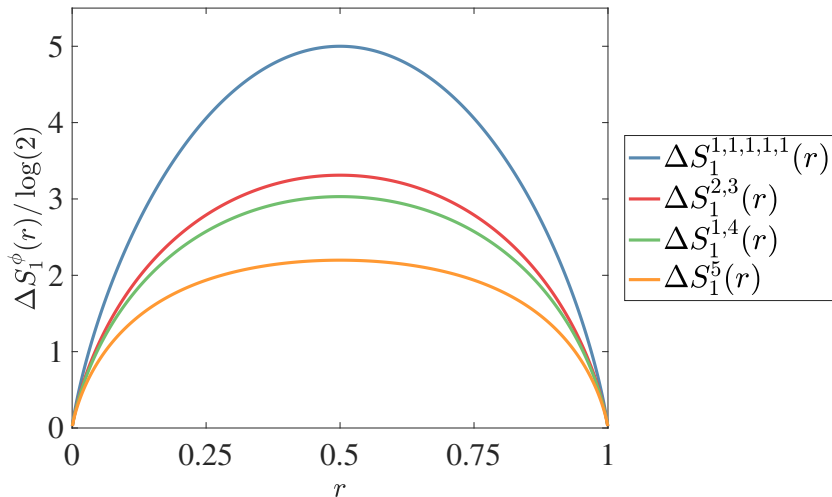


Figure 4.5 Entanglement entropy of various combinations of equal and distinct rapidities that lead to five-particle states. The higher the number of indistinguishable rapidities the lower the maximum at $r = 1/2$. The maximal entropy contribution of the state with only distinct particles $\Delta S_1^{1,1,1,1,1}(1/2)$ is exactly 5 bits.

and has maximum $k \log 2$ at $r = 1/2$. Therefore, if the rapidities are distinct, the contribution to the entanglement entropy of k particles is exactly k times the contribution of a single particle excitation, while if they are equal, this is not true: the contribution is in fact smaller. Indeed for multi-particles states composed of particles of all equal rapidities we have that

$$\Delta S_1^k(r) = - \sum_{q=0}^k f_q^k(r) \log f_q^k(r). \quad (4.131)$$

The function above maximises again at $r = 1/2$, but according to the qubit picture there are now configurations more likely to occur than others and this leads to a lower maximum than (4.130), signalling that there is less uncertainty on the localization of identical quasiparticles. In particular, the maximum is given by

$$\Delta S_1^k\left(\frac{1}{2}\right) = \sum_{q=0}^k \frac{1}{2^k} \binom{k}{q} \log \left[\frac{1}{2^k} \binom{k}{q} \right] < k \log 2, \quad \text{for } k > 1. \quad (4.132)$$

Similarly to the Rényi entropies, we may easily obtain entanglement entropy contributions given by generic states. In particular, the increment of entanglement entropy $\Delta S_1^{k_1, k_2, \dots}(r)$ of an excited state consisting of k_i particles of momentum p_i with $p_i \neq p_j$ for $i \neq j$ is

$$S_1^{k_1, k_2, \dots}(r) = \sum_i \Delta S_1^{k_i}(r) = \sum_i \left[- \sum_{q_i=0}^{k_i} f_{q_i}^{k_i}(r) \log f_{q_i}^{k_i}(r) \right], \quad (4.133)$$

where $f_{q_i}^{k_i}(r)$ is the function (4.128) for $k = k_i$ and $q = q_i$. More generally the presence of indistinguishable particles will lead to smaller entanglement contributions. Examples for various five-particle states are displayed in Fig. 4.5 .

4.8.2 Increment of single-copy entropy

Another quantity that can be evaluated through the functions (4.128) is the single-copy entropy, defined in Section 2.3.1 as the $n \rightarrow \infty$ limit of the n th Rényi entropy. In the Schmidt decomposition such quantity is given by $-\log \lambda^*$, where λ^* is the largest eigenvalue of the reduced density matrix [61]. Interestingly, excited state contributions to the single-copy entropy present non-analytic features. For a single-particle excitation, we have

$$\Delta S_{\infty}^1(r) = \begin{cases} -\log(1-r) & \text{for } 0 \leq r < \frac{1}{2} \\ -\log r & \text{for } \frac{1}{2} \leq r \leq 1. \end{cases} \quad (4.134)$$

Again, the result is just multiplied by k for a state consisting of k distinct-momentum particles. For equal momenta it is a function which is non-differentiable at k points in the interval $r \in (0, 1)$ (generalizing (4.134)). The positions of these cusps are given by the values

$$r = \frac{1+q}{1+k} \quad \text{for } q = 0, \dots, k-1, \quad (4.135)$$

and the single copy entropy is given by

$$\Delta S_{\infty}^k(r) = -\log f_q^k(r) \quad \text{for } \frac{q}{1+k} \leq r < \frac{1+q}{1+k} \quad (4.136)$$

and $q = 0, \dots, k$. Similarly to the other entropies, the single-copy entanglement contribution given by a generic excited state is

$$\Delta S_{\infty}^{k_1, k_2, \dots}(r) = \sum_i \Delta S_{\infty}^{k_i}(r), \quad (4.137)$$

where particles are organised in groups of k_i particles of momentum p_i with $p_i \neq p_j$ for $i \neq j$. With the formulae above we have described all the entanglement entropies' contributions of any multi-particle state with finite number of excitations and thus completed the task of this chapter. Some particular examples obtained with formulae (4.117), (4.133) and (4.137) are displayed in Fig. 4.6.

In conclusion, under the qubit interpretation and its general assumptions, the contributions

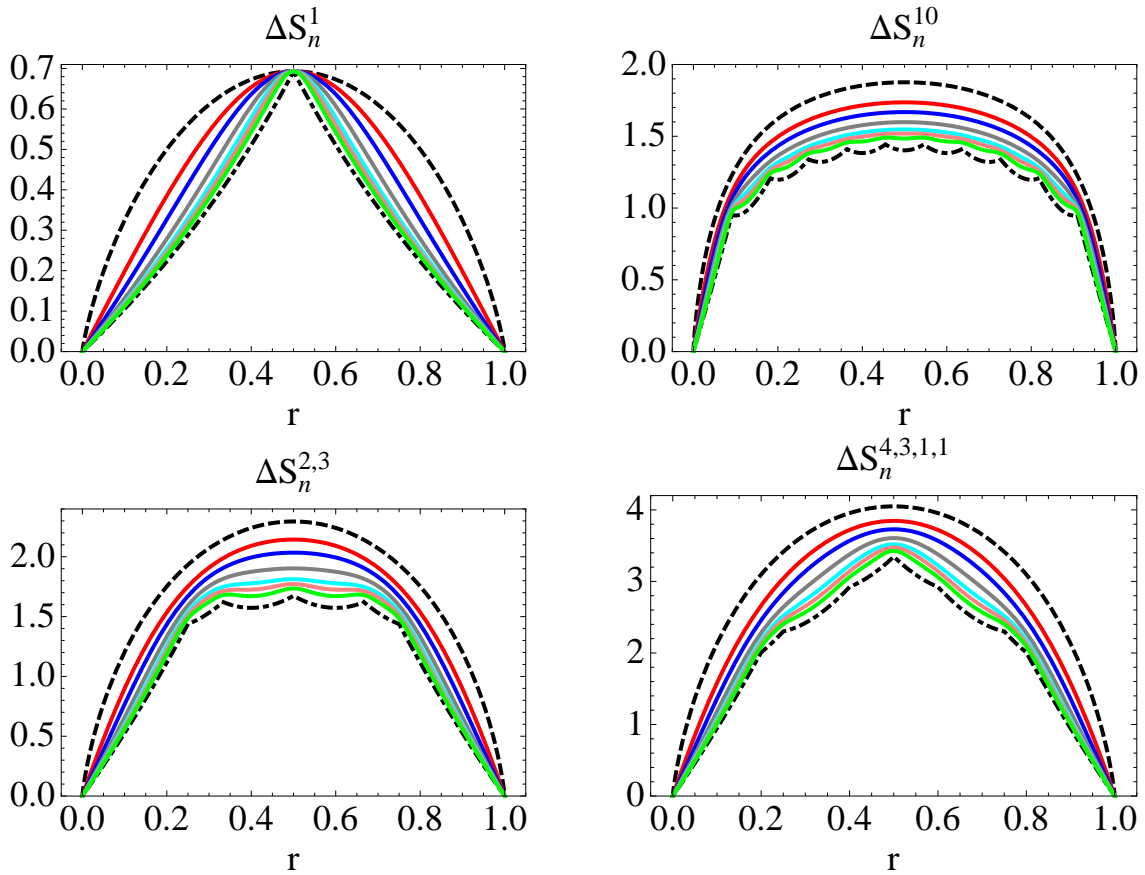


Figure 4.6 The functions (4.117), (4.133) and (4.137) for a single particle state (top-left), a state of 10 equal momenta (top-right) and for two “mixed” states with some equal and some distinct momenta (bottom). In each figure, the colorful functions are Rényi entropies for $n = 2, 3, 5, 8, 11, 17$, the dashed (outer-most) curve is the von Neumann entropy and the dot dashed (inner-most) curve is the single-copy entropy.

to the various entropies that an excited state generates with respect to the ground state encodes information on the occupancy distributions of the excitations in the entanglement region. In particular, the (in)distinguishability of the excitations is the key property that fully defines the entanglement content of any excited state. This suggests that the results presented above are universal, in the sense that they only depend on the quasiparticle content of the state and its statistics. This is a suggestion that will be further confirmed in the next chapter where we analyse different partitions.

EXCITED STATE ENTANGLEMENT OF TWO REGIONS

5.1 The case of two disconnected regions

In this chapter we extend our study started in Chapter 4 to two entanglement regions. We consider the situation represented in Fig. 5.1. In particular we consider a closed finite-volume system of volume L with two disconnected regions A and B immersed in an environment C , and described by a free massive boson theory.

As pointed out several times, the entanglement entropies and the logarithmic negativity are all suitable entanglement measures in this setting, but they capture different information about the state. In particular, the entanglement entropies measure the entanglement of the union of the two regions relative to the environment, while the logarithmic negativity measures the entanglement of a certain region, say A , with respect to the other region B in the presence of the environment C . Results for excited state entanglement increments in two regions have been first obtained [26], which will be also the paper we will mostly refer to in the course of this chapter.

Along similar lines to Chapter 4, we assume the system to be in a zero-density state $|\phi\rangle$ and at zero-temperature. We want to analyse the two entanglement measures in a carefully chosen scaling limit. Defining the new variables:

$$r_i := \frac{\ell_i}{L}, \quad \text{for } i = 1, 2, 3, \quad \text{and} \quad r := 1 - r_1 - r_3, \quad (5.1)$$

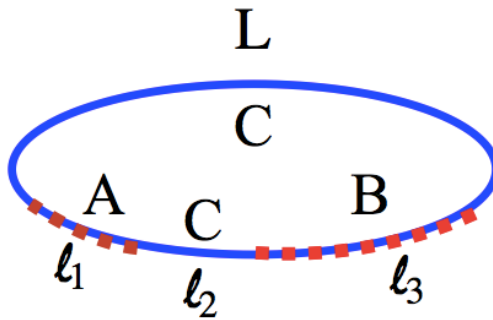


Figure 5.1 Two disconnected regions in a closed one-dimensional system.

this scaling limit is obtained by sending the entanglement regions' sizes and the entire system's size to infinity in a fixed proportion

$$L, \ell_1, \ell_2, \ell_3 \rightarrow \infty, \quad \text{with} \quad r, r_1, r_2, r_3 \text{ finite,} \quad \text{and} \quad 0 \leq r, r_1, r_2, r_3 \leq 1. \quad (5.2)$$

In such a limit, the increment of the Rényi entropies of two disconnected regions can be expressed in terms of branch-point twist field correlators as :

$$\begin{aligned} \Delta S_n^\phi(r) &:= S_n^\phi(r_1, r_2, r_3) - S_n^0(r_1, r_2, r_3) \\ &= \lim_{L \rightarrow \infty} \frac{1}{1-n} \log \left[\frac{{}_L \langle \phi | \mathcal{T}(0) \tilde{\mathcal{T}}(r_1 L) \mathcal{T}((r_1 + r_2)L) \tilde{\mathcal{T}}((r_1 + r_2 + r_3)L) | \phi \rangle_L}{{}_L \langle 0 | \mathcal{T}(0) \tilde{\mathcal{T}}(r_1 L) \mathcal{T}((r_1 + r_2)L) \tilde{\mathcal{T}}((r_1 + r_2 + r_3)L) | 0 \rangle_L} \right], \end{aligned} \quad (5.3)$$

where $S_n^0(r_1, r_2, r_3)$ are the entropies in the ground state. As the notation suggests, we will see later that the increments $\Delta S_n^\phi(r)$ are functions of r *only*. In the same limit, the increments of the replica logarithmic negativities are given by:¹

$$\begin{aligned} \Delta \mathcal{E}_n^\phi(r_1, r_3) &:= \mathcal{E}_n^\phi(r_1, r_2, r_3) - \mathcal{E}_n^0(r_1, r_2, r_3) \\ &= \lim_{L \rightarrow \infty} \log \left[\frac{{}_L \langle \phi | \mathcal{T}(0) \tilde{\mathcal{T}}(r_1 L) \tilde{\mathcal{T}}((r_1 + r_2)L) \mathcal{T}((r_1 + r_2 + r_3)L) | \phi \rangle_L}{{}_L \langle 0 | \mathcal{T}(0) \tilde{\mathcal{T}}(r_1 L) \tilde{\mathcal{T}}((r_1 + r_2)L) \mathcal{T}((r_1 + r_2 + r_3)L) | 0 \rangle_L} \right], \end{aligned} \quad (5.4)$$

and are functions of r_1 and r_3 *only*. As standard, \mathcal{T} is the branch-point twist field, $\tilde{\mathcal{T}}$ is its Hermitian conjugate and $|0\rangle_L$ is the ground state in the compactified space of Fig. 5.1. One should expect that $\mathcal{T} = \tilde{\mathcal{T}}$ in the doubled copy replica model $n = 2$ as they implement the same symmetry transformation. As a consequence, the results for the replica logarithmic negativity equal those for the Rényi entropy (up to a sign) for $n = 2$. When employing the branch-point twist field technique, we will therefore be computing ratios of four-point functions in the infinite volume limit. As seen in Section 3.2.2, exact explicit formulae for the four-point

¹Note that the state $|\phi\rangle$ is real. When we consider a generic complex state we usually denote it as $|\Phi\rangle$.

functions above are generally hard to access even in the ground state and/or CFT. Remarkably though, the increments considered here, in this particular scaling limit, turn out to be effectively computable. Additionally the qubit picture can be extended to two entanglement regions and provides an effective method to evaluate explicitly the increments of Von Newman entropy and the logarithmic negativity even in the case of disconnected regions.

5.2 Computation by branch-point twist fields

Compared to the situation explored in Section 4.3, the infinite-volume correlators of twist fields in (5.3) and (5.4) are defined in two new replica models, both characterised by the presence of an additional branch cut along the space direction. Many considerations developed in the study of the single-region problem can be extended to these two cases. One similarity is the state considered, which is again a zero-density state $|\phi\rangle$ in a free boson theory. Suppose this state to be formed of K particles whose rapidities are not necessary distinct from one another. Commutation relations among free boson fields ensure that the state $|\phi\rangle$ can be decomposed into independent blocks $|\phi\rangle = |k_1\rangle \otimes |k_2\rangle \otimes \dots$, each one containing k_j identical rapidities, and such that the sum of the particle numbers reproduces the total number of particles in $|\phi\rangle$ that is $k_1 + k_2 + \dots = K$. It seems thus convenient to treat each block as a separate case, and thus to focus on the case of a k -particle excitation state $|k\rangle$ of all equal momenta/rapidities.

As seen in the previous chapter, the doubling trick can be successfully implemented to convert correlators of branch twist fields into much simpler correlators of $U(1)$ -fields. Here, the trick consists of evaluating the four-point functions in a complex state $|\mathbf{k}\rangle$ that reproduce real results i.e. the state (4.21) derived in Section 4.3 (up to normalisation). We have thus that:²

$$\frac{\langle \mathbf{k} | \mathcal{T}(0) \tilde{\mathcal{T}}(x_1) \mathcal{T}(x_2) \tilde{\mathcal{T}}(x_3) | \mathbf{k} \rangle}{\langle \mathbf{0} | \mathcal{T}(0) \tilde{\mathcal{T}}(x_1) \mathcal{T}(x_2) \tilde{\mathcal{T}}(x_3) | \mathbf{0} \rangle} = \frac{\langle k | \mathcal{T}(0) \tilde{\mathcal{T}}(x_1) \mathcal{T}(x_2) \tilde{\mathcal{T}}(x_3) | k \rangle}{\langle 0 | \mathcal{T}(0) \tilde{\mathcal{T}}(x_1) \mathcal{T}(x_2) \tilde{\mathcal{T}}(x_3) | 0 \rangle} \quad (5.5)$$

and a similar expression for the correlator associated to the replica negativity. When doubling the replica model, the diagonalisation of the cyclic permutation action (discussed in Subsection 4.3.1 for the single-region problem) can be naturally extended to replica models arising from multiple branch cuts, and the basis in which the symmetry acts diagonally can be obtained via the transformation (4.31). Although in the diagonal basis the computation of correlators is enormously simplified, the price to pay is a more complicated structure for the excited states which must now be also expressed in this new basis (see e.g. (4.62) for an example).

²Along similar lines to Chapter 4, we use bond letters for complex states.

When implementing the finite-volume in each replica model, the branch-cuts need to be deformed by following the same instructions provided in Subsection 3.2.3. In the end of this process, we deal with four semi-infinite branch cuts along the time-direction of the cylinder. In the new finite-volume replica models, the complex fields Φ_j s satisfy periodic boundary conditions which are affected by the presence of the four branch cuts, and that more generally depends on which sector of the cylinder these fields are defined. As a consequence quasiparticles are described by rapidities which will be quantized in finite volume and the quantization conditions will depend upon the sector p the corresponding creation/annihilation operator is acting on, and upon an index α that parametrizes the periodicity conditions for the fields $\Phi_j(x + L) = \Phi_{j+\alpha}(x)$. A set of generalized Bethe-Yang equations (developed in Section 4.4.1 for single-regions) can be written as

$$Q_p^{\epsilon,\alpha}(\theta) = 2\pi J^{\epsilon,\alpha} \quad \text{with} \quad Q_p^{\epsilon,\alpha}(\theta) = mL \sinh(\theta) - 2\pi\epsilon\alpha \frac{p}{n}, \quad (5.6)$$

where $\epsilon = \pm$ is the $U(1)$ charge of the particle and $J^{\epsilon,\alpha} \in \mathbb{Z}$.

In order to obtain form factor expansions we need first to insert three complete sets of states in each four-point correlator. We can define some operator $\mathbb{1}_p^{(\alpha)}$ inserting a complete set of states with quantization condition α . For any α and p we have that $\mathbb{1}_p^{(\alpha)} \equiv \mathbb{1}_p$ is trivially the identity operator. The sum over a complete set of states in sector p with quantization condition α can be written as

$$\mathbb{1}_p^{(\alpha)} = \sum_{m^\pm=0}^{\infty} \sum_{\{J_i^{\pm,\alpha}\}_{m^\pm}} \frac{1}{m^+!m^-!} |\{J_i^{\pm,\alpha}\}_{m^\pm}\rangle_{p;L} \langle\{J_i^{\pm,\alpha}\}_{m^\pm}| \quad (5.7)$$

where each state $|\{J_i^{\pm,\alpha}\}_{m^\pm}\rangle_{p;L}$ is characterised by a rapidity set $\{\theta_1^{+,\alpha}, \dots, \theta_{m^+}^{+,\alpha}, \theta_1^{-,\alpha}, \dots, \theta_{m^-}^{-,\alpha}\}$ formed of the Bethe-Yang equation (5.6) with a fixed α . We can then define the complete sum over all sectors

$$\mathbb{1}^{(\alpha)} = \otimes_{p=1}^n \mathbb{1}_p^{(\alpha)}. \quad (5.8)$$

The branch-point twist fields intertwine between the different quantization sectors. Denoting the corresponding Hilbert space by $\mathcal{H}^{(\alpha)}$ we can write

$$\mathcal{T} : \mathcal{H}^{(\alpha)} \rightarrow \mathcal{H}^{(\alpha+1)}, \quad \tilde{\mathcal{T}} : \mathcal{H}^{(\alpha)} \rightarrow \mathcal{H}^{(\alpha-1)}. \quad (5.9)$$

As seen in Section 4.4.1, we assume that field Φ satisfies standard quantization conditions, which corresponds to having the associated excited state $|\mathbf{k}\rangle_L$ in the trivial quantization sector $\mathcal{H}^{(0)}$. This, combined with the properties of the branch-point twist fields means that the four point functions of interest may be spanned as

$${}_L\langle\mathbf{k}|\mathcal{T}(0)\tilde{\mathcal{T}}(x_1)\mathcal{T}(x_2)\tilde{\mathcal{T}}(x_3)|\mathbf{k}\rangle_L = {}_L\langle\mathbf{k}|\mathcal{T}(0)\mathbb{1}^{(1)}\tilde{\mathcal{T}}(x_1)\mathbb{1}^{(0)}\mathcal{T}(x_2)\mathbb{1}^{(1)}\tilde{\mathcal{T}}(x_3)|\mathbf{k}\rangle_L, \quad (5.10)$$

$${}_L\langle\mathbf{k}|\mathcal{T}(0)\tilde{\mathcal{T}}(x_1)\tilde{\mathcal{T}}(x_2)\mathcal{T}(x_3)|\mathbf{k}\rangle_L = {}_L\langle\mathbf{k}|\mathcal{T}(0)\mathbb{1}^{(1)}\tilde{\mathcal{T}}(x_1)\mathbb{1}^{(0)}\tilde{\mathcal{T}}(x_2)\mathbb{1}^{(-1)}\mathcal{T}(x_3)|\mathbf{k}\rangle_L, \quad (5.11)$$

where $x_{1,2,3}$ denote the positions of the branch-point twist fields which is related to the original lengths in Fig. 5.1 as

$$x_1 := \ell_1, \quad x_2 := \ell_1 + \ell_2, \quad \text{and} \quad x_3 := \ell_1 + \ell_2 + \ell_3. \quad (5.12)$$

5.2.1 Four-point correlation functions in single-particle excited states

Let us focus on the calculation for a single-particle excited state which in infinite volume is given by:

$$|\mathbf{1}\rangle = \sum_{\{N^\pm\}} C_n(\{N^\pm\}) \prod_{p=1}^n [\mathbf{a}_p^\dagger(\theta)]^{N_p^+} [\mathbf{b}_p^\dagger(\theta)]^{N_p^-} |\mathbf{0}\rangle. \quad (5.13)$$

Note that the state above is of the same form as the one considered in Subsection 4.5 in the computation of a two-point function, and $C_n(\{N^\pm\})$ are exactly the same coefficients defined in (4.62). In finite volume, the rapidity is the solution of the quantization condition (5.6)

$$Q_p^{\epsilon,0}(\theta) = mL \sinh(\theta) = 2\pi I^0, \quad \epsilon = \pm. \quad (5.14)$$

Following previous considerations, the finite volume four-point functions are

$$\begin{aligned} {}_L\langle\mathbf{1}|\mathcal{T}(0)\tilde{\mathcal{T}}(x_1)\mathcal{T}(x_2)\tilde{\mathcal{T}}(x_3)|\mathbf{1}\rangle_L &= \sum_{\{N^\pm\}} \sum_{\{\tilde{N}^\pm\}} [C_n(\{N^\pm\})]^* C_n(\{\tilde{N}^\pm\}) \\ &\quad \times \prod_{p=1}^n \hat{\mathcal{F}}_p(N_p^\pm, \tilde{N}_p^\pm), \end{aligned} \quad (5.15)$$

$$\begin{aligned}
 {}_L \langle \mathbf{1} | \mathcal{T}(0) \tilde{\mathcal{T}}(x_1) \tilde{\mathcal{T}}(x_2) \mathcal{T}(x_3) | \mathbf{1} \rangle_L &= \sum_{\{N^\pm\}} \sum_{\{\tilde{N}^\pm\}} [C_n(\{N^\pm\})]^* C_n(\{\tilde{N}^\pm\}) \\
 &\times \prod_{p=1}^n \tilde{\mathcal{F}}_p(N_p^\pm, \tilde{N}_p^\pm), \tag{5.16}
 \end{aligned}$$

with the different sector contributions

$$\hat{\mathcal{F}}_p(N_p^\pm, \tilde{N}_p^\pm) = {}_{p;L} \langle \{I^0\}_{N_p^\pm} | \mathcal{T}_p(0) \mathbb{1}_p^{(1)} \tilde{\mathcal{T}}_p(x_1) \mathbb{1}_p^{(0)} \mathcal{T}_p(x_2) \mathbb{1}_p^{(1)} \tilde{\mathcal{T}}_p(x_3) | \{I^0\}_{\tilde{N}_p^\pm} \rangle_{p;L}, \tag{5.17}$$

$$\tilde{\mathcal{F}}_p(N_p^\pm, \tilde{N}_p^\pm) = {}_{p;L} \langle \{I^0\}_{N_p^\pm} | \mathcal{T}_p(0) \mathbb{1}_p^{(1)} \tilde{\mathcal{T}}_p(x_1) \mathbb{1}_p^{(0)} \tilde{\mathcal{T}}_p(x_2) \mathbb{1}_p^{(-1)} \mathcal{T}_p(x_3) | \{I^0\}_{\tilde{N}_p^\pm} \rangle_{p;L}. \tag{5.18}$$

In sector n the $U(1)$ twist fields coincide with the identity operator, hence the contributions from this sector are just the normalization of the state

$$\hat{\mathcal{F}}_n(N_n^\pm, \tilde{N}_n^\pm) = \tilde{\mathcal{F}}_n(N_n^\pm, \tilde{N}_n^\pm) = N_n^+! N_n^-! \delta_{N_n^+, \tilde{N}_n^+} \delta_{N_n^-, \tilde{N}_n^-}. \tag{5.19}$$

The functions $\hat{\mathcal{F}}_n$ and $\tilde{\mathcal{F}}_n$ can be systematically computed by using the contour integral approach discussed in detail in Subsection 4.5.1. However the calculation for four-point functions turns out to be much more involved. The main conceptual difference arises from the fact that now also first-order and third-order poles contribute to the leading contribution and need to be taken into account. Crucially, once the sums in (5.7) have been transformed in into contour integrals, in order to regularise the correlators one needs to account for all possible contractions $\theta_j^{\epsilon,\alpha} \approx \theta$ generating such poles in the form factors involving the rapidities θ . This tedious task was rigorously addressed in [26] where the full computation is presented. In appendix A we focus on the subtle points of the computation, with special attention to the extension of the computational steps described in Subsection 4.5.1 to this particular case. Following the computational instructions, one arrives to the following final result for the n th Rényi entropy increment:

$$\lim_{L \rightarrow \infty} \frac{{}_L \langle \mathbf{1} | \mathcal{T}(0) \tilde{\mathcal{T}}(x_1) \mathcal{T}(x_2) \tilde{\mathcal{T}}(x_3) | \mathbf{1} \rangle_L}{{}_L \langle \mathbf{0} | \mathcal{T}(0) \tilde{\mathcal{T}}(x_1) \mathcal{T}(x_2) \tilde{\mathcal{T}}(x_3) | \mathbf{0} \rangle_L} = \sum_{\{N^\pm\}} |C_n(\{N^\pm\})|^2 \prod_{p=1}^n \prod_{\epsilon=\pm} N_p^\epsilon! [g_{\epsilon p}^n(r_1 + r_3)]^{N_p^\epsilon}. \tag{5.20}$$

where $g_{ep}^n(r)$ is the function in in (4.79). Hence this is exactly the same result as for single region entanglement entropy. We can set $r_1 + r_3 = 1 - r$ and use the fact that the correlator is invariant under $r \rightarrow 1 - r$ to rewrite the result above as in formula (6.3). The final result for the replica negativity is instead

$$\lim_{L \rightarrow \infty} \frac{L \langle \mathbf{1} | \mathcal{T}(0) \tilde{\mathcal{T}}(x_1) \tilde{\mathcal{T}}(x_2) \mathcal{T}(x_3) | \mathbf{1} \rangle_L}{L \langle \mathbf{0} | \mathcal{T}(0) \tilde{\mathcal{T}}(x_1) \tilde{\mathcal{T}}(x_2) \mathcal{T}(x_3) | \mathbf{0} \rangle_L} = \sum_{\{N^\pm\}} |C_n(\{N^\pm\})|^2 \prod_{p=1}^n \prod_{\epsilon=\pm} N_p^\epsilon! [\hat{g}_{ep}^n(r_1, r_3)]^{N_p^\epsilon}. \quad (5.21)$$

where we have introduced the function:

$$\hat{g}_{ep}^n(r_1, r_3) = 1 - r_1 - r_3 + r_1 e^{2\pi i \frac{ep}{n}} + r_3 e^{-2\pi i \frac{ep}{n}}. \quad (5.22)$$

We conclude that, in the scaling limit (5.2), the increments of Rényi entropies and those of replica logarithmic negativities do not depend on the distance between the two regions (which is associated to the ratio r_2).

5.2.2 Multi-particle states

In infinite volume a state $|\mathbf{k}\rangle$ of all coinciding rapidities takes the exact form of (4.98). Generalising the results in Subsection 4.6.2, one easily obtains that

$$L \langle \mathbf{k} | \mathcal{T}(0) \tilde{\mathcal{T}}(x_1) \mathcal{T}(x_2) \tilde{\mathcal{T}}(x_3) | \mathbf{k} \rangle_L = \frac{1}{(k!)^n} \sum_{\{N^\pm\}} \sum_{\{\tilde{N}^\pm\}} [D_n^k(\{N^\pm\})]^* D_n^k(\{\tilde{N}^\pm\}) \prod_{p=1}^n \hat{\mathcal{F}}_p(N_p^\pm, \tilde{N}_p^\pm),$$

and

$$L \langle \mathbf{k} | \mathcal{T}(0) \tilde{\mathcal{T}}(x_1) \tilde{\mathcal{T}}(x_2) \mathcal{T}(x_3) | \mathbf{k} \rangle_L = \frac{1}{(k!)^n} \sum_{\{N^\pm\}} \sum_{\{\tilde{N}^\pm\}} [D_n^k(\{N^\pm\})]^* D_n^k(\{\tilde{N}^\pm\}) \prod_{p=1}^n \tilde{\mathcal{F}}_p(N_p^\pm, \tilde{N}_p^\pm),$$

where the functions $\hat{\mathcal{F}}_p$ and $\tilde{\mathcal{F}}_p$ are the same as in (5.15) and (5.16). Compared to the single-particle case, the coefficients satisfy different constraints (as argued in Section 4.6.2). It is straightforward to generalise the results in the previous section to the case of multiparticle states:

$$\lim_{L \rightarrow \infty} \frac{\hat{\mathcal{F}}_p(\{N_p^\pm\}, \{N_p^\pm\})}{p;L \langle \mathbf{0} | \mathcal{T}_p(0) \tilde{\mathcal{T}}_p(x_1) \mathcal{T}_p(x_2) \tilde{\mathcal{T}}_p(x_3) | \mathbf{0} \rangle_{p;L}} = \prod_{\epsilon=\pm} N_p^\epsilon! [g_{ep}^n(r_1 + r_3)]^{N_p^\epsilon}, \quad (5.23)$$

$$\lim_{L \rightarrow \infty} \frac{\tilde{\mathcal{F}}_p(\{N_p^\pm\}, \{N_p^\pm\})}{p;L \langle \mathbf{0} | \mathcal{T}_p(0) \tilde{\mathcal{T}}_p(x_1) \tilde{\mathcal{T}}_p(x_2) \mathcal{T}_p(x_3) | \mathbf{0} \rangle_{p;L}} = \prod_{\epsilon=\pm} N_p^\epsilon! [\hat{g}_{ep}^n(r_1, r_3)]^{N_p^\epsilon}. \quad (5.24)$$

and obtain finally

$$\Delta S_n^k(r) = \frac{1}{1-n} \log \left(\sum_{\{N^\pm\}} \frac{|D_n^k(\{N^\pm\})|^2}{(k!)^n} \prod_{p=1}^n \prod_{\epsilon=\pm} N_p^\epsilon! [g_{ep}^n(r)]^{N_p^\epsilon} \right), \quad (5.25)$$

$$\Delta \mathcal{E}_n^k(r_1, r_3) = \log \left(\sum_{\{N^\pm\}} \frac{|D_n^k(\{N^\pm\})|^2}{(k!)^n} \prod_{p=1}^n \prod_{\epsilon=\pm} N_p^\epsilon! [\hat{g}_{ep}^n(r_1, r_3)]^{N_p^\epsilon} \right), \quad (5.26)$$

In order to obtain explicit formulae one needs to compute the coefficients $D_n^k(\{N^\pm\})$, which are the same for any fixed number of excitation considered. As pointed out in Chapter 4, these coefficients can be numerically evaluated by looking at specific excited states, usually with the help of computational software. However, the evaluation of (5.26) and (5.26) is much more efficient if one employs instead the qubit picture, introduced in Section 4.8. The qubit picture provides indeed a systematic way to predict the general polynomial structure of the results above for any number k of excitations involved in the state and any copy number n . In the next section, we will extend the idea discussed in Section 4.8 to two regions and obtain closed formulae for the increments above.

5.3 Computation by qubit picture

Consider a state formed of k particle excitations of equal momenta/rapidities. According to the qubit picture, there exists a k -qubit state $|\Psi_{\text{qb}}^{(k)}\rangle$ describing the occupancy distribution of the k -particles excitations in the three regions of the partition in Fig. 5.1. This multi-qubit state lives in a factorised Hilbert state $\mathcal{H}_{\text{qb}} = \mathcal{H}_1 \otimes \mathcal{H}_2 \otimes \mathcal{H}_3$, whose components \mathcal{H}_1 and \mathcal{H}_3 represent respectively the interior of regions A and B in Fig. 5.1, while \mathcal{H}_2 is associated to their exterior. Consider an orthonormal basis of \mathcal{H}_{qb} , the state $|\Psi_{\text{qb}}^{(k)}\rangle$ is expressed by

$$|\Psi_{\text{qb}}^{(k)}\rangle = \sum_{\{k_1, k_2, k_3\} \in \sigma_0^3(k)} c_{k_1, k_2, k_3} |k_1 k_2 k_3\rangle, \quad (5.27)$$

where the sums run over positive integers forming a tripartition of k , and the coefficients c_{k_1, k_2, k_3} are explicit functions of the ratios in the definition (5.1):

$$c_{k_1, k_2, k_3} := \sqrt{\frac{k! r_1^{k_1} r_2^{k_2} r_3^{k_3}}{k_1! k_2! k_3!}} \delta_{k_1 + k_2 + k_3, k}. \quad (5.28)$$

Note that the Kronecker delta $\delta_{k_1+k_2+k_3,k}$ constrains the sums above. Provided that all vectors $|k_1k_2k_3\rangle$ are normalized to one, then the vector $|\Psi_{\text{qb}}^{(k)}\rangle$ is also a unit vector,

$$\langle \Psi_{\text{qb}}^{(k)} | \Psi_{\text{qb}}^{(k)} \rangle = \sum_{\{k_1, k_2, k_3\} \in \sigma_0^3(k)} c_{k_1, k_2, k_3}^2 = (r_1 + r + r_3)^k = 1. \quad (5.29)$$

The state $|\Psi_{\text{qb}}^{(k)}\rangle$ in (5.27) may be interpreted as follow: each state $|k_1k_2k_3\rangle$ is a state of k_1 excitations in region A , k_3 excitations in region B and k_2 excitations in the rest of the system. The square of the corresponding coefficient c_{k_1, k_2, k_3}^2 is the associated probability that this configuration occurs if we were to place randomly and independently, with uniform distribution, k particles on the interval $[0, 1]$ covered by three non-intersecting subintervals of lengths r_1, r and r_3 .

From expression (5.27) it is then possible to explicitly construct the reduced density matrix and its partially transposed version as:

$$\langle k_1k_3 | \rho_{A \cup B} | k'_1k'_3 \rangle = \sum_{k_2 \in \mathbb{N}_0} c_{k_1k_2k_3} c_{k'_1k_2k'_3}, \quad (5.30)$$

$$\langle k_1k_3 | \rho_{A \cup B}^{T_B} | k'_1k'_3 \rangle = \sum_{k_2 \in \mathbb{N}_0} c_{k_1k_2k'_3} c_{k'_1k_2k_3}, \quad (5.31)$$

Here the sums run over all non-negative integers, and whenever the constraint $k_1 + k_2 + k_3 = k$ is violated, the corresponding coefficient c_{k_1, k_2, k_3} is zero by definition. From this constraint we know in fact that $0 \leq k_2 \leq k$ so we could have restricted the summation range $k_2 \in \mathbb{N}_0$ much more. However we will write it like this for now, for simplicity, and discuss the summation ranges more precisely at the end of our calculation. With these results we can now evaluate the matrix elements of the n -th powers of the reduced density matrices above. These are given by:

$$\langle k_1^1 k_3^1 | \rho_{A \cup B}^n | k_1^{n+1} k_3^{n+1} \rangle = \sum_{\substack{k_1^s, k_3^s \in \mathbb{N}_0; s=2, \dots, n \\ k_2^j \in \mathbb{N}_0; r \in I_n}} \prod_{j=1}^n c_{k_1^j k_2^j k_3^j} c_{k_1^{j+1} k_2^j k_3^{j+1}}, \quad (5.32)$$

$$\langle k_1^1 k_3^1 | (\rho_{A \cup B}^{T_B})^n | k_1^{n+1} k_3^{n+1} \rangle = \sum_{\substack{k_1^s, k_3^s \in \mathbb{N}_0; s=2, \dots, n \\ k_2^j \in \mathbb{N}_0; r \in I_n}} \prod_{j=1}^n c_{k_1^j k_2^j k_3^{j+1}} c_{k_1^{j+1} k_2^j k_3^j}, \quad (5.33)$$

where $I_n := \{1, \dots, n\}$. Finally, we are interested in the Rényi entropies and the replica logarithmic negativities, which means we need to take the trace over $A \cup B$ of the matrices

above. This gives the following results:

$$S_n^{\Psi_{\text{qb}}^{(k)}}(r_1, r_3) = \frac{1}{1-n} \log \left(\sum_{\{k_i^s \in \mathbb{N}_0; i \in I_3; s \in I_n\}} \prod_{j=1}^n C_{k_1^j k_2^j k_3^j} C_{k_1^{j+1} k_2^j k_3^{j+1}} \right), \quad (5.34)$$

$$\mathcal{E}_n^{\Psi_{\text{qb}}^{(k)}}(r_1, r_3) = \log \left(\sum_{\{k_i^s \in \mathbb{N}_0; i \in I_3; s \in I_n\}} \prod_{j=1}^n C_{k_1^j k_2^j k_3^{j+1}} C_{k_1^{j+1} k_2^j k_3^j} \right), \quad (5.35)$$

where we adopt the convention $k_i^1 \equiv k_i^{n+1}$ for $i = 1, 2, 3$. We can write these formulae more explicitly by employing the definition (5.28), giving

$$S_n^{\Psi_{\text{qb}}^{(k)}}(r_1, r_3) = \frac{1}{1-n} \log \left(\sum_{\{k_i^s \in \mathbb{N}_0; i \in I_3; s \in I_n\}} \prod_{j=1}^n \frac{k! r_1^{k_1^j} r_2^{k_2^j} r_3^{k_3^j}}{k_1^j! k_2^j! k_3^j!} \delta_{k_1^j + k_2^j + k_3^j, k} \delta_{k_1^{j+1} + k_2^j + k_3^{j+1}, k} \right), \quad (5.36)$$

$$\mathcal{E}_n^{\Psi_{\text{qb}}^{(k)}}(r_1, r_3) = \log \left(\sum_{\{k_i^s \in \mathbb{N}_0; i \in I_3; s \in I_n\}} \prod_{j=1}^n \frac{k! r_1^{k_1^j} r_2^{k_2^j} r_3^{k_3^j}}{k_1^j! k_2^j! k_3^j!} \delta_{k_1^j + k_2^j + k_3^{j+1}, k} \delta_{k_1^{j+1} + k_2^j + k_3^j, k} \right). \quad (5.37)$$

In the next subsections we examine each of these functions separately.

5.3.1 Results for Rényi entropies

We can now eliminate the delta-functions by implementing their constraints. Let us start with the Rényi entropies. We can substitute:

$$k_1^j = k - k_2^{j-1} - k_3^j, \quad \forall j, \quad (5.38)$$

and this will eliminate the sums over k_1^j with $j = 1, \dots, n$. We then have sums over k_2^j and k_3^j left but we can also eliminate one of these by implementing the second set of delta-functions together with the conditions above. This gives the constraints,

$$k_2^j = k_2^{j+1} =: p \quad \forall j. \quad (5.39)$$

Therefore, $k_1^j = k - p - k_3^j$. This means that the factor $\prod_j r_1^{k_1^j} r_2^{k_2^j} r_3^{k_3^j}$ in (5.36) becomes

$$\prod_{j=1}^n r_1^{k_1^j} r_2^{k_2^j} r_3^{k_3^j} = r_1^{n(k-p)-q} r_2^{np} r_3^q, \quad (5.40)$$

where we defined $q := \sum_{j=1}^n k_3^j$. This finally allows us to rewrite (5.36) as

$$S_n^{\Psi^{(k)}_{\text{qb}}}(r_1, r_3) = \frac{1}{1-n} \log \left(\sum_{p=0}^k \sum_{q=0}^{n(k-p)} \mathcal{Z}_{p,q} r_1^{n(k-p)-q} r_3^q \right), \quad (5.41)$$

where

$$\mathcal{Z}_{p,q} = \sum_{\{k_1, \dots, k_n\} \in \sigma_0^n(q)} \prod_{j=1}^n \frac{k!}{p! k_j! (k-p-k_j)!}, \quad (5.42)$$

and $\sigma_0^n(q)$ represents the set of integer partitions of q into n non-negative parts. We have relabelled $k_3^j := k_j$, and the range of the sums in p and q is determined by the condition $\mathcal{Z}_{p,q} \neq 0$. From the definition (5.39), $0 \leq p \leq k$. Regarding the values of q , we know that q can not be negative (by definition) so $q \geq 0$. Its maximum value is obtained if $k-p-k_j = 0$ for all j . This corresponds to $q = n(k-p)$. In fact the sum over q can be rewritten as

$$\sum_{q=0}^{n(k-p)} \mathcal{Z}_{p,q} r_1^{n(k-p)-q} r_3^q = \prod_{j=1}^n \sum_{k_j=0}^{k-p} \frac{k!}{p! k_j! (k-p-k_j)!} r_1^{k-p-k_j} r_3^{k_j} = \left[\binom{k}{p} (r_1 + r_3)^{k-p} \right]^n, \quad (5.43)$$

with $r_1 + r_3 = 1 - r$ so that

$$S_n^{\Psi^{(k)}_{\text{qb}}}(r_1, r_3) =: S_n^{\Psi^{(k)}_{\text{qb}}}(r) = \frac{1}{1-n} \log \left(\sum_{p=0}^k \left[\binom{k}{p} r^p (1-r)^{k-p} \right]^n \right). \quad (5.44)$$

Therefore, the entanglement entropy depends *only* on the parameter r and is given by exactly the same expression found in Section 4.8. In other words, in the qubit picture, the entanglement entropy depends only on the overall size of regions and not on whether or not they are connected.

5.3.2 Results for replica logarithmic negativity

A similar analysis can be carried out for the replica logarithmic negativity. Starting with (5.37) the second delta function gives the condition:

$$k_1^j = k - k_2^{j-1} - k_3^{j-1}, \quad \forall j, \quad (5.45)$$

and this eliminates the sums over k_1^j with $j = 1, \dots, n$. We then have sums over k_2^j and k_3^j left but we can also eliminate one of these by implementing the second set of delta-functions together with the conditions above. This gives the constraints,

$$k_2^j - k_2^{j-1} = k_3^{j-1} - k_3^{j+1}, \quad \forall j. \quad (5.46)$$

We may regard this equation as a first order difference equation for the sequence k_2^j . The solution to such an equation is the sum of the solution to its homogenous version (a constant) and a particular solution of the full equation which can be worked out by inspection to be $-k_3^j - k_3^{j+1}$. The general solution is then

$$k_2^j = \gamma - k_3^j - k_3^{j-1}, \quad (5.47)$$

where γ is an arbitrary constant. With this we also have that $k_1^j = k - \gamma + k_3^j$. We can now evaluate the product

$$\prod_{j=1}^n r_1^{k_1^j} r_2^{k_2^j} r_3^{k_3^j} = r_1^{np+q} r_2^{n(k-p)-2q} r_3^q, \quad (5.48)$$

where $q := \sum_{j=1}^n k_3^j$ and $p = k - \gamma$. Relabelling $k_3^{j+1} := k_j$ we then find

$$\mathcal{E}_n^{\Psi_{\text{qb}}^{(k)}}(r_1, r_3) = \frac{1}{1-n} \log \left(\sum_{p=-k}^k \sum_{q=\max(0, -np)}^{\lfloor \frac{n}{2}(k-p) \rfloor} \mathcal{A}_{p,q} r_1^{np+q} r_2^{n(k-p)-2q} r_3^q \right), \quad (5.49)$$

where

$$\mathcal{A}_{p,q} = \sum_{\{k_1, \dots, k_n\} \in \sigma_0^n(q)} \prod_{j=1}^n \frac{k!}{(p+k_j)!(k-p-k_j-k_{j+1})!k_j!}. \quad (5.50)$$

The range of sums in p and q is fixed by selecting out those contributions for which $\mathcal{A}_{p,q} \neq 0$. This requires that the arguments of the factorials in the denominator remain non-negative, which in turn restricts the type of partitions that can contribute to the sum over k_1, \dots, k_n .

Consider the sum in p . The range of this sum can be determined easily from the relation (5.47). This implies that $0 \leq \gamma \leq 2k$. Together with the definition of p this gives $-k \leq p \leq k$. This guarantees that all arguments of the factorials in the denominator remain non-negative.

The range of values of q can also be determined as follows. The lower limit is easy to establish as whenever $p < 0$ the partitions contributing to $\mathcal{A}_{p,q}$ must have $k_j \geq -p$. Thus, the smallest value of q giving a non-vanishing contribution corresponds to taking all $k_j = -p$ for all j which gives $q = -np$. On the other hand, if $p \geq 0$ then the smallest value q can take is zero corresponding to all $k_j = 0$. This fixes the lower bound to $\max(0, -np)$. Let us now consider the upper bound. Given a certain p , the largest value q can take corresponds to having $k - p - k_j - k_{j+1} = 0$ for all j , or $k_j + k_{j+1} = k - p$. Writing

$$\sum_{j=1}^n (k_j + k_{j+1}) = \sum_{j=1}^n (k - p), \quad (5.51)$$

we have obviously that the right hand side gives $n(k-p)$ whereas the left hand side gives $2\sum_{j=1}^n k_j = 2q$. Therefore, for generic parity of n and $k-p$, we obtain $q = \lceil \frac{n(k-p)}{2} \rceil$. This gives the range $\max(0, -np) \leq q \leq \lceil \frac{n(k-p)}{2} \rceil$.

5.4 The analytic continuation in n

Similarly to the case of a single region, the qubit picture in two regions provides a systematic way to obtain the the entanglement entropy and logarithmic negativity. Given a qubit state, the only ingredients we need are the eigenvalues of its reduced density matrix (for the entanglement entropy) and those of its partial transposition (for the logarithmic negativity).

In the case of the entanglement entropy, these ingredients are easily accessible: since the result (5.44) is independent on the connectivity of the two regions, the desired eigenvalues are simply the functions $f_q^k(r)$ in (4.128). The increments of von Neumann entropy are accordingly given by formula (4.131) for any number of excitations k . The case of the logarithmic negativity is generally more complicated. However for states composed of a low number of qubits, the diagonalisation of ρ_A^{TB} turns out to be easier to access, and it is effectively possible to derive closed formulae for the logarithmic negativity. To clarify this point we present below a very simple example: the computation of both entanglement entropy and logarithmic negativity for a single-qubit state. By using similar analyses, it is possible to obtain explicit formulae for the logarithmic negativity of two- and three-particle states [26]. Unlike the entanglement entropy, the analytic continuation in the parameter n of the functions (5.49) shows a non-trivial structure, even in the simple example below.

5.4.1 Example of a single-particle excitation

We consider the qubit state (5.27) for $k = 1$

$$|\Psi_{\text{qb}}^{(1)}\rangle = \sqrt{r_1}|100\rangle + \sqrt{r}|010\rangle + \sqrt{r_3}|001\rangle. \quad (5.52)$$

where the first qubit represents the presence (1) or not (0) of a particle in region A , the second qubit represents the same for region C , and the final qubit likewise for region B . Tracing over the mid-qubit we have that

$$\rho_{A \cup B} = r_1|10\rangle\langle 10| + r|00\rangle\langle 00| + r_3|01\rangle\langle 01| + \sqrt{r_1 r_3}(|10\rangle\langle 01| + |01\rangle\langle 10|), \quad (5.53)$$

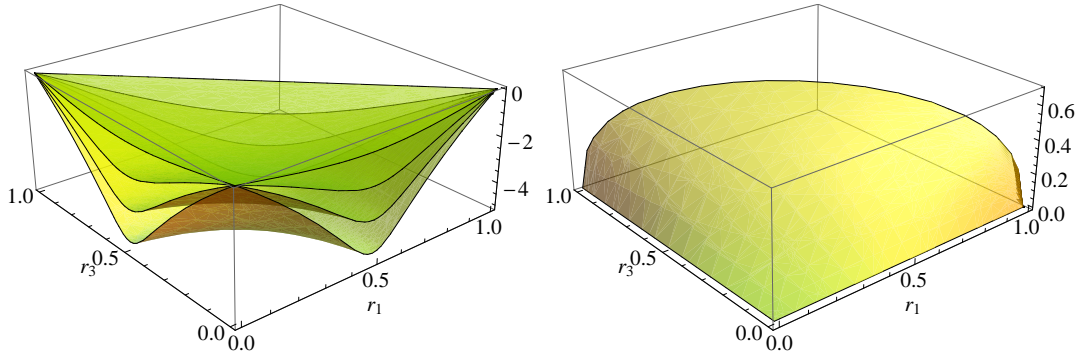


Figure 5.2 Left: The function (5.60) for $n = 2, 4, 6$ and 8 (the higher the value of n , the more negative the value of the function). Right: The function (5.61). Recall that $0 \leq r_1 + r_3 \leq 1$, which restricts the domain of definition of the functions shown.

$$\rho_{A \cup B}^{T_B} = r_1 |10\rangle\langle 10| + r |00\rangle\langle 00| + r_3 |01\rangle\langle 01| + \sqrt{r_1 r_3} (|11\rangle\langle 00| + |00\rangle\langle 11|). \quad (5.54)$$

In matrix form we have

$$\rho_{A \cup B} = \left(\begin{array}{c|cccc} & 11 & 10 & 01 & 00 \\ \hline 11 & 0 & 0 & 0 & 0 \\ 10 & 0 & r_1 & \sqrt{r_1 r_3} & 0 \\ 01 & 0 & \sqrt{r_1 r_3} & r_3 & 0 \\ 00 & 0 & 0 & 0 & r \end{array} \right), \quad \rho_{A \cup B}^{T_B} = \left(\begin{array}{c|cccc} & 11 & 10 & 01 & 00 \\ \hline 11 & 0 & 0 & 0 & \sqrt{r_1 r_3} \\ 10 & 0 & r_1 & 0 & 0 \\ 01 & 0 & 0 & r_3 & 0 \\ 00 & \sqrt{r_1 r_3} & 0 & 0 & r \end{array} \right), \quad (5.55)$$

where the first row and first column refer to the states involved in (5.53)-(5.54). The eigenvalues of $\rho_{A \cup B}$ are:

$$\lambda_1 = 0, \quad \lambda_2 = 0, \quad \lambda_3 = 1 - r, \quad \lambda_4 = r, \quad (5.56)$$

and those of $\rho_{A \cup B}^{T_B}$

$$\lambda_1^t = r_1, \quad \lambda_2^t = r_3, \quad \lambda_3^t = \frac{r + \sqrt{r^2 + 4r_1 r_3}}{2}, \quad \lambda_4^t = \frac{r - \sqrt{r^2 + 4r_1 r_3}}{2}, \quad (5.57)$$

Note that in the latter case, the last eigenvalue is clearly negative. This means that, for a one-particle excitation we have:

$$S_n^1(r) = \frac{\log(r^n + (1-r)^n)}{1-n}, \quad (5.58)$$

which is what we expected, and

$$\mathcal{E}_n^1(r_1, r_3) = \log \left(r_1^n + r_3^n + \frac{(r + \sqrt{r^2 + 4r_1 r_3})^n}{2^n} + \frac{(r - \sqrt{r^2 + 4r_1 r_3})^n}{2^n} \right). \quad (5.59)$$

Note that, although (5.58) and (5.59) are in general rather different functions, it is easy to show that the polynomials inside the logarithm coincide for $n = 2$. Interestingly, for n integer, even or odd, there is no square-root dependence of the polynomial in (5.59) (the square-roots always cancel). Indeed, it can be equivalently written from the expression given in the previous Section 5.49 by setting $k = 1$:

$$\mathcal{E}_n^1(r_1, r_3) = \log \left(r_1^n + r_3^n + \sum_{p=0}^{\lfloor \frac{n}{2} \rfloor} \frac{n}{n-p} \binom{n-p}{p} r^{n-2p} r_1^p r_3^p \right), \quad (5.60)$$

where $\lfloor \cdot \rfloor$ denotes the integer part. However, the logarithmic negativity itself involves the square root in (5.59). From the eigenvalues above this gives

$$\mathcal{E}^1(r_1, r_3) = \log \left(\sum_{i=1}^4 |\lambda_i^t| \right) = \log \left(r_1 + r_3 + \sqrt{r^2 + 4r_1 r_3} \right), \quad (5.61)$$

As we can see in Fig. 5.2, there is a change of curvature when taking the limit $n \rightarrow 1$. This result gives a representative example of the non-trivial nature of the analytic continuation from n even to $n = 1$.

5.5 Replica negativity of two adjacent regions

An important observation arising from results (5.20) and (5.21) is that increments of both entropies and negativities are independent of the distance between the two subsystems A and B i.e. the parameter r_2 . The results (5.49) and (5.44) obtained by the qubit picture further confirm such a feature, suggesting that it is even more general. In fact we can think to approach the problem in a simpler way by considering the quantity (5.4) in the limit when $r_2 \rightarrow 0$. In this limit the two intermediate fields $\tilde{\mathcal{T}}(r_1 L) \tilde{\mathcal{T}}((r_1 + r_2)L)$ would sit at the same space position and consequently they produce a new field, with new scaling properties:

$$\tilde{\mathcal{T}}^2(r_1 L) := \lim_{r_2 \rightarrow 0} \tilde{\mathcal{T}}(r_1 L) \tilde{\mathcal{T}}((r_1 + r_2)L). \quad (5.62)$$

It is known that this field has very different properties depending on whether n is even or odd [13]. However, in order to compute the logarithmic negativity, only the even case is of interest. In this case the field $\tilde{\mathcal{T}}^2$ is a twist field implementing the replica permutation symmetry among evenly spaced copies of the theory. As seen at the end of Subsection 3.2.1, (where we first introduced the field above), it connects even-labelled and odd-labelled copies

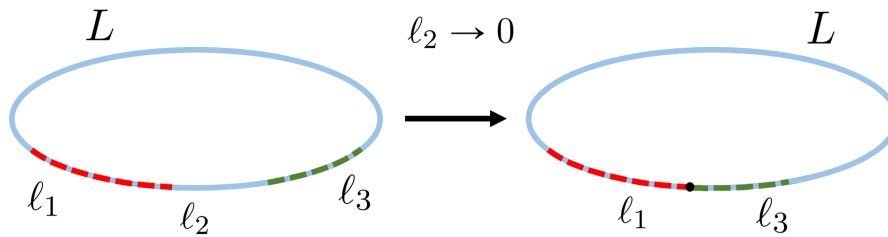


Figure 5.3 Procedure of connecting two regions in a ring.

within themselves, effectively acting as the action of two standard branch-point twist fields in an $n/2$ replica theory.

In the special limit (5.62), we can define the increment of logarithmic negativity as:

$$\Delta \mathcal{E}_n^\phi(r_1, r_3) = \lim_{L \rightarrow \infty} \log \left[\frac{L \langle \phi | \mathcal{T}(0) \tilde{\mathcal{T}}^2(r_1 L) \mathcal{T}((r_1 + r_3)L) | \phi \rangle_L}{L \langle 0 | \mathcal{T}(0) \tilde{\mathcal{T}}^2(r_1 L) \mathcal{T}((r_1 + r_3)L) | 0 \rangle_L} \right], \quad (5.63)$$

where we have implicitly considered the scaling limit (5.2). As pointed out in Chapter 3, if we reduce the distance between A and B to zero, and evaluate the Rényi entropy this would reproduce exactly the situation analysed in Chapter 4. For this reason we do not consider the Rényi entropy in such a setting.

5.5.1 $U(1)$ -field decomposition of the $\tilde{\mathcal{T}}^2$ -field

We assume n to be an even number. The fields \mathcal{T}^2 and $\tilde{\mathcal{T}}^2$ implement permutations symmetries over the exchange of copies $j \mapsto j \pm 2$ which form a subset of the $U(n)$ symmetry group, therefore the $U(1)$ -field basis diagonalise their action. We can employ the basis (4.31) once again to decompose the fields \mathcal{T}^2 and $\tilde{\mathcal{T}}^2$ in terms of $U(1)$ -fields. More precisely we need to consider $U(1)$ -fields $\mathcal{T}_{\lambda p}$ acting on sector p that satisfy the following exchange property with the fields $\tilde{\Phi}$:

$$\begin{aligned} \mathcal{T}_{\lambda p}(x) \tilde{\Phi}_q(y) &= e^{\frac{2\pi i \lambda}{n} \delta_{qp}} \tilde{\Phi}_q(y) \mathcal{T}_{\lambda p}(x) \quad \text{for } y^1 > x^1, \\ &= \tilde{\Phi}_q(y) \mathcal{T}_{\lambda p}(x) \quad \text{for } x^1 > y^1, \end{aligned} \quad (5.64)$$

$q, p = 1, \dots, n$. In terms of these fields, the fields \mathcal{T}^2 and $\tilde{\mathcal{T}}^2$ can both be diagonalized as follows

$$\mathcal{T}^2 = \prod_{p=1}^n \mathcal{T}_{2p} \quad \tilde{\mathcal{T}}^2 = \prod_{p=1}^n \mathcal{T}_{2(n-p)}. \quad (5.65)$$

For free bosons, the $U(1)$ fields $\mathcal{T}_{\lambda p}$ have scaling dimensions [105]:

$$\Delta_\lambda = \frac{\lambda}{2n} \left(1 - \frac{\lambda}{n} \right) \quad (5.66)$$

so that

$$\Delta_{\mathcal{T}^2} = 2 \sum_{p=1}^{\frac{n}{2}} \Delta_{2p} = \frac{1}{6} \left(\frac{n}{2} - \frac{2}{n} \right), \quad (5.67)$$

which reproduces the conformal weight (3.21) for $c = 2$ (the central charge of the complex free boson).

5.5.2 The three-point correlation function

As usual, the presence of branch cuts in finite volume replica models affects the quantization conditions of momenta associated to single-particle excitations, which consequently live in different Hilbert spaces $\mathcal{H}^{(\alpha)}$ defined by quasi-periodic boundary conditions of the fields $\Phi_j(x + L) = \Phi_{j+\alpha}(x)$. The branch-point twist fields connect the various sectors as in (5.9), and the \mathcal{T}^2 and $\tilde{\mathcal{T}}^2$ act accordingly as

$$\mathcal{T}^2 : \mathcal{H}^{(\alpha)} \rightarrow \mathcal{H}^{(\alpha+2)}, \quad \tilde{\mathcal{T}}^2 : \mathcal{H}^{(\alpha)} \rightarrow \mathcal{H}^{(\alpha-2)}. \quad (5.68)$$

As before we assume $|\mathbf{k}\rangle_L$ to be in the trivial section $\mathcal{H}^{(\alpha)}$. Thus combining the actions of the various fields we obtain

$${}_L \langle \mathbf{k} | \mathcal{T}(0) \tilde{\mathcal{T}}^2(x_1) \mathcal{T}(x_3) | \mathbf{k} \rangle_L = {}_L \langle \mathbf{k} | \mathcal{T}(0) \mathbb{1}^{(1)} \tilde{\mathcal{T}}^2(x_1) \mathbb{1}^{(-1)} \mathcal{T}(x_3) | \mathbf{k} \rangle_L. \quad (5.69)$$

Consider a single-particle state such as (5.13), the finite volume three-point function above can be expressed as:

$${}_L \langle \mathbf{1} | \mathcal{T}(0) \tilde{\mathcal{T}}^2(x_1) \mathcal{T}(x_3) | \mathbf{1} \rangle_L = \sum_{\{N^\pm\}} \sum_{\{\tilde{N}^\pm\}} [C_n(\{N^\pm\})]^* C_n(\{\tilde{N}^\pm\}) \prod_{p=1}^n \bar{\mathcal{F}}_p(N_p^\pm, \tilde{N}_p^\pm),$$

with sector contributions given by

$$\bar{\mathcal{F}}_p(N_p^\pm, \tilde{N}_p^\pm) = {}_{p;L} \langle \{I^0\}_{N_p^\pm} | \mathcal{T}_p(0) \mathbb{1}_p^{(1)} \mathcal{T}_{n-2p}(x_1) \mathbb{1}_p^{(-1)} \mathcal{T}_p(x_3) | \{I^0\}_{\tilde{N}_p^\pm} \rangle_{p;L}, \quad (5.70)$$

where $x_3 := r_1 + r_3$, and rapidities in the external state satisfy (5.14). The computational steps developed in appendix A can be easily extended to the case of the three-point function above.

Crucially, the intertwining action of the field \mathcal{T}_{n-2p} is such as to have intermediate states with rapidities only in $\mathcal{H}^{(1)}$ and $\mathcal{H}^{(-1)}$. This is structurally different from what we observe in the four-point functions (5.17) and (5.18). There, contractions among external states and intermediate states in $\mathcal{H}^{(0)}$ may lead to third order-pole residue, which are found to be dominant in the limit (5.2) and thus to contribute to the leading term of the expansion. This situation can be actually avoided in the case of the three-point function (5.70), where only first- and second-order pole residua can contribute. Despite the different origin of the dominant terms, the full computation (which will be presented in the work [27]) leads to the same result (A.30),

$$\lim_{L \rightarrow \infty} \frac{\tilde{\mathcal{F}}_p(N_p^\pm, N_p^\pm)}{p;L \langle \mathbf{0} | \mathcal{T}_p(0) \mathcal{T}_{n-2p}(x_1) \mathcal{T}_p(x_3) | \mathbf{0} \rangle_{p;L}} = \prod_{\epsilon=\pm} N_p^{\epsilon!} [\hat{g}_{\epsilon p}^n(r_1, r_3)]^{N_p^\epsilon}, \quad (5.71)$$

where $\hat{g}_{\epsilon p}^n(r_1, r_3)$ is defined in (5.22). Multi-particle state results follow directly from the arguments in Subsection 5.2.2. We thus conclude that also partitions arising from the limit of adjoint regions reproduce the qubit results.

5.6 Qubit picture for multiple regions

The results obtained in the previous sections have shown that, the qubit picture (so simple in its formulation) describes perfectly well the entanglement contributions of excited states in the massive free boson. The only underlying assumption is that, since single excitations are supposed to be de-localised within the volume, they have flat probability of being found anywhere in the volume L . Under this assumption, qubit states describe how these excitations distribute within the partitioned intervals and their simple properties crucially determine the excited state entanglement contributions.

We conclude this chapter by extending the qubit picture to an arbitrary number of disconnected regions. Indeed, as we will see in the following subsections (where we present the full computation by qubit states) we can prove that formulae (5.44) and (5.49) hold more generally for any connectivity.

5.6.1 Rényi entropies of multiple disconnected regions

Let us consider the case when one of our subsystems is composed of α disconnected regions R_m with $m = 1, \dots, \alpha$. Let R_0 be the rest of the system and $R' := \bigcup_m R_m$. Suppose that the entire bipartite system is composed by $R_0 \bigcup R'$, and that we are interested in the entanglement

entropy of a particular k -particle excited state. According to the qubit picture we can consider a bipartite Hilbert space $\mathcal{H} = \mathcal{H}_0 \otimes \mathcal{H}'$, and associate \mathcal{H}_0 to the exterior, and its complement \mathcal{H}' to the interior of the multiple-entanglement regions. Moreover the interior Hilbert space decomposes into α independent components $\mathcal{H}' = \mathcal{H}_1 \otimes \cdots \otimes \mathcal{H}_\alpha$.

In this setting the qubit states can be defined as follow: we define an orthonormal basis $\{|\underline{k}\rangle \in \mathcal{H} : \underline{k} = (k_0, \dots, k_\alpha) \in \mathbb{N}_0^{\alpha+1}\}$ such that k_m is the number of excitations in region R_m and $\sum_{m=1}^{\alpha} k_m = k$ for a state of k identical excitations. Let

$$r' = \sum_{m=1}^{\alpha} r_m = 1 - r_0 \quad (5.72)$$

where r_m is the scaled length of region R_m . We define the qubit state:

$$|\Psi_{\alpha, \text{qb}}^{(k)}\rangle = \sum_{\underline{k}=\{k_0, \dots, k_\alpha\} \in \sigma_0^{\alpha+1}(k)} \left[k! \prod_{\ell=0}^{\alpha} \frac{r_\ell^{k_\ell}}{k_\ell!} \right]^{1/2} \delta_{\sum_{i=0}^{\alpha} k_i, k} |\underline{k}\rangle, \quad (5.73)$$

where $\sigma_0^{\alpha+1}(k)$ represents the set of integer partitions of k into $\alpha + 1$ non-negative parts. It is easy to extend the definition (2.13) to the case of multiple disconnected regions. Indeed, if we now introduce $\mathcal{S}_n^k(r_1, \dots, r_\alpha) := \exp\left\{\{(1-n)S_n^{\Psi_{\alpha, \text{qb}}^{(k)}}(r_1, \dots, r_\alpha)\}\right\}$ where $S_n^{\Psi_{\alpha, \text{qb}}^{(k)}}(r_1, \dots, r_\alpha)$ is the n th Rényi entropy in the qubit state (5.73) it is easy to see that this can be written as:

$$\mathcal{S}_n^k(r_1, \dots, r_\alpha) = \sum_{\{k_p^j \in \mathbb{N}_0; j \in I_n; p \in I_\alpha^0\}} \prod_{i=1}^n k! \left(\prod_{\ell=0}^{\alpha} \frac{r_\ell^{k_\ell^i}}{k_\ell^i!} \right) \delta_{k_0^i + \sum_{m=1}^{\alpha} k_m^i, k} \delta_{k_0^{i+1} + \sum_{m=1}^{\alpha} k_m^{i+1}, k}, \quad (5.74)$$

where $I_n = \{1, \dots, n\}$ and $I_\alpha^0 = \{0, \dots, \alpha\}$. The delta-functions introduce the constraints

$$\sum_{m=1}^{\alpha} k_m^i + k_0^i = k \quad \text{and} \quad \sum_{m=1}^{\alpha} k_m^{i+1} + k_0^{i+1} = k, \quad \text{for } i = 1, \dots, n, \quad (5.75)$$

with the identifications $k_m^0 \equiv k_m^n$ and $k_m^1 \equiv k_m^{n+1}$. These constraints are equivalent to

$$\sum_{m=1}^{\alpha} k_m^i = \sum_{m=1}^{\alpha} k_m^{i+1} := \gamma, \quad (5.76)$$

where γ is an arbitrary constant. As a consequence

$$k_\alpha^i = \gamma - \sum_{m=1}^{\alpha-1} k_m^i \quad \text{and} \quad k_0^i = k - \gamma =: q \quad \text{for } i = 1, \dots, n. \quad (5.77)$$

As in the two region case k_0^i does not depend on any k_m^i s. Substituting (5.77) into (5.74) we have:

$$\mathcal{S}_n^k(r_1, \dots, r_\alpha) = \sum_{q \in \mathbb{Z}} \sum_{\{k_p^j \in \mathbb{N}_0; j \in I_n; p \in I_{\alpha-1}\}} \left[\binom{k}{q} r_0^q \right]^n \prod_{i=1}^n \left(\frac{(k-q)! r_\alpha^{k-q-\sum_{m=1}^{\alpha-1} k_m^i}}{(k-q-\sum_{m=1}^{\alpha-1} k_m^i)!} \prod_{m=1}^{\alpha-1} \frac{r_m^{k_m^i}}{(k_m^i)!} \right). \quad (5.78)$$

Again the multinomial coefficients constrain the sums. The presence of $q!$ in the denominator means that $q \geq 0$. We know also that k_m^i must be non-negative for all $i = 1, \dots, n$ and $m = 1, \dots, \alpha-1$. Furthermore the only non-zero terms in the sums are given by $k-q-\sum_{m=1}^{\alpha-1} k_m^i \geq 0$ and thus $q \leq k$. In summary, for the same reasons as in the two region case $0 \leq q \leq k$.

We can re-write (5.78) as:

$$\mathcal{S}_n^k(r_1, \dots, r_\alpha) = \sum_{q=0}^k \left[\binom{k}{q} \right]^n r_0^{nq} \prod_{i=1}^n \sum_{s_i=0}^{k-q} \sum_{\{k_1^i, \dots, k_{\alpha-1}^i\} \in \sigma_0^{\alpha-1}(s_i)} \left[\binom{k-q}{s_i} r_\alpha^{k-q-s_i} s_i! \prod_{m=1}^{\alpha-1} \frac{r_m^{k_m^i}}{(k_m^i)!} \right]. \quad (5.79)$$

It is easy to see that

$$\sum_{\{k_1^i, \dots, k_{\alpha-1}^i\} \in \sigma_0^{\alpha-1}(s_i)} s_i! \prod_{m=1}^{\alpha-1} \frac{r_m^{k_m^i}}{(k_m^i)!} = \left(\sum_{m=1}^{\alpha-1} r_m \right)^{s_i}, \quad \forall i = 1, \dots, n, \quad (5.80)$$

and thus (5.79) becomes:

$$\mathcal{S}_n^k(r_1, \dots, r_\alpha) = \sum_{q=0}^k \left[\binom{k}{q} \right]^n r_0^{nq} \prod_{i=1}^n \left[\sum_{s_i=1}^{k-q} \binom{k-q}{s_i} r_\alpha^{k-q-s_i} \left(\sum_{m=1}^{\alpha-1} r_m \right)^{s_i} \right]. \quad (5.81)$$

Furthermore we can notice that

$$\begin{aligned} \prod_{i=1}^n \left[\sum_{s_i=1}^{k-q} \binom{k-q}{s_i} r_\alpha^{k-q-s_i} \left(\sum_{m=1}^{\alpha-1} r_m \right)^{s_i} \right] &= \left[\sum_{s=0}^{k-q} \binom{k-q}{s} r_\alpha^{k-q-s} \left(\sum_{m=1}^{\alpha-1} r_m \right)^s \right]^n \\ &= \left[\left(\sum_{m=1}^{\alpha} r_m \right)^{k-q} \right]^n \\ &= (1-r_0)^{n(k-q)}, \end{aligned} \quad (5.82)$$

where in the last line we used (5.72). By recalling the Rényi entropy, we finally have:

$$S_n^{\Psi_{\alpha, \text{qb}}^{(k)}}(r_1, \dots, r_\alpha) =: S_n^{\Psi_{\text{qb}}^{(k)}}(r_0) = \frac{1}{1-n} \log \left(\sum_{q=0}^k \left[\binom{k}{q} r_0^q (1-r_0)^{k-q} \right]^n \right). \quad (5.83)$$

notice it takes the same form as (5.44) (with r replaced by r_0). Therefore, the Rényi (and

related) entropies of this particular class of qubit states depend only on the relative size of the two parts in the bipartition and not on whether or not they are connected.

5.6.2 Replica logarithmic negativities of disconnected regions

A very similar computation can be performed for the replica logarithmic negativities. The starting point is the assumption that regions A and B are now disconnected, namely

$$A = \bigcup_{i=1}^{\alpha} A_i \quad \text{and} \quad B = \bigcup_{i=1}^{\beta} B_i, \quad (5.84)$$

so that A consists of a number α and B of a number β of disconnected regions. Let regions A_i and B_i have scaled lengths given by r_1^i and r_3^i , respectively. Then our results for the (replica) logarithmic negativities will still hold up to the identifications:

$$r_1 = \sum_{i=1}^{\alpha} r_1^i, \quad r_3 = \sum_{i=1}^{\beta} r_3^i, \quad \text{and} \quad r = 1 - r_1 - r_3. \quad (5.85)$$

In the qubit picture this can be shown in a very similar way as for the Rényi entropies in the previous section, so we do not present the computation here.

ENTANGLEMENT INCREMENTS OF LOCALISED
EXCITATIONS

6.1 Summary of the main results in the free boson

In Chapters 4 and 5 we have studied the free boson theory in two different bipartitions, composed respectively of a single region or two (either connected or disconnected) regions. In this section we aim to summarise the main results obtained for both the entanglement entropies and the logarithmic negativities.

Let us consider two regions, say A and B , of lengths¹ ℓ_1 and ℓ_{-1} respectively. The region C corresponds to the rest of the system, specifically of length $\ell_0 = L - \ell_1 - \ell_{-1}$. Note a single-region bipartition such as the one analysed in Chapter 4 can be obtained by fixing one entanglement region's size (say ℓ_{-1}) to zero, in such a way to identify ℓ_1 with the length of the entanglement region, and ℓ_0 with the length of its complement. As usual we are interested in the scaling limit obtained by sending the regions' size and the volume L simultaneously to infinity while keeping their ratios finite in the process:

$$L \rightarrow \infty, \quad \ell_j \rightarrow \infty, \quad \text{fixed } r_j := \frac{\ell_j}{L}, \quad (6.1)$$

where $j = -1, 0, 1$ for two regions and $j = 0, 1$ for a single-region. We assume the system to

¹Note that we have changed a bit the notation employed in Chapter 5, where we have usually called the two regions' lengths ℓ_1 and ℓ_3 . This change is convenient to generalise the results for both partitions.

be in a zero-density state, namely a state composed of a finite number of excitations. The first interesting result is that the entanglement increments generated by $|\phi\rangle$ with respect to the ground state $|0\rangle$ depend on the ratios r_1, r_0, r_{-1} , only:

$$\lim_{L \rightarrow \infty} (S_n^\phi - S_n^0)(r_0 L) = \Delta S_n^\phi(r_0), \quad \lim_{L \rightarrow \infty} (\mathcal{E}_n^\phi - \mathcal{E}_n^0)(r_1 L, r_0 L, r_{-1} L) = \Delta \mathcal{E}_n^\phi(r_1, r_0, r_{-1}). \quad (6.2)$$

In particular, the entropy increment for a single particle excitation is:

$$\Delta S_n^1(r_0) = \frac{\log(r_0^n + (1 - r_0)^n)}{1 - n}, \quad (6.3)$$

whereas the increment of von Neumann entropies generated by the same state is given by

$$\Delta S_1^1(r_0) = -r_0 \log r_0 - (1 - r_0) \log(1 - r_0). \quad (6.4)$$

Therefore the functional forms are the same for both single region (i.e. $r_0 = 1 - r_1$) and double regions (i.e. $r_0 = 1 - r_1 - r_{-1}$). The same holds for multiparticle states. Indeed when considering states formed of many excitations, the entanglement entropies increase in a way that depends only on two factors: the (in)distinguishability of the excitations (if they have identical or distinct momenta), and the size of the regions A and B relative to that of the whole system. For a state composed of k distinct particles (distinct momenta), the entropy increments is just k times the single-particle ones. More interesting are the entropy increments of a k -particle excitations with identical momenta:

$$\Delta S_n^k(r_0) = \frac{1}{1 - n} \log \sum_{q=0}^k \left[\binom{k}{q} r_0^q (1 - r_0)^{k-q} \right]^n, \quad (6.5)$$

$$\Delta S_1^k(r_0) = - \sum_{q=0}^k \binom{k}{q} r_0^q (1 - r_0)^{k-q} \log \left[\binom{k}{q} r_0^q (1 - r_0)^{k-q} \right]. \quad (6.6)$$

Remarkably all the entropy increments do *not depend on the connectivity of the regions* and are functions of r_0 only. The replica logarithmic negativity is found to be a function of r_1, r_{-1} , where each parameter now enters independently. For a state consisting of a single particle excitation the increment of the replica logarithmic negativity is given by the simple expression:

$$\Delta \mathcal{E}_n^1(r_1, r_{-1}) = \log \left(r_1^n + r_{-1}^n + \sum_{p=0}^{\lfloor \frac{n}{2} \rfloor} \frac{n}{n-p} \binom{n-p}{p} r_0^{n-2p} r_1^p r_{-1}^p \right), \quad (6.7)$$

where $\lfloor . \rfloor$ denotes the integer part. Note that for a single region (i.e. $r_0 = 1 - r_1$), the result

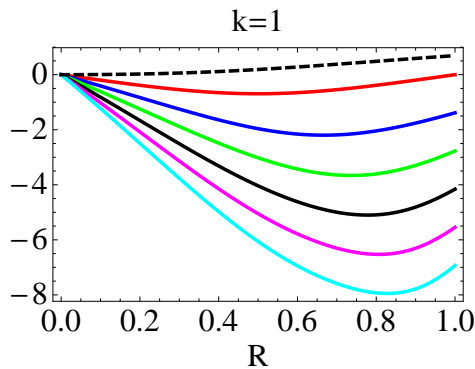


Figure 6.1 The functions (6.7) for $n = 2, 4, 6, 8, 10$ and 12 (solid lines) and the function (6.9) (dashed line). In all cases we consider $r_1 = r_{-1} = \frac{R}{2}$. The replica logarithmic negativities take more negative values for larger values of n . This figure illustrates the gradual change in curvature as $n \rightarrow 1$.

(6.7) trivially reproduces the Rényi entropy increments therefore below we focus only on two regions $r_0 = 1 - r_1 - r_{-1}$. The increment of the logarithmic negativity can be obtained by analytically continuing this expression from n even to $n = 1$. Evaluation of the sum above for $n = 2m$ and $m \in \mathbb{N}$ gives

$$\Delta \mathcal{E}_{2m}^1(r_1, r_{-1}) = \log \left(r_1^{2m} + r_{-1}^{2m} + \left(\frac{\sqrt{r_0^2 + 4r_1 r_{-1}} + r_0}{2} \right)^{2m} + \left(\frac{\sqrt{r_0^2 + 4r_1 r_{-1}} - r_0}{2} \right)^{2m} \right). \quad (6.8)$$

so that the analytic continuation is simply,

$$\Delta \mathcal{E}^1(r_1, r_{-1}) := \lim_{m \rightarrow \frac{1}{2}} \Delta \mathcal{E}_{2m}^1(r_1, r_{-1}) = \log \left(r_1 + r_{-1} + \sqrt{r_0^2 + 4r_1 r_{-1}} \right). \quad (6.9)$$

Note that the functions (6.9) gives a nice simple illustration of the non-trivial nature of the analytic continuation from n even to $n = 1$. This can be better understood by looking at Fig. 6.1.

For a state consisting of k distinct excitations (particles with distinct momenta), the result is simply k times the above, just as for the Rényi entropies. The case of identical excitations (identical momenta) is more interesting. Consider an excited state of k identical excitations. The increment of the replica logarithmic negativity is given by:

$$\Delta \mathcal{E}_n^k(r_1, r_{-1}) = \log \left(\sum_{p=-k}^k \sum_{q=\max(0, -np)}^{\lfloor \frac{n}{2}(k-p) \rfloor} \mathcal{A}_{p,q} r_1^{np+q} r_0^{n(k-p)-2q} r_{-1}^q \right), \quad (6.10)$$

where the coefficients $\mathcal{A}_{p,q}$ are defined as follows:

$$\mathcal{A}_{p,q} = \sum_{\{k_1, \dots, k_n\} \in \sigma_0^n(q)} \prod_{j=1}^n \frac{k!}{(p+k_j)!(k-p-k_{j+1}-k_j)!k_{j+1}!}, \quad (6.11)$$

and $\sigma_0^n(q)$ represents the set of integer partitions of q into n non-negative parts. Note that the coefficients are zero whenever any of the arguments of the factorials in the denominator becomes negative and this selects out the partitions that contribute to each coefficient for given values of p and q . As should be, formula (6.7) is the $k = 1$ case of (6.10). Indeed the coefficients inside the sum (6.7) are nothing but the number of partitions of p into n parts, p of which are 1 and $n - p$ of which are 0, with the constraint that there are no consecutive 1s.

Since the coefficients $\mathcal{A}_{p,q}$ are rather non-trivial, it is not easy to perform the sums in (6.10) explicitly and the analytic continuation leading to the logarithmic negativity is rather involved. Nevertheless, consider few excitations, we can explicitly compute the eigenvalues of the partially transposed reduced density matrix obtained from the qubit interpretation. An example for a single-particle excitation is provided in Subsection 5.4.1, and additional closed formula for $k = 2, 3$ have been presented [26].

The qubit interpretation (introduced in Section 4.8 and extended in Section 5.3 to two regions) is based on the simple observation that the entanglement contributions above equate those of a much simpler states:

$$\Delta S_n^k(r_0) = S_n^{\Psi_{\text{qb}}^{(k)}}(r_0), \quad \Delta \mathcal{E}_n^k(r_1, r_{-1}) = \mathcal{E}_n^{\Psi_{\text{qb}}^{(k)}}(r_1, r_{-1}), \quad \Delta \mathcal{E}^k(r_1, r_{-1}) = \mathcal{E}^{\Psi_{\text{qb}}^{(k)}}(r_1, r_{-1}), \quad (6.12)$$

for any k and n . The state $|\Psi_{\text{qb}}^{(k)}\rangle$ lives in a bipartite Hilbert space of which one part is associated to the interior and the other one to the exterior of the entanglement regions A and B . More precisely, it is formed of k qubits and takes the following form :

$$|\Psi_{\text{qb}}^{(k)}\rangle = \sum_{k_1 k_0 k_{-1}} \sqrt{\frac{k! r_1^{k_1} r_0^{k_0} r_{-1}^{k_{-1}}}{k_1! k_0! k_{-1}!}} \delta_{k_1+k_0+k_{-1}, k} |k_1, k_0, k_{-1}\rangle \quad (6.13)$$

Each state $|k_1 k_0 k_{-1}\rangle$ is interpreted as describing a specific occupancy configuration that is k_1 excitations in region A , k_{-1} excitations in region B and k_0 excitations in the rest of the system. For a single region we assume $k_{-1} = 0$. The square of the corresponding coefficient is the associated probability that this configuration occurs if we were to place randomly and independently, with uniform distribution, k particles on the interval $[0, 1]$ covered by three

non-intersecting subintervals of lengths r_1, r_0 and r_{-1} .

Under the qubit interpretation all the entanglement increments in (6.12) are independent of the connectivity of the two regions, and as seen in 5.6, the same conclusion can be even drawn for a system consisting of any number of disconnected regions. In Section 5.5 we have also used the branch-point twist field approach to explore specifically the case of two connected regions, and obtained exactly the same results above.

Furthermore, the expression (6.10) with (6.11) suggests a combinatorial interpretation for the polynomials in the logarithmics, and such interpretation is made more concrete in Appendix B, based on a graph approach introduced in [28].

Finally we expect the state $|\phi\rangle$ to be more generally a mixed excited state consisting of k_i particles of identical momentum p_i with $i = 1, \dots, m$ and $p_i \neq p_j$ for $i \neq j$. For such a state we have that the Rényi entropies and the (replica) logarithmic negativities can be expressed in terms of the building blocks given above, namely:

$$\Delta S_n^{k_1, \dots, k_m}(r_0) = \sum_{q=1}^m \Delta S_n^{k_q}(r_0), \quad (6.14)$$

$$\Delta \mathcal{E}_n^{k_1, \dots, k_m}(r_1, r_{-1}) = \sum_{q=1}^m \Delta \mathcal{E}_n^{k_q}(r_1, r_{-1}). \quad (6.15)$$

6.2 Generalisations and extensions

According to the qubit interpretation, the entanglement increments due to particle excitations depend on very few features of the state, namely the ratios r_i s associated to each region ℓ_i of the partition, the number of quasiparticles and the statistics of the excitations (if they have equal or distinct momenta). Since these are quite general features, one may reasonably wonder if our results may hold much more generally. There is indeed both analytical and numerical evidence suggesting that the results presented in Section 6.1 are universal. To conclude part I of this thesis we want to give a flavour of the diverse contexts in which (under appropriate conditions) the qubit picture can be exploited to predict the entanglement contributions of zero-density states:

- **The massive free fermion:** In [24] the excited state entanglement entropies of a single region have been studied also in the free fermion theory. Indeed the techniques discussed in Chapter 4 can be easily extended to the massive free fermion, having even a simpler application as fermionic states are formed of only distinct particles. Taking into account

the different statistics of the states, the entanglement contributions of multiple-particle excitations exactly reproduce formulae (6.3), (6.4) for single particles, and (6.14) for multiple particles in the scaling limit (6.1).

- **The harmonic chain:** In [24, 26] the (free boson) formulae (6.3)-(6.15) have been numerically checked in the harmonic chain by implementing the wave functional method². The harmonic chain is indeed a discrete theory whose continuum limit reproduces the massive free boson. The dispersion relation for a single-particle excitation is

$$E(p) = \sqrt{m^2 + 4\Delta x^{-2} \sin^2 \frac{\Delta x p}{2}}, \quad (6.16)$$

where Δx is the lattice spacing, m is the mass and p is the momentum of the excitation. Numerical results are expected to reproduce the free-boson results where $\Delta x \cdot p \ll 1$, and the relativistic dispersion relation is recovered in (6.16). In this regime both the entropy and replica logarithmic negativity increments (in their simple formulations given by the qubit pictures (6.12)) have shown perfect agreement with the numerical outcomes in both the single- and double- region cases. Remarkably all entanglement increments are found to be correct even in a regime of parameters that goes beyond the universal scaling regime of QFT (some figures are shown in the end of the chapter). This includes large momenta regions, beyond the low-energy QFT regime, and holds independently of the value of the lattice spacing Δx . The domain of applicability of the free-boson results is characterized by the condition [23]:

$$\min \left(m^{-1}, \frac{2\pi}{P} \right) \ll \ell_{\min}, \quad (6.17)$$

where P is the largest momentum of any of the excitations in the state and $2\pi/P$ can be interpreted as the De Broglie wave length associated to that particular excitation, and $\xi = m^{-1}$ is the system's correlation length. The length ℓ_{\min} is the smallest region's size in the partition considered, precisely $\min(\ell_{-1}, \ell_0, \ell_1)$ for doubled regions and $\min(\ell_0, \ell_1)$ for single regions. Some examples are displayed in Fig. 6.2 for two regions, and Fig. 6.3 (left) for one region. Crucially, the validity regime (6.17) suggests that the entanglement contributions of excitations reproduce the simple formulae (6.12) *as long as the excitations*

²This numerical procedure is based on constructing the exact wave functional for the ground state of the chain in the fundamental-field basis, and the exact branch-point twist operator acting on this basis. It reduces the problem to a multi-dimensional Gaussian integral. For the entanglement increment, a ratio of the reduced density matrices of the excited and ground states, the result takes the form of a multi-point function of Gaussian variables associated to the particles in the excited state, which is evaluated by Wick's theorem in terms of the inverse of the corresponding Gaussian kernel. More detail on the equations implemented can be found in Appendix A of [24].

may be localised within the entanglement regions i.e. the wave lengths of the excitations are much smaller than the regions' lengths. It is indeed in this particular regime that we can make sense of the probabilistic interpretation provided by the qubit picture.

- **Free bosons in higher dimensions:** The entanglement increments (6.12) can be explored also in higher dimensions. In [23] the wave functional method has been used to study numerically the increments of entanglement entropies in a two-dimensional harmonic lattice on $[0, L]^2$. The numerical outcomes perfectly reproduce formulae (6.3) and (6.4) where now the r_i s are interpreted as ratios of regions' volumes and total system's volume $r_i = v_i/V$ (an example is shown in the right picture of Fig. 6.3). This suggests that the qubit picture may be applicable to higher dimensional systems. For the massive boson theory this can be even proven analytically [28]. Of course this first requires the extension of the notion of twist fields, now acting on multi-dimensional boundary regions, to higher dimensions. The proof is based on the combined application of exchange relations of higher-dimensional branch-point twist operators, clustering properties (i.e. factorization of correlators at large volume) and Wick's theorem. Indeed the graph partition functions and all the graph rules discussed in Appendix B can be derived in this context in terms of Wick contractions in an appropriate Fock space representation of qubit states. Finally the generalisation to multiple regions seen in Section 5.6 ensures that even in higher dimensions the excited state entanglement contributions are independent of the connectivity of the regions involved in the bipartition.

- **Interacting models:** In [23] the entanglement increments have been also analysed in interacting magnonic states. Previous analyses exist [103, 104], which however concentrated on less universal regimes. In the ferromagnetic Heisenberg chain, two-particle states with respect to the ferromagnetic vacuum have the simple form

$$\sum_{x,y \in \mathbb{Z}} e^{ipx+iqy} S_{\text{sgn}(x-y)}(p, q) | \uparrow \cdots \downarrow_x \cdots \uparrow \cdots \downarrow_y \cdots \uparrow \rangle, \quad (6.18)$$

where $S_\epsilon(p, q)$ is the scattering matrix. More generally, for the purpose of evaluating large-distance quantities these are abstract states representing two-particle asymptotic states, with $S_\epsilon(p, q)$ the two-body scattering matrix of the field theory (via the TBA formalism of integrable QFT [29, 30]). Consider a single entanglement regions of length ℓ_0 , explicit computations for entanglement entropy increments of one- and two-particle

states such as (6.18) (of equal or distinct momenta) lead to formulae (6.3), (6.14) and (6.5) (see Supplementary Material in [23] for more detail). There is no need to fix the momenta via the Bethe ansatz, therefore these results hold for any states of the form (6.18). Bound states of the Heisenberg chains (Bethe strings) have been studied in [104]; these have an intrinsic length scale ξ (inversely proportional to the bounding energy), and one can see that in the regime (6.17) and scaling limit (6.1) their entropy contributions are given by (6.3), suggesting that once more that our results are rather generic and also valid in interacting theories.

In summary, the entanglement increments associated with zero-density excited states in the scaling limit discussed here, takes a universal form that we expect to hold for a wide variety of theories, from interacting QFT models, to higher-dimensional theories and spin chain models. At the heart of this universality lies the basic assumption of locality, that is, the assumption that excitations are localized, either because the correlation length is finite and much smaller than the entanglement regions or because particles have a small De Broille wave length. Once locality is present, the particular scaling limit taken here, leads to a theory where the few excitations above the ground state form a zero-density set, that is, in effect behave as non-interacting degrees of freedom, whose only defining property is their location within a particular entanglement regions, and the corresponding probabilistic occupancy distribution of such excitations into the partition considered. In this sense, the qubit picture, although it is a naive non-interacting model, provides a natural way to display such a simple locality property, and we expect that interaction and dimensionality are unimportant in this context. In contrast they will inevitably matter if we consider finite-volume corrections and also if we do not subtract the ground state contribution.

Finally, it is worth mentioning that, very recently, generalizations of our results have been published in [108–113]. These works have demonstrated the presence of non-universal finite-volume corrections as well as finding precise examples (e.g. XY chains) where our universal formulae cease to apply. These are cases where the assumption of locality is no longer holds. They demonstrate that, as we have argued here, locality of excitations is an essential property of all theories where our results apply.

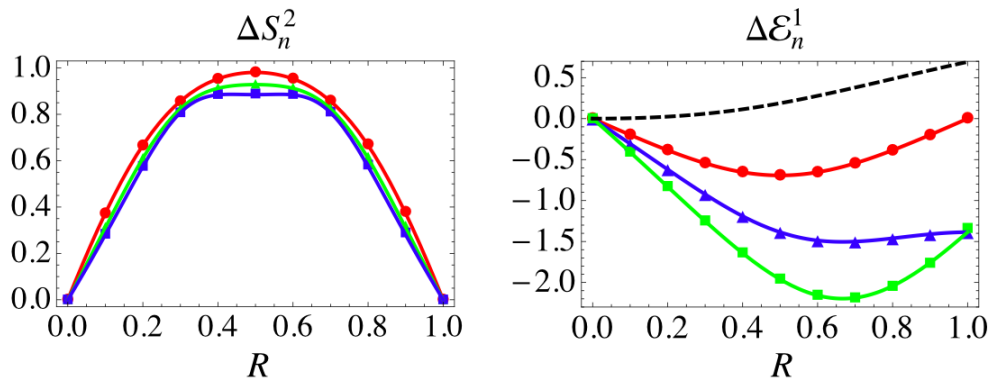


Figure 6.2 Numerical results for the harmonic chain in two disconnected regions. In both pictures the parameters are chosen as $\Delta x = 0.02$, $L = 20$ and $m = 1$, and the results are displayed in the cross-section $r_1 = r_{-1} = R/2$. The symbols are numerical data and the solid curves are obtained from the formula. Left: numerical outcomes for the increment of the 2nd (red circles), 3rd (green triangles) and 4th (blue squares) Rényi entropies for a state of two identical excitations with momenta for $p_1 = p_2 = 4\pi$. The solid lines are given by formula (6.5) for $n = 2, 3, 4$. Right: Results for $k = 1$ and $p = 4\pi$ with $n = 2$ (red circles), $n = 3$ (blue triangles), and $n = 4$ (green squares). The dashed curve is the logarithmic negativity (6.9), showing once again the gradual change in curvature as $n \rightarrow 1$. The colorful lines are obtained from (6.7) for $n = 2, 3, 4$.

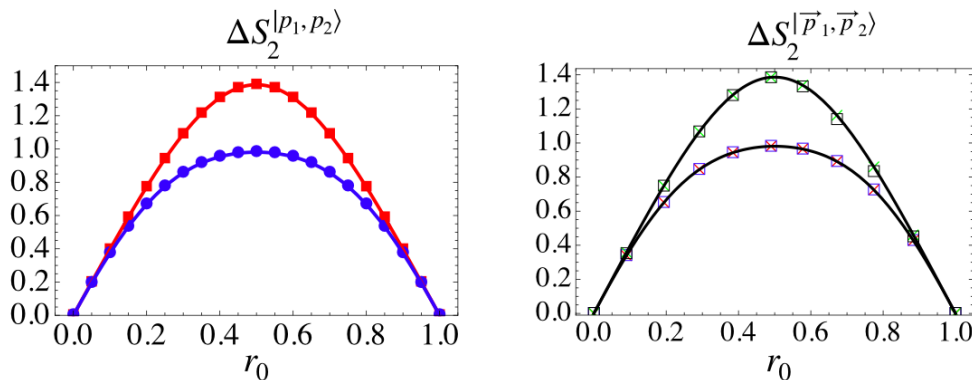


Figure 6.3 Comparison between analytic results (continuous curves) and numerical values (markers) of the 2nd Rényi entropies for two-particle states in two models: the harmonic chain (left) and the two-dimensional harmonic lattice (right). In both cases the entropies are evaluated in a single regions, and the solid line are given by (6.3) and (6.14) for $n = 2$. Although the excitations considered in the two cases are of very different momenta and masses, and defined in two different spacial dimensions, the numerical results reproduce the same functions $\Delta S_2^{1,1}$ and ΔS_2^2 in both pictures. Left: we show the 2nd Rényi entropy increments with distinct momenta given by $p_1 \approx 30$, $p_2 \approx 45$ (squares, red curve) and with equal momenta $p_1 = p_2 \approx 50$ (dots, blue curve). The other numerical parameters are $m = 1$, $L = 10$, $\Delta x = 0.01$. Right: we fix $L = 50$ and $\Delta x = 1$, and explore the 2nd Rényi entropy increments for mass $m = 1$ and small momenta (squares), and for mass $m = 0.001$ and large momenta (crosses), both cases satisfying condition (6.17). Numerical results for distinct momenta $\vec{p}_1 = (0, 0)$, $\vec{p}_2 = (0.26, 0) = (4\pi/L, 0)$ (squares) and $\vec{p}_1 = (2.51, 1.26) = (40\pi/L, 20\pi/L)$, $\vec{p}_2 = (3.14, 0) = (50\pi/L, 0)$ (crosses) perfectly agree with the upper curve, whereas those for equal momenta $\vec{p}_1 = \vec{p}_2 = (0.13, 0) = (2\pi/L, 0)$ (squares) and $\vec{p}_1 = \vec{p}_2 = (2.51, 1.26)$ (crosses) are in great agreement with the lower curve.

PART II : GENERALISED HYDRODYNAMICS OF UNSTABLE
EXCITATIONS

GENERALISED HYDRODYNAMICS OF UNSTABLE EXCITATIONS

7.1 The model

In part II of this thesis we are going to explore the dynamics of unstable excitations in integrable models. Remarkably the severe constraints imposed by the infinite-many local conserved charges, in combination with the low dimensions of the theory, do not forbid the formation of unstable particles. Unlike stable bound states, which are notoriously a common feature of most interacting integrable QFTs, unstable bound states are a rare occurrence. The largest family of relativistic field theories known to possess both integrability and unstable particles are the homogeneous sine-Gordon (HSG) models. Despite their name, they have little in common with the sine-Gordon model. In particular, their scattering matrices are diagonal.

The homogeneous sine-Gordon models can be seen as massive perturbations of a critical Wess-Zumino-Novikov-Witten model [114–118] associated to cosets $G_k/U(1)^{r_g}$ where G is some simply-laced algebra, k is the level (an integer), and r_g is the rank of G . They have been extensively studied in a series of papers in the late 90s, where their classical and quantum integrability were established [19, 20], their particle spectrum determined [21], and an exact scattering matrix eventually proposed [22]. The scattering matrix was then tested extensively by employing the TBA [29, 30] and the form factor approach [84, 85]. The TBA of these

models was studied in detail in [31, 45, 119], while the form factors of local operators were constructed in [120, 121]. The effect of the presence of unstable particles in the renormalisation group flow (RG-flow) of several quantities was also explored using form factor techniques in [122, 123]. More recently, the mass-coupling relation was determined [124, 125]. Furthermore, the HSG models can be seen as particular cases of a larger family of theories, associated to two simply-laced Lie algebras g and \tilde{g} and known as $g|\tilde{g}$ -theories, for which the scattering matrix is provided in [126].

In this part of the thesis, we focus on the simplest theory of the family which is the $SU(3)_2$ -homogeneous sine-Gordon model. Its asymptotic spectrum consists of two stable self-conjugate particles of equal masses. Label these stable particles \pm , the S-matrix of the theory has the following simple form

$$S_{\pm\pm}(\theta) = -1, \quad S_{\pm\mp}(\theta) = \pm \tanh \frac{1}{2} \left(\theta \pm \sigma - \frac{i\pi}{2} \right), \quad (7.1)$$

where σ is a free parameter. Hence, the interaction involves only particles of different species, and the S-matrix reveals some interesting features of the theory, one of this is the parity breaking

$$S_{+-}(\theta) = S_{-+}(-\theta) \neq S_{-+}(\theta). \quad (7.2)$$

In addition we have that

$$\lim_{|\sigma| \rightarrow \infty} S_{\pm\mp}(\theta) = 1, \quad (7.3)$$

which means that in this limit parity symmetry is restored and the theory may be seen as two independent, mutually commuting free Majorana fermions. For finite σ , the theory is interacting and the scattering amplitudes $S_{\pm\mp}(\theta)$ have a pole outside the physical sheet at $\theta = \mp\sigma - \frac{i\pi}{2}$, in the strip $-\pi \leq \text{Im}(\theta) \leq 0$. According to Subsection 1.2.2, this pole is associated to an unstable bound state of the otherwise two free Majorana fermion species. As discussed in [122] from the Breit-Wigner formula it follows that, for this particular S-matrix,

$$M^2 = m^2(1 + \cosh \sigma) \quad \text{and} \quad \Gamma^2 = 4m^2(-1 + \cosh \sigma), \quad (7.4)$$

where M is the mass of the unstable particle and Γ its decay width. In this thesis, we will mostly focus on the regime $|\sigma| \gg 0$, where we have that

$$M \sim \frac{1}{\sqrt{2}} m e^{\frac{|\sigma|}{2}} \quad \text{and} \quad \Gamma \sim \sqrt{2} m e^{\frac{|\sigma|}{2}}. \quad (7.5)$$

Thus, the larger $|\sigma|$ is, the more massive and short-lived the unstable excitation becomes. For $|\sigma|$ large, one would then expect a clear separation of energy scales. That is at small temperatures compared to the scale set by the mass M and decay width Γ , the physics is dominated by the two free fermions as unstable bound states decay quickly. In contrast, at large temperatures with respect to this scale, there is enough energy for a finite proportion of particles to be found within bound states, which re-populate fast enough. At large temperatures, the unstable particle has nontrivial, large-scale effects. The goal of part II is to obtain a clearer, dynamical picture of these effects, and to identify the unstable particle in a more physically clear fashion that goes beyond the pole structure of the S-matrix. The study of the TBA of the $SU(3)_2$ -HSG model, in the next section, provides an important step in this direction.

Without loss of generality, we choose

$$\sigma > 0 \tag{7.6}$$

for the remainder of this thesis.

7.2 The thermodynamic Bethe ansatz equations

The starting point of the TBA approach is provided by some equations that we have introduced in Section 3.3.2 in a quite different context: the Bethe-Yang equations. these equations are simply the outcomes of dragging particles \pm along the world line¹. For the $SU(3)_2$ -HSG model [31] we have:

$$e^{iLm \sinh \theta^\pm} S_{\pm\mp}(\theta^\pm - \theta^\mp) = 1. \tag{7.7}$$

where θ^\pm are the rapidity associated to particles \pm . The logarithm of the equation above (times $-i$) gives:

$$Lm \sinh \theta^\pm - i \log S_{\pm\mp}(\theta^\pm - \theta^\mp) = 2\pi J^\pm. \tag{7.8}$$

where $-i \log S_{\pm\mp}$ are scattering phases and J^\pm are integers. For a given set of quantum numbers $\{J_i^\pm\}_{N^\pm}$ there will be a set of Bethe-Yang solutions $\{\theta_i^\pm\}_{N^\pm}$, these are usually called *roots*. There

¹The reader may note that such condition is less trivial for HSG-models with richer particle spectra. Due to the parity violation it actually matters if the particles are moved clockwise or anticlockwise along the world line and this leads to two different quantization conditions. In the case of the $SU(3)_2$ -HSG model, since there are only two particles there is actually no difference between the two choices and we accordingly implement only one quantization condition.

might be also quantum numbers not allowed for the system. Solutions of the equation above obtained with these quantum numbers are usually called *holes*. The TBA equations are obtained from (7.8) in the thermodynamic limit, i.e. when $L \rightarrow \infty$, $N^\pm \rightarrow \infty$ with N^\pm/L kept fixed [29, 30]. In this limit we can introduce the following quantities: the *densities of states* $\rho_s(\theta; \pm)$ and the *quasiparticle densities* or *spectral densities* $\rho_p(\theta; \pm)$, i.e. the density of states filled by the quasiparticles in the rapidity interval $[\theta, \theta + d\theta]$. We can then define the *quasiparticle occupation numbers*:

$$n(\theta; \pm) := \rho_p(\theta; \pm) / \rho_s(\theta; \pm), \quad (7.9)$$

which are related to the *pseudoenergies* through the equation:

$$n(\theta; \pm) = \frac{1}{1 + e^{\varepsilon(\theta; \pm)}}. \quad (7.10)$$

The TBA equations can be expressed as non-linear integral equations for the pseudoenergies:

$$\varepsilon^\pm(\theta; \pm) = w(\theta) - \varphi_{\pm\mp} \star L(\theta; \mp), \quad (7.11)$$

Below, we explain all the ingredients of the equation above. The quantity $w(\theta)$ is called TBA driving term and is an intrinsic way of fixing the macroscopic state. Indeed it determines the weight of the states in the ensemble, it is such that every state formed of rapidities $\{\theta_i\}$ has weight $\exp[-\sum_i w(\theta_i)]$. In the case above, since we are at equilibrium, we have implicitly considered a thermal state²:

$$w(\theta) = m\beta \cosh \theta, \quad (7.12)$$

where the parameter β is the inverse of the temperature T . The interaction enters in the kernels $\varphi_{\pm\mp}(\theta)$, which are formally defined as the rapidity derivatives of the scattering phases (times -1). In our theory they are simply:

$$\varphi_{\pm\mp}(\theta) := -i \frac{d}{d\theta} \log S_{\pm\mp}(\theta) = \frac{1}{\cosh(\theta \pm \sigma)}. \quad (7.13)$$

The integral part of the equation is incorporated in the convolution, which is denoted by \star on the right hand side of the same equation. We define the convolution as:

$$a \star b(\theta) := \frac{1}{2\pi} \int_{-\infty}^{\infty} a(\theta - \theta') b(\theta') d\theta', \quad (7.14)$$

²For the theory and the set-ups considered in this thesis, the TBA driving term is the same for both particles \pm , and for this reason, we have omitted the particle species in their arguments.

the L-functions depend on the pseudoenergies and implement the non-linearity of the equation

$$L(\theta; \pm) = \ln\left(1 + e^{-\varepsilon^\pm(\theta; \pm)}\right). \quad (7.15)$$

Note that when the two particles \pm behave as free Majorana fermions $\varphi_{\pm\mp} \approx 0$ the TBA equation is $\varepsilon(\theta; \pm) = \beta m \cosh \theta$ where $m \cosh \theta$ is simply the single-particle energy eigenvalue. For interacting regimes, the TBA equations (7.11) can be solved analytically only at very high temperature, where it is possible to implement the so-called constant TBA (see e.g. [31] for a treatment in the present model). For this reason, we need to investigate the equations above numerically. Indeed there exists a standard recursive procedure to solve numerically TBA equations, of which the state (via the TBA driving term), and the theory (via the kernel) provide the only inputs. This numerical procedure typically shows fast convergence to the numerical solutions (after very few iterations). For the $SU(3)_2$ -HSG model, we provide a numerical recipe in Appendix C.

Thus the TBA solutions can be explored numerically as functions of the temperature T (or analogously of $\beta = 1/T$) and of the parameter σ , and the TBA quantities introduced above can be accordingly expressed as functions of these parameters once the pseudoenergies have been computed. Furthermore, an important observation is that the equations (7.11) can be mapped into

$$\phi(\theta; \pm) = \beta m \cosh\left(\theta \mp \frac{\sigma}{2}\right) - (\varphi \star K)(\theta; \mp) \quad \text{with} \quad \varphi(\theta) := \operatorname{sech} \theta. \quad (7.16)$$

for the shifted functions

$$\phi(\theta; \pm) := \varepsilon^\pm\left(\theta \mp \frac{\sigma}{2}\right) \quad \text{and} \quad K^\pm(\theta) = \log(1 + e^{-\phi(\theta; \pm)}). \quad (7.17)$$

Note that under this shift and a change of variables in the convolution integral, the σ -dependence of the TBA kernel is eliminated so that it is now only explicit in the TBA driving term.

Then, if σ or θ are large and positive we can approximate

$$\phi(\theta; \pm) = e^{\mp\theta - \kappa} - (\varphi \star K)(\theta; \mp) \quad (7.18)$$

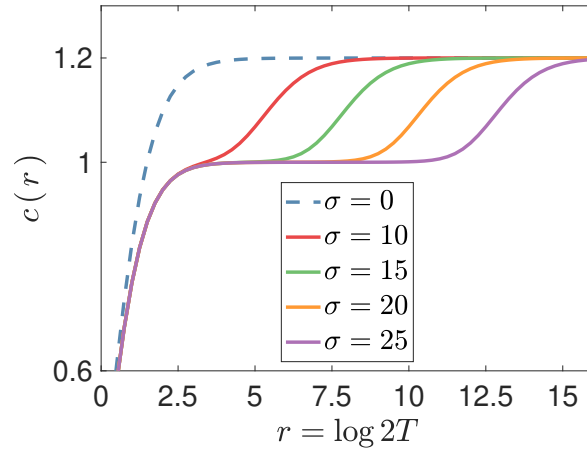


Figure 7.1 TBA scaling function of the $SU(3)_2$ -HSG model for various σ . The mass is $m = 1$ in all cases.

where

$$\kappa = \log(2T) - \frac{\sigma}{2}. \quad (7.19)$$

This shows that for σ large enough, the TBA equations and their solutions are function of the parameter κ and rapidity only. Interestingly the variable κ gives an indication on energy scale of the system (in the variable $\log(2T)$), in particular we have that

$$T \gtrsim M \quad \iff \quad \kappa \gtrsim 0 \quad \text{Interacting Regime} \quad (7.20)$$

$$T \sim M \quad \iff \quad \kappa \sim 0 \quad \text{Formation of the unstable particle} \quad (7.21)$$

$$T \lesssim M \quad \iff \quad \kappa \lesssim 0 \quad \text{Non-interacting Regime} \quad (7.22)$$

where M is the mass of the unstable excitation defined previously.

7.2.1 The TBA scaling function

The three regimes (7.20), (7.21), and (7.22) can be better understood by analysing the TBA scaling function, formally defined as:

$$c(T) = \frac{3m}{\pi^2 T} \int_{-\infty}^{\infty} d\theta \cosh \theta (L(\theta; +) + L(\theta; -)). \quad (7.23)$$

A natural way to plot this function is against $r = \log 2T$ (or similarly $-\log \beta/2$) as this variable gives information on the energetic regime of the theory according to the definition (7.19) and the regimes identified earlier. Numerical results for the function (7.23) were first presented [31]. In this paper, a common feature of the HSG-models was observed, that is, that many physical

quantities, such as the function above develop staircase patterns.

In Fig. 7.1 the function (7.23) has been calculated for various values of σ by using a software called iFluid (this will be used in Chapter 9, numerical details are given in Appendix D). The position and size of the steps (or plateaux) reflect the interpretation of $c(r)$ as a function describing the RG-flow between the two fixed points of the theory. This is also in accordance with the separation of energy scales discussed in the previous sections.

Indeed, for large σ , at temperatures that are large with respect to the mass scale m but small with respect to the separation scale M (that is negative κ), the theory reaches the UV limit of the two-free-fermion theory, with central charge $c = 1$. In contrast, for temperatures beyond this separation scale (positive κ) the UV fixed point is determined by the coset $SU(3)_2/U(1)^2$ and corresponds to $c = \frac{6}{5} = 1.2$. The various curves correspond to different values of σ with a step, occurring around $\frac{\sigma}{2}$ ($\kappa = 0$), and representing the on-set of the interaction. Thus at intermediate values of temperatures we observe that the flow approaches these two fixed points in succession, giving rise to the staircase pattern that is typical of this model. From the RG-viewpoint, this pattern reflects the presence of a larger amount of degrees of freedom as energy is increased, interaction is turned on, and the unstable particle is formed.

It is worth noting that staircase patterns in RG flows are also found for other theories, typically the roaming trajectory model [127, 128] and generalizations thereof [129]. However a direct connection to unstable excitations is missing in those cases.

7.3 Generalised Hydrodynamics

We stress that unstable excitations are not part of the asymptotic states, and thus their dynamics cannot be directly described by the usual scattering picture (seen in Chapter 1). For this reason unstable particles are typically hard to study and their dynamics can be only outlined indirectly, in terms of the stable constituents.

In the next two chapters we will explore the $SU(3)_2$ -HSG model in two different out-of-equilibrium set-ups and analyse several dynamical quantities associated to the stable particles. The out-of-equilibrium physics is the most natural context to seek signatures of instability in the physical quantities of individual particles. We can then use these signatures to identify the unstable excitation and study its dynamics. The main tool we employ in order to compute such quantities is the generalized hydrodynamic approach (GHD), a leading

method in the study of the dynamics of many-body quantum systems, particularly integrable ones [32, 33, 130]. In this section we want to introduce this approach and its application to the study of unstable particles.

To explain the basis of GHD we start from a very general example. Suppose we have a certain system originally at equilibrium, and we engineer a set-up to drive the system out-of-equilibrium, for instance, by preparing independently two semi-infinite homogeneous quantum systems at different temperatures and let these evolve at time $t \neq 0$ (this set-up is exactly what we consider in the next chapter, and is generally known as *partitioning protocol*). After a transient period, the system may thermalise. This is indeed the typical situation we study in thermodynamics where the system reaches a new equilibrium, described by the *Gibbs ensemble*. The thermodynamic quantities (free energy, entropy, etc...) are accordingly local averages in the new macroscopic state, evaluated through the partition function:

$$\mathcal{Z}^{(\text{GE})} \sim \mathbf{Tr}\{e^{-\beta \hat{H}}\}, \quad (7.24)$$

where \hat{H} represents the energy operator and $\beta = 1/T$ is the inverse of the temperature. However, the intersection of low dimensionality and multiple conserved charges may give rise to a distinct kind of dynamics, one in which there is no long-term thermalization (an example is the quantum Newton's cradle experiment [131]). This behaviour is due to the fact that the multiple conserved charges are involved in determining the long time dynamics, and need to be included in the dynamical description by extending the concept of Gibbs ensemble to *generalized Gibbs ensemble* (GGE) [34]. In GGE, the partition function accounts for multiple conserved charges \hat{Q}_i in the system:

$$\mathcal{Z}^{(\text{GGE})} \sim \mathbf{Tr}\{e^{-\sum_i \beta_i \hat{Q}_i}\}, \quad (7.25)$$

where the *generalised inverse temperatures* β_i s are the Lagrangian parameters associated to the conserved charges \hat{Q}_i s. As a consequence, quantum integrable models, do not thermalise (to Gibbs ensembles) but instead equilibrate to GGEs. Precisely, in the set-up designed above, the presence of multiple local conserved charges give rise to ballistic transport meaning that, after a transient period, steady state currents flowing between the right and left subsystems emerge (see [132] for a review). The GHD approach provides a method to compute such currents, as we will see in Chapter 8.

Furthermore, out-of-equilibrium systems are typically characterised by a time- and space-dependence of the local observables, which reflect the inhomogeneities of the state. The GHD approach works at the mesoscopic scale, and the “hydrodynamics” enters the picture through the concept of fluid cells: a fluid cell is a region of space-time which is small enough for the state to look homogeneous, whilst containing a large enough number of particles. The assumption of *local entropy maximization*, also known as *GHD principle*, enters naturally in this context. Technically, this is the assumption that averages of local quantities tend uniformly enough, at large times, to averages evaluated in GGE states of the form (7.25), involving all the local and quasi-local charges of the system³, with space-time dependent potentials $\beta_i(x, t)$:

$$\langle \mathcal{O}(x, t) \rangle \approx \langle \mathcal{O}(0, 0) \rangle_{\underline{\beta}(x, t)}, \quad \underline{\beta}(x, t) := (\beta_1(x, t), \beta_2(x, t), \dots). \quad (7.26)$$

The above assumption is particularly meaningful in integrable models, where we are equipped with a specific methodology to evaluate exact expectation values of currents and densities associated to the local conserved charges of the theories. This is indeed the methodology given by the TBA discussed in the previous section (which can be generalised to GGEs [134]), and to a large extent by the scattering picture introduced in Chapter 1 as it provides the main ingredients for the TBA equations. In the context of integrable models GHD was first introduced in [32] in QFT, and in [33] in quantum chains. Since the original papers, a lot of developments have been achieved, such as the inclusion of force terms [135–138], diffusive and higher corrections [139–142], noise [143], integrability breaking terms [144–146]. There is now even experimental evidence that GHD provides a better description of transport in an atom chip than conventional hydrodynamics [147].

Another interesting development is the inclusion of theories possessing unstable excitations. This was first implemented in [35] for the $SU(3)_2$ -HSG model in the simple set-up described earlier. In [36, 148] the same theory has been recently explored in inhomogeneous set-ups. In Chapters 8 and 9 we will make full use of the GHD approach to study numerically the out-of-equilibrium dynamics arising from these set-ups and, for this reason, we focus only on the $SU(3)_2$ -HSG model for the remainder of the thesis.

³Here, with local or quasi-local conserved charges we mean quantities of the form $Q_i = \int dx q_i(x, t)$ such that $\partial_t Q_i = 0$ and that the density $q_i(x, t)$ is local i.e. supported on finite regions, or quasi-local i.e. supported on infinite regions but with an “envelope” that decays sufficiently fast. A review of quasi-local charges in integrable discrete systems can be found in [133].

7.3.1 Quasiparticle description via TBA

As mentioned earlier GHD requires a quasiparticle description. The TBA approach introduced in Section 7.2, combined with the GHD principle, can be naturally extended for such a purpose. The main difference is that now we need to implement GGE macroscopic states and such a change enters in the TBA equations via the TBA driving term:

$$w(x, t, \theta) = \sum_i \beta_i(x, t) h_i(\theta), \quad (7.27)$$

Above, the single-particle eigenvalues $h_i(\theta)$ ⁴ of all local conserved charges of the system are included, and the corresponding generalized inverse temperatures $\beta_i(x, t)$ are fluid-cell dependent (that means they incorporate the space- and time-dependence of the state). As a consequence, all TBA quantities will generally be functions of space and time. In particular the TBA equations become

$$\varepsilon(x, t, \theta; \pm) = w(x, t, \theta) - \varphi_{\pm\mp} \star L(x, t, \theta; \mp), \quad (7.28)$$

where the kernel is given exactly by (7.13), the convolution is (7.14), and the L-functions are now time- and space- dependent via (7.15). From these objects, averages of all local operators can in principle be calculated. We will concentrate on densities $q_i(x, t)$ of conserved charges $Q_i = \int dx q_i(x, t)$, and their currents $j_i(x, t)$ satisfying:

$$\partial_t q_i(x, t) + \partial_x j_i(x, t) = 0. \quad (7.29)$$

For these quantities, simple expressions exist. Their averages are fully fixed by giving the one-particle eigenvalues of the associated conserved charge, $h_i(\theta)$. The averages are obtained by using the “dressed” quantities $h_i^{\text{dr}}(x, t, \theta; \pm)$, which solve the linear integral equations

$$h_i^{\text{dr}}(x, t, \theta; \pm) = h_i(\theta) + \varphi_{\pm\mp} \star (h_i^{\text{dr}}(x, t, \theta; \mp) n(x, t, \theta; \mp)) \quad (7.30)$$

where

$$n(x, t, \theta; \pm) = \frac{1}{1 + e^{\varepsilon(x, t, \theta; \pm)}} \quad (7.31)$$

⁴Since in the model considered the eigenvalues $h_i(\theta)$ are the same for both particles, following a similar argument as for Section 7.2, we drop the dependence of \pm to simplify the notation.

is the occupation function associated to particle \pm . Equations (7.30) are simply another way to express the TBA equations (7.28) and the dressing operation represents the action of the interactions on the eigenvalues $h_i(\theta)$. Note the dressing operation make these quantities space- and time-dependent, and as a result the dressed quantity will be generally different for each particle \pm .

Specifically, the GGE averages of local charge densities q_i and of their associated currents j_i are defined via the GHD principle (7.26) as:

$$q_i(x, t) = \langle q_i(0, 0) \rangle_{\underline{\beta}(x, t)}, \quad j_i(x, t) = \langle j_i(0, 0) \rangle_{\underline{\beta}(x, t)}, \quad (7.32)$$

(recall that $\underline{\beta}$ was the set of generalized inverse temperatures in the GGE), and are expressed as

$$\begin{aligned} q_i(x, t) &= \sum_{b=\pm} \int_{-\infty}^{\infty} \frac{d\theta}{2\pi} e(\theta) h_i^{\text{dr}}(x, t, \theta; b) n(x, t, \theta; b) \\ &= \sum_{b=\pm} \int_{-\infty}^{\infty} \frac{d\theta}{2\pi} e^{\text{dr}}(x, t, \theta; b) h_i(\theta) n(x, t, \theta; b), \end{aligned} \quad (7.33)$$

and

$$\begin{aligned} j_i(x, t) &= \sum_{b=\pm} \int_{-\infty}^{\infty} \frac{d\theta}{2\pi} p(\theta) h_i^{\text{dr}}(x, t, \theta; b) n(x, t, \theta; b) \\ &= \sum_{b=\pm} \int_{-\infty}^{\infty} \frac{d\theta}{2\pi} p^{\text{dr}}(x, t, \theta; b) h_i(\theta) n(x, t, \theta; b). \end{aligned} \quad (7.34)$$

Above the energy and momentum one-particle eigenvalues are $e(\theta) = m \cosh \theta$ and $p(\theta) = m \sinh \theta$. We have also used a symmetry of the equations that allows us to interchange the “dressing” operation inside the integral and the sum.

There are a number of natural conserved charges available in the model. In this thesis we will focus only on the energy and particle number. Their single-particle eigenvalues are:

$$\begin{aligned} h_0(\theta) &= 1 && \text{(particle number)} \\ h_1(\theta) &= e(\theta) = m \cosh \theta && \text{(energy)}. \end{aligned} \quad (7.35)$$

Further, as the scattering is diagonal, the number of particles, energy and other charges carried by each individual particle type are also conserved charges themselves. We will use the notation

\mathbf{q}_i^\pm and \mathbf{j}_i^\pm for the associated average densities and currents, which therefore take the form

$$\mathbf{q}_i^\pm = \int_{-\infty}^{\infty} \frac{d\theta}{2\pi} e^{\text{dr}}(x, t, \theta; \pm) h_i(\theta) n(x, t, \theta; \pm), \quad \mathbf{j}_i^\pm = \int_{-\infty}^{\infty} \frac{d\theta}{2\pi} p^{\text{dr}}(x, t, \theta; \pm) h_i(\theta) n(x, t, \theta; \pm). \quad (7.36)$$

Note how the particle types are not summed over in these expressions.

In the next chapters we will focus our attention on two intermediate functions in the above expressions: these are the spectral densities (already introduced for the equilibrium case in Section 7.2), and the effective velocities (which first appeared in [149]),

$$\rho_p(x, t, \theta; \pm) = \frac{1}{2\pi} e^{\text{dr}}(x, t, \theta; \pm) n(x, t, \theta; \pm), \quad v^{\text{eff}}(x, t, \theta; \pm) = \frac{p^{\text{dr}}(x, t, \theta; \pm)}{e^{\text{dr}}(x, t, \theta; \pm)}, \quad (7.37)$$

respectively.

The spectral densities define the density of the two quasiparticles \pm in the phase-space and are a conserved quantity. Specifically, at fixed time t the quantity $\rho_p(x, t, \theta; \pm) d\theta dx$ represents the number of particles of type \pm in a phase-space element $d\theta dx$, while $v_{\text{eff}}(x, t, \theta; \pm) \rho_p(x, t, \theta; \pm) d\theta dx$ is the associated current. Furthermore, with the quasiparticle description introduced above, the effective velocities possess a very clear physical meaning. Indeed according to the GHD equations [32]:

$$\partial_t n(x, t, \theta; \pm) + v_{\text{eff}}(x, t, \theta; \pm) \partial_x n(x, t, \theta) = 0, \quad (7.38)$$

they represent the propagation velocities of the convective evolution of the occupation functions, identified with the normal modes of particle $+$ and $-$ respectively. In particular, at a given fluid cell (x, t) the effective velocities are

$$v^{\text{eff}}(x, t, \theta; \pm) = v^{\text{gr}}(\theta) + \int d\alpha \frac{\varphi_{\pm\mp}(\theta - \alpha)}{e(\theta)} \rho_p(x, t, \theta; \mp) \left(v^{\text{eff}}(x, t, \alpha; \mp) - v^{\text{eff}}(x, t, \theta; \mp) \right), \quad (7.39)$$

and can be seen as a modification of the group velocity $v^{\text{gr}}(\theta) = p(\theta)/e(\theta)$ of each quasiparticle under the effect of the interaction.

7.3.2 Effects of parity violation on scattering dynamics

In the next two chapters we will study numerically the average particle and energy densities and currents, as well as the spectral density and the effective velocities. Before doing so, one can already predict certain properties of the dynamics of the model from the structure of the

kernels (7.13) in the above TBA description.

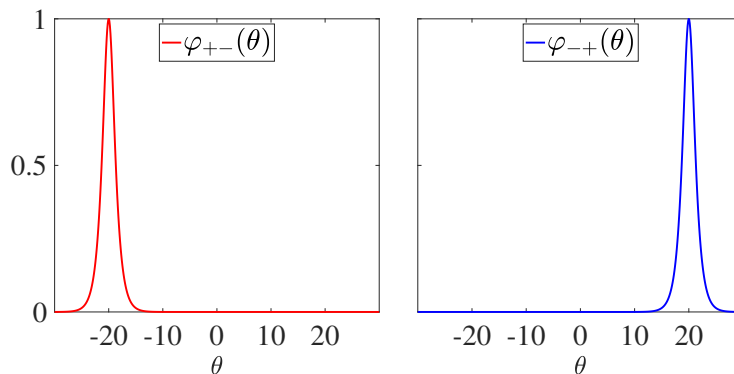


Figure 7.2 Kernels $\varphi_{\pm,\mp}(\theta)$ of the $SU(3)_2$ -HSG model, for $\sigma = 20$. Analytical formulae are given by (7.13).

We conclude this chapter with a few observations, based on Fig. 7.2:

- Parity breaking:** We have seen that in the TBA/GGE equations (7.30) the interaction enters in the kernel, in integrable QFT this has standard properties, such as a fast decay at large $|\theta|$, characteristic of the local interaction of the model, as well as interaction peaks around $\theta = 0$. For instance, the sinh-Gordon kernel at the self-dual point is $2\operatorname{sech}\theta$, which satisfies the two properties. However, the kernels (7.13) are exceptional in that as they are peaked around a rapidity that is generally non-zero. Indeed, due to (7.2) TBA quantities are not symmetric in θ even though they are identical under the simultaneous change of signs of rapidities $\theta \rightarrow -\theta$ and particle types $\pm \rightarrow \mp$. This is a remnant of the fact that the scattering phases (7.1) themselves, and the underlying action of the model, break parity.
- Scattering:** The kernels are maximal at $\theta = \mp\sigma$, taking values $\varphi_{\pm\mp}(\mp\sigma) = 1$, and rapidly decreasing functions away from their maximum (i.e. $\operatorname{sech}\theta$ is strongly peaked around zero). For instance, for $\sigma > 0$, this means that $\varphi_{+-}(\theta)$ is maximal for $\theta = -\sigma < 0$. Recalling that $\theta = \theta_1 - \theta_2$ is the difference of the rapidities of the two incoming particles with types $\epsilon_1 = +$ and $\epsilon_2 = -$, we see that, for σ large and positive, the scattering can be nontrivial only in the region $\theta_1 < \theta_2$. This, physically, corresponds to a collision where the particle of type $-$ moves towards the right, and that of type $+$ towards the left, in the rest frame. Analysing $\varphi_{-+}(\theta)$, the same conclusion is reached upon exchanging the roles of \pm particles. Thus nontrivial scattering occurs only in one direction, for $\sigma > 0$ when particle $-$ travels rightwards towards particle $+$ (and the opposite for $\sigma < 0$),

and it is this scattering that is expected to give rise to the unstable particle. For this reason, the functions of interest have quite different behaviours for $\theta > 0$ and $\theta < 0$ for \pm particles, with one choice giving the free fermion result and the other what we can term an “interaction” result.

- **Separation into right- and left-movers:** We have seen in equation (7.39) that the propagation velocities of the individual particles are generally different from their group velocities as a result of particle interactions. Furthermore, it emerges from comparison with soliton gases and the flea gas model [150] that the value of the kernels can be interpreted as the distance jumped by particles upon collision. Positive kernels give the “natural” picture, whereby a tagged particle, travelling rightwards (leftwards) and hitting another particle, experiences a jump leftwards (rightwards), by the amount given by the scattering kernel. Thus, from the previous point, we expect that, say for $\sigma > 0$, particle $+$ ($-$) is mostly hit from the left (right) and therefore is mostly displaced toward the right (left); its effective velocity will receive a positive (negative) correction, as compared to its group velocity. We may therefore broadly identify particles of type $+$ with right-movers, and of type $-$ with left-movers. This picture becomes exact near the UV fixed points, and will be further investigated numerically in the next chapter.

SET-UP 1: PARTITIONING PROTOCOL

8.1 The bipartite quench

In Chapter 7 we have introduced the GHD equations and the corresponding TBA description for the $SU(3)_2$ -HSG model. We want now to engineer an out-of-equilibrium set up by employing the partitioning protocol. This is the easiest way to drive a system out-of-equilibrium and, as seen in Section 7.3, the dynamics arising from this particular quench protocol is well understood, leading to a clear separation between integrable and non-integrable systems.

We consider two semi-infinite systems, described by two Gibbs ensembles at inverse temperatures $\beta_{R,L}$ for the right (left) baths such that the initial state is homogeneous everywhere, except at the separation point $x = 0$. We assume that the two halves are of the same nature, and described by a $SU(3)_2$ -HSG model (with the same free parameter σ). When putting the two systems in contact at $t = 0$, flows of energy and other charges are immediately produced. After waiting long enough, relaxation occurs and these flows are expected to reach a steady regime in a region close enough to the contact point. As pointed out in Section 7.3, the nature of this steady regime is non-trivial in integrable models, as non-equilibrium steady states are produced in the intermediate region between subsystems, carrying non-trivial flows. These flows are powered by the original baths that act as asymptotic reservoirs. As seen in Subsection (7.3.1), hydrodynamic conservation equations and TBA equations can be combined to characterize the currents of the system. Remarkably,

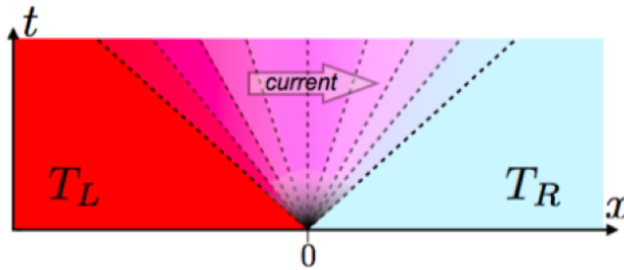


Figure 8.1 Dynamics of integrable systems after a bipartite quench. After a sufficiently large time the system is described by a continuum of GGE states with generalised inverse temperature $\underline{\beta}(\xi)$ parametrised by the ray $\xi = x/t$. The large-time evolution is characterised by emergent steady state currents within the light cone $\xi = \pm 1$ (for relativistic systems) originated at the contact point at time $t = 0$. Picture taken from [32].

in the set-up designed above, GHD solutions for the large-scale non-equilibrium occupation functions are known [32, 33] and are simply:

$$n(\xi, \theta; \pm) = n_R(\theta; \pm) \Theta(\theta - \theta_\xi^\pm) + n_L(\theta; \pm) \Theta(\theta_\xi^\pm - \theta), \quad (8.1)$$

where the time- and space-dependence is included in θ_ξ^\pm , which is a function of the ray $\xi = x/t$, and Θ is the Heaviside step function. The resulting large-scale evolution of the system is represented graphically in Fig. 8.1. Thus, to determine the solutions of the occupation functions at any fixed ray ξ , we need two ingredients: $n_{L,R}(\theta; \pm)$ and θ_ξ^\pm . The former are the occupation numbers in the original baths, and can be evaluated by the TBA equations (7.11) with driving terms $\omega_{L,R}(\theta) = m\beta_{L,R} \cosh \theta$ (as expected, for $\xi \rightarrow \pm\infty$, (8.1) reproduces the original bath of the right and left subsystems, respectively). The latter are the discontinuity positions θ_ξ^\pm , which are solutions to the equations:

$$v_{\text{eff}}(\xi, \theta_\xi^\pm; \pm) = \xi. \quad (8.2)$$

Above, the effective velocities are assumed to be monotonic functions of rapidity, which guarantees a unique solution at any fixed ray ξ . We remark that the equations above require the implementation of the TBA equations and for the reason explained in Section 7.2, they are solved numerically.

Another important observation is that for CFT the total energy current and total energy density are known in this particular quench protocol. These were indeed investigated in [151,

152] and found to be homogeneous within the light cone $\xi = \pm 1$, in particular

$$j_1 \stackrel{\text{CFT}}{=} \frac{c\pi}{12} (T_L^2 - T_R^2) \quad \text{and} \quad q_1 \stackrel{\text{CFT}}{=} \frac{c\pi}{12} (T_L^2 + T_R^2), \quad (8.3)$$

where c is the central charge and as usual $T_{R,L} = \beta_{R,L}^{-1}$. This result will be useful in the next section to describe the UV regime of the system.

8.1.1 Numerical analysis

In the rest of this chapter, we will present the numerical results reported in [35] and obtained by implementing standard TBA numerical methods. We provide a more detailed description of the algorithm in Appendix C. In our analysis we look at the “ray” located exactly in the middle of the steady-state region so that we fix

$$\xi = 0. \quad (8.4)$$

Our numerics have shown that the physical picture does not change substantially for other rays. At $\xi = 0$, the equations become:

$$n(\theta; \pm) = n_R(\theta; \pm) \Theta(\theta - \theta_0^\pm) + n_L(\theta; \pm) \Theta(\theta_0^\pm - \theta), \quad v_{\text{eff}}(\xi, \theta_0^\pm; \pm) = 0. \quad (8.5)$$

Above, as well as in the remainder of this chapter, we omit the ξ -dependence of GHD quantities in order to simplify the notation. Hence, at $\xi = 0$, the θ_0^\pm are simply the zeros of the effective velocities, and equation (8.2) accordingly expresses the fact that the occupation functions of particles with positive (negative) effective velocities take the form of those in the original ensembles on the left (right) sub-system.

To conclude this section, we provide some basic information on the physical parameters and motivation for the corresponding domain explored in our numerical simulations. In much of our analysis we will fix the ratio of temperatures and vary β_L only. It is thus convenient to introduce the following variable

$$\mathbf{x} = \frac{\beta_R}{\beta_L}, \quad (8.6)$$

(not to be confused with the position variable which is never explicitly used in this chapter). Hence the ratio \mathbf{x} defines the initial state of the system and gives rise to non equilibrium dynamics for $\mathbf{x} \neq 1$. In particular, $\mathbf{x} > 1$ ($\mathbf{x} < 1$) corresponds to introducing a positive (negative) temperature gradient $T_L > T_R$ ($T_L < T_R$) in the system. Now, we may easily observe

that if $|\mathbf{x}|$ is too large, the resulting large-time dynamics will be almost fully determined by only one side of the system, that is the one at highest temperature. This will be confirmed by our numerics, and indeed we have found the most interesting physics when $|\mathbf{x}| \lesssim 3$ and thus when the two inverse temperatures are comparable.

We will also study the system at $\mathbf{x} = 1$ which corresponds to the system at equilibrium. Although the equilibrium properties of this model have been studied at length using TBA techniques [31], we find that the new ideas brought by the recently developed hydrodynamic picture shed new light into the main features of the theory, especially the nature of the unstable particle (this will be analysed in detail in Section 8.3). In addition, understanding the equilibrium case in terms of its underlying hydrodynamic properties will be extremely helpful when interpreting the out-of-equilibrium dynamics.

Finally, it is well known from standard equilibrium TBA arguments that non-vanishing values of the functions $L(\theta; \pm)$ and $n(\theta; \pm)$ are strongly localized in the range

$$\log \frac{\beta}{2} < \theta < \log \frac{2}{\beta}, \quad (8.7)$$

as the functions fall off double-exponentially outside this range. In out-of-equilibrium set-ups $\beta = \min\{\beta_L, \beta_R\}$. In our numerics we will exploit this property to implement numerical integrals of TBA functions of interest.

Throughout the remainder of this chapter we will set the mass scale to $m = 1$. We are now ready to analyse several quantities of interest. We will start from energy current and energy densities in the next section.

8.2 Hydrodynamic scaling functions

One of the most effective ways to visualize the effect of the unstable particle is to look at temperature-dependent quantities, for a wide range of temperatures. For instance, in Section 7.2.1 we have studied, the temperature-dependence of the TBA scaling function (7.23), and established that the resulting staircase pattern is connected to the degrees of freedom of the theory, and in particular to its RG-flow. Interestingly, when connecting two halves of temperature ratio \mathbf{x} , many GHD quantities display similar information if explored as functions of the initial inverse temperature β_L (or similarly β_R).

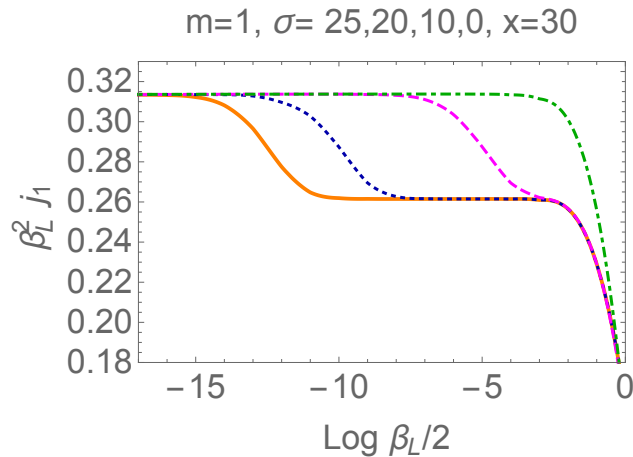


Figure 8.2 The scaled energy current as a c -like function for several values of σ and temperature ratio $x = 30$. The plateaux are located at $\beta_L^2 j_1 \stackrel{\text{CFT}}{=} \frac{\pi}{12} (1 - \frac{1}{900}) = 0.261508$ and $\beta_L^2 j_1 \stackrel{\text{CFT}}{=} \frac{\pi}{10} (1 - \frac{1}{900}) = 0.31381$. Similarly to the TBA-scaling function plotted in Fig. 7.1, the scaled energy current encodes information about the RG-flow, but for out-of-equilibrium systems.

An example is shown in Fig. 8.2, where we have evaluated the energy current (7.34) for $i = 1$, scaled it by a factor β_L^2 , and plotted the results for various σ . Multiplication by β_L^2 is dictated by the CFT result (8.3), and is a convenient way to reveal a staircase pattern which reflects the presence of two UV fixed points (with central charges $c = 1$ and $c = 1.2$), reached for (relatively) low and high temperatures as previously described in Section 7.2.1. Similar scaling patterns can be found for the total energy density (7.33). Therefore, one may think of the quantities $\frac{12|j_1|\beta^2}{\pi}$, $\frac{12q_1\beta^2}{\pi}$, where β is the largest temperature, as new scaling functions. This idea is however not new. Indeed many such scaling functions were proposed in the work [153] and, more recently, for the roaming trajectories model in [154].

Under the above considerations the corresponding growth of degrees of freedom observed at the onset of the unstable particle, can be measured in terms of some very concrete physical quantities such as the energy flows and densities, and this can help us to outline a more physical understanding of the unstable bound states. Following this idea, in the next two subsections we set $\sigma = 20$ and analyse the equilibrium and out-of-equilibrium energy currents and energy densities of the individual particles.

8.2.1 Equilibrium energy currents and energy densities

We start from the system at equilibrium (i.e. both baths at the same inverse temperature $\beta := \beta_L = \beta_R$ that is $\mathbf{x} = 1$). The numerical outcomes for energy currents and energy densities as functions of $\log \beta/2$ are shown in Fig. 8.3. Looking at this figure, we can identify the following

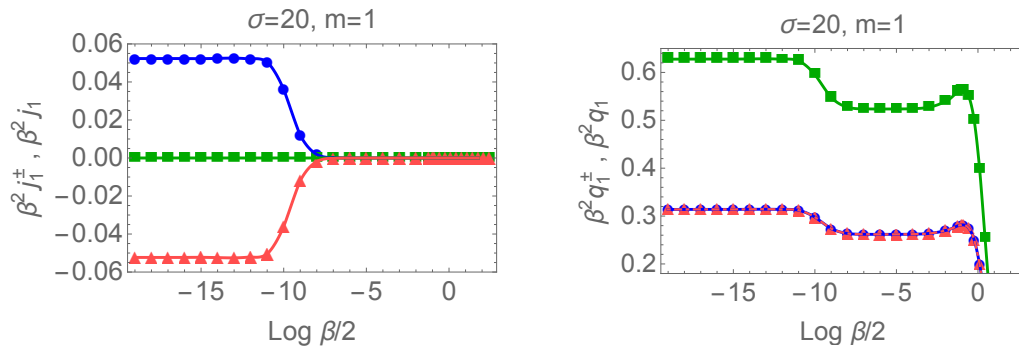


Figure 8.3 We consider the system at equilibrium i.e. $\mathbf{x} = 1$, and set the parameters $m = 1$, and $\sigma = 20$. Left: The total scaled energy current $\beta^2 \mathbf{j}_1$ (squares, green), the contribution $\beta^2 \mathbf{j}_1^+$ (triangles, red) and $\beta^2 \mathbf{j}_1^-$ (circles, blue). Right: The total scaled energy density $\beta^2 \mathbf{q}_1$ (squares, green), the contribution $\beta^2 \mathbf{q}_1^+$ (triangles, red) and $\beta^2 \mathbf{q}_1^-$ (circles, blue).

properties:

- **Parity breaking:** Although the total energy current is zero at equilibrium (as expected), the individual contributions from \pm particles are non-vanishing (and opposite) for some energy scales. This is allowed due parity breaking in the theory. More precisely, in TBA, under parity, the signs of the currents and the particle types are exchanged. Here we observe that this gives rise to a negative (positive) energy current carried by $+$ ($-$) particles.
- **Onset of the unstable particle:** The individual particle contributions to the energy density and current, and also the total energy density, display a staircase pattern with a step whose onset is located around $\log \frac{\beta}{2} = -\frac{\sigma}{2} = -10$. This energy value represents the onset of the unstable particle. For $\log \frac{\beta}{2} > -\frac{\sigma}{2}$ the individual contributions to the current are vanishing as this is the regime where the theory behaves as two decoupled free fermions and parity is restored. Energetically speaking, this is the region where energy is not high enough to allow for the formation of the unstable excitation.
- **CFT values:** The staircase patterns observed for the individual contributions to the energy density are identical, because parity preserves the sign of the energy. Their two plateaux can be predicted from CFT. For lower temperatures $\log \frac{\beta}{2} > -\frac{\sigma}{2}$ the energy densities tend to their massless free fermion value,

$$\beta^2 \mathbf{q}_1^\pm \stackrel{\text{FF}}{=} \lim_{\beta \rightarrow 0} \frac{\beta^2}{2\pi} \int_{-\infty}^{\infty} d\theta \frac{\cosh^2 \theta}{1 + e^{\beta \cosh \theta}} = \frac{1}{\pi} \int_0^{\infty} \frac{u}{1 + e^u} du = \frac{\pi}{12} = 0.261799. \quad (8.8)$$

This corresponds exactly to the height of the lowest plateau of the lower curve on the right panel of Fig. 8.3. Similarly, the highest plateau is located at the value

$$\beta^2 q_1^\pm \stackrel{\text{CFT}}{=} \frac{\pi c}{12} = 0.314159, \quad (8.9)$$

which is the CFT result for $c = 1.2$.

8.2.2 Out-of-equilibrium energy currents and energy densities

In this subsection we discuss the main features of the out-of-equilibrium energy currents and energy densities for different temperature ratios, focussing on the main changes with respect to the equilibrium situation. Our discussion focusses on Fig. 8.4. The main important features

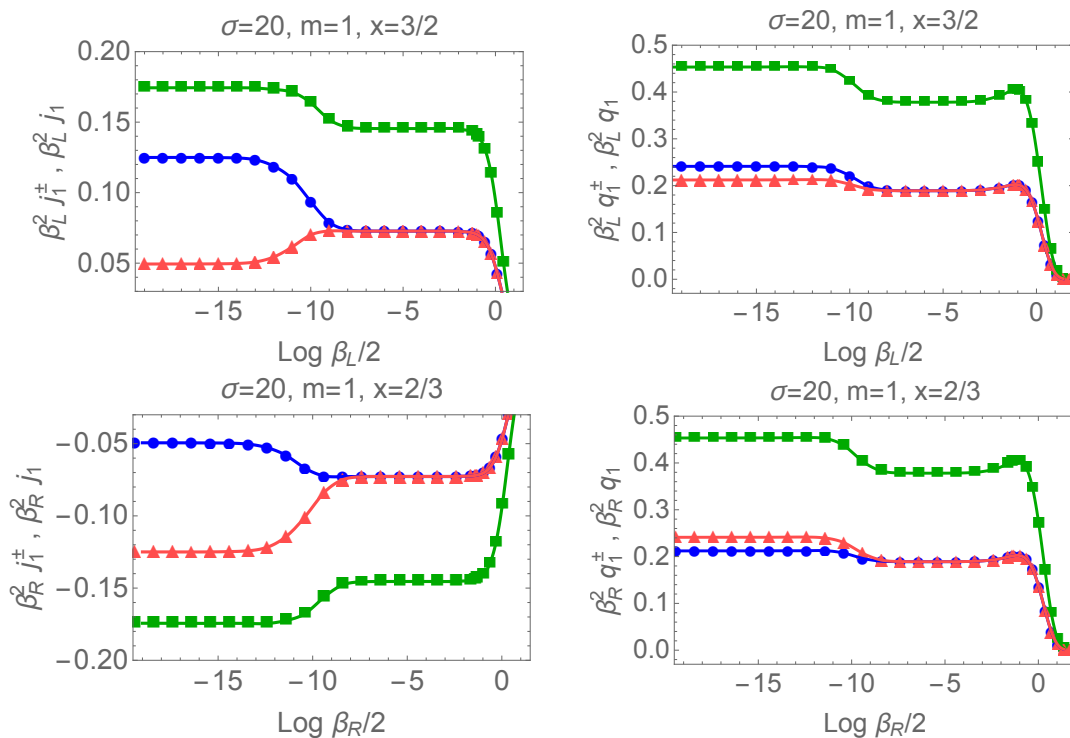


Figure 8.4 The total (scaled) energy current $\beta_i^2 j_1$ (squares, green), the contribution $\beta_i^2 j_1^+$ (triangles, red) and $\beta_i^2 j_1^-$ (circles, blue) and similarly for the energy density. We consider the cases $x = 3/2$ ($i = L$) and $x = 2/3$ ($i = R$). In all cases $\sigma = 20, m = 1$.

are the following:

- **Symmetry:** A clear feature from the pictures is the following symmetry under the exchange $x \rightarrow x^{-1}$ (or $\beta_L \leftrightarrow \beta_R$):

$$j_1^\pm(\beta_L, \beta_R) \rightarrow -j_1^\mp(\beta_R, \beta_L) \quad \text{and} \quad j_1(\beta_L, \beta_R) \rightarrow -j_1(\beta_R, \beta_L), \quad (8.10)$$

and similarly

$$\mathbf{q}_1^\pm(\beta_L, \beta_R) \rightarrow \mathbf{q}_1^\mp(\beta_R, \beta_L) \quad \text{and} \quad \mathbf{q}_1(\beta_L, \beta_R) \rightarrow \mathbf{q}_1(\beta_R, \beta_L). \quad (8.11)$$

This is in agreement with the parity symmetry of the TBA equations.

- **Conformal limits:** The height of the plateaux is predicted as in the equilibrium case by the formula (8.3). For instance, for $\mathbf{x} = 3/2$ the scaled total current has plateaux at

$$\beta_L^2 \mathbf{j}_1 \stackrel{\text{CFT}}{=} \frac{\pi c}{12} \left(1 - \frac{4}{9}\right) = \frac{5\pi c}{108}, \quad (8.12)$$

which gives values 0.174533 and 0.145444, for $c = 1.2$ and $c = 1$, respectively. The same holds for the total spectral density:

$$\beta_L^2 \mathbf{q}_1 \stackrel{\text{CFT}}{=} \frac{\pi c}{12} \left(1 + \frac{4}{9}\right) = \frac{13\pi c}{108}, \quad (8.13)$$

predicting the values 0.453786 and 0.378155 for $c = 1.2$ and $c = 1$.

- **Unstable particle onset:** In all figures we also see the location of the start of the plateau at $-\sigma/2 = -10$ with respect to the scales $\log \frac{\beta_{L,R}}{2}$. In fact, quantities associated with particle $+$ develop a plateau for $\log \frac{\beta_L}{2} > -\frac{\sigma}{2}$ whereas for particles of $-$ type the plateau's onset occurs at $\log \frac{\beta_R}{2} = -\frac{\sigma}{2}$. This is hardly detectable in these figures because $\log \frac{3}{2} = 0.405\dots$ and therefore there is little difference between the values $\log \frac{\beta_{L,R}}{2}$; but we have verified this fact for larger values of \mathbf{x} . Such a difference is also evident in other out-of-equilibrium quantities we will analyse in Section 8.4, in particular in Fig. 8.9.
- **Particles couple mainly to one bath:** The previous point suggests that type $+$ particles are particularly sensitive to the value of β_L whereas particles of type $-$ couple strongly to the value of β_R . This is related to the structure of the kernels described in Subsection 7.3.2 and also to the structure of the occupation numbers (8.1). For particle $+$ this means that it will feel strong interaction with particle $-$ only when $\theta < 0$ and close to $-\sigma$. At the same time, for $\theta < 0$ the occupation number is largely described by its equilibrium value on the left bath (see Fig. 8.9 for more details) and so particle $+$ mainly interacts at inverse temperature β_L . A similar argument can be made for particle $-$.
- **Equilibrium currents vs temperature gradient:** In contrast to the equilibrium case, here both particle type contributions to the currents have the same sign, although they

are different from each other. For $\mathbf{x} > 1$ both contributions are positive, even though the contribution of particle $+$ is always smaller (the opposite is true for $\mathbf{x} < 1$). This change can be explained as the result of interference (sometimes constructive, sometimes destructive) between two phenomena: the equilibrium dynamics and that induced by the temperature gradient. If $\mathbf{x} > 1$ we have that $T_L > T_R$ and so from the temperature gradient we expect a positive current. However, for particle $+$ the equilibrium current would have the opposite sign and so, even if temperature “wins” in the end, we still have a reduced current. For particle $-$ on the other hand both the gradient and the equilibrium tendency support a positive current, so its total contribution is enhanced. The opposite effect is seen for $\mathbf{x} < 1$.

In summary, the growth observed in Fig. 8.2 at intermediate temperatures (i.e. $\log \frac{\beta}{2} \lesssim -\frac{\sigma}{2}$) of the original baths, can be interpreted as a combined effect of the formation of unstable bound states and the emergent obstacle that the temperature gradient creates to such formation when the system is driven out of equilibrium. The formation of the unstable particles, and the corresponding increase in degrees of freedom captured by the scaling functions, seems closely related to the dynamics of the individual particles, and in particular to the scattering processes that determine the sign of the individual energy currents in Fig. 8.3, even at equilibrium. This will be further investigated in the next section.

8.3 Equilibrium physics with unstable particles

Following the conclusion of the previous section, we want now to give a closer look at the scattering dynamics of the two stable quasiparticles, and this can be better understood if we look into rapidity-dependent TBA/GHD functions. We now focus on two very fundamental phase-space quantities, namely, the spectral densities and the effective velocities, defined in (7.37). For the $SU(3)_2$ -HSG model, this phase-space analysis was first conducted in [35], and was motivated by the important roles of both quantities ρ_p^\pm and v^{eff} in GHD. However, these quantities can be of course explored also at equilibrium as they are both functions of the occupation functions $n(\theta; \pm)$. Remarkably, a very interesting physical picture of the unstable bound states emerges already at equilibrium, and we want indeed to discuss this in detail in Subsection 8.3.3.

In the next two subsections, we will investigate further the equilibrium dynamics of the two stable particles by studying the two phase-space quantities of interest separately in three

different regimes. Indeed, a common features observed in both Sections 8.2.1 and 8.2.2 it that either the equilibrium and the out-of-equilibrium dynamics change drastically when the formation of unstable particles is allowed in the system. In this analysis, it is worth recalling the parameter $\kappa = -\log \frac{\beta}{2} - \frac{\sigma}{2}$. Once the parameter σ has been fixed (and along with it, the mass scale M), the three regimes (7.20), (7.21) and (7.20) are identified by the inverse temperature of the system only¹.

Throughout the section, we consider the system described by a Gibbs ensemble at $\beta = \beta_L = \beta_R$ i.e. $\mathbf{x} = 1$, and as earlier, we fix $\sigma = 20$.

8.3.1 Effective velocities

We start from the effective velocities. Fig. 8.5 shows three “snapshots” of the velocities as functions of the rapidity variable at three different temperatures. The main noteworthy features are the following:

- **Free fermion regime** ($\kappa < 0$): For low temperatures the two velocities are well described by the free fermion result $v^{\text{eff}}(\theta; \pm) = \tanh \theta$. In particular, at large rapidities, we have non-interacting right- and left-movers propagating at the speed of light.
- **Unstable particle and parity breaking** ($\kappa \gtrsim 0$): For intermediate temperatures the onset of the unstable particles triggers a parity breaking effect. Velocity profiles exhibit the symmetry

$$v^{\text{eff}}(\theta; +) = -v^{\text{eff}}(-\theta; -). \quad (8.14)$$

The presence of the unstable particle marks the interaction and this reduces the absolute values of the velocities, down from their conformal values ± 1 , and gives rise to two distinct plateaux, one in each effective velocity. The heights of the intermediate plateaux for both particle types change with temperature until reaching again the values ± 1 at very high temperatures. Some of the features may be explained using the flea gas picture, as explained below.

- **UV limit** ($\kappa \gg 0$)²: In the deep UV limit the velocities reach once more their CFT values ± 1 but are “shifted” in comparison with their free fermion value. In fact they are

¹In the next sections we may often refer to low, intermediate, and high temperatures of the system. The implicit reference is always the mass scale of the unstable excitation via the regimes mentioned above.

²In our numerics we observe that the TBA scaling function (7.23) approaches the UV limit for $\kappa \gtrsim 3$ that is what we mean here by denoting $\kappa \gg 0$.

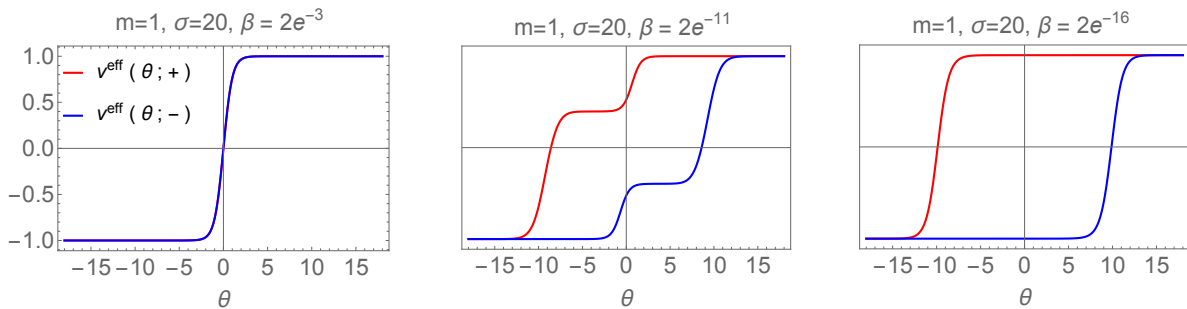


Figure 8.5 Effective velocity profiles at equilibrium for three temperatures: for low temperatures (left figure) we observe the free fermion result, the group velocity $\tanh \theta$; for intermediate temperatures (middle figure) we observe the onset of the unstable particle; for high temperatures (right figure), where a new CFT is reached, effective velocities of $+$ ($-$) particles are shifted so that they appear to be mostly right-moving (left-moving). The evolution of the effective velocities as functions of temperature can be further explored in [this video](#) [155].

very well approximated by the functions (8.18) which are derived below. We have again large regions of right- and left- movers propagating at the speed of light, and we observe that the $+$ ($-$) particle acquires “mostly” right-moving (left-moving) properties. This is again in agreement with the flea-gas picture, which, as we explained, indicates that $+$ ($-$) particles should be right-movers (left-movers).

- **Plateaux and the “flea gas” picture :** The flea gas scattering picture described at the end of Subsection 7.3.2 explains the presence of the intermediate plateaux in the middle panel of Fig. 8.5. For instance, the $+$ particle may only scatter by collisions on its left, and these collisions generate jumps rightwards. Thus, only for $\theta < 0$, where the particles are not moving rightwards at the speed of light, can such collisions happen; and when they happen, they “slow down” the particle. This only happens in a small interval of values of θ (for the $+$ particle this is approximately the interval $[-\sigma/2, 0]$) and the precise boundaries of this intermediate plateau, are more subtle to explain. They are determined by an interplay between spectral densities and the effective velocity. For instance, a change of the effective velocities at rapidities $|\theta| > \sigma/2$ is precluded for low temperatures $\log \frac{\beta}{2} > -\sigma/2$, because no particles are present at such rapidities. The configuration achieved at large temperatures, for instance the right-most panel of Fig. 8.5, has however a clear meaning. Indeed, scattering may only happen between $+$ and $-$ particles for rapidity differences near to σ , but does not happen if particles are co-moving (have the same effective velocity). Thus, for instance, $+$ particles at rapidities -15 and $-$ particles at rapidities 5 do not scatter according to the right-panel of Fig 8.5. Interestingly, a more involved plateau structure of effective velocities has been observed recently in [156]

for the roaming trajectory model.

- **Vanishing Velocities** ($\kappa \approx 0$): Interestingly, at the onset of the unstable particle, the intermediate plateaux both have heights zero. The physical interpretation is that for such temperatures, + and – particles of rapidities $|\theta| < \sigma/2$ are essentially stationary, and this allows them to form the finitely-lived bound state represented by the unstable particle. We will observe the formation of the unstable particle more precisely in Subsection 8.3.3.

The behaviour of the effective velocities for very high temperatures as described in the item on “UV limit” can be analytically derived from the TBA equations under some simple assumptions. Recall the definition of the effective velocities (7.37) and of the dressing operation (7.30). We know that the kernels $\varphi_{\pm\mp}(\theta)$ are functions that are strongly peaked around $\theta = \mp\sigma$ and we also know that the functions $n(\theta; \pm)$ develop a plateau in the region (8.7). For high temperatures this will be a very wide plateau of height $n = \frac{\sqrt{5}-1}{2} = 0.618\dots$ (this can be derived from the constant TBA equations [31]) so that within the region where the kernel is non-vanishing the occupation numbers are constant and may be taken out of the integral. Thus, at high temperatures we can approximately write

$$h_i^{\text{dr}}(\theta; \pm) \approx h_i(\theta) + \frac{n}{2\pi} \int_{-\infty}^{\infty} d\lambda \varphi_{\pm\mp}(\theta - \lambda) h_i^{\text{dr}}(\lambda; \mp). \quad (8.15)$$

An even cruder approximation consists of treating the kernel as a δ -function $\delta(\theta - \lambda \pm \sigma)$ and writing

$$h_i^{\text{dr}}(\theta; \pm) \approx h_i(\theta) + n h_i^{\text{dr}}(\theta \pm \sigma; \mp). \quad (8.16)$$

The equations above are solved by the following functions

$$h_i^{\text{dr}}(\theta; \pm) = \frac{h_i(\theta) + n h_i(\theta \pm \sigma)}{1 - n^2}. \quad (8.17)$$

For the effective velocities this means that

$$v^{\text{eff}}(\theta; \pm) \approx \frac{\sinh \theta + n \sinh(\theta \pm \sigma)}{\cosh \theta + n \cosh(\theta \pm \sigma)} \quad \text{for} \quad \log \frac{\beta}{2} \gg -\frac{\sigma}{2}. \quad (8.18)$$

If $n = 1$ the functions above are exactly $\tanh(\theta \pm \frac{\sigma}{2})$. In this case n is not 1 but the function above still resembles a shifted hyperbolic tangent very much. That is the reason why the curves in the rightmost panel in Fig. 8.5 look a lot like shifted versions of those in the leftmost panel.

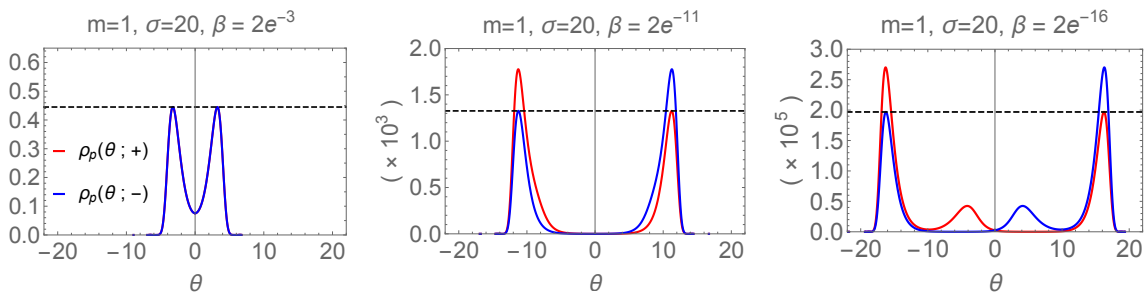


Figure 8.6 Spectral densities for three values of the temperature: $\beta = 2e^{-3}$, $2e^{-11}$ and $2e^{-16}$. In the two rightmost panels, the vertical axis labels should be multiplied by factors 10^3 and 10^5 , respectively, as indicated. In all panels, a dashed horizontal line indicates the height of the free-fermion peak, $0.04431\dots/\beta$. For low temperatures (left panel) we observe the free fermion result; for intermediate temperatures (middle panel) we observe the onset of the unstable particle with one of the peaks growing beyond the free fermion value; for high temperatures (right panel) the densities develop one additional local maximum. The evolution of the densities as functions of temperature can be further explored in [this video](#) [157].

8.3.2 Spectral densities

In this section we analyse the main features of the spectral densities $\rho_p(\theta; \pm)$ defined in (7.37) by considering three density profiles for low, intermediate and high temperatures. These are presented in Fig. 8.6, where, for comparison, the values of the maxima of the free-fermion densities at large temperatures, $\rho_{\max}^{\text{FF}} = \frac{\ell-1}{2\pi\beta}$ with $\ell = 1.27846\dots$ (dashed black line), are shown. The most important features of the spectral densities at equilibrium are the following:

- **Free fermion regime** ($\kappa < 0$): The spectral densities for sufficiently low energies (Fig. 8.6, left panel) are those of a free fermion and are described by the corresponding formula

$$\rho_p(\theta; \pm) = \frac{1}{2\pi} \frac{\cosh \theta}{1 + e^{\beta \cosh \theta}} =: \rho_p^{\text{FF}}(\theta). \quad (8.19)$$

This function has maxima around $\theta = \pm \log \frac{\beta}{2}$, as seen in the figure; more precisely, the positions of the maxima scale, for β small, as $\theta \sim \pm \log \frac{\beta}{2^\ell} + o(1)$ where $\ell = 1.27846\dots$ solves $e^{-\ell} = \ell - 1$. These maxima are at a height that scales as $\sim \frac{\ell-1}{2\pi\beta}$, as also seen in the figure.

- **Turning on the interaction** ($\kappa \sim 0$): For higher temperatures (Fig. 8.6, middle and right panels) we still have maxima around $\pm \log \frac{\beta}{2}$, but the heights of some of the maxima start to change as soon as the unstable particle comes into play. For intermediate energies we observe that for each given particle type, one of the maxima (the right (left) one for $+$ ($-$) particles) coincides with its free fermion value whereas the other maximum is higher,

indicating an “excess” density generated by the onset of the interaction. This asymmetry is justified by the structure of the kernels, as discussed in Subsection 7.3.2. That is the $\varphi_{+-}(\theta)$ kernel is maximized at $\theta = -\sigma < 0$ and is negligible for $\theta > 0$ thus the effect of interaction only manifests itself for $\theta < 0$ while the free fermion physics persists for $\theta > 0$. This excess grows as temperature increases and gradually leads to the formation of an additional peak for each particle. The gradual growth can be displayed more clearly in [this video](#) [157].

- **Three local maxima** ($\kappa > 0$): Following the observation above, for high temperatures (compared to the unstable particle’s mass) two new local maxima, one for each density, emerge located around $\pm(\log \frac{\beta}{2} + \sigma)$ (Fig. 8.6, right panel). Thus, at high temperatures, each spectral density exhibits three local maxima: the free fermion peak expected for that temperature, the “interacting peak” whose maximum is largest, and a smaller, “subsidiary peak”. We observe two important features for these peaks. First, the position of the maxima is once more justified by the scattering matrix which dictates that interaction is maximized for rapidity differences $\pm\sigma$. In particular, the rapidity difference between the + particle (red) interacting peak and the – particle (blue) subsidiary peak is, at all temperatures, around $-\sigma$, the value at which the scattering interaction $\varphi_{+-}(\theta)$ is maximal; and viceversa. Second, for each particle type, the excess area of the interacting peak compared to the free fermion peak roughly coincides with the area of the subsidiary peak. The implications of the observation above will be discussed in detail in Subsection 8.3.3.

8.3.3 Emergence of bound states in the scattering dynamics

We now argue that by simultaneously analysing features of the effective velocities and spectral densities, we gain a new, dynamical insight into the equilibrium scattering theory of the model.

Recalling Chapter 7, the conventional understanding of unstable particles is based on the presence of a pole in the scattering amplitudes and on the notion of how the presence of this particle adds, at large temperatures, new degrees of freedom to the theory: it drives an RG flow between, in the IR, a double free fermion theory and, in the UV, a non-trivial coset model. However, the introduction of dynamical quantities such as the effective velocities, in combination with the two observations we have made in the last point of Subsection 8.3.2, brings a new, perhaps more intuitive perspective into the interpretation of this unstable particle.

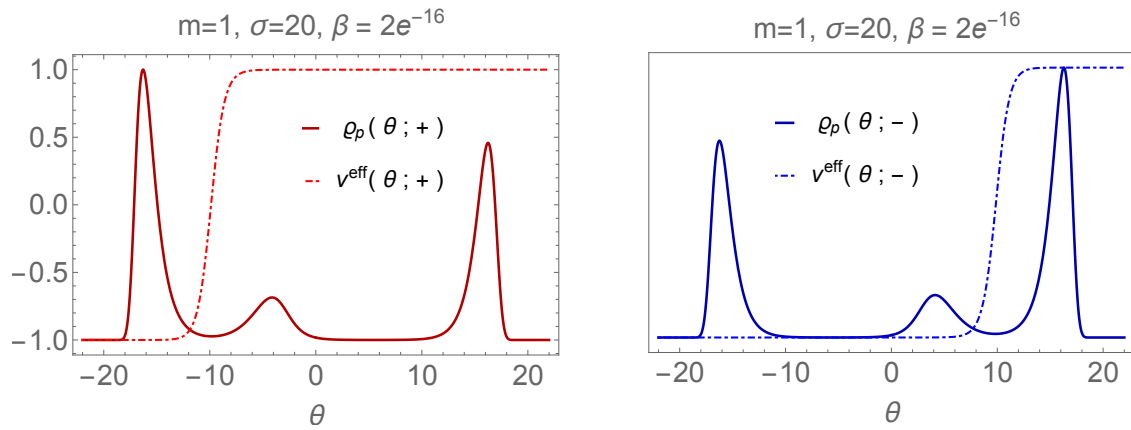


Figure 8.7 The effective velocities versus the normalized spectral densities $\rho_p(\theta; \pm) = 2\rho_p(\theta; \pm)/\tilde{\rho}^\pm - 1$ where $\tilde{\rho}^\pm$ is the height of the largest local maximum. The inverse temperature is $\beta = 2e^{-16}$. The subsidiary peak of particle + (particle -) and the interacting peak of particle - (particle +) are co-moving at velocity +1 (-1). This is a direct consequence of the formation of unstable bonds and of the homogeneity of the equilibrium state.

We illustrate this with Fig. 8.7, which shows the same high temperature physics we have seen in Subsections 8.3.1 and 8.3.2 and combines scaled versions of the curves found in the right panels of Figs. 8.5 and 8.6. Consider the positions of the local maxima of the spectral densities in Fig. 8.7 and the corresponding values of the velocities. For particle + (left panel, red) the density has maxima around $\log \frac{\beta}{2} \approx +16$ (free fermion peak), ≈ -4 (subsidiary peak) and ≈ -16 (interacting peak). Comparing with the effective velocity curve, the particles these peaks represent have velocities very nearly +1, +1 and -1, respectively. For particle - (right panel, blue), the maxima of the free fermion, interacting and subsidiary peaks are around $\log \frac{\beta}{2} \approx -16$, ≈ 4 and $\approx +16$, respectively, with velocities -1, -1 and 1, respectively.

Thus, the velocities associated with the interacting peak of each distribution and the subsidiary peak of the other distribution are *always the same*. These particles are co-moving and thus have the opportunity to bond. Since, as we observed in Subsection 8.3.2, their rapidity separation $\pm\sigma$ are at the maxima of the scattering kernel $\varphi_{\pm\mp}(\theta)$, these particles are indeed subject to a strong interaction, and can form bound states (even if only finitely-lived). Further, as the “excess” area of the interacting peaks are roughly the same as the areas of the subsidiary peaks, the excess density created by the onset of interaction and the subsidiary peak can be interpreted as pairs of bound (+-) and (-+) particles propagating at the same speed. These are the unstable particles, gathered within two clouds, one right-moving and one left-moving. The population of unstable, finitely-lived particles thus formed is rendered stable by the high energy of the thermal bath and the continuous availability of co-moving,

interacting particles of opposite types.

In summary, varying the temperature and observing the various structures form with their respective effective velocities, is the most direct way we know of “visualizing” the formation of the unstable particle. This visualization is particularly striking when observing the continuous change of the densities as temperature is increased in [this video](#).

Finally, this new perspective connects to the hydrodynamic scaling functions as follows. In the UV, we have degrees of freedom coming from two free fermions (each with its right- and left-moving components), and, in addition, one unstable particle (also with its right- and left-moving components). In order to account for these quantitatively, we need to look at the energy per unit temperature-square carried by the particles, namely

$$\frac{6\beta^2}{\pi} e(\theta) \rho_p(\theta; \pm) \quad (8.20)$$

The total area under the curves is exactly the energy density $(6\beta^2/\pi)\mathbf{q}_1^\pm$, and according to Section 8.2 the sum gives the central charge. If we then subtract the free fermion contributions we obtain an effective measure of the degrees of freedom of the unstable particle:

$$\frac{6\beta^2}{\pi} \Delta\mathbf{q}_1 = \frac{6\beta^2}{\pi} \sum_{b=\pm} \int d\theta e(\theta) (\rho_p(\theta; \pm) - \rho_p^{\text{FF}}(\theta)) \quad (8.21)$$

This represents 1/5 of the energy area covered by the free fermion parts (this corresponds to $c = 1$ for two free fermions), as it should. We then observe that the contributions coming from the excess area of the interacting peaks largely dominate the contributions from the subsidiary peaks, as the subsidiary peaks are at smaller values (in absolute values) of rapidities (thus they carry less energy). Therefore, the contribution of each \pm particle to the energy current and densities, and to the central charge, coming from the clouds of unstable particles is dominated by the excess density of the interacting peak.

Furthermore, for + particles, say, the interacting peak consists of particles propagating with velocity -1 . As this dominates any contribution from the subsidiary peak, this means that there are more highly energetic + particles propagating with velocity -1 than there are with velocity $+1$. Therefore a negative energy current is generated, as observed in Subsection 8.2.1.

8.4 Out-of-equilibrium dynamics with unstable particles

We now consider the two subsystems with temperature ratio $x \neq 1$, and explore the resulting out-of-equilibrium effective velocities and spectral densities. As pointed out earlier, when driving the system out of equilibrium this gives rise to different dynamics whether or not the original baths admit formation of unstable particles. It is thus helpful to introduce the variable $\kappa_{L,R} = -\log \frac{\beta_{L,R}}{2} - \frac{\sigma}{2}$ associated to each bath of the system at $t = 0$ to identify their initial energetic regimes given by (7.20), (7.21) and (7.20).

8.4.1 Effective Velocities

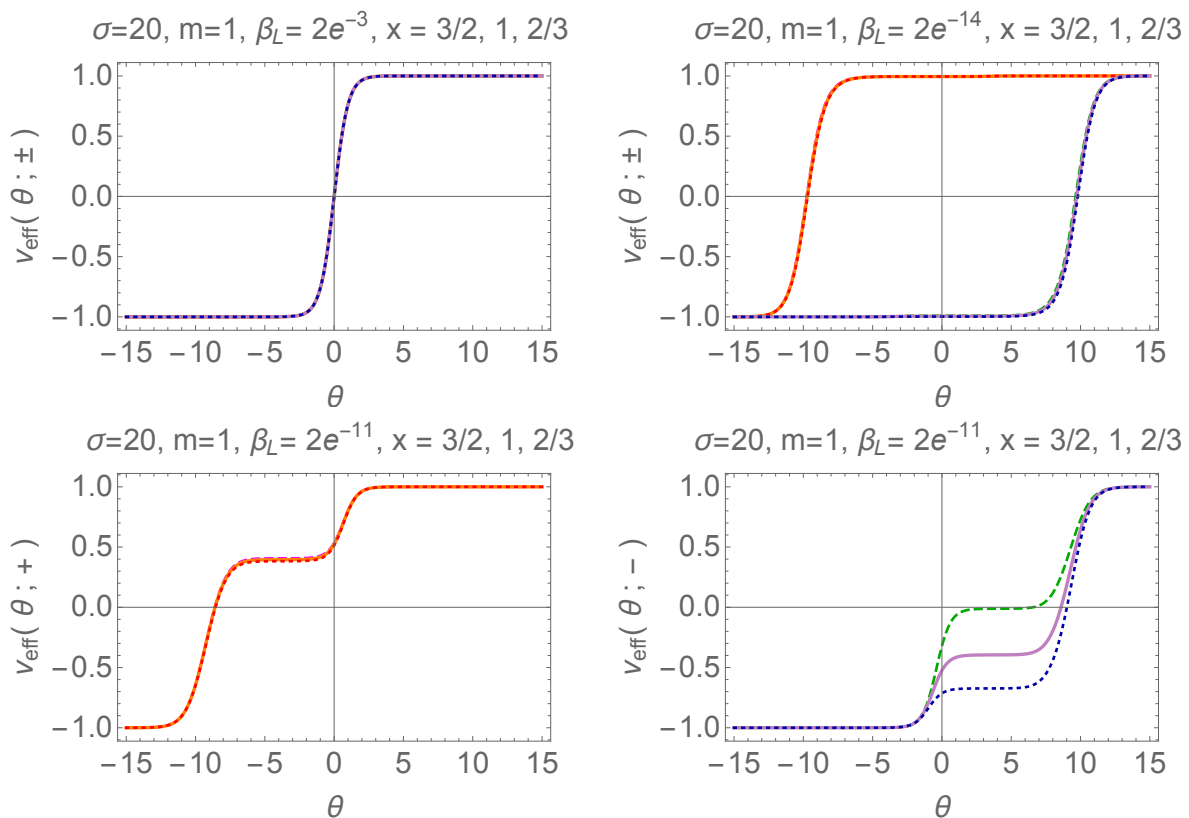


Figure 8.8 Steady state effective velocities for three values of β_L and three values of x , including (for comparison) the equilibrium case $x = 1$. The velocity profiles retain many of their equilibrium features. In the bottom right figure $x = \frac{3}{2}$ (dashed, green), $x = 1$ (solid, pink) and $x = \frac{2}{3}$ (dotted, blue). The variation of the velocities with temperature can be further explored in [this video](#) [158].

In this section we take another look at the effective velocities with a focus on changes with respect to the equilibrium behaviour. Fig. 8.8 explores this behaviour for low, intermediate and high temperatures. Our main observations are the following:

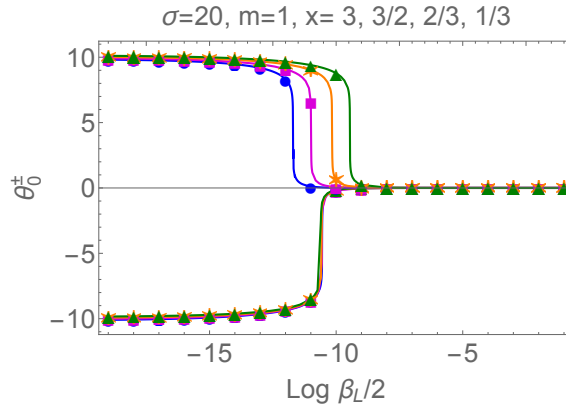


Figure 8.9 Values of θ_0^\pm for various ratios x as functions of $\log \frac{\beta_L}{2}$, with $\theta_0^+ \leq 0$ and $\theta_0^- \geq 0$. The signs are as expected from the behaviours of the effective velocities seen in Fig. 8.8. The same symbols are employed for θ_0^\pm and each given x .

- **Conformal regime** ($\kappa_{L,R} \ll 0$, $\kappa_{L,R} \gg 0$): Both at low and high temperatures the equilibrium behaviours are recovered. For low temperatures we find the free fermion result. For very high temperatures we find the conformal equilibrium result. Once temperature is high enough the UV result is approached even if $\beta_L \neq \beta_R$.
- **Particles couple mainly to one bath** ($\kappa_{L,R} \gtrsim 0$): For intermediate temperatures, like the ones considered in the second row of Fig. 8.8, we observe that whereas $v^{\text{eff}}(\theta; +)$ is virtually unchanged as long as β_L is fixed, even if β_R is changed, $v^{\text{eff}}(\theta; -)$ is very much dependent on the values of β_R . This can be explained by the same arguments presented in Subsection 8.2.2.
- **Effective velocities zeroes** ($\kappa_{L,R} \sim 0$): The height of the intermediate plateau of the velocities that emerges for intermediate temperatures changes with temperature so that there exists a choice of temperatures $\log \frac{\beta_R}{2} \approx -10$ for which the plateau of the $-$ particle velocity is at height zero (as on the dashed green line in the bottom right panel of Fig. 8.8) and similarly for particle $+$. This suggests that the effective velocities at this particular temperature have a continuous set of zeroes. However this is a numerical effect. The results for θ_0^\pm shown in Fig. 8.9 shows that the values of θ_0^\pm are always unique but that for some small range of temperatures our algorithm is not accurate enough to precisely identify these values. In other words, the intermediate plateau of the effective velocities is never exactly flat, but its slope is too small to be seen numerically.
- **Intermediate regime** ($\min\{\kappa_{L,R}\} \lesssim 0$, $\max\{\kappa_{L,R}\} \gtrsim 0$): At intermediate temperatures the on set of unstable particles may be only on one original bath. This is clear in Fig.

8.9 as the plateaux at velocity zero are clear signatures of the formation of the unstable particles, and these occur at distinct temperature for + and - particles. Following the second point, there is not a drastic change in the dynamics as each particle is mainly coupled to one bath.

8.4.2 Spectral densities

Let us now discuss how the spectral densities change in an out-of-equilibrium situation. Fig. 8.10 shows three examples for low, intermediate and large temperature which can be easily compared with Fig. 8.6. We notice the following new features:

- **Free fermion regime** ($\kappa_{L,R} < 0$): For low temperatures (Fig. 8.10, left panel) we recover the out-of-equilibrium free fermion behaviour

$$\rho_p(\theta; \pm) = \frac{1}{2\pi} \cosh \theta \left(\frac{\Theta(\theta)}{1 + e^{\beta_L \cosh \theta}} + \frac{\Theta(-\theta)}{1 + e^{\beta_R \cosh \theta}} \right).$$

The maxima are centered around $\theta = \log \frac{\beta_R}{2}$ and $\theta = -\log \frac{\beta_L}{2}$ and continue to be so even at higher temperatures.

- **Onset of the interaction** ($\kappa_{L,R} \sim 0$): As in the equilibrium situation, the heights of the free fermion peaks start to change after the onset of the unstable particle (Fig. 8.10, middle panel). However still the right peak of particle + density coincides with the free fermion peak at temperature β_L and the left peak of the - spectral density coincides with the free fermion peak at inverse temperature β_R . These are the free fermion peaks that we had identified in the equilibrium situation. The opposite peaks, which have higher heights than they would in a free fermion theory, are the interacting peaks, as also identified in the equilibrium situation. Importantly, by contrast here the peaks of + and - particles have different heights.
- **Three Local Maxima** ($\kappa_{L,R} \gg 0$): For very high temperatures (Fig. 8.10, right panel), we observe once more a structure with three local maxima per density. The additional (smaller) maxima are located at $-\log \frac{\beta_L}{2} - \sigma$ (red curve, + spectral density) and $\log \frac{\beta_R}{2} + \sigma$ (blue curve, - spectral density). Following the nomenclature used in the equilibrium situation, these are the subsidiary peaks. Once more, the excess area of the left-most, interacting peak in the density of + particles (compared to the free fermion peak at inverse temperature β_R) roughly coincides with the area of the subsidiary peak in the density of

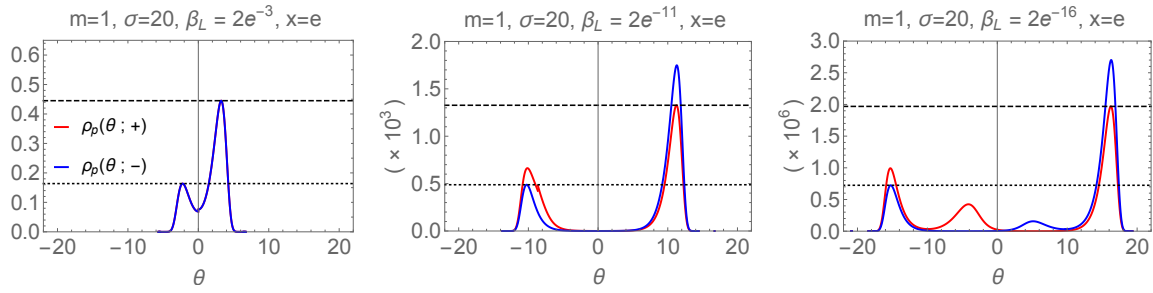


Figure 8.10 Spectral Densities for $\mathbf{x} = e$ ($T_L > T_R$) and three values of the inverse temperatures ($\beta_L = 2e^{-3}, 2e^{-11}$ and $2e^{-16}$). For the two highest temperatures the vertical axis labels should be multiplied by 10^3 and 10^6 , respectively, as indicated. In all panels, dashed (dotted) horizontal lines indicate the height of the free-fermion peaks, $0.04431.../\beta_L$ ($0.04431.../\beta_R$). A more complete picture of the dynamics can be gained from [this video](#) [159].

– particles. This is made more precise at the end of this subsection.

- **Formation of the Unstable Particle** ($\kappa_{L,R} \gg 0$): As for the equilibrium case we can argue that the excess density of the interacting peak of the + spectral density “couples” to the subsidiary peak of the – spectral density and viceversa to form a finitely-lived unstable particle. The only difference with respect to the equilibrium case is that the areas and heights of all six maxima in the two spectral densities are distinct. In particular, the smallest maxima of both distributions are now different as one is governed by the right temperature and the other by the left temperature. This can be seen more precisely in the additional Fig. 8.11. By computing the areas of all the peaks and comparing them to each other, this out-of-equilibrium analysis confirms the dynamical explanation of the formation of unstable particles, by allowing for an unambiguous identification of the coupling between + and – particles. A numerical evaluation of these areas is presented below.
- **Comparison to Equilibrium:** Considering the densities in Fig. 8.11 we observe the following: for the + particles density we find that the two right-most peaks – the free fermion and subsidiary peaks – are perfectly well described by the equilibrium density at inverse temperature $\beta = \beta_L = 2e^{-16}$ whereas the left-most peak – the interacting peak – is described by the equilibrium density at inverse temperature $\beta = \beta_R = 2e^{-15}$. The same “cut and paste” structure is observed for the – particles distribution, where the “cut” is now located around $\theta = 10$ (this is the the value of θ_0^- as seen from Fig. 8.9). This behaviour can be best explained when matching densities with effective velocities. The velocities associated to the various types of peaks (free fermion, subsidiary and interacting) are distributed as in the equilibrium case, but now, these determine the

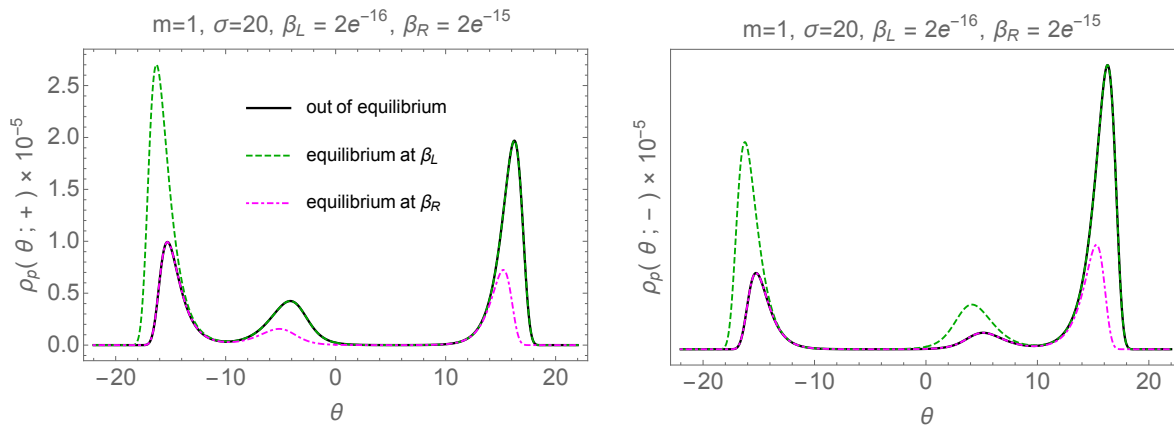


Figure 8.11 Spectral densities at equilibrium for temperatures $\beta = \beta_R = 2e^{-15}$ and $\beta = \beta_L = 2e^{-16}$ and out of equilibrium for the same temperatures. The out-of-equilibrium spectral densities exhibit a “copy and paste” effect as each peak reproduces exactly a local maximum of the equilibrium spectral densities at one of the two bath temperatures β_L and β_R . As a result, many of the GHD quantities (described in Subsections 8.2.2 and 8.4.1) couple mainly to one bath.

initial bath the particles come from, and thus the temperature they carry.

$\log \beta_L/2$	t_{\min}^+	t_{\min}^-	A_+	B_+	B_-	A_-
-15	-9.9099	9.4771	26433.3	68869.5	24477.7	70810.8
-16	-9.9802	9.6275	70689.5	189237.	68793.3	191195.
-17	-9.9802	9.7162	191302.	516162.	189231.	518292.

Table 8.1: Excess areas of the interaction peaks of the spectral densities A_{\pm} compared to the areas of the subsidiary peaks B_{\pm} . As expected $A_+ \approx B_-$ and $A_- \approx B_+$.

Before concluding this subsection we would like to make our statements about the areas of the various maxima of the spectral densities a little bit more precise. For this purpose let us define the following quantities:

$$\begin{aligned}
 A_+ &:= \int_{-R}^{t_{\min}^+} d\theta (\rho_p(\theta, +) - \rho_p^{FF}(\theta, +)_{\beta_L}), & A_- &:= \int_{t_{\min}^-}^R d\theta (\rho_p(\theta, -) - \rho_p^{FF}(\theta, -)_{\beta_R}), \\
 B_+ &:= \int_{t_{\min}^+}^5 d\theta \rho_p(\theta, +), & B_- &:= \int_{-5}^{t_{\min}^-} d\theta \rho_p(\theta, -).
 \end{aligned} \tag{8.22}$$

where $R = \log 2/\beta_L + 6$, t_{\min}^{\pm} is the position of the local minimum of the spectral density that is located between the interacting and subsidiary peaks (that is approximately ± 10 in Fig. 8.11). $\rho_p^{FF}(\theta; \pm)_{\beta}$ is the free fermion spectral density given by (8.19) at inverse temperature β . The subsidiary peaks of the \pm spectral densities are then located approximately in the intervals $[t_{\min}^+, 5]$ and $[-5, t_{\min}^-]$. The choice of the integration limits is of course slightly arbitrary, so

the areas below are just an illustration of the general statement that $A_+ \approx B_-$ and $A_- \approx B_+$. In contrast to the equilibrium case it is now clear that $A_+ \neq B_+$ and $A_- \neq B_-$, therefore our argument based on attributing a certain area of the spectral density curves to the formation of unstable particles is only plausible if we “couple” the \pm spectral density curves.

8.5 Conclusions

In conclusion, our numerical study of the $SU(3)_2$ -HSG model in the partitioning protocol has shown that it is possible to outline a more physical understanding of unstable excitation in integrable models by employing the GHD approach. Even at equilibrium, we found a very direct evidence for such unstable bound states, that is the identification of mutual interacting areas of quasiparticle densities which are co-moving in the phase-space. We observe a similar physics when driving the system out of equilibrium, the only difference is that the resulting areas are in different proportions, signaling that, one bath is more energetic in the initial state and the stable particles there have more occasion to bond. In both cases, we can identify these areas with a stable population of unstable excitations, where the stability is due to the homogeneity and the high-energy of the initial state as well as the large-time dynamic description employed in this particular set-up. It is thus reasonable to look into more general set-ups where we can fully exploit the power of the GHD approach to look for truly dynamic signatures of instability. This will be the purpose of the final chapter of this thesis.

SET-UP 2: INHOMOGENEOUS QUENCH

9.1 The inhomogeneous quench

In this chapter we study the $SU(3)_2$ -HSG model in an inhomogeneous quench. In particular we prepare the system in an initial state characterised by spacial inhomogeneities via the following Gaussian temperature profile:

$$T(x) = T_a + (T_m - T_a)e^{-x^2} \quad \text{with} \quad T_a, T_m \in \mathbb{R}_{\geq 0}, \quad (9.1)$$

and all the TBA functions will be accordingly space-dependent. We will refer to T_a as the *bath temperature* and T_m as the *maximal temperature*. Given such an initial configuration, the quench consists in letting the system evolve at time $t \neq 0$, and the resulting out-of-equilibrium dynamics is described by the GHD equations (7.38) as seen for instance in [160–163] and also summarised in Section 7.3. In free theories $v^{\text{eff}}(x, t, \theta) = \tanh \theta$, and therefore, at large temperatures, where large rapidities are involved, excitations mostly move at velocities ± 1 . Typically, interaction in most integrable QFTs does not qualitatively change the effective velocity, and the same holds near interacting conformal points. This leads to the splitting of the original particle density maximum at $x = 0$ into two identical maxima propagating in opposite directions [160–163].

In this chapter, we will see that the presence of unstable particles modifies this picture substantially. We will analyse the numerical results presented in [36], and obtained by adapting the iFluid package [164], which is a MATLAB code that solves GHD for a wide range

of conditions and integrable models. More details are presented in Appendix D. Before exploring the evolution, in the next subsection we want to discuss the choice of the simulations parameters

9.1.1 The initial state

In our numerics the initial state is defined by the simulation parameters T_a , T_m , and the free parameter of the theory σ . Since this state is at equilibrium, we know quite well its properties from the analysis in Section 8.3. Indeed a time $t = 0$, the TBA functions of interest are simply a three-dimensional version of those seen at equilibrium in the homogeneous state (an example is shown in Fig. 9.1 for the spectral density of particle + and will be analysed in detail in the next section).

A conclusion from the previous chapter is that even out of equilibrium, the initial conditions of the system may “hide” the decay of the finitely lived excitations, so that now we can ask: in which state do we need to initialise the system in such a way as to observe direct evidence of the instability of the bound states?

To answer this question we make some simple observations based on the analysis in Sections 8.3 and 8.4. We introduce the parameters $\kappa_{a,m} = \log 2T_{a,m} - \sigma/2$, and set the maximal temperature T_m in an interacting regime i.e. $\kappa_m > 0$ in such a way as to define certain regions of the phase-space with high populations of mutually interacting particles: these are indeed the particles that bound to create unstable particles. One should observe that in the partitioning protocol, the excess areas identified in Subsection 8.3.3 and 8.4.2, are associated with unstable excitations that are constantly created and destroyed, giving rise to stable populations of unstable particles even out of equilibrium. This is because the stable particles are homogeneously distributed in space and thus provide a constant particle reservoir to form such unstable bonds. In contrast, in this set-up, the out-of-equilibrium evolution of the particle modes, combined with the inhomogeneities of the initial state give rise to a situation where created and destroyed unstable particles may be not sufficiently balanced and we should be able to observe effective evidence of the short-time life of the particle in the GHD quantities of interest. One way to engineer such a physical situation is by releasing these hot and highly interacting finite densities of particles into a low-temperature environment, and thus choose the simulation parameters in the following regimes:

$$\kappa_a < 0 < \kappa_m \ll \kappa_{UV}. \quad (9.2)$$

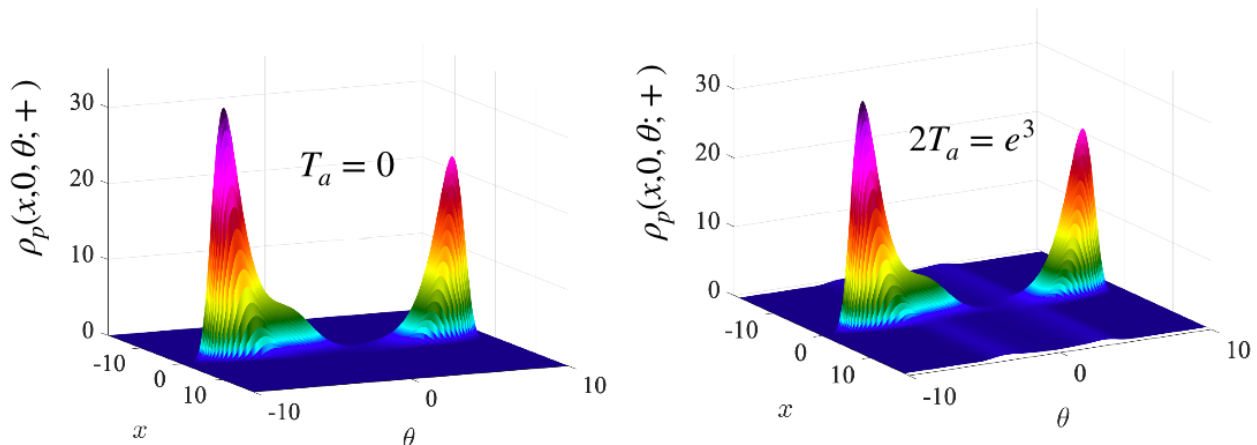


Figure 9.1 The equilibrium spectral density of particle $+$ initialised in the two numerical simulations analysed in this chapter, with fixed parameters $\sigma = 10$ and $2T_m = e^7$ and bath temperature either $2T_a = 0$ or $2T_a = e^3$. In this last case, the environment is filled by spacial homogeneous densities of free fermions.

In this set-up the population of unstable particles will be accordingly modified by the lower particle reservoirs of the bath. Note that, above, we have additionally required that our system is far from the UV, which occurs for $\kappa_{UV} \sim 3$ according to our numerics at equilibrium. Indeed in the UV regime, the finite densities of quasiparticles are found to be too energetic and more likely to interact, which makes it much harder to observe any signatures of unstable particle decay.

9.2 Full dynamics

We are now ready to present our numerical results. In this section, we aim to capture the full dynamical picture and we then want to analyse it in more detail in the next two sections. We choose $\sigma = 10$, $2T_m = e^7$ (i.e. $\kappa_m = 2$) and the bath temperature T_a is either 0 or within the free fermion regime $2T_a = e^3$.

We focus our analysis on the spectral densities and effective velocities of particles $+$, defined in (7.37), and on the particle densities defined in (7.36) for $i = 1$. Another quantity of interest is obtained by subtracting the free fermion contribution \mathbf{q}_0^{FF} to each particle density q_0^+ :

$$\Delta \mathbf{q}_0^+(x, t) = \mathbf{q}_0^+(x, t) - q_0^{\text{FF}}(x, t), \quad (9.3)$$

where

$$\mathbf{q}_0^{\text{FF}}(x, t) = \frac{1}{2\pi} \int_{-\infty}^{\infty} d\theta \frac{\cosh \theta}{1 + e^{-\beta(x, t, \theta) \cosh \theta}}, \quad (9.4)$$

For the free fermion, an explicit solution to the GHD equation is known and is

$$\beta(x, t, \theta) = \frac{1}{(T_m - T_a)e^{-(x-t \tanh \theta)^2} + T_a}, \quad (9.5)$$

given the initial state (9.1) and the fact that the free fermion propagation velocity is simply $\tanh \theta$.

Due to the symmetry of the initial state, and the parity transformations of the model, the dynamical quantities of particle + and - satisfy the following relations:

$$\rho_p(x, t, \theta; +) = \rho_p(-x, t, -\theta; -), \quad v^{\text{eff}}(x, t, \theta; +) = -v^{\text{eff}}(-x, t, -\theta; -). \quad (9.6)$$

$$\mathbf{q}_0^+(x, t) = \mathbf{q}_0^-(-x, t) \quad \Delta \mathbf{q}_0^+(x, t) = \Delta \mathbf{q}_0^-(-x, t). \quad (9.7)$$

Thus we can only focus on the dynamics of one particle, say +, and use the transformation above to obtain the dynamics of particle -. Alternatively, we can focus on both particles and consider only $x > 0$ (or similarly $x < 0$).

As emphasised in Chapter 8, the analysis of spectral densities is helpful in determining the composition of finite-density states. For our choice of parameters, the spectral density of particle + at time $t = 0$ is shown in Fig. 9.1. We can identify three peaks respectively at $\theta \approx -\log(2T_m) = -7$ (interacting peak), $\theta \approx +\log(2T_m) = 7$ (free fermion peak), and $\theta \approx +\log(2T_m) - \sigma = -3$ (subsidiary peak). The subsidiary peak represents the proportion of particles + loosely bound with particles -. In Fig. 9.1 the interacting and the subsidiary peaks are not completely apart, but they will evolve in opposite directions as we know from Section 8.3 that their effective velocities are of opposite signs (this can be seen also in Fig. 9.2, in the next subsection). Additionally in the presence of a bath, two identical ridges are formed around $\theta \approx \pm 3$ and represent a continuum of free propagating particles.

9.2.1 Tail and decay

Consider a zero-temperature environment as in the colorspace plots in Fig. 9.2. The first row illustrates the behaviour of the spectral density of particle + as a function of time. At time $t = 0$ this is exactly the three-dimensional function plotted on the left picture in Fig. 9.1. The effective velocity (the second row), for $t = 0$, shows that the interacting (free fermion) peak moves at speed -1 ($+1$), and the subsidiary peak contains a spectrum of effective velocities captured by the ‘rainbow’ colouring which indicates the presence of intermediate plateaux in

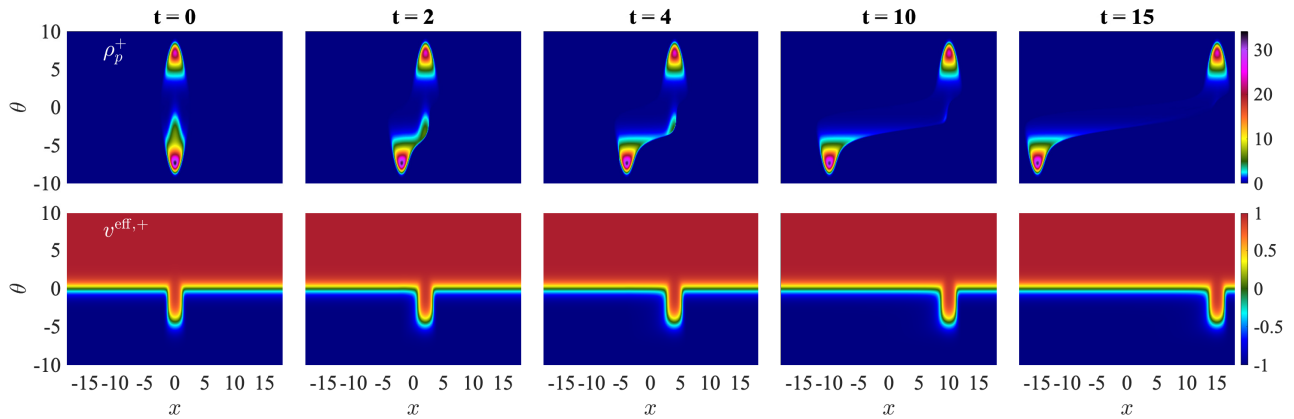


Figure 9.2 Particle + dynamics for various time snapshots, the parameters are $\sigma = 10$, $T_a = 0$ (no bath) and $2T_m = e^7$. Particle – dynamics follows from (9.6). We introduce the short notation $\rho_p^+ = \rho_p(x, t, \theta; +)$ and $v^{\text{eff},+} = v^{\text{eff}}(x, t, \theta; +)$. Row 1: Spectral density exhibiting three characteristic local maxima, the least of which decays in time leading to the formation of a tail. Row 2: Effective velocities dominated by the values ± 1 but exhibiting an intermediate plateau in rapidity space which is correlated with the decaying peak of the spectral density.

the rapidity variable.

Turning on time, the most salient feature is that the subsidiary peak moves as per the initial splitting, but then falls apart, leaving behind a tail of particles moving with velocities tending to -1 . Unstable particles start moving at speed near $+1$, but, as they enter the zero-temperature environment, decay faster than they can form, and we see the particle + components un-binding and recovering their non-interacting speeds near to -1 . After the initial splitting, the right-moving wave reduces in time, leaving just the free fermion contribution (which remains unchanged for larger times) and a tail attached to the left-moving wave at $x < 0$.

9.2.2 Magnetic-fluid effect

Do these behaviours change in the presence of a bath at nonzero temperature? Fig. 9.3 shows the $x \geq 0$ part of the functions $\rho_p^\pm(x, t, \theta)$ (see also [this video \[165\]](#) for a complete three-dimensional view). The presence of a bath does not significantly change the effective velocities as free fermions propagate with velocity $\tanh \theta$.

In contrast, an important change occurs in the spectral densities: the subsidiary peak observed at time $t = 0$ no longer fully disintegrates under time evolution. Instead, it largely persists, propagating on top of the $\theta = -3$ ridge. Because of the spread of effective velocities in the initial subsidiary peak, this cannot be explained by a large population of particles at constant velocity $+1$. Indeed, there is a large difference between the effective velocity of these

particles and the propagation velocity of the peaks (this will be discussed in details in Section 9.3). Why is this wave travelling at speed $+1$, riding on the bath? The answer is that the large wave of particles $-$ going at velocity $+1$ interacts with particles $+$ in the bath, because they are present around the rapidities of the subsidiary peak. They form unstable particles as they pass by, thus changing the bath density. The phenomenon observed in Fig. 9.3 is reminiscent of

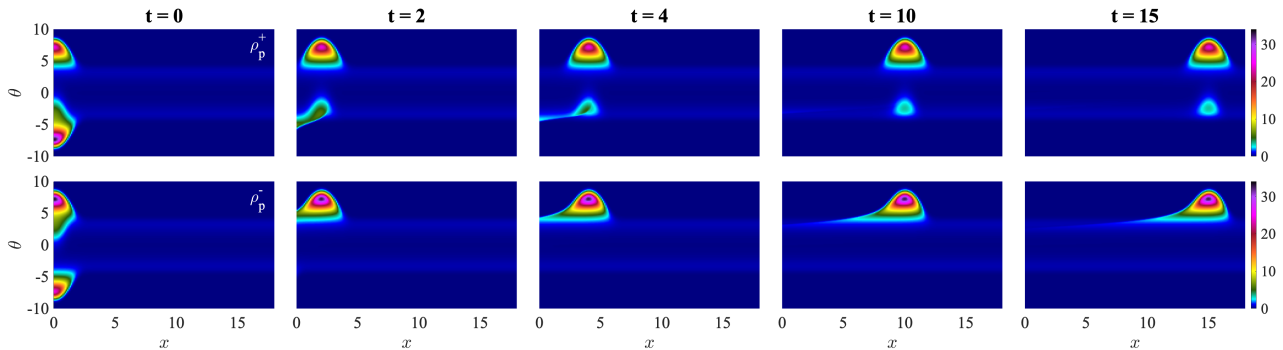


Figure 9.3 Snapshots of the spectral densities $\rho_p^\pm = \rho_p(x, t, \theta; \pm)$ for $x \geq 0$ in the presence of a bath at temperature $2T_a = e^3$, $\sigma = 10$ and $2T_m = e^7$. Recalling (9.6), the dynamics for $x < 0$ is straightforward. Whilst the interacting and free fermion peaks remain largely unchanged, the bath facilitates the formation of a persistent peak that travels at speed $+1$ “riding” on the bath. The two light-blue ridges are also due to the bath whose temperature is in the free fermion region of the theory. The ridges look “static” because they are uniformly distributed in space but represent particles propagating with opposite effective velocities ± 1 . See also the videos [165, 166].

that of a magnet passing by a magnetic fluid: here, the decaying subsidiary peak is driven over the bath as the bath interacts with the magnet-like interacting peak travelling at velocity $+1$ (these are indeed found at the rapidity distance that maximises their interaction). The overall effect is the creation of a wave that follows the magnet. However the fluid itself does not need to move at velocity $+1$, meaning that this wave is always formed of different particles coming from either the bath and the subsidiary peak that under the effect of the magnet give rise to a *persistent peak*. We remark that the life-time of the unstable particles is of order $e^{-\frac{\sigma}{2}}$, and thus is not directly observable: unstable particles rapidly decay and reform within the persistent peak, with the end result of preserving it for large times.

9.2.3 Bath vs. no bath

The full dynamical picture described earlier can be summarised in [this video](#) [166]. Furthermore, similar features such as tail and decay can be found in the particle densities, as we can see for particle $+$ in left figures Fig. 9.4 and bath temperatures $2T_a = 0$ (top) and $2T_a = e^3$ (bottom). We recall that the particle densities are simply the spectral densities

integrated in θ , therefore they describe the same physics seen earlier but in real space. Finally we explore the function (9.3) for particle + in the right pictures. For $x \geq 0$ this function describes only particles of the (either decaying or persistent) subsidiary peak and the tail. The effect of the bath is seen starkly in the right-bottom picture: the persistent peak of the spectral density displayed in Fig. 9.3 corresponds to a right-mover peak propagating with velocity +1, which remains unchanged over time. In contrast for $T_a = 0$ the peak is decaying and only the tail is left at large time.

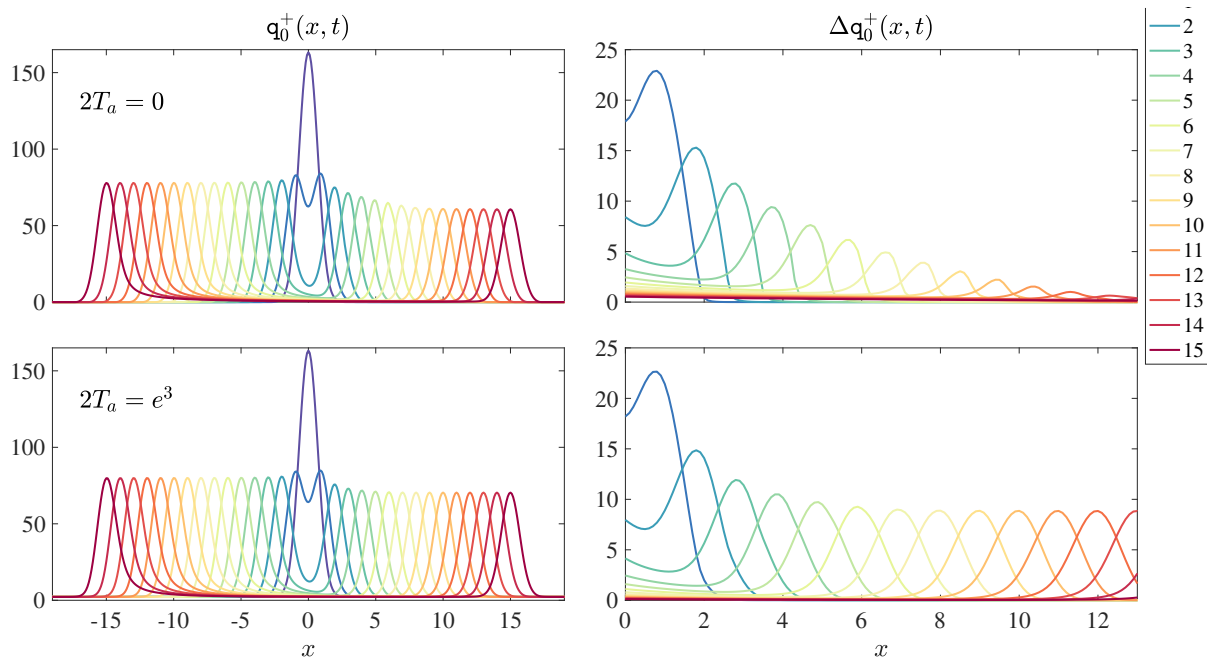


Figure 9.4 Particle density of particle + (left) and Δq_0^+ (right) at time t indicated in the legend. The pictures show the full decay of the left-mover peak in the absence of a bath (top), and its persistence in the presence of a bath (bottom). The highest functions in the top left and bottom left figures are at $t = 0$.

It is worth mentioning that the presence of a persistent peak is not a consequence of fine tuning of parameters but a robust effect, present more generally for initial states in the regime (9.2), as peaks have finite extension and will overlap for a wide range of temperatures. Other examples will be shown in [148], where a more detailed analysis on the variation of parameters will be conducted. Further evidence that the signatures of decay found here provide a non-trivial characterisation of unstable particles is provided in the next two subsections.

9.3 A closer look to the subsidiary peak

We have seen that both the function Δq_0 (see Fig. 9.4) and the spectral density (see Figs. 9.2 and 9.3) exhibit a peak which either decays or persists for large times, depending on whether or

not there is a bath. In this section, we examine the features of this peak in more detail. We will look at cross-sections of the spectral density's subsidiary peak and of the velocity distribution for particles in this peak, for fixed values of x and t . We will make an important distinction between effective and propagation velocities and show that these are in general different, a feature that is dictated by interaction with the interacting peak of the opposite particle type and would therefore be absent if evolution was free, as explored in Section 9.4.

9.3.1 Effective vs. propagation velocities

Let us consider the effective velocity of particles both in the presence and in the absence of a bath. We will report on particle + with particle – admitting an analogous analysis. Data facilitating this discussion is presented in Table 4.

t	No bath					Bath				
	x^*	θ^*	h^*	x^*/t	v^*	x^*	θ^*	h^*	x^*/t	v^*
2.00	1.90	-3.30	5.89	0.95	0.61	1.80	-3.44	5.89	0.90	0.54
3.00	2.80	-3.15	5.50	0.93	0.65	2.80	-3.07	5.47	0.93	0.67
4.00	3.80	-2.70	5.07	0.95	0.76	3.80	-2.70	5.03	0.95	0.76
5.00	4.90	-2.17	4.80	0.98	0.84	4.70	-2.54	4.53	0.94	0.77
6.00	5.70	-2.17	4.57	0.95	0.82	5.70	-2.24	4.06	0.95	0.81
7.00	6.50	-2.17	3.78	0.93	0.78	6.90	-2.39	3.42	0.99	0.81
8.00	7.50	-1.79	2.90	0.94	0.81	7.90	-2.39	3.41	0.99	0.81
9.00	8.40	-1.64	2.19	0.93	0.79	9.00	-2.39	3.41	1.00	0.81
10.00	9.40	-1.26	1.50	0.94	0.80	10.00	-2.39	3.41	1.00	0.81
11.00	10.30	-1.03	0.96	0.94	0.77	11.00	-2.39	3.42	1.00	0.81
12.00	11.30	-0.50	0.56	0.94	0.78	12.00	-2.39	3.42	1.00	0.81

Table 9.1: Numerical results for the subsidiary peak of the spectral density of particle + in the absence ($T_a = 0$) and presence ($2T_a = e^3$) of a bath. The other parameters are fixed to $\sigma = 10$ and $T_m = 2e^7$ as before. x^* , θ^* and h^* are the phase-space coordinates and the height of the local maximum of the subsidiary peak, respectively and $v^* \equiv v^{\text{eff},+}(x^*, t, \theta^*)$. The quantity x^*/t represents the observed propagation velocity of the subsidiary peak of particle + resulting from its interaction with the interacting peak of particle – which propagates at speed +1. The numerical uncertainty of phase-space coordinates is $\Delta x^* = 0.10$ and $\Delta \theta^* = 0.07$ to 0.08, with lower rapidity resolution for less negative values of θ^* (as discussed in Appendix D).

We consider two different velocities: the standard effective velocity $v^* := v^{\text{eff}}(x^*, t, \theta^*)$ evaluated at the maximum of the subsidiary peak, and the *propagation* velocity, x^*/t that is the actual speed at which the maximum of the peak is seen to propagate. The choices of times $t \in [2, 12]$ was dictated by the time of clear separation of the subsidiary peak from the interacting peak at $t = 2$ and the time at which almost complete decay of the subsidiary peak is observed for no bath at $t = 12$.

Looking at this table it is perhaps most striking that the effective and propagation velocities

are markedly different both in the presence and in the absence of a bath. Thus, even if the presence of a bath gives rise to the magnetic fluid phenomenon described in the paper, that is, the emergence of a persisting peak that seems to ride on top of the bath, the fact is that, in the absence of a bath, the interaction with particles of type $-$ still has a huge influence on the propagation velocity of the subsidiary peak. Indeed, the peak propagates faster than would be expected from its effective velocity distribution and this can only be attributed to non-trivial interaction with particles of type $-$ which is inextricably linked to the presence of unstable particles. This increase in velocity is however larger in the presence of a bath and for large times it reaches the maximum value $+1$.

In addition, we can make the following interesting observations:

- For early times data are very similar both in the presence and absence of a bath. Indeed, for times $t \in [2, 7]$ decay occurs whether or not there is a bath. We can see this decay most clearly from the table and the height of maximum h^* which reduces from 5.89 at $t = 2$ to 3.42 at $t = 7$. The way in which this decay or particle loss occurs is asymmetric in θ and results in an “under-cut” in the shape of the subsidiary peak, with the lost particles contributing to a growing tail linking the subsidiary peak to the interacting peak of the same particle species (this tail is seen most clearly in Fig. 9.2). As a result, not only the height of the maximum is reduced but its position in phase-space shifts towards less negative values of θ .
- In the absence of a bath, further asymmetric decay of the subsidiary peak continues until the peak disintegrates first into a front-like feature and ultimately into a section of the tail joining the free fermion and the interacting peak of the same species.
- In the presence of a bath, the subsidiary peak becomes persistent from time $t = 7$, with the rapidity space position fixed at $\theta^* = -2.39$, height $h^* = 3.42$ and propagation velocity $x^*/t = 1$. The fact that the subsidiary peak moves along the interacting peak at velocity $+1$ rather than the much slower effective velocity of its constituents is the embodiment of the magnetic-fluid mechanism, explained in Subsection 9.2.2. The subsidiary peak does not consist of the same particles propagating but instead of newly formed bound-states between the particles of the interacting peak of particle $-$ and the particle reservoir of particle $+$ available from the bath ridge. Nevertheless, the asymmetric decay process, being independent from the persistent feature, is still present in the case with bath. It is only masked by the dominant mechanism of the magnetic-fluid for times larger than

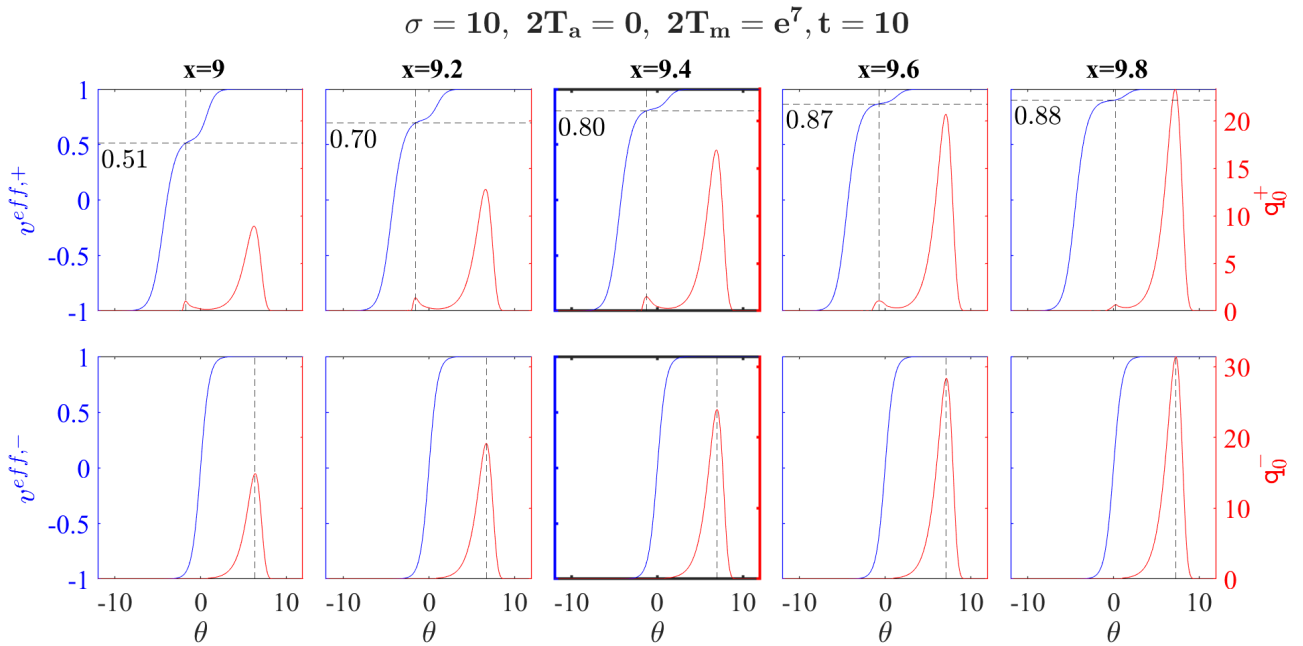


Figure 9.5 Effective velocities (left axis, blue) and spectral density cross-sections (right axis, red) of particle + in row 1 and – in row 2 at time $t = 10$ in the case of no bath. For particle + we see the subsidiary (decaying) and free fermion peaks whereas for particle – we see the interacting peak. Columns show these quantities sequentially for positions $x = 9, 9.2, 9.4, 9.6, 9.8$. The central emphasised column corresponds to $x = x^* = 9.4$, that is the position of the maximum of the subsidiary peak of particle +. The vertical dashed lines indicate the maximum of particle + subsidiary peak ($\theta^* = -1.26$) in row 1 and the maximum of particle – interacting peak in row 2, which is around the value $\theta^* + \sigma$ as dictated by the structure of the scattering phases. The horizontal dashed lines indicate the effective velocity of the maximum of particle + subsidiary peak and are annotated with the corresponding numerical values.

$$t = 7.$$

9.3.2 On the shape of the subsidiary peak

For time $t = 10$, a deeper understanding of the data can be reached in conjunction with FIGs. 9.5 and 9.6 which show cross-sections of the effective velocity and spectral density of particles \pm for the bath and no bath situations. In particular, we focus here on the shape of the subsidiary peak which can now be accessed more clearly through cross-sections at fixed space-time positions. Let us summarize our main observations:

- In Fig. 9.5. the subsidiary peak of particle +, although very small compared to the free fermion peak, can still be seen to be highly asymmetric both in the x -coordinate and rapidity space. In fact, it is more akin to a wave-front, with particles at the back slower than those in the front. It is worth noticing that by time $t = 10$ the decaying peak is also significantly lagging behind the interacting peak of particle – (since its propagating

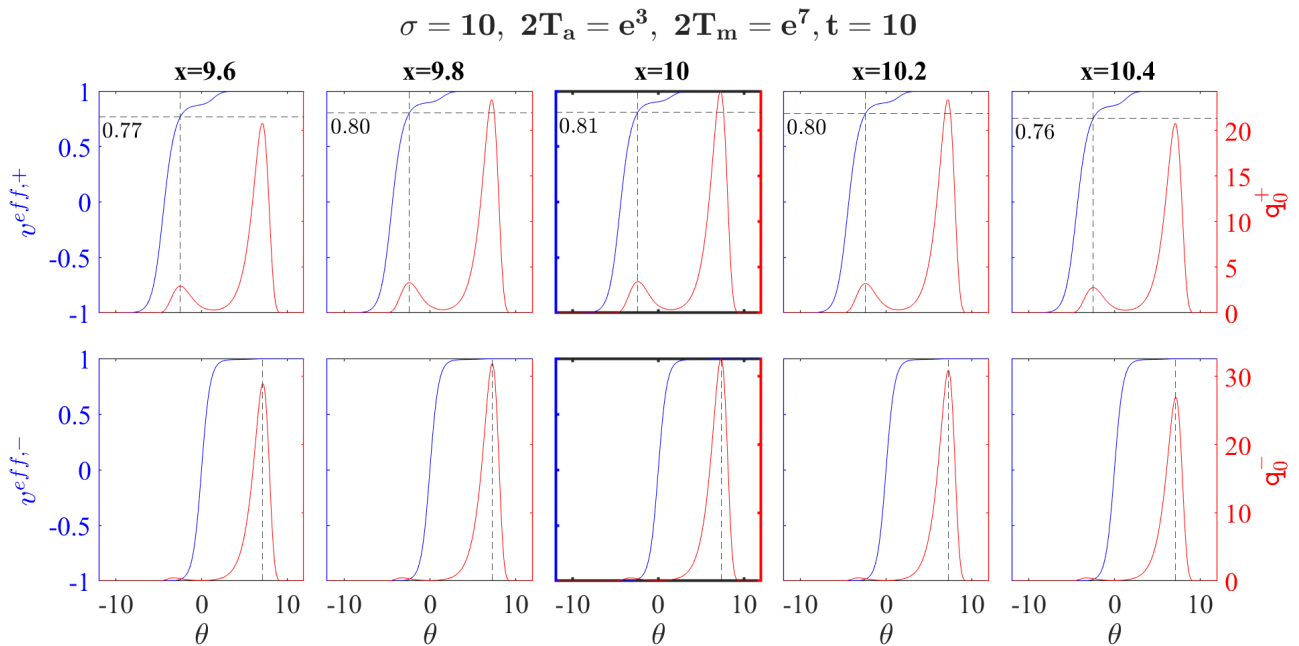


Figure 9.6 Effective velocities (left axis, red) and spectral density cross-sections (right axis, blue) of particle + in row 1 and – in row 2 at time $t = 10$ in the case of bath temperature $2T_a = e^3$. For particle + we see the subsidiary (persisting) and free fermion peaks whereas for particle – we see the (large) interacting peak a very small bump corresponding to the bath (for particle + this is masked by the persisting peak sitting right on top). Columns show these quantities sequentially for positions $x = 9.6, 9.8, 10, 10.2, 10.4$. The emphasised central column corresponds to $x = x^* = 10$ the position of the maximum of subsidiary peak of particle +. The vertical dashed lines indicate the maximum of particle + subsidiary peak ($\theta^* = -2.39$) in row 1 and the maximum of particle – interacting peak in row 2, which is around the value $\theta^* + \sigma$ as dictated by the structure of the scattering phases. The horizontal dashed lines indicate the effective velocity of the maximum of particle + subsidiary peak and are annotated with the corresponding numerical values.

velocity is 9.4 whereas for the interacting peak it is +1) and eventually falls out of its interaction range.

- In contrast with the last point, in Fig. 9.6 the peak is symmetric in the coordinate space and is accompanied by a velocity profile symmetric with respect to its maximum. The maximum of the subsidiary peak of particle + coincides in the coordinate space with the maximum of the interacting peak of particle – and both can be found at $x = 10$ for $t = 10$. Despite slower effective velocity, the propagation velocity of the subsidiary peak equals that of the magnet-like interacting peak, which interacts with the bath and drags the subsidiary peak along. This is the magnetic-fluid mechanism reported in Subsection (9.2.2).

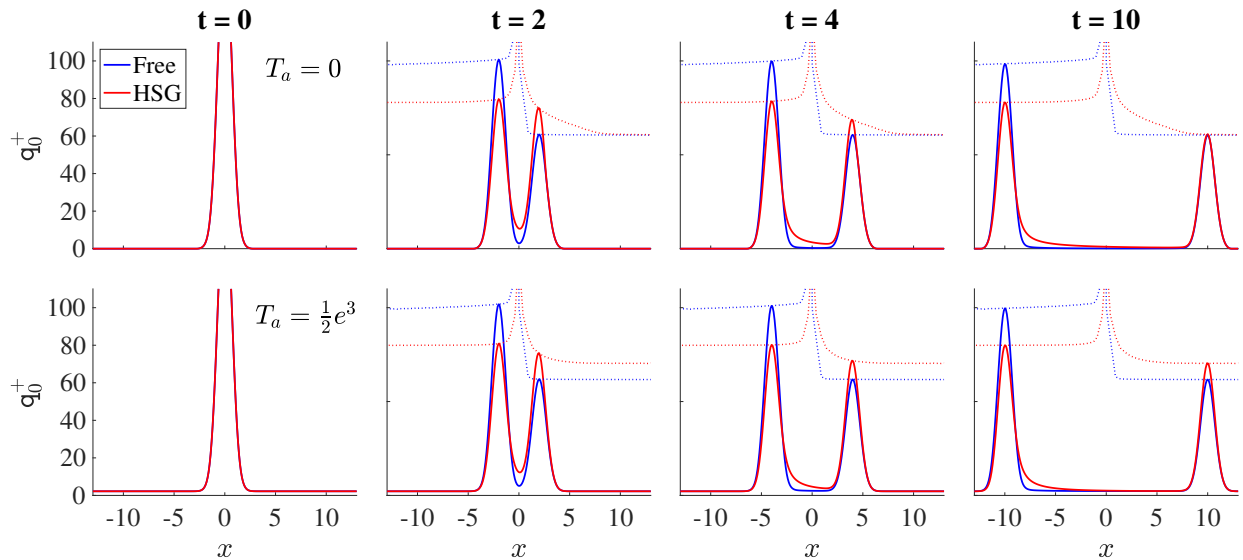


Figure 9.7 Particle density in the HSG-model $\rho_p(x, t, \theta; +)$ (red) versus $\rho_p(x - t \tanh \theta, 0, \theta; +)$ (blue). The top/bottom rows correspond to the absence/presence of a bath. The peak in the first column has been cut so as to show the remaining figures more clearly. The dotted curves represent the change in the height of the local maxima of the spectral densities as function of time. Red and blue curves generally differ in the height of the local maxima as well as the presence (absence) of a tail.

9.4 Comparison with free-particle evolution

We want now to compare the numerical results presented in the previous sections with results obtained in the absence interactions. We can then ask: are the properties of decay, tails and persistence really characteristics of the formation and decay of unstable particles due to nontrivial interaction? In this section we show that this is the case: the interaction is essential in order to explain the observed effects.

There are many ways how one can realise a free-particle evolution. One might consider the same quench problem, with the same initial temperature distribution, in a free theory. This however leads to a different initial density distribution, hence any comparison with the interacting case is not very meaningful. Instead, one may compare with what would happen for a free-particle system with the same initial spectral distribution of particles: the distribution in space-rapidity $\rho_p^\pm(x, 0, \theta)$, describing the density of particles with positions x and relativistic velocities $\tanh \theta$ at time $t = 0$.

The comparison is presented in Fig. 9.7, where we see stark differences between free and interacting evolution of the particle density of particle $+$. In particular, the two emitted waves remain stable in the free-evolution. In order to interpret these results, we remark that in the free

evolution, the distribution of velocities is very different from that of the initial effective velocities seen in Fig. 9.2: particles $+$ with negative rapidities that pertain to the subsidiary peak have negative effective velocities, instead of positive. Hence, with the free dynamics, these particles will start moving towards the left instead of the right as observed with interactions. Thus, free-particle evolution according to the initial spectral distribution is significantly different from the outset, with peaks of very different sizes. Furthermore, the distribution of rapidities leads to sharply defined velocities, which are all either very near to 1 or to -1 . Hence there is very little dispersion, and *no tail or decay is observed*. Those are thus a stark indication of the presence of interaction.

It is also striking to observe that in the case without bath, the decay under interacting evolution leads to a final right-moving wave that agrees precisely with the right-moving wave emitted from the initial distribution in the free evolution case. This indicated that all unstable particles, represented by the original subsidiary peak, have decayed, and lie within the tail. With a bath, there remains an additional particle density, representing the population of unstable particles stabilised by the presence of the bath.

9.5 Conclusions

By studying the $SU(3)_2$ -HSG model in an inhomogeneous set-up (with temperature profile (9.1)), we have found further and even more direct evidence of the unstable excitation on the out-of-equilibrium densities and effective velocities of the individual particles. In particular, signatures of instability can be found in the decay of and the resulting formation of tails in the subsidiary peaks of the out-of-equilibrium spectral densities of the individual particles. These signatures can be only explained in terms of a non-trivial interaction among the stable particles, as seen in comparison with the free evolution obtained from the same initial spectral density profile. Moreover, the large-time evolution of the interacting system changes whether or not there is a bath. In the presence of a bath, a novel “magnetic fluid effect” emerges: for each individual particle \pm the subsidiary peak does not entirely decay and gives rise to a persistent wave of particles “riding” on top of the bath and following the magnet-like interacting peak as this passes by. Within the persistent peak unstable particles are created and destroyed in a stable proportion, but involving always different stable particles. As a consequence a stark difference between the propagation velocities and the effective velocities at the top of the peaks is observed and is fully explained by the instability of the bound state.

CONCLUSION

In this thesis we have looked at two different problems in the context of integrable QFT: the universal properties of the excited state entanglement and the dynamics of unstable excitations. Although these are two very different problems, a common feature is that their solution relies on a simple quasiparticle description. In the course of this thesis we have provided various types of evidence that the study of the properties of quasiparticles as well as of their dynamics is crucial to achieve a better understanding of both problems.

In part I we have investigated the entanglement content of multi-particle states by analysing different partitions of the massive free boson, in the limit where both the volume L and regions' sizes ℓ_i are sent to infinity in fixed proportions $r_i = \ell_i/L$. The results (summarised in Section 6.1) take a simple and universal form as functions of r_i . They are independent of the mass and energy of the excitations, and of the connectivity of the entanglement regions. The qubit picture (introduced in Section 4.8 for a connected region and extended in Sections 5.3 and 5.6 for two and multiple regions) provides a natural probabilistic interpretation for the entanglement carried by quasiparticles: this is, under the flat probability assumption, the entanglement of a multi-qubit state, where qubits describe the occupancy configuration of the quasiparticles in the regions of the partition. This configuration fully determines the associated entanglement. We expect these results to take a universal form for a wide variety of theories (discussed in Section 6.2) as long as the quasiparticles can be localised within the entanglement regions. In this context, the qubit interpretation combines the semiclassical picture of localised excitations, controlled by correlation lengths and De Broglie wave-length, with the quantum effect of “indistinguishability”. These interconnected properties of locality and indistinguishability are what best characterise the entanglement content of a finite number of quasiparticles.

The results presented in part I of this thesis provide a complete understanding of the most

popular measures of entanglement in zero-density excited states of the one-dimensional massive free boson at zero-temperature. An interesting direction for future work is to extend the study to other measures of entanglement. In [167], this extension will be addressed for the symmetry resolved entanglement, an entanglement measure defined in terms of internal symmetries of the model. Many of the techniques seen in Chapters 4 and 5 generalise to this case. Indeed a twist field description to the symmetry resolved entanglement has been recently provided [168], and used to treat the ground state in [169–171]. Another possible development is to consider the next-to-leading corrections for the entanglement increments in the limit (6.1). We now expect these contributions to depend on the details of the state, such as the energy and rapidity. It would be interesting to see if the qubit picture can be modified to also capture these features. More challenging will be to address the problem of excited state entanglement in interacting integrable QFT. Despite the evidence discussed in Section 6.2, a rigorous proof of the validity of our results for interacting field theories is missing. The challenge consists in finding a good finite-volume regularisation for branch-point twist fields that, as discussed in Subsection 3.2.3, is still an open problem. Our analysis of the massive free boson provides evidence that this is rather a technical problem than a real limitation, and thus it should be possible to extend the finite-volume techniques [86, 87] at least for non-diagonal form factors. It would be interesting to investigate under which conditions the results are still valid in the presence of interactions and if they come only from non-diagonal form factors also in these cases.

In part II we have shown how unstable particles can be seen in a new light within the GHD framework. By looking at the dynamics of the individual constituent particles, we have found new direct and physically meaningful signatures of instability. One of the most surprising results is that even at equilibrium it is possible to speak of a rich physics. In particular, at high temperatures we observe areas of quasiparticle densities which are co-moving in the phase space, forming finitely-lived bound states. We can identify these areas with a stable population of unstable particles. Indeed these bound states are continuously replenished thanks to the high temperature and the homogeneity of the state. In the partitioning protocol (discussed in Chapter 8), this picture does not change substantially, as we observe the stable areas of quasiparticles even out of equilibrium, but now these are in different proportions for particle + and – as they couple mainly to one bath. In contrast, in the inhomogeneous quench (discussed in Chapter 9), the instability of the bound state is made visible by the inhomogeneity of the

state. We thus observe direct signatures of instability such as decay and formation of tails in the spectral densities and particle densities. Importantly, in the presence of a bath, a new hydrodynamic phenomenon comes into play: the long-time persistence of a small but significant wave of particles “riding” on top of the bath, propelled by its interaction with the large wave of particles of the opposite type.

Given how rich the dynamics of this simple model is, it would be very interesting to study other models of the same HSG family with richer particle spectra, where more unstable particles with tunable masses and decay widths are present. There is also still much to learn about the time evolution of hydrodynamic quantities under variation of T_a, T_m and σ , and this will be addressed in [148], where also a more quantitative analysis of the phenomena discussed in this thesis will be presented. The hope is that, with a good qualitative and quantitative characterisation of these features, we may lay the foundation for an effective theory where the large-time stable populations of stable particles (observed in the two different set-ups considered in this thesis) are representative of the unstable excitations.

CONTOUR-INTEGRAL APPROACH FOR TWO DISCONNECTED REGIONS

In this appendix we outline the computational steps of the four-point functions (5.17) and (5.18), re-written below:

$$\hat{\mathcal{F}}_p \left(N_p^\pm, \tilde{N}_p^\pm \right) = {}_{p;L} \langle \{I^0\}_{N_p^\pm} | \mathcal{T}_p(0) \mathbb{1}_p^{(1)} \tilde{\mathcal{T}}_p(x_1) \mathbb{1}_p^{(0)} \mathcal{T}_p(x_2) \mathbb{1}_p^{(1)} \tilde{\mathcal{T}}_p(x_3) | \{I^0\}_{\tilde{N}_p^\pm} \rangle_{p;L}, \quad (\text{A.1})$$

$$\tilde{\mathcal{F}}_p \left(N_p^\pm, \tilde{N}_p^\pm \right) = {}_{p;L} \langle \{I^0\}_{N_p^\pm} | \mathcal{T}_p(0) \mathbb{1}_p^{(1)} \tilde{\mathcal{T}}_p(x_1) \mathbb{1}_p^{(0)} \tilde{\mathcal{T}}_p(x_2) \mathbb{1}_p^{(-1)} \mathcal{T}_p(x_3) | \{I^0\}_{\tilde{N}_p^\pm} \rangle_{p;L}. \quad (\text{A.2})$$

We focus on the sector correlator $\hat{\mathcal{F}}_p$ associated to the n th Rényi entropy. The same procedure can be implemented for $\tilde{\mathcal{F}}_p$. Of course the different intermediate states and the different product of fields involved in (A.2) will lead to different outcomes.

Notation:

We denote the rapidities of the complete sets of states (referring to the correlator in (A.1) and starting from left to right) by $\beta_i^\epsilon, \alpha_i^\epsilon, \tilde{\beta}_i^\epsilon$ and their numbers by $m^\epsilon, k^\epsilon, \tilde{m}^\epsilon$, respectively. As

usual $\epsilon = \pm$. The rapidities satisfy the following Bethe-Yang quantization conditions (5.6)

$$Q_p^{\epsilon,1}(\beta_i^\epsilon) = mL \sinh(\beta_i^\epsilon) - 2\pi\epsilon \frac{p}{n} = 2\pi J_i^\epsilon, \quad (\text{A.3})$$

$$Q_p^{\epsilon,0}(\alpha_i^\epsilon) = mL \sinh(\alpha_i^\epsilon) = 2\pi I_i^\epsilon, \quad (\text{A.4})$$

$$Q_p^{\epsilon,1}(\tilde{\beta}_i^\epsilon) = mL \sinh(\tilde{\beta}_i^\epsilon) - 2\pi\epsilon \frac{p}{n} = 2\pi \tilde{J}_i^\epsilon. \quad (\text{A.5})$$

Additionally, we introduce the following notation for the sets of rapidities in the various intermediate states

$$\begin{aligned} \underline{\mathbf{m}}^\pm &= \{\beta_1^\pm, \dots, \beta_{m^+}^\pm, \beta_1^\mp, \dots, \beta_{m^-}^\mp\}, \\ \underline{\mathbf{k}}^\pm &= \{\alpha_1^\pm, \dots, \alpha_{k^+}^\pm, \alpha_1^\mp, \dots, \alpha_{k^-}^\mp\}, \\ \tilde{\underline{\mathbf{m}}}^\pm &= \{\tilde{\beta}_1^\pm, \dots, \tilde{\beta}_{m^+}^\pm, \tilde{\beta}_1^\mp, \dots, \tilde{\beta}_{m^-}^\mp\}, \end{aligned} \quad (\text{A.6})$$

and in the external states of equal rapidities:

$$\underline{\mathbf{N}}^\pm = \{\theta\}_{N_p^+} \cup \{\theta\}_{N_p^-}, \quad \tilde{\underline{\mathbf{N}}}^\pm = \{\theta\}_{\tilde{N}_p^+} \cup \{\theta\}_{\tilde{N}_p^-}. \quad (\text{A.7})$$

The quantization conditions for rapidities in $\underline{\mathbf{N}}$ and $\tilde{\underline{\mathbf{N}}}$ are the same for both particles and antiparticles and are given by equation (5.14).

The expansion

Using the transformation (3.47) we can expand (A.1) into infinite volume form factors:

$$\begin{aligned} \mathcal{F}_p(N_p^\pm, \tilde{N}_p^\pm) &= \prod_{\epsilon=\pm} \sum_{m^\epsilon=0}^{\infty} \frac{1}{m^\epsilon!} \sum_{\{J^\epsilon\}} \sum_{k^\epsilon=0}^{\infty} \frac{1}{k^\epsilon!} \sum_{\{I^\epsilon\}} \sum_{\tilde{m}^\epsilon=0}^{\infty} \frac{1}{\tilde{m}^\epsilon!} \sum_{\{\tilde{J}^\epsilon\}} \frac{e^{-ix_3 \tilde{N}_p^\epsilon P(\theta)}}{\left[\sqrt{LE(\theta)}\right]^{N_p^\epsilon + \tilde{N}_p^\epsilon}} \\ &\times \frac{e^{ix_1 \sum_{i=1}^{m^\epsilon} P(\beta_i^\epsilon)} e^{i(x_2-x_1) \sum_{i=1}^{k^\epsilon} P(\alpha_i^\epsilon)} e^{i(x_3-x_2) \sum_{i=1}^{\tilde{m}^\epsilon} P(\tilde{\beta}_i^\epsilon)}}{\left[\prod_{i=1}^{m^\epsilon} LE(\beta_i^\epsilon)\right] \left[\prod_{i=1}^{k^\epsilon} LE(\alpha_i^\epsilon)\right] \left[\prod_{i=1}^{\tilde{m}^\epsilon} LE(\tilde{\beta}_i^\epsilon)\right]} \\ &\times \langle \underline{\mathbf{N}}^\pm | \mathcal{T}_p(0) | \underline{\mathbf{m}}^\pm \rangle \langle \underline{\mathbf{m}}^\pm | \mathcal{T}_{-p}(0) | \underline{\mathbf{k}}^\pm \rangle \langle \underline{\mathbf{k}}^\pm | \mathcal{T}_p(0) | \tilde{\underline{\mathbf{m}}}^\pm \rangle \langle \tilde{\underline{\mathbf{m}}}^\pm | \mathcal{T}_{-p}(0) | \tilde{\underline{\mathbf{N}}}^\pm \rangle. \end{aligned} \quad (\text{A.8})$$

where $P(\theta) = m \sinh \theta$ and $E(\theta) = m \cosh \theta$ are the single-particle momenta and single-particle energy respectively. The elements in the last row can be of course written in terms of elementary form factors of $U(1)$ -fields such as (4.39), which is the form that one usually considers to treat the expansion above. However, in this appendix we intend to clarify some computational subtle points, and refer the curious reader to [28] for full details. For this purpose it is fine to keep

the form factors in their general form as above to simplify the notation.

In Section 4.5 we have presented a computational recipe for the two-point function. This has a natural extension to correlators involving an higher number of fields and we discuss below the main changes that one needs to account for in the treatment of four-point correlators. Similar to the two-point case the $U(1)$ -charge constrains the numbers of particles in the intermediate states but we now have more constraints:

$$N_p^+ - N_p^- = m^+ - m^- = k^+ - k^- = \tilde{m}^+ - \tilde{m}^- = \tilde{N}_p^+ - \tilde{N}_p^-. \quad (\text{A.9})$$

One interesting difference is that due to the quantization conditions (A.4), some rapidities in the intermediate states $|\underline{\mathbf{k}}\rangle$ may coincide with those of the external states. This does not change the fact that the form factors are non-diagonal, as in each form factor the rapidities on the two sides are always distinct. In order to correctly account for the different contributions, we separate the rapidities into two groups $\underline{\mathbf{k}}^\pm \mapsto \underline{\mathbf{k}}^\pm \cup \underline{\mathbf{K}}^\pm$, one coinciding with θ

$$\underline{\mathbf{K}}^\pm = \{\theta\}_{K^+} \cup \{\theta\}_{K^-}, \quad (\text{A.10})$$

and the rest $\underline{\mathbf{k}}^\pm$. We can thus also separate the quantum number sums as

$$\sum_{k^\epsilon=0}^{\infty} \frac{1}{k^\epsilon!} \sum_{\{I^\epsilon\}} f(\underline{\mathbf{k}}^\epsilon, \dots) \rightarrow \sum_{K^\epsilon=0}^{\infty} \frac{1}{K^\epsilon!} \sum_{k^\epsilon=0}^{\infty} \frac{1}{k^\epsilon!} \sum_{\{I^\epsilon\} \neq I^0} f(\underline{\mathbf{k}}^\epsilon, \underline{\mathbf{K}}^\epsilon, \dots). \quad (\text{A.11})$$

The functions f represents the product of form factors in (A.8), note that the order of the rapidities in each set does not matter (since we are dealing with free bosons, the form factors are symmetric in all rapidities). We stress that at this stage all the rapidities in the formula are solutions of the appropriate Bethe-Yang equations. This will not be the case anymore when we advance to the first computational step.

Step 1: Transforming sums into contour integrals

We rewrite our formulae in terms of contour integrals:

$$\sum_{J_i^\epsilon \in \mathbb{Z}} \frac{f(\beta_i^\epsilon, \dots)}{LE(\beta_i^\epsilon)} = \sum_{J_i^\epsilon} \int_{\mathcal{C}_{J_i^\epsilon}} \frac{d\beta_i^\epsilon}{2\pi} \frac{f(\beta_i^\epsilon, \dots)}{e^{iQ_p^{\epsilon,1}(\beta_i^\epsilon)} - 1}, \quad (\text{A.12})$$

$$\sum_{I_i^\epsilon \in \mathbb{Z}} \frac{f(\alpha_i^\epsilon, \dots)}{LE(\alpha_i^\epsilon)} = \sum_{I_i^\epsilon} \int_{\mathcal{C}_{I_i^\epsilon}} \frac{d\alpha_i^\epsilon}{2\pi} \frac{f(\alpha_i^\epsilon, \dots)}{e^{iQ_p^{\epsilon,0}(\alpha_i^\epsilon)} - 1}, \quad (\text{A.13})$$

$$\sum_{\tilde{j}_i \in \mathbb{Z}} \frac{f(\tilde{\beta}_i^\epsilon, \dots)}{LE(\tilde{\beta}_i^\epsilon)} = \sum_{\tilde{j}_i} \int_{\mathcal{C}_{\tilde{j}_i}} \frac{d\tilde{\beta}_i^\epsilon}{2\pi} \frac{f(\tilde{\beta}_i^\epsilon, \dots)}{e^{iQ_p^{\epsilon,1}(\tilde{\beta}_i^\epsilon)} - 1}, \quad (\text{A.14})$$

where the \mathcal{C} s are small contours around solutions of the Bethe-Yang equations and the functions $Q_p^{\epsilon,\alpha}$ defined in (A.3) ensure that the integrand has a pole exactly when the Bethe-Yang equation is satisfied.

We remark that in the equations above the integral variables on the right hand side are no longer Bethe-Yang solutions.¹ This means that they can cross points where the function f shows singularities i.e. where the form factors in (A.8) has some equal rapidities on the two sides (note that this is only possible within the contour integrals). When this happens we use the kinematic pole property (4.45) of two-particle form factors to “contract” such rapidities. In the next computational step we want to identify all the possible contractions involving rapidities of the intermediate states and look into the pole structures of the form factors “inside” their contour integrals. As seen for the two-point functions, the analysis of the form factor poles provides the right prescription to evaluate the dominant contributions to the expansion (A.8) in the scaling limit (5.2).

Step 2: manipulating contour integrals

In order to implement correctly the contour integral approach it is convenient to treat one type of intermediate states at a time and to convert their sums at the exact moment when we work on that specif type. Note that the expansion (A.8) never involves the sets of states $|\underline{\mathbf{m}}^\pm\rangle$ and $|\tilde{\mathbf{m}}^\pm\rangle$ in the same form factors. A good strategy is to treat first these two sets where we need to focus on only two form factors at a time, and finally consider the states $|\underline{\mathbf{k}}\rangle$.

We concentrate on the states $|\underline{\mathbf{m}}^\pm\rangle$. Once we transforms their sums into contour integral we notice that rapidities in $|\underline{\mathbf{m}}^\pm\rangle$ can be contracted with others in three different ways, schematically:

$$\dots \langle \overbrace{\underline{\mathbf{N}}^\pm | \mathcal{T}_p(0) | \underline{\mathbf{m}}^\pm} \rangle \langle \overbrace{\underline{\mathbf{m}}^\pm | \mathcal{T}_{-p}(0) | \underline{\mathbf{k}}^\pm, \underline{\mathbf{K}}^\pm} \rangle \dots \quad (\text{A.15})$$

Note that only contractions between particles of the same $U(1)$ -charge are allowed as these correspond to elementary form factors of opposite charge. We know in fact from Subsection 4.3.3 that these are the only non-zero form factors of $U(1)$ -fields. Each single contraction in equation (A.15) corresponds to a single-pole residue. However there will be terms of the

¹In a way, denoting the two variables on the right and left hand sides of equations (A.12), (A.13), (A.14) with the same symbols is an abuse of notation that is however convenient to keep track of the different origins of the contour integrals.

expansion where the function f shows a double-pole. This precisely occurs when a rapidity β_j^ϵ is contracted with a θ rapidity in both form factors (as both states $|\underline{\mathbf{N}}^\pm\rangle$ and $|\underline{\mathbf{K}}^\pm\rangle$ are composed of only θ s). Similarly to the case seen in Subsection 4.5.1.1, we need to subtract the contribution generated by these poles. The contour after the deformation is:

$$\mathcal{C}^\epsilon := \sum_{J_i^\epsilon \in \mathbb{Z}} \mathcal{C}_{J_i^\epsilon} = \mathcal{C}_{\leftrightarrow} - \mathcal{C}_\theta - \sum_j \mathcal{C}_{\alpha_j^\epsilon}, \quad \epsilon = \pm, \quad (\text{A.16})$$

where $\alpha_j^\epsilon \neq \theta$, and \mathcal{C}_θ and $\mathcal{C}_{\alpha_j^\epsilon}$ are contours crossing the kinematic poles $\beta_i^\epsilon = \theta$ and $\beta_i^\epsilon = \alpha_j^\epsilon$ respectively whereas the function f is regular at any points of the contour $\mathcal{C}_{\leftrightarrow}$. The multi-contour for all β_i^ϵ rapidities is

$$[\mathcal{C}^\epsilon]^{m^\epsilon} = \underbrace{\mathcal{C}^\epsilon \times \mathcal{C}^\epsilon \times \dots \times \mathcal{C}^\epsilon}_{m^\epsilon}. \quad (\text{A.17})$$

The order of contours does not matter due to the symmetry of the function f mentioned above. We can expand the integration multi-contour by substituting (A.16) into (A.17). As a result there are several terms of the multi-contour that give the same residue and we can write

$$[\mathcal{C}_p^\epsilon]^{m^\epsilon} \sim \sum_{m_{\leftrightarrow}^\epsilon, m_\theta^\epsilon, m_\alpha^\epsilon} (-1)^{m_{\leftrightarrow}^\epsilon + m_\theta^\epsilon} G(m_{\leftrightarrow}^\epsilon, m_\theta^\epsilon, m_\alpha^\epsilon) [\mathcal{C}_{\leftrightarrow}]^{m_{\leftrightarrow}^\epsilon} \times \left[\prod_{j=1}^{m_\alpha^\epsilon} \mathcal{C}_{\gamma_j^\epsilon} \right] \times [\mathcal{C}_\theta]^{m_\theta^\epsilon}, \quad (\text{A.18})$$

where γ_j s are some rapidities in $\underline{\mathbf{k}}^\epsilon$, and $G(m_{\leftrightarrow}^\epsilon, m_\theta^\epsilon, m_\alpha^\epsilon)$ is a combinatorial factor resulting from the power expansion. Crucially the non-negative integer summation indices in (A.18) are constrained by

$$m^\epsilon = m_{\leftrightarrow}^\epsilon + m_\theta^\epsilon + m_\alpha^\epsilon, \quad (\text{A.19})$$

Consider integrals over $\mathcal{C}_{\gamma_j^\epsilon}$, form factors there produce only first order poles, as this correspond to contracting rapidities only in the second form factor. Consider instead \mathcal{C}_θ , as mentioned before, if $M^\epsilon \neq 0$, the product of the two first form factors produces both second and first order poles. We denote by $m_{\theta,1/2}^\epsilon$ the number of first order poles arising from the first/second form factor, and by $m_{\theta,d}^\epsilon$ the number of second order poles. They satisfy the condition

$$m_\theta^\epsilon = m_{\theta,1}^\epsilon + m_{\theta,2}^\epsilon + m_{\theta,d}^\epsilon. \quad (\text{A.20})$$

Evaluating the residua of these poles produces several types of factors in the resulting expansion,

after appropriate relabelling of the rapidity sets. We refer the reader to [26] for the full computations. Below we wish to use some simple arguments to give a flavour of how the different poles contribute to the expansions.

In Subsection 4.5.1.2, we have evaluated a number N_*^ϵ of second order pole residua and after relabelling $m^\pm \rightarrow m^\epsilon - N_*^\epsilon$ these introduce a factor proportional to $[LE(\theta)g_{ep}^n(r)]^{N_*^\epsilon}$ in the expansion. Similar poles may occur also in this case and the corresponding residua give the same contribution as above with r replaced by a linear combination of the ratios r_1, r_2, r_3 . The exact combination depends on the specific residue and comes from different exponential functions involved there.

In contrast, when we consider four-point functions we need also to account for first order poles. The way how these change the structure of the expansion can be understood by looking at the case of a single first-order pole for instance $\beta_i^\epsilon = \theta$. After evaluating a first-order pole and relabelling the rapidity set appropriately $m^\epsilon \rightarrow m^\epsilon - 1$, we obtain schematically:

$$\begin{aligned} \dots \int_{-c_\theta} \frac{d\beta_i^\epsilon}{2\pi} \frac{e^{x_1 P(\beta_i^\epsilon)}}{e^{iQ_p^{\epsilon,1}(\beta_i^\epsilon)} - 1} \langle \overline{\mathbf{N}^\pm} | \mathcal{T}_p(0) | \underline{\mathbf{m}^\pm} \rangle \langle \underline{\mathbf{m}^\pm} | \mathcal{T}_{-p}(0) | \underline{\mathbf{k}^\pm}, \underline{\mathbf{K}^\pm} \rangle \dots \\ \rightarrow \dots \mathcal{R}^{\epsilon,1} \langle \underline{\mathbf{N}^\epsilon} \setminus \{\theta\} | \mathcal{T}_p(0) | \underline{\mathbf{m}^\pm} \rangle \langle \underline{\mathbf{m}^\pm}, \{\theta\} | \mathcal{T}_{-p}(0) | \underline{\mathbf{k}^\pm}, \underline{\mathbf{K}^\pm} \rangle \dots \end{aligned} \quad (\text{A.21})$$

Thus as a result of the residue, the contracted rapidity θ is trivially replaced in the regular form factors. Additionally the residue contributes a constant factor $\mathcal{R}^{\epsilon,1}$ that is independent of the ratios r_1, r_2, r_3 . When we consider other first-order residua (such as those involving α_j^ϵ rapidities) these generate different factors as the exponential functions in the integrand would be generally different. For this reason the factors $\mathcal{R}^{\epsilon,1}$ depend also on the quantization conditions. Although first-order poles contribute to the expansion (A.8) with only volume-independent factors, they reshuffle rapidities in the four form factors. These rapidities may eventually recombine with others in $|\underline{\mathbf{k}}\rangle$ and produce higher order form factor poles, which do contribute to the expansion with volume-dependent factors².

The computational recipe consists of evaluating all the residua involved in equations (A.19) and (A.20) and relabel accordingly rapidities in $|\underline{\mathbf{m}^\pm}\rangle$. Then, the exact same considerations above are valid for states $|\underline{\tilde{\mathbf{m}}^\pm}\rangle$. Indeed, one can easily notice that in the expansion (A.8) the third and fourth form factors are the mirrored version of the first and second ones, up to replacement of the states $|\underline{\tilde{\mathbf{m}}^\pm}\rangle$ with $|\underline{\mathbf{m}^\pm}\rangle$, and $|\underline{\mathbf{N}^\pm}\rangle$ with $|\underline{\tilde{\mathbf{N}}^\pm}\rangle$. The case of $|\underline{\mathbf{k}^\pm}\rangle$ is instead

²Note that this scenario could not happen in the case of two-point functions such as that in Subsection (4.5.1.2) as there we have inserted only a complete set of state, and for this reason we have not considered first-order pole at all.

more involved. Indeed after manipulating contour integrals associated to the rapidity sets $\underline{\mathbf{m}}^\epsilon$ and $\tilde{\underline{\mathbf{m}}}^\epsilon$ there will be rapidities α_j^ϵ s in each form factors of the expansion (A.8), resulting from first-order poles of either $\beta_j^\epsilon = \alpha_k^\epsilon$ and $\tilde{\beta}_j^\epsilon = \alpha_i^\epsilon$ (which give results similar to (A.21) both producing different factors). To reflect this the original set $\underline{\mathbf{k}}^\epsilon$ can be partitioned into four parts, namely $\underline{\mathbf{k}}^\epsilon = \underline{\mathbf{k}}_{12}^\epsilon \cup \underline{\mathbf{k}}_{23}^\epsilon \cup \underline{\mathbf{k}}_{34}^\epsilon \cup \underline{\mathbf{k}}_{41}^\epsilon$ where each subset $\underline{\mathbf{k}}_{ik}^\epsilon$ is composed of rapidities α_{ik}^ϵ that at the end of the manipulation process will appear in the i th and k th form factors. Although each of these subsets needs to be treated in a separate way, we can make some general statements by concentrating on a particular rapidity α_{ik}^ϵ . Once the sums have been transformed into contour integrals, we want to deform the contour into one encircling the real axis $\tilde{\mathcal{C}}_{\leftarrow}$, however, we need to subtract the residua of poles at $\alpha_{ik}^\epsilon = \theta$, since these poles are not included in the original contour. That is

$$\mathcal{C}_0^\epsilon := \sum_{I \neq I^0} \mathcal{C}_{\alpha_{ik}^\epsilon} = \tilde{\mathcal{C}}_{\leftarrow} - \mathcal{C}_\theta. \quad (\text{A.22})$$

It is important to note that $\tilde{\mathcal{C}}_{\leftarrow}$ must be chosen such as to run closer to the real axis than the contour \mathcal{C}_{\leftarrow} , for rapidities in $\underline{\mathbf{m}}^\epsilon$ and $\tilde{\underline{\mathbf{m}}}^\epsilon$, to avoid capturing undesired residua. Although the resulting multi-contour integral has similar structure to the one analysed in Subsection 4.5.1.2, it finally leads to a different residue calculation. In this particular case, in fact, the denominator $e^{iQ_p^{\epsilon,0}(\alpha_{ik}^\epsilon)} - 1$ of the contour integral (A.13) is singular at $\alpha_{ik}^\epsilon = \theta$ and the form factors (which would be part of the function $f(\alpha_{ik}^\epsilon, \dots)$ in the numerator) can also have kinematic singularities at this point. Since any given rapidity α_{ik}^ϵ appears in two form factors it follows then that we can have first, second, and third order poles. However it is possible to prove that only the third order pole-contributions will survive in the scaling limit (5.2). Indeed each third-order pole residue introduces a factor $LE(\theta)\tilde{g}(x)$ in the expansion, and thus contributes to reducing the power of L in the denominator of expansion (A.8), while the residua resulting from the other poles turn out to be volume-independent. The function $\tilde{g}(x)$ is a second-order polynomial in x , where x is a linear combination of ratios r_1, r_2, r_3 . Again, the exact form of x depends on the integrand of the contour integral³. We need of course to consider all these contributions in each subset $\underline{\mathbf{k}}^\epsilon$ and correctly account for the combinatorial factors arising from pairing rapidities.

Once completed the entire procedure described above, the function f will be regular in all variable and we can move to the next computational step.

³If we are interested in the correlator (A.2), these poles would still produce factors $LE(\theta)\tilde{g}(x')$ but with different combination x' of ratios r_1, r_2, r_3 .

Step 3: establishing the large-volume leading contribution

The evaluations of residua introduce some constrains due to the limited total number of θ rapidities that can take part in the residue calculation. Computations for rapidity sets $\underline{\mathbf{m}}^\epsilon$ and $\underline{\mathbf{m}}^\epsilon$ imply

$$\begin{aligned}
 m_{\theta,d}^\epsilon &\leq \min(N_p^\epsilon, M^\epsilon), & \tilde{m}_{\theta,d}^\epsilon &\leq \min(\tilde{N}_p^\epsilon, M^\epsilon), \\
 m_{\theta,1}^\epsilon + m_{\theta,d}^\epsilon &\leq N_p^\epsilon, & \tilde{m}_{\theta,1}^\epsilon + \tilde{m}_{\theta,d}^\epsilon &\leq M^\epsilon, \\
 m_{\theta,2}^\epsilon + m_{\theta,d}^\epsilon &\leq M^\epsilon, & \tilde{m}_{\theta,2}^\epsilon + \tilde{m}_{\theta,d}^\epsilon &\leq \tilde{N}_p^\epsilon.
 \end{aligned} \tag{A.23}$$

We denote s_{ij}^ϵ the number of third order poles evaluated by rapidities α_{ij} belonging to the set $\underline{\mathbf{k}}_{ij}^\epsilon$. These numbers are constrained by the number of rapidities in $\underline{\mathbf{k}}_{ij}^\epsilon$, by the total number of θ rapidities. Additionally we have the following less trivial constraints

$$\begin{aligned}
 s_{13}^\epsilon + s_{14}^\epsilon &\leq N_p^\epsilon - m_{\theta,d}^\epsilon - m_{\theta,1}^\epsilon, & s_{23}^\epsilon + s_{24}^\epsilon &\leq m_{\theta,1}^\epsilon, \\
 s_{14}^\epsilon + s_{24}^\epsilon &\leq \tilde{N}_p^\epsilon - \tilde{m}_{\theta,d}^\epsilon - \tilde{m}_{\theta,2}^\epsilon, & s_{13}^\epsilon + s_{23}^\epsilon &\leq \tilde{m}_{\theta,2}^\epsilon, \\
 s_{13}^\epsilon + s_{14}^\epsilon + s_{23}^\epsilon + s_{24}^\epsilon &\leq \min\left(N_p^\epsilon - m_{\theta,d}^\epsilon, \tilde{N}_p^\epsilon - \tilde{m}_{\theta,d}^\epsilon\right).
 \end{aligned} \tag{A.24}$$

After evaluation of all residua, the volume dependence of the whole expression is $[LE(\theta)]^\Delta$. Since only second- and third- order pole residua have contributed to rising this power we have:

$$\Delta = \sum_{\epsilon=\pm} \left(m_{\theta,d}^\epsilon + \tilde{m}_{\theta,d}^\epsilon + s_{13}^\epsilon + s_{14}^\epsilon + s_{23}^\epsilon + s_{24}^\epsilon - \frac{N_p^\epsilon}{2} - \frac{\tilde{N}_p^\epsilon}{2} - M^\epsilon \right), \tag{A.25}$$

where the negative terms comes from the denominators in the expansion (A.8). The maximal Δ will give the leading large-volume contribution of the four-point function. We may rearrange the expression as

$$\begin{aligned}
 \Delta = \sum_{\epsilon=\pm} &\left(\frac{s_{13}^\epsilon + s_{14}^\epsilon + s_{23}^\epsilon + s_{24}^\epsilon - (N_p^\epsilon - m_{\theta,d}^\epsilon)}{2} + \frac{m_{\theta,d}^\epsilon - M^\epsilon}{2} \right. \\
 &\left. + \frac{s_{13}^\epsilon + s_{14}^\epsilon + s_{23}^\epsilon + s_{24}^\epsilon - (\tilde{N}_p^\epsilon - \tilde{m}_{\theta,d}^\epsilon)}{2} + \frac{\tilde{m}_{\theta,d}^\epsilon - M^\epsilon}{2} \right),
 \end{aligned} \tag{A.26}$$

due to the constraints (A.23) and (A.24) each fraction inside the sum is less or equal than zero.

Therefore, the maximum of Δ is achieved when all inequalities are saturated, namely

$$\begin{aligned}
 N_p^\epsilon &= \tilde{N}_p^\epsilon, & m_{\theta,d}^\epsilon &= \tilde{m}_{\theta,d}^\epsilon = M^\epsilon, \\
 m_{\theta,2}^\epsilon &= \tilde{m}_{\theta,1}^\epsilon = 0, & s_{13}^\epsilon &= \tilde{m}_{\theta,2}^\epsilon - s_{23}^\epsilon, \\
 s_{24}^\epsilon &= m_{\theta,1}^\epsilon - s_{23}^\epsilon, & s_{14}^\epsilon &= N_p^\epsilon - M^\epsilon - m_{\theta,1}^\epsilon - \tilde{m}_{\theta,2}^\epsilon + s_{23}^\epsilon,
 \end{aligned} \tag{A.27}$$

where M^ϵ , $m_{\theta,1}^\epsilon$, $\tilde{m}_{\theta,2}^\epsilon$ and s_{23}^ϵ are still free parameters within the range

$$\begin{aligned}
 0 &\leq M^\epsilon \leq N_p^\epsilon, & 0 &\leq m_{\theta,1}^\epsilon \leq N_p^\epsilon - M^\epsilon, \\
 0 &\leq \tilde{m}_{\theta,2}^\epsilon \leq N_p^\epsilon - M^\epsilon, & \max(M^\epsilon + m_{\theta,1}^\epsilon + \tilde{m}_{\theta,2}^\epsilon - N_p^\epsilon, 0) &\leq s_{23}^\epsilon \leq \min(m_{\theta,1}^\epsilon, \tilde{m}_{\theta,2}^\epsilon)
 \end{aligned} \tag{A.28}$$

The maximum power of the volume is then $\Delta = 0$. This corresponds to the situation when all dependency on the θ rapidities has been cancelled by the evaluation of residua. Hence there are no other poles to consider other than third order ones (as these will produce subleading contributions).

Step 4: obtaining results

The remaining sums (A.28) can be finally re-written in such a way as to obtain the factor $N_p^\epsilon! [g_{ep}^n(r_1 + r_3)]^{N_p^\epsilon}$. Since the leading contribution is θ -independent, the vacuum-correlator factorises out, and this gives the following final result

$$\lim_{L \rightarrow \infty} \frac{\hat{\mathcal{F}}_p(N_p^\pm, N_p^\pm)}{p;L \langle \mathbf{0} | \mathcal{T}_p(0) \tilde{\mathcal{T}}_p(x_1) \mathcal{T}_p(x_2) \tilde{\mathcal{T}}_p(x_3) | \mathbf{0} \rangle_{p;L}} = \prod_{\epsilon=\pm} N_p^{\epsilon!} [g_{ep}^n(r_1 + r_3)]^{N_p^\epsilon}. \tag{A.29}$$

where the dependence on the ratio r_2 has dropped out as a consequence of (A.27) and (A.28). As we can see the excess entanglement entropy depends only on the total length of region $A \cup B$ and not on how it is partitioned.

As mentioned in the beginning of the appendix, the same procedure can be extended to the replica negativity. The corresponding third-order and second-order residue calculations introduce respectively powers of $LE(\theta)\tilde{g}(x')$ and $LE(\theta)g_{\pm ep}^n(x')$ ⁴ in the resulting expansion in a

⁴More precisely, the signs \pm arise from the fact that in the correlator (A.2) we need to account also for rapidities with quantization conditions $\alpha = -1$, and this changes some results of the second-order pole residues. In the entanglement entropies (of either connected and disconnected regions) the leading large-volume contributions comes from second-order poles occurring always in rapidities inserted between as $\dots \mathcal{T}_p \mathbb{1}_p^{(1)} \tilde{\mathcal{T}}_p \dots$, and the second-order pole residua produce powers of $LE(\theta)g_{ep}^n(x)$. In contrast, in the case of the logarithmic negativities, the dominant contribution may also come from second-order poles in rapidities inserted as $\dots \tilde{\mathcal{T}}_p \mathbb{1}_p^{(-1)} \mathcal{T}_p \dots$, and the corresponding second-order pole residue produce powers of $LE(\theta)g_{-ep}^n(x')$.

very similar fashion. The difference is that now x' will be given by different linear combinations of r_1, r_2, r_3 as a result of the different quantization conditions satisfied by the rapidities in the intermediate states and the different combination of fields involved in (A.2). The final result will be:

$$\lim_{L \rightarrow \infty} \frac{\tilde{\mathcal{F}}_p(N_p^\pm, N_p^\pm)}{p;L \langle \mathbf{0} | \mathcal{T}_p(0) \tilde{\mathcal{T}}_p(x_1) \tilde{\mathcal{T}}_p(x_2) \mathcal{T}_p(x_3) | \mathbf{0} \rangle_{p;L}} = \prod_{\epsilon=\pm} N_p^\epsilon! [\hat{g}_{\epsilon p}^n(r_1, r_3)]^{N_p^\epsilon}, \quad (\text{A.30})$$

where $\hat{g}_{\epsilon p}^n(r_1, r_3)$ is defined in (5.22). It is then easy to see that equations (A.29) and (A.30) lead to the results (5.20) and (5.21).

GRAPH PARTITION FUNCTION

In [28] the existence of a one-to-one relationship between (6.10) and the generating functions of graphs satisfying certain connectivity conditions was shown. The resulting graph representation connects the probabilistic interpretation of "localised" excitations to the replica models (associated to the entanglement measures studied in this thesis) in a very natural way.

Suppose we want to evaluate the logarithmic negativities of a k -particle excited state for two disconnected regions. The following graph rules reproduce the connectivity properties of the replica model considered :

- The graphs are composed of two disjoint finite sets of vertices of equal cardinality kn , where k is the number of particles (assuming they all have equal momenta) and n the copy number associated to replica model. As a consequence the copy label is periodic i.e. $n + 1 = 1$.
- Each edge of the graph connects one vertex in a set to one in the other. Therefore there is no link between vertices in the same set.
- All vertices are connected exactly once. Therefore there is no unpaired vertex.
- Every edge connects copy m to $m' = m + i$ where i can be $-1, 0, 1$, and it contributes to the evaluation of a graph g a factor r_i .

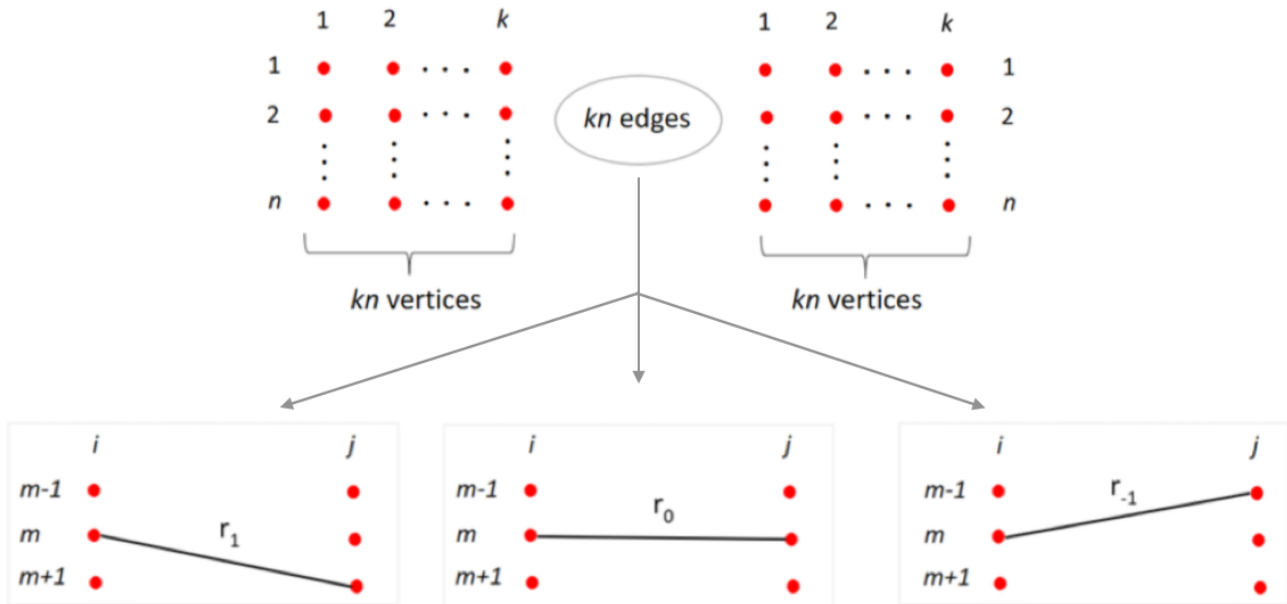


Figure B.1 Structure of the graphs

We can picture the graphs' structure as suggested in Fig. B.1, and call $\mathbf{G}_{k,n}$ the finite set of all graphs allowed by the rules above for a fixed k and n . For a graph $g \in \mathbf{G}_{k,n}$, we denote by $N_i(g)$, $i \in \{1, 0, -1\}$ the number of edges contributing as r_i . We finally define a *graph partition* as the sum over all possible graphs $g \in \mathbf{G}_{k,n}$ we can construct from the rules above, given two sets of kn vertices. More formally this corresponds to the following polynomial in three variables r_1, r_0, r_{-1} :¹

$$p_{k,n}(r_1, r_0, r_{-1}) = \sum_{g \in \mathbf{G}_{k,n}} \cdot \begin{cases} \prod_{i \in \{1, 0, -1\}} r_i^{N_i(g)} & (n > 2) \\ r_0^{N_0(g)} (r_1 + r_{-1})^{N_1(g)} & (n = 2). \end{cases} \quad (\text{B.1})$$

The connection with the entanglement problem is as follows: each left vertex represents a particle excitation in a certain copy of the replica model, and via the qubit interpretation, each graph represents a possible configuration of the occupancy distribution of the kn particles in three regions (now implemented in the replica model). In each graph, the edges implement the action of the cyclic permutation symmetry over the copies. This is formally implemented by twist operators, which in 1+1 QFT are identified with a product of branch-point twist fields, but they can be more generally considered as operators implementing special connectivity properties among the copies of a replica model. Particle excitations are of course associated to the fundamental fields of the theory, and satisfy appropriate exchange relations with the twist

¹Note that the notation in this appendix has changed slightly compared to Chapter 5, and we use instead the notation introduced in Chapter 6. In particular we use r_i with $i = -1, 0, 1$ instead of r_1, r , and r_3 . This is just a more suitable notation in the context of graphs.

operators. Suppose we consider a particle on copy m in a certain graph configuration, the twist operator acts on this excitation in such a way to permutes copy m to $m + 1$ if the excitation is found in a certain region of ratio r_1 , or permutes copy m to $m - 1$ if this is found in another distinct region of ratio r_{-1} . In contrast the twist operator acts trivially if the excitation is found in the rest of the system, associated to ratio r_0 .

Under the interpretation above, the graph partition function reproduces the polynomial in the logarithm of the increments $\Delta\mathcal{E}_n^k$ [28]:

$$\Delta\mathcal{E}_n^k = \mathcal{E}_n^{\Psi_{\text{qb}}^{(k)}} = \log \frac{p_{k,n}(r_1, r_0, r_{-1})}{(k!)^n} \quad (\text{B.2})$$

where the normalisation $1/(k!)^n$ comes from the fact that each vertex can be one of the k identical excitations (assuming the indistinguishability of such particles). The entropy increments ΔS_n^k are obtained by fixing $r_{-1} = 0$:

$$\Delta E_n^k = E_n^{\Psi_{\text{qb}}^{(k)}} = \log \frac{p_{k,n}(r_1, r_0, 0)}{(k!)^n}, \quad p_{k,n}(r_1, r_0, 0) = \sum_{g \in \mathcal{G}'_{k,n}} \prod_{i \in \{1,0\}} r_i^{N_i(g)}. \quad (\text{B.3})$$

The corresponding graphs form a subset $\mathcal{G}'_{k,n} \subset \mathcal{G}_{k,n}$, and are composed of edges r_0 or r_1 only.

B.1 Example: graph partition function for a single-particle state

Consider a single-particle state in a replica model with $n = 4$ copies, the increment of logarithmic negativity is :

$$\Delta\mathcal{E}_4^1(r_1, r_0, r_{-1}) = \log (r_1^4 + r_{-1}^4 + r_0^4 + 4r_0^2 r_1 r_{-1} + 2r_1^2 r_{-1}^2). \quad (\text{B.4})$$

The graph partition $p_{1,4}(r_1, r_0, r_{-1})$ is exactly the polynomial in the argument of the logarithm. Its graph representation is displayed in Fig. B.2, where the graphs are organised in three separate rows. The graph partition $p_{1,4}(r_1, r_0, 0)$ is simply given by the first two terms in the same figure.

Let us focus on the polynomial $p_{1,4}(r_1, r_0, r_{-1})$. We can identify three types of graph contributions, each associated to a particular row in Fig. B.2. The first three terms represent graph configurations where all excitations are found in the same region of ratio r_i for

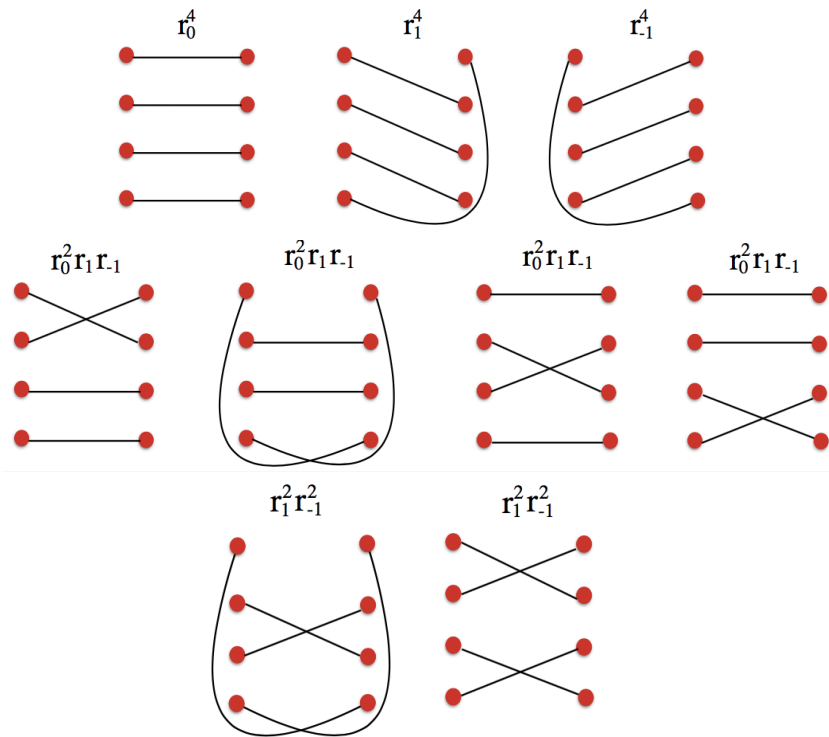


Figure B.2 All contributing graphs for $k = 1$, $n = 4$.

$i = 1, 0, -1$, and these contribute the highest power of r_i only to the polynomial (B.4). To the same polynomial, graphs in the second row equally contribute $r_0^2 r_1 r_{-1}$ while those in the third line equally contribute $r_1^2 r_{-1}^2$, producing a coefficient 4 and 2, respectively, which represent their graph multiplicity.

The graph partition function can help us to better understand the structure of the polynomial (B.4). Below, we indeed make a simple observation, which turns out to be quite general for single-particle excitations. Consider a left vertex in copy m (for instance $m = 2$) and suppose that this is joint to the right by a edge r_1 (connecting vertices $2 \rightarrow 3$). Then, consider the left vertex in the next copy $m + 1$ ($m = 3$). Since according to the rules the straight connection is not allowed, we have only two choices to connect such a vertex: by another edge r_1 (that is $3 \rightarrow 4$) or by an edge r_{-1} (that is $3 \rightarrow 2$). The former leads inevitably to a graph in the first row of Fig. B.2 whereas the latter forms a “cross” of weight $r_1 r_{-1}$ with the other edge $m \rightarrow m + 1$ ($2 \rightarrow 3$). Recalling the periodicity in the copy number, the graphs in the second and third rows can only result from combinations of crosses and straight lines, and in particular the second row involves exactly one cross, and the third row involves exactly two crosses. As a consequence the terms $4r_0^2 r_1 r_{-1} + 2r_1^2 r_{-1}^2$ in (B.4) account for all the possible configurations we obtain if we use only crosses (at least one) and straight lines to connect the four left vertices to the right. This simple argument can be extended for any

single-excitation, and any copy number n :

$$p_{1,n}(r_1, r_0, r_{-1}) = r_1^n + r_0^n + r_{-1}^n + \sum_{q=1}^{\lfloor \frac{n}{2} \rfloor} \frac{n}{n-q} \binom{n-q}{q} r_0^{n-2q} (r_1 r_{-1})^q \quad (\text{B.5})$$

where q represents the number of crosses, $n - q$ the number of straight lines. The coefficients in the sum select the indices appropriately to reproduce crosses in the graphs with the right combinatorial multiplicity.

Note that if we consider multi-particle states of only distinct particles, we can only connect a left and a right vertex to the right if the two vertices are associated to the same excitation i.e. labelled by the same particle number. Thus the cross-and-line argument presented above is still valid in this case, and as expected the resulting graph partition function is exactly k time the one in (B.1). In contrast, when we consider particles of equal momenta, also connections among different particle numbers are allowed (as they are indistinguishable) and although the cross-terms still contribute $r_1 r_{-1}$, there will be also other combinations of r_1 and r_{-1} allowed and one needs to properly account for these other contributions.

NUMERICS WITH MATHEMATICA

In this appendix we discuss briefly some details of the Mathematica programme, implemented to generate all the numerical results presented in Chapter 8 of this thesis. As usual in the TBA context, the TBA/GHD equations are solved numerically starting with a discretization of the variable θ within a finite interval. For this we exploit a well-known property of all relevant TBA functions namely, that they double-exponentially fall off for rapidities larger than $\log 2/\beta$ or smaller than $\log \beta/2$ (and similarly in the out-of-equilibrium situation). In our numerics we have chosen a slightly larger interval $[\log \beta/2 - \sigma/4, \log 2/\beta + \sigma/4]$ which grows with temperature. In the out-of-equilibrium regime we choose β to be the inverse of the highest temperature.

We have kept the number M of discrete equidistant rapidity values fixed. It is clear that the larger M is, the better the approximation to the continuum. However, a very large M increases drastically the running time of the programme. In all our numerical analysis we have set $M = 200$. This value has been chosen in such a way as to ensure that a number of benchmark results are reproduced. For instance, we reproduce the expected pattern of the c -function at equilibrium (see Fig. 7.1) as well as the known free Majorana fermion results in the relevant temperature range, both at and out of equilibrium.

We have focussed on studying the temperature-dependence of the TBA quantities described in Subsection 7.3.1 exactly in the middle of the light-cone (so, for ray $x/t = 0$). For this reason, we omit the space- and time-dependence of the TBA quantities considered. For simplicity, we have set the parameters of the theory as $m = 1$ and $\sigma = 20$. We can summarise the algorithm

we have implemented as follows:

- (a) For fixed values of $\beta_{L,R}$ solve (7.11) for the left and right steady states and compute $n^R(\theta; \pm)$ and $n^L(\theta; \pm)$ using (7.31).
- (b) Solve (7.30) for $h_i(\theta) = p(\theta)$ recursively. Start by setting θ_0^\pm in (8.1) to some trial value (say 0). Solve recursively for $p^{\text{dr}}(\theta; \pm)$ until convergence is achieved.
- (c) Once a solution for $p^{\text{dr}}(\theta; \pm)$ has been obtained, find the solution to $p^{\text{dr}}(\theta; \pm) = 0$. This will give a new value of θ_0^\pm .
- (d) Repeat (b) and (c) with this new value of θ_0^\pm and again as many times as necessary until a stable value of θ_0^\pm is reached.
- (e) Employ the solution (8.1) to evaluate any dressed quantity of interest $h^{\text{dr}}(\theta; \pm)$.
- (f) Evaluate (7.33) and (7.34).
- (g) Repeat for a different right- and left-temperatures.

In (c) and (e) the convergence of the dressing operation is ensured by the condition that the difference of the outcome given by the last iteration and the preceding one is smaller than the module of a certain number α . In all of the cases, α has been chosen to be no larger than 10^{-4} generally ensuring very high precision. Similar arguments hold for the convergence of (a) and (d).

NUMERICS WITH IFLUID

In this Appendix we describe in more detail the numerical simulations reported in [36], and presented in Chapter 9 of this thesis, focussing on possible error sources, precision issues and consistency checks.

D.1 Generalities

As mentioned in Chapter 9, our numerical simulations have been obtained by implementing a new numerical tool, called iFluid (integrable-Fluid, version 1.1.0 which is an open-source MATLAB framework specifically designed for solving the GHD equations in integrable models [164]. It is worth mentioning also that an integral-equation solution to the GHD equation (7.38) is also known [162], but its numerical stability has not been sufficiently studied yet.

Thanks to a tensor-based numerical environment, iFluid boasts high efficiency and high process running speed. Additionally, a new model can be easily implemented by extending the iFluid package with a model-specific class. Such implementation can be done by following the instructions provided in [164]. However, the $SU(3)_2$ -HSG model requires additional modifications and we have implemented them in this study.

The quantities studied in part II of this thesis feature in the `iFluidCore` class, which provides solutions to the TBA equations and inputs for the GHD equations. By default, the definition of spatial particle density included in the `iFluidCore` class, depends on the

type-array. It is a fundamental property of the class and is included in the model implementation as a one-dimensional array composed of integers which label the particle types. In massive integrable QFTs with more than one particle in the spectrum, this definition of the particle density introduces multiplicative factors in its type components, which can lead to wrong results. We have instead implemented the definition that reproduces the total spatial particle density $\mathbf{q}_0(x, t) = \mathbf{q}_0^+(x, t) + \mathbf{q}_0^-(x, t)$ as defined in (7.33) and leads to a correct result. Moreover, in our implementation of the model, some `iFluidCore` functions have been modified to output the contributions from each particle type to a given quantity separately (i.e. the functions $\mathbf{q}_0^\pm(x, t)$).

In `iFluid`, the propagation of the GHD quantities is computed via `iFluidSolver` class. In our numerical simulation we have employed the `SecondOrderSolver` solver, whose details can be found in Section 3.2 in [164].

The work [36] has provided the first application of the `iFluid` package to a system which is initially prepared in a state involving temperatures $T \gg 1$. Earlier examples provided with the package (i.e. sinh-Gordon model) were tested for temperatures $T \approx 1$. The convergence of the thermodynamic Bethe ansatz equations has been successfully ensured for temperatures up to $\mathcal{O}(e^{10})$, and the results have been checked in the several ways, as we will see in the next section.

D.2 Precision and consistency checks

In order to make sure that the modified code gave meaningful results we carried out various consistency checks, mainly comparing the outputs of `iFluid` with standard results that are accessible by other numerical procedures.

A preliminary check was done on the initial state, which is given by the solution of the (equilibrium) TBA equations for a given fixed temperature $T(x)$ for each value of x . In the `iFluid` code, the precision is controlled by two parameters, namely, the tolerance and the maximal number of iterations allowed. In order to guarantee the highest accuracy, we set the former to 10^{-32} and the latter to 5000. We made these choices in part by comparing the outputs of `iFluid` in the initial state to results obtained for the same functions with a `Mathematica` code used in Chapter 8, and established that, for the choices above, we achieved higher precision with `iFluid`.

A similar check was performed by evaluating the TBA scaling function (7.23) over a range of

temperatures (especially at high temperatures), and seeing that plateaus at the expected values of the central charge [31] were reproduced. An example is displayed in Fig. 7.1. Likewise we computed the energy densities and currents in the UV (high temperature) limit, reproducing the results of Section 8.2.

t	0	3	6	9	12	15
Q_0	561.2520	561.2541	561.1937	561.1511	561.1156	561.0970

Table D.1: Numerical values of the total integrated particle density Q_0 at several times. Here, the parameters are: $\sigma = 10$, $\log(2T_m) = 7$ and $T_a = 0$ (no bath). To evaluate Q_0 , we have computed (7.33) for $i = 0$ and performed a cubic spline interpolation, implementing additional grid points whose spacing in x is $\Delta x = 1. \times 10^{-5}$. Q_0 is numerically conserved, up to a variation on the first decimal place, which can be attributed to the discretisation procedure.

Having established that the initial state is accurately described, we then turned to consistency checks of dynamical quantities. We calculated the total particle density Q_0 given by the x -integral of the total particle density (7.33) for $i = 0$. Q_0 should be conserved in time and so its computation for various values of times provides a consistency check for numerical solutions of the GHD equations. In Table D.1 we have reported the numerical values of the total particle density evaluated in the no-bath case. Q_0 is confirmed to be conserved, up to a numerical variation on the first decimal place, which is the order of the grid spacing implemented in the simulation (see Table D.2 for details).

Finally, we performed other consistency checks which exploit the connection of our model with free theories. In particular, as explained in 7.1, we have that for $T \ll e^{|\sigma|/2}$ our model should reduce to two Majorana free fermions. Thus, performing numerics for the $SU(3)_2$ -HSG model with $\sigma = 20$ for the same temperature choices discussed in Chapter 9, we should obtain results which are fully in the free fermion regime where the time-evolution equations can be solved exactly. Thus, in this regime numerical results from iFluid can be compared to analytical solutions. We have confirmed that they are in perfect agreement.

D.3 Space and rapidity discretisations

Besides convergence of the numerical solution of the TBA equations, we have established that the key source of numerical error is the choice of space discretisation. The values adopted in our computations are given in Table D.2.

We have devoted special attention to the discretisation of the rapidity interval. iFluid employs Gauss-Legendre quadrature integration, which has excellent convergence properties for

	Δ_{\max}	No. Points	Max. Val.	Quadrature
t	0.2500	61	15.	Rectangular
x	0.1000	441	22.	Rectangular
θ	0.0762	700	17.	Gauss-Legendre

Table D.2: Discretisation parameters and quadratures chosen for the two numerical simulations (i.e. with and without a bath) presented in [36] and discussed in Chapter 9. From the left, the columns indicate (respectively for t, x, θ): the variable, the lowest resolution (i.e. the largest spacing between two grid points Δ_{\max}), the number of grid points, the largest absolute value the variable takes, and the type of quadrature implemented. In the rectangular quadrature we have implemented equidistant grid points with fixed spacing Δ_{\max} .

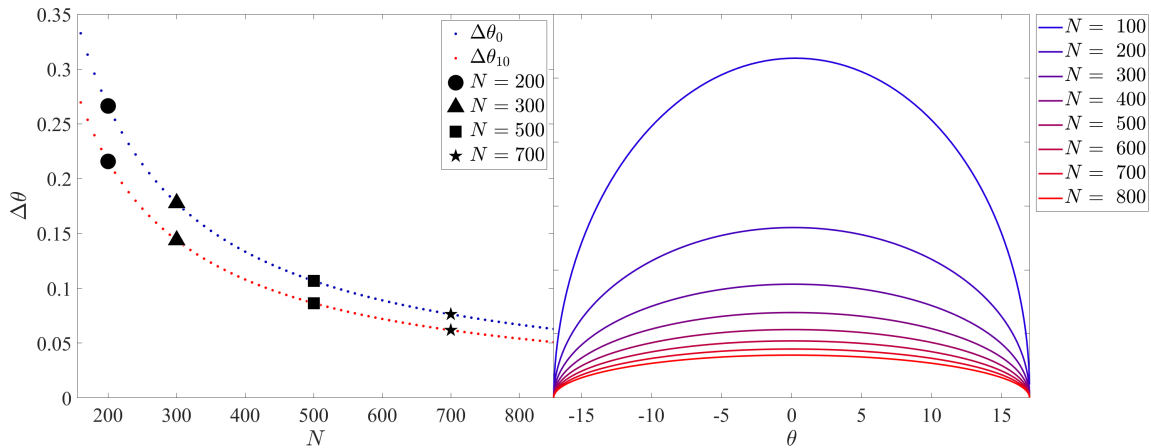


Figure D.1 Right: The rapidity discretisation interval as a function of rapidity for different numbers of points in a fixed rapidity interval $\theta \in [-17, 17]$. The markers indicate the values of N that are considered in Fig. D.2. Left: Comparison of the rapidity discretisation interval in the middle and towards the edges of the interval with non-trivial dynamics. $\Delta\theta_0$ and $\Delta\theta_{10}$ are defined to be the rapidity discretisation intervals for $\theta = 0$ and $\theta = 10$, respectively.

integrals over a finite interval [172, 173]. However, this quadrature is optimised for minimising boundary errors. This means that the number of data intervals is lowest in the middle of the interval, precisely where we find the non-trivial behaviour of the thermodynamic quantities of interest. The dependence of the size of the rapidity intervals, $\Delta\theta$ on the rapidity θ and the number of points in the interval considered N for a fixed range of rapidities is shown in Fig. D.1.

As a point of reference, we have chosen to compare the resolution at $\theta = 0$ and 10, as a primary region with non-trivial dynamics. Although the discretisation interval for $\theta = 0$ remains the largest for any value of N , the distribution quickly flattens out when the number of points is increased. Investigating the range of N values from 200 to 700, we achieve an order of magnitude increase in resolution for both $\theta = 0$ and 10. Significantly smaller is also the difference between these two quantities, which is consistent with the flattening of the curve in the right panel of fig. D.1. The numerical values of the size of the discretisation interval for a

chosen numbers of points in the rapidity interval are included in Table D.3.

N	$\Delta\theta_0$	$\Delta\theta_{10}$	$\Delta\theta_0 - \Delta\theta_{10}$
200	0.2664	0.2157	0.0506
300	0.1777	0.1439	0.0338
500	0.1067	0.0864	0.0203
700	0.0762	0.0617	0.0145

Table D.3: Numerical values of the rapidity discretisation intervals $\Delta\theta$, for a given number of rapidity points N in the range of rapidities used in this investigation $\theta \in [-17, 17]$.

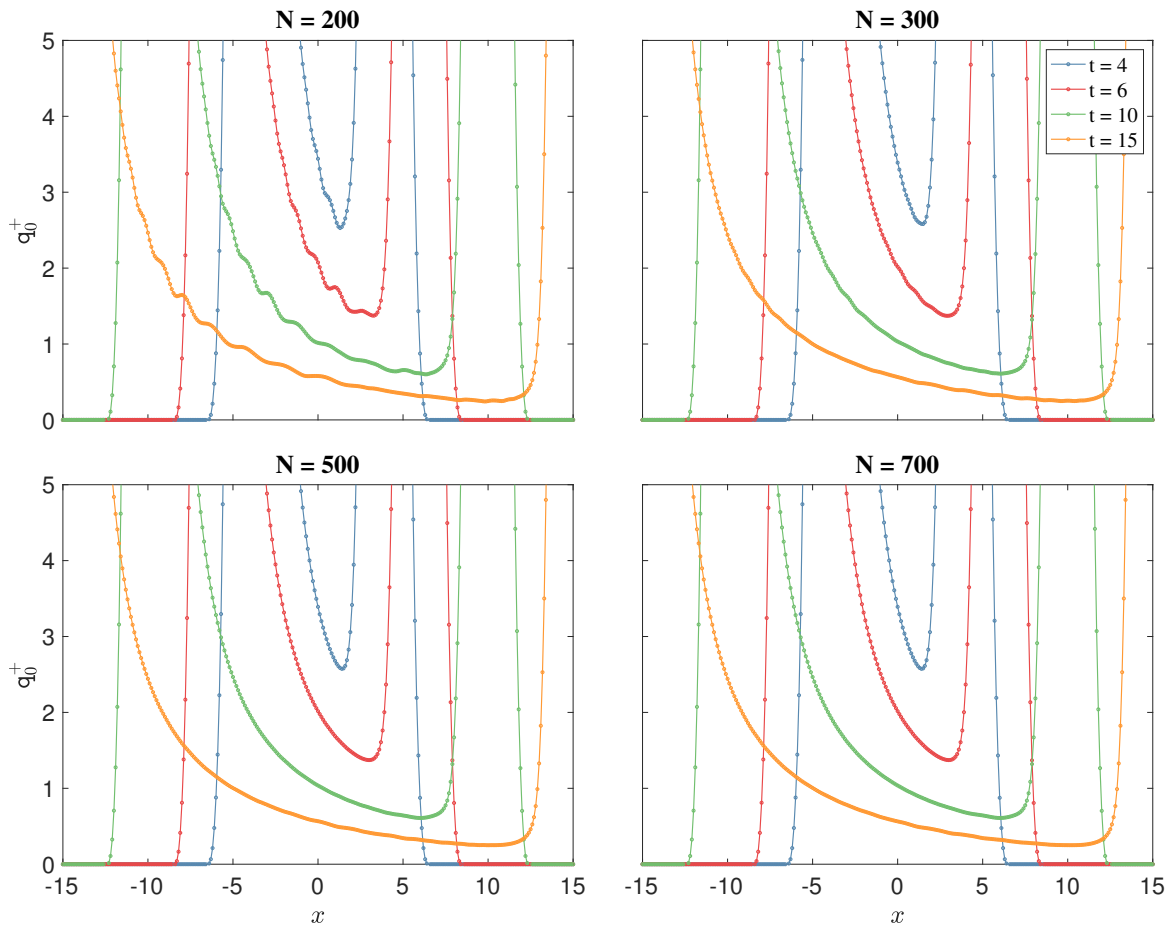


Figure D.2 Spatial particle density of particle + for different numbers of points in the fixed rapidity interval $\theta \in [-17, 17]$. The $N = 200$ panel shows regular oscillations. The oscillations persist for $N = 300$, disappear around $N = 500$ and are consistently absent for higher numbers of points, such as $N = 700$. Variations of space and time discretisation parameters have not produced any significant changes in the same functions.

In order to obtain the averages of conserved charges and currents in the $SU(3)_2$ -HSG model, it is necessary to integrate over the rapidity variable, as defined in (7.33). This integration procedure leads to the “accumulation” of any numerical errors present in the original function and to the formation of regular structures that could be easily mistaken for genuine physical phenomena. An example of this effect can be seen in the particle density associated to particle

+ computed with different rapidity discretisations. Four examples are presented in Fig. D.2. As expected, the problem arises from the middle of the rapidity interval where resolution is lowest. By changing N we can identify a large enough value that guarantees a stable solution for the spatial particle density. In our code we have chosen $N = 700$. The quantities not integrated over the rapidity integral did not exhibit any unusual behaviour even for the values of N as low as 200. Interestingly, this applies also to the spectral density, which produces then spatial particle density when integrated over rapidity. This further confirms that the emergence of of the oscillations seen in the top left fig. D.2 is genuinely a numerical effect arising due to integration.

REFERENCES

- [1] S. Weinberg. *The Quantum Theory of Fields: Volume 1: Foundations*. Vol. 1. Cambridge: Cambridge University Press, 1995. DOI: [10.1017/CBO9781139644167](https://doi.org/10.1017/CBO9781139644167).
- [2] R. D. Mattuck. *A Guide to Feynman Diagrams in the Many-body Problem*. 2nd. Vol. 1. McGraw-Hill Publishing Company, 1967.
- [3] N. Bogolubov. “On the theory of superfluidity”. In: *Journal of Physics* 11.1 (1947), pp. 23–32.
- [4] C. H. Bennett, H. J. Bernstein, S. Popescu, and B. Schumacher. “Concentrating partial entanglement by local operations”. In: *Phys. Rev. A* 53.4 (1996), pp. 2046–2052. DOI: [10.1103/PhysRevA.53.2046](https://doi.org/10.1103/PhysRevA.53.2046).
- [5] A. Rényi. “On Measures of Entropy and Information”. In: *Proceedings of the Fourth Berkeley Symposium on Mathematical Statistics and Probability, Volume 1: Contributions to the Theory of Statistics*. Berkeley, Calif.: University of California Press, 1961, pp. 547–561.
- [6] M. B. Plenio. “Logarithmic Negativity: A Full Entanglement Monotone That is not Convex”. In: *Phys. Rev. Lett.* 95.9 (2005), p. 090503. DOI: [10.1103/PhysRevLett.95.090503](https://doi.org/10.1103/PhysRevLett.95.090503).
- [7] M. B. Plenio. “Publisher’s Note: Logarithmic Negativity: A Full Entanglement Monotone That Is not Convex [Phys. Rev. Lett. 95, 090503 (2005)]”. In: *Phys. Rev. Lett.* 95.11 (2005), p. 119902. DOI: [10.1103/PhysRevLett.95.119902](https://doi.org/10.1103/PhysRevLett.95.119902).
- [8] C. G. Callan Jr. and F. Wilczek. “On geometric entropy”. In: *Phys. Lett. B* 333 (1994), pp. 55–61. DOI: [10.1016/0370-2693\(94\)91007-3](https://doi.org/10.1016/0370-2693(94)91007-3).
- [9] C. Holzhey, F. Larsen, and F. Wilczek. “Geometric and renormalized entropy in conformal field theory”. In: *Nucl. Phys. B* 424.3 (1994), pp. 443–467.

- [10] P. Calabrese and J. Cardy. “Entanglement entropy and quantum field theory”. In: *J. Stat. Mech.* 2004.06 (2004), P06002. DOI: [10.1088/1742-5468/2004/06/p06002](https://doi.org/10.1088/1742-5468/2004/06/p06002).
- [11] P. Calabrese, J. Cardy, and E. Tonni. “Entanglement entropy of two disjoint intervals in conformal field theory”. In: *J. Stat. Mech.* 2009.11 (2009), P11001. DOI: [10.1088/1742-5468/2009/11/p11001](https://doi.org/10.1088/1742-5468/2009/11/p11001).
- [12] P. Calabrese, J. Cardy, and E. Tonni. “Entanglement entropy of two disjoint intervals in conformal field theory: II”. In: *J. Stat. Mech.* 2011.01 (2011), P01021. DOI: [10.1088/1742-5468/2011/01/p01021](https://doi.org/10.1088/1742-5468/2011/01/p01021).
- [13] P. Calabrese, J. Cardy, and E. Tonni. “Entanglement Negativity in Quantum Field Theory”. In: *Phys. Rev. Lett.* 109.13 (2012), p. 130502. DOI: [10.1103/PhysRevLett.109.130502](https://doi.org/10.1103/PhysRevLett.109.130502).
- [14] P. Calabrese, J. Cardy, and E. Tonni. “Entanglement negativity in extended systems: a field theoretical approach”. In: *J. Stat. Mech.* 2013.02 (2013), P02008.
- [15] J. L. Cardy, O. A. Castro-Alvaredo, and B. Doyon. “Form Factors of Branch-Point Twist Fields in Quantum Integrable Models and Entanglement Entropy”. In: *Journal of Statistical Physics* 130.1 (2008), pp. 129–168.
- [16] O. A. Castro-Alvaredo and B. Doyon. “Bi-partite entanglement entropy in massive (1+1)-dimensional quantum field theories”. In: *J. Phys. A: Math. Theor.* 42.50 (2009), p. 504006. DOI: [10.1088/1751-8113/42/50/504006](https://doi.org/10.1088/1751-8113/42/50/504006).
- [17] B. Doyon. “Bipartite Entanglement Entropy in Massive Two-Dimensional Quantum Field Theory”. In: *Phys. Rev. Lett.* 102.3 (2009), p. 031602. DOI: [10.1103/PhysRevLett.102.031602](https://doi.org/10.1103/PhysRevLett.102.031602).
- [18] O. Blondeau-Fournier, O. A. Castro-Alvaredo, and B. Doyon. “Universal scaling of the logarithmic negativity in massive quantum field theory”. In: *J. Phys. A: Math. Theor.* 49.12 (2016), p. 125401.
- [19] C. R. Fernández-Pousa, M. V. Gallas, T. J. Hollowood, and J. L. Miramontes. “Solitonic integrable perturbations of parafermionic theories”. In: *Nucl. Phys. B* 499.3 (1997), pp. 673–689.
- [20] C. R. Fernandez-Pousa, M. V. Gallas, J. Hollowood, and J. Luis Miramontes. “The symmetric space and homogeneous sine-Gordon theories”. In: *Nucl. Phys. B* 484.3 (1997), pp. 609–630.

-
- [21] C. R. Fernández-Pousa and J. L. Miramontes. “Semi-classical spectrum of the homogeneous sine-Gordon theories”. In: *Nucl. Phys. B* 518.3 (1998), pp. 745–769.
- [22] J. L. Miramontes and C. R. Fernández-Pousa. “Integrable quantum field theories with unstable particles”. In: *Physics Letters B* 472.3 (2000), pp. 392–401.
- [23] O. A. Castro-Alvaredo, C. De Fazio, B. Doyon, and I. M. Szécsényi. “Entanglement Content of Quasiparticle Excitations”. In: *Phys. Rev. Lett.* 121.17 (2018), p. 170602. DOI: [10.1103/PhysRevLett.121.170602](https://doi.org/10.1103/PhysRevLett.121.170602).
- [24] O. A. Castro-Alvaredo, C. De Fazio, B. Doyon, and I. M. Szécsényi. “Entanglement content of quantum particle excitations. Part I. Free field theory”. In: *J. High Energ. Phys.* 2018.10 (2018), p. 39. DOI: [10.1007/JHEP12\(2019\)079](https://doi.org/10.1007/JHEP12(2019)079).
- [25] P. Fonseca and A. Zamolodchikov. “Ward identities and integrable differential equations in the Ising field theory”. In: (2003). arXiv: [hep-th/0309228](https://arxiv.org/abs/hep-th/0309228).
- [26] O. A. Castro-Alvaredo, C. De Fazio, B. Doyon, and I. M. Szécsényi. “Entanglement content of quantum particle excitations. Part II. Disconnected regions and logarithmic negativity”. In: *J. High Energ. Phys.* 11 (2019), p. 058. DOI: [10.1007/JHEP11\(2019\)058](https://doi.org/10.1007/JHEP11(2019)058).
- [27] C. De Fazio. “Contour integral approach to excited state logarithmic negativity of adjacent regions”. In: *Preparation* (2022).
- [28] O. A. Castro-Alvaredo, C. De Fazio, B. Doyon, and I. M. Szécsényi. “Entanglement content of quantum particle excitations. III. Graph partition functions”. In: *Journal of Mathematical Physics* 60.8 (2019), p. 082301. DOI: [10.1063/1.5098892](https://doi.org/10.1063/1.5098892).
- [29] A. Zamolodchikov. “Thermodynamic Bethe ansatz in relativistic models. Scaling three state Potts and Lee-Yang models”. In: *Nucl. Phys.* B342 (1990), pp. 695–720.
- [30] T. R. Klassen and E. Melzer. “The Thermodynamics of purely elastic scattering theories and conformal perturbation theory”. In: *Nucl. Phys.* B350 (1991), pp. 635–689.
- [31] O. A. Castro-Alvaredo, A. Fring, C. Korff, and J. L. Miramontes. “Thermodynamic Bethe ansatz of the homogeneous sine-Gordon models”. In: *Nucl. Phys. B* 575.3 (2000), pp. 535–560.
- [32] O. A. Castro-Alvaredo, B. Doyon, and T. Yoshimura. “Emergent Hydrodynamics in Integrable Quantum Systems Out of Equilibrium”. In: *Phys. Rev. X* 6.4 (2016), p. 041065. DOI: [10.1103/PhysRevX.6.041065](https://doi.org/10.1103/PhysRevX.6.041065).

- [33] B. Bertini, M. Collura, J. De Nardis, and M. Fagotti. “Transport in Out-of-Equilibrium XXZ Chains: Exact Profiles of Charges and Currents”. In: *Phys. Rev. Lett.* 117.20 (2016), p. 207201. DOI: [10.1103/PhysRevLett.117.207201](https://doi.org/10.1103/PhysRevLett.117.207201).
- [34] M. Rigol, V. Dunjko, V. Yurovsky, and M. Olshanii. “Relaxation in a Completely Integrable Many-Body Quantum System: An Ab Initio Study of the Dynamics of the Highly Excited States of 1D Lattice Hard-Core Bosons”. In: *Phys. Rev. Lett.* 98.5 (2007), p. 050405. DOI: [10.1103/PhysRevLett.98.050405](https://doi.org/10.1103/PhysRevLett.98.050405).
- [35] O. A. Castro-Alvaredo, C. De Fazio, B. Doyon, and F. Ravanini. “On the hydrodynamics of unstable excitations”. In: *J. High Energ. Phys.* 2020.9 (2020), p. 45. DOI: [10.1007/JHEP09\(2020\)045](https://doi.org/10.1007/JHEP09(2020)045).
- [36] O. A. Castro-Alvaredo, C. De Fazio, B. Doyon, and A. Ziólkowska. “Tails of Instability and Decay: a Hydrodynamic Perspective”. In: (2021). arXiv: [2103.03735 \[hep-th\]](https://arxiv.org/abs/2103.03735).
- [37] G. Mussardo. *Statistical Field Theory: an introduction to exactly solved models in statistical physics*. 1st. Oxford University Press, 2010, pp. 557–601.
- [38] P. Dorey. “Exact S matrices”. In: *Eotvos Summer School in Physics: Conformal Field Theories and Integrable Models*. 1996, pp. 85–125. arXiv: [hep-th/9810026](https://arxiv.org/abs/hep-th/9810026).
- [39] A. B. Zamolodchikov and A. B. Zamolodchikov. “Factorized S-matrices in two dimensions as the exact solutions of certain relativistic quantum field theory models”. In: *Annals of Physics* 120.2 (1979), pp. 253–291.
- [40] S. Parke. “Absence of particle production and factorization of the S-matrix in 1 + 1 dimensional models”. In: *Nucl. Phys. B* 174.1 (1980), pp. 166–182.
- [41] C. N. Yang. “Some Exact Results for the Many-Body Problem in one Dimension with Repulsive Delta-Function Interaction”. In: *Phys. Rev. Lett.* 19.23 (1967), pp. 1312–1315. DOI: [10.1103/PhysRevLett.19.1312](https://doi.org/10.1103/PhysRevLett.19.1312).
- [42] R. J. Baxter. “One-dimensional anisotropic Heisenberg chain”. In: *Annals of Physics* 70.2 (1972), pp. 323–337. DOI: [10.1016/0003-4916\(72\)90270-9](https://doi.org/10.1016/0003-4916(72)90270-9).
- [43] L. Castillejo, R. H. Dalitz, and F. J. Dyson. “Low’s Scattering Equation for the Charged and Neutral Scalar Theories”. In: *Phys. Rev.* 101.1 (1956), pp. 453–458. DOI: [10.1103/PhysRev.101.453](https://doi.org/10.1103/PhysRev.101.453).
- [44] G. F. Chew, R. J. Eden, P. V. Landshoff, D. I. Olive, J. C. Polkinghorne, and T. Regge. “The Analytic S Matrix: A Basis for Nuclear Democracy and The Analytic S Matrix”. In: *Physics Today* 20.9 (1967), pp. 82–87.

-
- [45] O. A. Castro-Alvaredo, J. Dreißig, and A. Fring. “Integrable scattering theories with unstable particles”. In: *The European Physical Journal C - Particles and Fields* 35.3 (2004), pp. 393–411.
- [46] G. Breit and E. Wigner. “Capture of Slow Neutrons”. In: *Phys. Rev.* 49.7 (1936), pp. 519–531. DOI: [10.1103/PhysRev.49.519](https://doi.org/10.1103/PhysRev.49.519).
- [47] E. Schrödinger. “Discussion of Probability Relations Between Separated Systems”. In: *Proceedings of the Cambridge Philosophical Society*. Vol. 31. 1935, pp. 555–563.
- [48] A. Einstein, B. Podolsky, and N. Rosen. “Can Quantum-Mechanical Description of Physical Reality Be Considered Complete?” In: *Phys. Rev.* 47.10 (1935), pp. 777–780. DOI: [10.1103/PhysRev.47.777](https://doi.org/10.1103/PhysRev.47.777).
- [49] J. S. Bell. “On the Einstein-Podolsky-Rosen paradox”. In: *Physics* 1 (1964), pp. 195–200.
- [50] A. Aspect, P. Grangier, and G. Roger. “Experimental Realization of Einstein-Podolsky-Rosen-Bohm Gedankenexperiment: A New Violation of Bell’s Inequalities”. In: *Phys. Rev. Lett.* 49.2 (1982), pp. 91–94. DOI: [10.1103/PhysRevLett.49.91](https://doi.org/10.1103/PhysRevLett.49.91).
- [51] M. A. Nielsen and I. L. Chuang. *Quantum Computation and Quantum Information*. 10th. Cambridge University Press, 2011. ISBN: 1107002176, 9781107002173.
- [52] L. Amico, R. Fazio, A. Osterloh, and V. Vedral. “Entanglement in many-body systems”. In: *Rev. Mod. Phys.* 80.2 (2008), pp. 517–576. DOI: [10.1103/RevModPhys.80.517](https://doi.org/10.1103/RevModPhys.80.517).
- [53] R. Islam, R. Ma, P. M. Preiss, M. Eric Tai, A. Lukin, M. Rispoli, and M. Greiner. “Measuring entanglement entropy in a quantum many-body system”. In: *Nature* 528.7580 (2015), pp. 77–83.
- [54] M. B. Plenio and S. Virmani. “An Introduction to Entanglement Measures”. In: *Quantum Info. Comput.* 7.1 (2007), pp. 1–51. ISSN: 1533-7146.
- [55] J. I. Latorre and A. Riera. “A short review on entanglement in quantum spin systems”. In: *J. Phys. A: Math. Theor.* 42.50 (2009), p. 504002. DOI: [10.1088/1751-8113/42/50/504002](https://doi.org/10.1088/1751-8113/42/50/504002).
- [56] P. Calabrese, J. Cardy, and B. Doyon. “Entanglement entropy in extended quantum systems”. In: *J. Phys. A: Math. Theor.* 42.50 (2009), p. 500301. DOI: [10.1088/1751-8121/42/50/500301](https://doi.org/10.1088/1751-8121/42/50/500301).

- [57] P. Calabrese and J. Cardy. “Entanglement and correlation functions following a local quench: a conformal field theory approach”. In: *J. Stat. Mech.* 2007.10 (2007), P10004–P10004. DOI: [10.1088/1742-5468/2007/10/p10004](https://doi.org/10.1088/1742-5468/2007/10/p10004).
- [58] P. Calabrese and J. Cardy. “Quantum quenches in 1 + 1 dimensional conformal field theories”. In: *J. Stat. Mech.* 2016.6 (2016), p. 064003. DOI: [10.1088/1742-5468/2016/06/064003](https://doi.org/10.1088/1742-5468/2016/06/064003).
- [59] V. Alba and P. Calabrese. “Entanglement and thermodynamics after a quantum quench in integrable systems”. In: *Proceedings of the National Academy of Sciences* 114.30 (2017), p. 7947. DOI: [10.1073/pnas.1703516114](https://doi.org/10.1073/pnas.1703516114).
- [60] T. Nishioka, S. Ryu, and T. Takayanagi. “Holographic Entanglement Entropy: An Overview”. In: *J. Phys. A* 42 (2009), p. 504008. DOI: [10.1088/1751-8113/42/50/504008](https://doi.org/10.1088/1751-8113/42/50/504008).
- [61] J. Eisert and M. Cramer. “Single-copy entanglement in critical quantum spin chains”. In: *Phys. Rev. A* 72.4 (2005), p. 042112. DOI: [10.1103/PhysRevA.72.042112](https://doi.org/10.1103/PhysRevA.72.042112).
- [62] I. Peschel and J. Zhao. “On single-copy entanglement”. In: *J. Stat. Mech.* 2005.11 (2005), P11002–P11002. DOI: [10.1088/1742-5468/2005/11/p11002](https://doi.org/10.1088/1742-5468/2005/11/p11002).
- [63] A. Dimić and B. Dakić. “Single-copy entanglement detection”. In: *npj Quantum Information* 4.1 (2018), p. 11. DOI: [10.1038/s41534-017-0055-x](https://doi.org/10.1038/s41534-017-0055-x).
- [64] A. Peres. “Separability Criterion for Density Matrices”. In: *Phys. Rev. Lett.* 77.8 (1996), pp. 1413–1415. DOI: [10.1103/PhysRevLett.77.1413](https://doi.org/10.1103/PhysRevLett.77.1413).
- [65] G. Vidal and R. F. Werner. “Computable measure of entanglement”. In: *Phys. Rev. A* 65.3 (2002), p. 032314. DOI: [10.1103/PhysRevA.65.032314](https://doi.org/10.1103/PhysRevA.65.032314).
- [66] R. A. Horn and C. R. Johnson. *Matrix analysis*. Cambridge University Press, 1985. DOI: [10.1017/CB09780511810817](https://doi.org/10.1017/CB09780511810817).
- [67] R. Bhatia. *Matrix analysis*. Springer New York, 1997.
- [68] V. G. Knizhnik. “Analytic fields on Riemann surfaces. II”. In: *Communications in Mathematical Physics* 112.4 (1987), pp. 567–590.
- [69] T. D. Schultz, D. C. Mattis, and E. H. Lieb. “Two-Dimensional Ising Model as a Soluble Problem of Many Fermions”. In: *Rev. Mod. Phys.* 36.3 (1964), pp. 856–871. DOI: [10.1103/RevModPhys.36.856](https://doi.org/10.1103/RevModPhys.36.856).

-
- [70] O. Babelon and D. Bernard. “From form factors to correlation functions. The Ising model”. In: *Physics Letters B* 288.1 (1992), pp. 113–120.
- [71] V. P. Yurov and A. B. Zamolodchikov. “Correlation Functions Of Integrable 2D Models Of The Relativistic Field Theory: Ising Model”. In: *Int. J. of Mod. Phys. A* 06.19 (1991), pp. 3419–3440. DOI: [10.1142/S0217751X91001660](https://doi.org/10.1142/S0217751X91001660).
- [72] D. Bernard and A. LeClair. “Differential equations for sine-Gordon correlation functions at the free fermion point”. In: *Nucl. Phys. B* 426.3 (1994), pp. 534–558.
- [73] O. A. Castro-Alvaredo and B. Doyon. “Bi-partite entanglement entropy in integrable models with backscattering”. In: *J. Phys. A: Math. Theor.* 41.27 (2008), p. 275203. DOI: [10.1088/1751-8113/41/27/275203](https://doi.org/10.1088/1751-8113/41/27/275203).
- [74] O. A. Castro-Alvaredo, B. Doyon, and E. Levi. “Arguments towards a c-theorem from branch-point twist fields”. In: *J. Phys. A: Math. Theor.* 44.49 (2011), p. 492003. DOI: [10.1088/1751-8113/44/49/492003](https://doi.org/10.1088/1751-8113/44/49/492003).
- [75] E. Levi. “Composite branch-point twist fields in the Ising model and their expectation values”. In: *J. Phys. A: Math. Theor.* 45.27 (2012), p. 275401. DOI: [10.1088/1751-8113/45/27/275401](https://doi.org/10.1088/1751-8113/45/27/275401).
- [76] O. A. Castro-Alvaredo and B. Doyon. “Bi-partite Entanglement Entropy in Massive QFT with a Boundary: the Ising Model”. In: *J Stat Phys* 134.1 (2009), pp. 105–145. DOI: [10.1007/s10955-008-9664-2](https://doi.org/10.1007/s10955-008-9664-2).
- [77] D. Bianchini and O. A. Castro-Alvaredo. “Branch point twist field correlators in the massive free Boson theory”. In: *Nucl. Phys. B* 913 (2016), pp. 879–911. DOI: <https://doi.org/10.1016/j.nuclphysb.2016.10.016>.
- [78] D. Bianchini, O. A. Castro-Alvaredo, and B. Doyon. “Entanglement entropy of non-unitary integrable quantum field theory”. In: *Nucl. Phys. B* 896 (2015), pp. 835–880. DOI: <https://doi.org/10.1016/j.nuclphysb.2015.05.013>.
- [79] D. Bianchini, O. Castro-Alvaredo, B. Doyon, E. Levi, and F. Ravanini. “Entanglement entropy of non-unitary conformal field theory”. In: *J. Phys. A: Math. Theor.* 48.4 (2014), 04FT01. DOI: [10.1088/1751-8113/48/4/04ft01](https://doi.org/10.1088/1751-8113/48/4/04ft01).
- [80] O. A. Castro-Alvaredo, B. Doyon, and F. Ravanini. “Irreversibility of the renormalization group flow in non-unitary quantum field theory”. In: *J. Phys. A: Math. Theor.* 50.42 (2017), p. 424002. DOI: [10.1088/1751-8121/aa8a10](https://doi.org/10.1088/1751-8121/aa8a10).
-

- [81] O. A. Castro-Alvaredo, M. Lencsés, I. M. Szécsényi, and J. Viti. “Entanglement Oscillations near a Quantum Critical Point”. In: *Phys. Rev. Lett.* 124.23 (2020), p. 230601. DOI: [10.1103/PhysRevLett.124.230601](https://doi.org/10.1103/PhysRevLett.124.230601).
- [82] O. A. Castro-Alvaredo, M. Lencsés, I. M. Szécsényi, and J. Viti. “Entanglement dynamics after a quench in Ising field theory: a branch point twist field approach”. In: *J. High Energ. Phys.* 2019.12 (2019), p. 79. DOI: [10.1007/JHEP12\(2019\)079](https://doi.org/10.1007/JHEP12(2019)079).
- [83] J. Eisert, M. Cramer, and M. B. Plenio. “Colloquium: Area laws for the entanglement entropy”. In: *Rev. Mod. Phys.* 82.1 (2010), pp. 277–306. DOI: [10.1103/RevModPhys.82.277](https://doi.org/10.1103/RevModPhys.82.277).
- [84] M. Karowski and P. Weisz. “Exact Form-Factors in (1+1)-Dimensional Field Theoretic Models with Soliton Behavior”. In: *Nucl. Phys. B* 139 (1978), pp. 455–476. DOI: [10.1016/0550-3213\(78\)90362-0](https://doi.org/10.1016/0550-3213(78)90362-0).
- [85] F. A. Smirnov. *Form-factors in completely integrable models of quantum field theory*. Vol. 14. 1992.
- [86] B. Pozsgay and G. Takács. “Form factors in finite volume I: Form factor bootstrap and truncated conformal space”. In: *Nucl. Phys. B* 788.3 (2008), pp. 167–208. ISSN: 0550-3213. DOI: <https://doi.org/10.1016/j.nuclphysb.2007.06.027>.
- [87] B. Pozsgay and G. Takács. “Form factors in finite volume II: Disconnected terms and finite temperature correlators”. In: *Nucl. Phys. B* 788.3 (2008), pp. 209–251. ISSN: 0550-3213. DOI: <https://doi.org/10.1016/j.nuclphysb.2007.07.008>.
- [88] P. Fonseca and A. Zamolodchikov. “Ising field theory in a magnetic field: Analytic properties of the free energy”. In: (2001). arXiv: [hep-th/0112167](https://arxiv.org/abs/hep-th/0112167).
- [89] O. Blondeau-Fournier and B. Doyon. “Expectation values of twist fields and universal entanglement saturation of the free massive boson”. In: *J. Phys. A: Math. Theor.* 50.27 (2017), p. 274001. DOI: [10.1088/1751-8121/aa7492](https://doi.org/10.1088/1751-8121/aa7492).
- [90] H. Casini and M. Huerta. “Entanglement entropy in free quantum field theory”. In: *J. Phys. A* 42 (2009), p. 504007. DOI: [10.1088/1751-8113/42/50/504007](https://doi.org/10.1088/1751-8113/42/50/504007).
- [91] J. L. Cardy and G. Mussardo. “Form factors of descendent operators in perturbed conformal field theories”. In: *Nucl. Phys. B* 340.2 (1990), pp. 387–402.
- [92] A. Fring, G. Mussardo, and P. Simonetti. “Form factors for integrable lagrangian field theories, the sinh-Gordon model”. In: *Nucl. Phys. B* 393.1 (1993), pp. 413–441.

-
- [93] A. Koubek and G. Mussardo. “On the operator content of the sinh-Gordon model”. In: *Physics Letters B* 311.1 (1993), pp. 193–201.
- [94] H. Babujian, A. Fring, M. Karowski, and A. Zapletal. “Exact form factors in integrable quantum field theories: the sine-Gordon model”. In: *Nucl. Phys. B* 538.3 (1999), pp. 535–586.
- [95] A. B. Zamolodchikov. “Two-point correlation function in scaling Lee-Yang model”. In: *Nucl. Phys. B* 348.3 (1991), pp. 619–641.
- [96] O. A. Castro-Alvaredo and A. Fring. “Form factors from free fermionic Fock fields, the Federbush model”. In: *Nuclear Physics B* 618.3 (2001), pp. 437–464. DOI: [10.1016/S0550-3213\(01\)00462-X](https://doi.org/10.1016/S0550-3213(01)00462-X).
- [97] M. Sato, T. Miwa, and M. Jimbo. “Holonomic quantum fields. 4.” In: *Publ. Res. Inst. Math. Sci. Kyoto* 15 (1979), pp. 871–972. DOI: [10.2977/prims/1195187881](https://doi.org/10.2977/prims/1195187881).
- [98] H. Bethe. “On the theory of metals. 1. Eigenvalues and eigenfunctions for the linear atomic chain”. In: *Z. Phys.* 71 (1931), pp. 205–226. DOI: [10.1007/BF01341708](https://doi.org/10.1007/BF01341708).
- [99] C.-N. Yang and C. P. Yang. “Thermodynamics of one-dimensional system of bosons with repulsive delta function interaction”. In: *J. Math. Phys.* 10 (1969), pp. 1115–1122. DOI: [10.1063/1.1664947](https://doi.org/10.1063/1.1664947).
- [100] M. Lüscher. “Volume dependence of the energy spectrum in massive quantum field theories. I. Stable particle states”. In: *Comm. Math. Phys.* 104.2 (1986), pp. 177–206.
- [101] F. C. Alcaraz, M. I. Berganza, and G. Sierra. “Entanglement of low-energy excitations in Conformal Field Theory”. In: *Phys. Rev. Lett.* 106 (2011), p. 201601. DOI: [10.1103/PhysRevLett.106.201601](https://doi.org/10.1103/PhysRevLett.106.201601).
- [102] M. Ibáñez Berganza, F. C. Alcaraz, and G. Sierra. “Entanglement of excited states in critical spin chains”. In: *J. Stat. Mech.* 2012.01 (2012), P01016. DOI: [10.1088/1742-5468/2012/01/p01016](https://doi.org/10.1088/1742-5468/2012/01/p01016).
- [103] V. Alba, M. Fagotti, and P. Calabrese. “Entanglement entropy of excited states”. In: *J. Stat. Mech.* 2009.10 (2009), P10020. DOI: [10.1088/1742-5468/2009/10/p10020](https://doi.org/10.1088/1742-5468/2009/10/p10020).
- [104] J. Mölter, T. Barthel, U. Schollwöck, and V. Alba. “Bound states and entanglement in the excited states of quantum spin chains”. In: *J. Stat. Mech.* 2014.10 (2014), P10029. DOI: [10.1088/1742-5468/2014/10/p10029](https://doi.org/10.1088/1742-5468/2014/10/p10029).
-

- [105] L. J. Dixon, D. Friedan, E. J. Martinec, and S. H. Shenker. “The Conformal Field Theory of Orbifolds”. In: *Nucl. Phys. B* 282 (1987), pp. 13–73. DOI: [10.1016/0550-3213\(87\)90676-6](https://doi.org/10.1016/0550-3213(87)90676-6).
- [106] B. Pozsgay and G. Takács. “Form factor expansion for thermal correlators”. In: *J. Stat. Mech.* 2010.11 (2010), P11012.
- [107] I. M. Szécsényi and G. Takács. “Spectral expansion for finite temperature two-point functions and clustering”. In: *J. Stat. Mech.* 2012.12 (2012), P12002.
- [108] A. Jafarizadeh and M. A. Rajabpour. “Bipartite entanglement entropy of the excited states of free fermions and harmonic oscillators”. In: *Phys. Rev. B* 100.16 (2019). DOI: [10.1103/physrevb.100.165135](https://doi.org/10.1103/physrevb.100.165135).
- [109] J. Zhang and M. Rajabpour. “Excited state Rényi entropy and subsystem distance in two-dimensional non-compact bosonic theory. Part I. Single-particle states”. In: *J. High Energ. Phys.* 2020.12 (2020). DOI: [10.1007/jhep12\(2020\)160](https://doi.org/10.1007/jhep12(2020)160).
- [110] J. Zhang and M. A. Rajabpour. *Universal Rényi Entropy of Quasiparticle Excitations*. 2020. arXiv: [2010.13973 \[cond-mat.stat-mech\]](https://arxiv.org/abs/2010.13973).
- [111] J. Zhang and M. A. Rajabpour. “Corrections to universal Rényi entropy in quasiparticle excited states of quantum chains”. In: *Journal of Statistical Mechanics: Theory and Experiment* 2021.9 (2021), p. 093101. DOI: [10.1088/1742-5468/ac1f28](https://doi.org/10.1088/1742-5468/ac1f28).
- [112] J. Zhang and M. A. Rajabpour. “Excited state Rényi entropy and subsystem distance in two-dimensional non-compact bosonic theory. Part II. Multi-particle states”. In: *J. High Energ. Phys.* 2021.8 (2021). DOI: [10.1007/jhep08\(2021\)106](https://doi.org/10.1007/jhep08(2021)106).
- [113] J. Zhang and M. A. Rajabpour. *Entanglement of magnon excitations in spin chains*. 2021. arXiv: [2109.12826 \[cond-mat.stat-mech\]](https://arxiv.org/abs/2109.12826).
- [114] J. Wess and B. Zumino. “Consequences of anomalous ward identities”. In: *Physics Letters B* 37.1 (1971), pp. 95–97.
- [115] S. Novikov. “Multivalued functions and functionals. An analogue of the Morse theory”. In: *Sov. Math. Dokl.* 24 (1981), p. 222.
- [116] S. Novikov. “The Hamiltonian formalism and a many-valued analogue of Morse theory”. In: *Russ. Math. Sur.* 37 (1982), p. 1.
- [117] E. Witten. “Global aspects of current algebra”. In: *Nucl. Phys. B* 223.2 (1983), pp. 422–432.

-
- [118] E. Witten. “Non-abelian bosonization in two dimensions”. In: *Communications in Mathematical Physics* 92.4 (1984), pp. 455–472.
- [119] P. Dorey and J. L. Miramontes. “Mass scales and crossover phenomena in the homogeneous sine-Gordon models”. In: *Nucl. Phys. B* 697.3 (2004), pp. 405–461.
- [120] O. A. Castro-Alvaredo, A. Fring, and C. Korff. “Form factors of the homogeneous sine-Gordon models”. In: *Physics Letters B* 484.1 (2000), pp. 167–176.
- [121] O. A. Castro-Alvaredo and A. Fring. “Identifying the operator content, the homogeneous sine-Gordon models”. In: *Nucl. Phys. B* 604.1 (2001), pp. 367–390.
- [122] O. A. Castro-Alvaredo and A. Fring. “Renormalization group flow with unstable particles”. In: *Phys. Rev. D* 63.2 (2000), p. 021701. DOI: [10.1103/PhysRevD.63.021701](https://doi.org/10.1103/PhysRevD.63.021701).
- [123] O. A. Castro-Alvaredo and A. Fring. “Decoupling the $SU(N)_2$ -homogeneous sine-Gordon model”. In: *Phys. Rev. D* 64.8 (2001), p. 085007. DOI: [10.1103/PhysRevD.64.085007](https://doi.org/10.1103/PhysRevD.64.085007).
- [124] Z. Bajnok, J. Balog, K. Ito, Y. Satoh, and G. Z. Tóth. “On the mass-coupling relation of multi-scale quantum integrable models”. In: *J. High Energ. Phys.* 2016.6 (2016), p. 71.
- [125] Z. Bajnok, J. Balog, K. Ito, Y. Satoh, and G. Z. Tóth. “Exact Mass-Coupling Relation for the Homogeneous Sine-Gordon Model”. In: *Phys. Rev. Lett.* 116.18 (2016), p. 181601. DOI: [10.1103/PhysRevLett.116.181601](https://doi.org/10.1103/PhysRevLett.116.181601).
- [126] A. Fring and C. Korff. “Colour valued scattering matrices”. In: *Physics Letters B* 477.1 (2000), pp. 380–386. DOI: [10.1016/S0370-2693\(00\)00226-4](https://doi.org/10.1016/S0370-2693(00)00226-4).
- [127] A. B. Zamolodchikov. “Resonance factorized scattering and roaming trajectories”. In: *J. Phys. A: Math. Gen.* 39.41 (2006), pp. 12847–12861.
- [128] P. Dorey, G. Siviour, and G. Takács. “Form factor relocalisation and interpolating renormalisation group flows from the staircase model”. In: *J. High Energ. Phys.* 2015.3 (2015), p. 54.
- [129] P. Dorey and F. Ravanini. “Generalising the staircase models”. In: *Nucl. Phys. B* 406.3 (1993), pp. 708–726.
- [130] B. Doyon. “Lecture Notes On Generalised Hydrodynamics”. In: *SciPost Phys. Lect. Notes* (2020), p. 18. DOI: [10.21468/SciPostPhysLectNotes.18](https://doi.org/10.21468/SciPostPhysLectNotes.18).
- [131] T. Kinoshita, T. Wenger, and D. S. Weiss. “A quantum Newton’s cradle”. In: *Nature* 440.7086 (2006), pp. 900–903.
-

- [132] D. Bernard and B. Doyon. “Conformal field theory out of equilibrium: a review”. In: *J. Stat. Mech.* 2016.6 (2016), p. 064005. DOI: [10.1088/1742-5468/2016/06/064005](https://doi.org/10.1088/1742-5468/2016/06/064005).
- [133] E. Ilievski, M. Medenjak, T. Prosen, and L. Zadnik. “Quasilocal charges in integrable lattice systems”. In: *J. Stat. Mech.* 2016.6 (2016), p. 064008. DOI: [10.1088/1742-5468/2016/06/064008](https://doi.org/10.1088/1742-5468/2016/06/064008).
- [134] J. Mossel and J.-S. Caux. “Generalized TBA and generalized Gibbs”. In: *J. Phys. A: Math. Theor.* 45.25 (2012), p. 255001. DOI: [10.1088/1751-8113/45/25/255001](https://doi.org/10.1088/1751-8113/45/25/255001).
- [135] B. Doyon and T. Yoshimura. “A note on generalized hydrodynamics: inhomogeneous fields and other concepts”. In: *SciPost Phys.* 2.2 (2017), p. 014. DOI: [10.21468/SciPostPhys.2.2.014](https://doi.org/10.21468/SciPostPhys.2.2.014).
- [136] A. Bastianello and A. De Luca. “Integrability-Protected Adiabatic Reversibility in Quantum Spin Chains”. In: *Phys. Rev. Lett.* 122.24 (2019), p. 240606. DOI: [10.1103/PhysRevLett.122.240606](https://doi.org/10.1103/PhysRevLett.122.240606).
- [137] A. Bastianello, V. Alba, and J.-S. Caux. “Generalized Hydrodynamics with Space-Time Inhomogeneous Interactions”. In: *Phys. Rev. Lett.* 123.13 (2019), p. 130602. DOI: [10.1103/PhysRevLett.123.130602](https://doi.org/10.1103/PhysRevLett.123.130602).
- [138] A. Bastianello, A. De Luca, and R. Vasseur. “Hydrodynamics of weak integrability breaking”. In: (2021). arXiv: [2103.11997 \[cond-mat.stat-mech\]](https://arxiv.org/abs/2103.11997).
- [139] J. De Nardis, D. Bernard, and B. Doyon. “Hydrodynamic Diffusion in Integrable Systems”. In: *Phys. Rev. Lett.* 121.16 (2018), p. 160603. DOI: [10.1103/PhysRevLett.121.160603](https://doi.org/10.1103/PhysRevLett.121.160603).
- [140] S. Gopalakrishnan, D. A. Huse, V. Khemani, and R. Vasseur. “Hydrodynamics of operator spreading and quasiparticle diffusion in interacting integrable systems”. In: *Phys. Rev. B* 98.22 (2018), p. 220303. DOI: [10.1103/PhysRevB.98.220303](https://doi.org/10.1103/PhysRevB.98.220303).
- [141] J. D. Nardis, D. Bernard, and B. Doyon. “Diffusion in generalized hydrodynamics and quasiparticle scattering”. In: *SciPost Phys.* 6.4 (2019), p. 49. DOI: [10.21468/SciPostPhys.6.4.049](https://doi.org/10.21468/SciPostPhys.6.4.049).
- [142] M. Fagotti. “Locally quasi-stationary states in noninteracting spin chains”. In: *SciPost Phys.* 8.3 (2020), p. 48. DOI: [10.21468/SciPostPhys.8.3.048](https://doi.org/10.21468/SciPostPhys.8.3.048).
- [143] A. Bastianello, J. De Nardis, and A. De Luca. “Generalized hydrodynamics with dephasing noise”. In: *Phys. Rev. B* 102.16 (2020), p. 161110. DOI: [10.1103/PhysRevB.102.161110](https://doi.org/10.1103/PhysRevB.102.161110).

-
- [144] X. Cao, V. B. Bulchandani, and J. E. Moore. “Incomplete Thermalization from Trap-Induced Integrability Breaking: Lessons from Classical Hard Rods”. In: *Phys. Rev. Lett.* 120.16 (2018), p. 164101. DOI: [10.1103/PhysRevLett.120.164101](https://doi.org/10.1103/PhysRevLett.120.164101).
- [145] A. J. Friedman, S. Gopalakrishnan, and R. Vasseur. “Diffusive hydrodynamics from integrability breaking”. In: *Phys. Rev. B* 101.18 (2020), p. 180302. DOI: [10.1103/PhysRevB.101.180302](https://doi.org/10.1103/PhysRevB.101.180302).
- [146] J. Durnin, M. J. Bhaseen, and B. Doyon. “Nonequilibrium Dynamics and Weakly Broken Integrability”. In: *Phys. Rev. Lett.* 127.13 (2021), p. 130601. DOI: [10.1103/PhysRevLett.127.130601](https://doi.org/10.1103/PhysRevLett.127.130601).
- [147] M. Schemmer, I. Bouchoule, B. Doyon, and J. Dubail. “Generalized Hydrodynamics on an Atom Chip”. In: *Phys. Rev. Lett.* 122.9 (2019), p. 090601. DOI: [10.1103/PhysRevLett.122.090601](https://doi.org/10.1103/PhysRevLett.122.090601).
- [148] O. A. Castro-Alvaredo, C. De Fazio, B. Doyon, and A. Ziólkowska. “Generalized Hydrodynamics of Particle Creation and Decay”. In: *preparation* (2021).
- [149] L. Bonnes, F. H. L. Essler, and A. M. Läuchli. ““Light-Cone” Dynamics After Quantum Quenches in Spin Chains”. In: *Phys. Rev. Lett.* 113.18 (2014), p. 187203. DOI: [10.1103/PhysRevLett.113.187203](https://doi.org/10.1103/PhysRevLett.113.187203).
- [150] B. Doyon, T. Yoshimura, and J.-S. Caux. “Soliton Gases and Generalized Hydrodynamics”. In: *Phys. Rev. Lett.* 120.4 (2018), p. 045301. DOI: [10.1103/PhysRevLett.120.045301](https://doi.org/10.1103/PhysRevLett.120.045301).
- [151] D. Bernard and B. Doyon. “Energy flow in non-equilibrium conformal field theory”. In: *J. Phys. A: Math. Theor.* 45.36 (2012), p. 362001. DOI: [10.1088/1751-8113/45/36/362001](https://doi.org/10.1088/1751-8113/45/36/362001).
- [152] D. Bernard and B. Doyon. “Non-Equilibrium Steady States in Conformal Field Theory”. In: *Annales Henri Poincaré* 16.1 (2015), pp. 113–161. DOI: [10.1007/s00023-014-0314-8](https://doi.org/10.1007/s00023-014-0314-8).
- [153] O. Castro-Alvaredo, Y. Chen, B. Doyon, and M. Hoogeveen. “Thermodynamic Bethe ansatz for non-equilibrium steady states: exact energy current and fluctuations in integrable QFT”. In: *J. Stat. Mech.* 2014.3 (2014), P03011. DOI: [10.1088/1742-5468/2014/03/p03011](https://doi.org/10.1088/1742-5468/2014/03/p03011).
-

- [154] D. X. Horváth. “Hydrodynamics of massless integrable RG flows and a non-equilibrium c-theorem”. In: *J. High Energ. Phys.* 2019.10 (2019), p. 20. DOI: [10.1007/JHEP10\(2019\)020](https://doi.org/10.1007/JHEP10(2019)020).
- [155] URL: <https://youtu.be/lvWd4qxMShQ>.
- [156] M. Mazzone, O. Pomponio, O. A. Castro-Alvaredo, and F. Ravanini. “The staircase model: massless flows and hydrodynamics”. In: *J. Phys. A: Math. Theor.* 54.40 (2021), p. 404005. DOI: [10.1088/1751-8121/ac2141](https://doi.org/10.1088/1751-8121/ac2141).
- [157] URL: <https://youtu.be/7jX0HFa1cgs>.
- [158] URL: <https://youtu.be/m2ApWaQkcHE>.
- [159] URL: <https://youtu.be/suIftU1oNcw>.
- [160] V. B. Bulchandani, R. Vasseur, C. Karrasch, and J. E. Moore. “Solvable Hydrodynamics of Quantum Integrable Systems”. In: *Phys. Rev. Lett.* 119.22 (2017), p. 220604. DOI: [10.1103/PhysRevLett.119.220604](https://doi.org/10.1103/PhysRevLett.119.220604).
- [161] B. Doyon, J. Dubail, R. Konik, and T. Yoshimura. “Large-Scale Description of Interacting One-Dimensional Bose Gases: Generalized Hydrodynamics Supersedes Conventional Hydrodynamics”. In: *Phys. Rev. Lett.* 119.19 (2017), p. 195301. DOI: [10.1103/PhysRevLett.119.195301](https://doi.org/10.1103/PhysRevLett.119.195301).
- [162] B. Doyon, H. Spohn, and T. Yoshimura. “A geometric viewpoint on generalized hydrodynamics”. In: *Nucl. Phys. B* 926 (2018), pp. 570–583. DOI: [10.1016/j.nuclphysb.2017.12.002](https://doi.org/10.1016/j.nuclphysb.2017.12.002).
- [163] F. S. Møller, G. Perfetto, B. Doyon, and J. Schmiedmayer. “Euler-scale dynamical correlations in integrable systems with fluid motion”. In: *SciPost Phys. Core* 3.2 (2020), p. 16. DOI: [10.21468/SciPostPhysCore.3.2.016](https://doi.org/10.21468/SciPostPhysCore.3.2.016).
- [164] F. S. Møller and J. Schmiedmayer. “Introducing iFluid: a numerical framework for solving hydrodynamical equations in integrable models”. In: *SciPost Phys.* 8.3 (2020), p. 41. DOI: [10.21468/SciPostPhys.8.3.041](https://doi.org/10.21468/SciPostPhys.8.3.041).
- [165] URL: <https://youtu.be/mvNnzBL7vYs>.
- [166] URL: <https://youtu.be/yyLcuTn41BY>.
- [167] L. Capizzi, O. A. Castro-Alvaredo, C. De Fazio, M. Manzoni, and L. Santamaría-Sanz. “Symmetry Resolved Entanglement: Excited States in Quantum Field Theory”. In: *preparation* (2021).

- [168] M. Goldstein and E. Sela. “Symmetry-Resolved Entanglement in Many-Body Systems”. In: *Phys. Rev. Lett.* 120.20 (2018), p. 200602. DOI: [10.1103/PhysRevLett.120.200602](https://doi.org/10.1103/PhysRevLett.120.200602).
- [169] S. Murciano, G. Di Giulio, and P. Calabrese. “Entanglement and symmetry resolution in two dimensional free quantum field theories”. In: *J. High Energ. Phys.* 2020.8 (2020), p. 73. DOI: [10.1007/JHEP08\(2020\)073](https://doi.org/10.1007/JHEP08(2020)073).
- [170] D. X. Horváth and P. Calabrese. “Symmetry resolved entanglement in integrable field theories via form factor bootstrap”. In: *J. High Energ. Phys.* 2020.11 (2020), p. 131. DOI: [10.1007/JHEP11\(2020\)131](https://doi.org/10.1007/JHEP11(2020)131).
- [171] D. X. Horváth, L. Capizzi, and P. Calabrese. “U(1) symmetry resolved entanglement in free 1+1 dimensional field theories via form factor bootstrap”. In: *J. High Energ. Phys.* 2021.5 (2021), p. 197. DOI: [10.1007/JHEP05\(2021\)197](https://doi.org/10.1007/JHEP05(2021)197).
- [172] G. H. Golub and J. H. Welsch. “Calculation of Gauss quadrature rules”. In: *Math. Comp.* 23 (1969), pp. 221–230. DOI: [10.1090/S0025-5718-69-99647-1](https://doi.org/10.1090/S0025-5718-69-99647-1).
- [173] I. Bogaert. “Iteration-free computation of Gauss–Legendre quadrature nodes and weights”. In: *SIAM J. Sci. Comput.* 36.3 (2014), A1008–A1026. DOI: [10.1137/140954969](https://doi.org/10.1137/140954969).